

(2)

PIEZOELECTRIC AND ELECTROSTRICTIVE MATERIALS  
FOR TRANSDUCERS APPLICATIONS

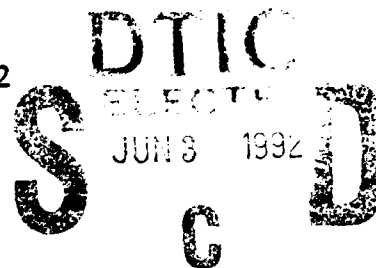
Period February 1, 1991 to January 31, 1992

AD-A250 891



Final Report

VOLUME III



OFFICE OF NAVAL RESEARCH  
Contract No. N00014-89-J-1689

APPROVED FOR PUBLIC RELEASE - DISTRIBUTION UNLIMITED

Reproduction in whole or in part is permitted for any purpose  
of the United States Government

L. E. Cross  
R. E. Newnham  
A. S. Bhalla  
J. P. Dougherty  
J. H. Adair  
V. K. Varadan  
V. V. Varadan

PENNSSTATE



THE MATERIALS RESEARCH LABORATORY  
UNIVERSITY PARK, PA

92 6 01 158

92-14489



## REPORT DOCUMENTATION PAGE

Form Approved  
GSA's No. 0704-0100

|  |       |   |   |                                       |
|--|-------|---|---|---------------------------------------|
| 1a. REPORT SECURITY CLASSIFICATION   |       |   | 1b. RESTRICTIVE MARKINGS  |                                       |
| 2a. SECURITY CLASSIFICATION AUTHORITY  |       |   | 3. DISTRIBUTION/AVAILABILITY OF REPORT<br>Reproduction in whole or in part is permitted for any purpose of the United States Government |                                       |
| 2b. DECLASSIFICATION/DOWNGRADING SCHEDULE  |       |   | 5. MONITORING ORGANIZATION REPORT NUMBER(S)   |                                       |
| 4. PERFORMING ORGANIZATION REPORT NUMBER(S)<br>N00014-89-J-1689  |       |   | 7a. NAME OF MONITORING ORGANIZATION   |                                       |
| 6a. NAME OF PERFORMING ORGANIZATION<br>MATERIALS RESEARCH LABORATORY   |       | 6b. OFFICE SYMBOL<br>(If applicable)        | 7b. ADDRESS (City, State, and ZIP Code)   |                                       |
| 6c. ADDRESS (City, State, and ZIP Code)<br>THE PENNSYLVANIA STATE UNIVERSITY<br>UNIVERSITY PARK, PA 16802  |       |   | 9. PROCUREMENT INSTRUMENT IDENTIFICATION NUMBER   |                                       |
| 8a. NAME OF FUNDING/SPONSORING ORGANIZATION  |       | 8b. OFFICE SYMBOL<br>(If applicable)        | 10. SOURCE OF FUNDING NUMBERS   |                                       |
| 8c. ADDRESS (City, State, and ZIP Code)  |       |   | PROGRAM<br>ELEMENT NO.  | PROJECT<br>NO.                        |
|  |       |   | TASK<br>NO.   | WORK UNIT<br>ACCESSION NO.            |
| 11. TITLE (Include Security Classification)<br>PIEZOELECTRIC AND ELECTROSTRICTIVE MATERIALS FOR TRANSDUCER APPLICATIONS  |       |   |   |                                       |
| 12. PERSONAL AUTHOR(S)<br>L. E. Cross, R. E. Newnham, A. S. Bhalla, J. P. Dougherty, J. H. Adair, V.K. Varadan, V.V. Varadan   |       |   |   |                                       |
| 13a. TYPE OF REPORT<br>FINAL   |       | 13b. TIME COVERED<br>FROM 2/1/91 TO 1/31/92 |   | 14. DATE OF REPORT (Year, Month, Day) |
| 15. PAGE COUNT   |       |   |   |                                       |
| 16. SUPPLEMENTARY NOTATION   |       |   |   |                                       |
| 17. COSATI CODES   |       |   | 18. SUBJECT TERMS (Continue on reverse if necessary and identify by block number)   |                                       |
| FIELD  | GROUP | SUB-GROUP                                   |   |                                       |
|  |       |   |   |                                       |
|  |       |   |   |                                       |
| 19. ABSTRACT (Continue on reverse if necessary and identify by block number)<br><br>SEE REVERSE SIDE OF PAGE.  |       |   |   |                                       |
| 20. DISTRIBUTION/AVAILABILITY OF ABSTRACT<br><input type="checkbox"/> UNCLASSIFIED/UNLIMITED <input type="checkbox"/> SAME AS RPT. <input type="checkbox"/> DTIC USERS |       |   | 21. ABSTRACT SECURITY CLASSIFICATION  |                                       |
| 22a. NAME OF RESPONSIBLE INDIVIDUAL  |       |   | 22b. TELEPHONE (Include Area Code)  | 22c. OFFICE SYMBOL                    |

## ABSTRACT

This report documents work carried out in the Materials Research Laboratory of The Pennsylvania State University on the third and final year of the program on "Piezoelectric and Electrostrictive Materials for Transducers Applications" sponsored by the Office of Naval Research (ONR) under grand No. N00014-89-J-1689. This marks the termination of a very long and highly productive sequence of contracts and grants focusing on the development of new materials for Piezoelectric and Electrostrictive transducer applications carried through under core ONR funding. Fortunately many elements of the work will be continuing on a new University Research Initiative (URI) program under ONR sponsorship.

Highlights of the past year's activities include: an increased emphasis upon the flexensional (moonie) type actuators, modeling both the internal stress distribution as a function of geometry, and the very interesting resonant mode structure of the composites; A more refined focus upon the performance of piezoelectric ceramic transducers, particularly under high drive levels is developing with concern for the extrinsic domain and phase boundary contributions to response. Measurement and modelling are being used to explore the nonlinearity and the frequency response and to examine the phase partitioning at the rhombohedral : tetragonal morpho-optic phase boundary in the PZT system. Phenomena limiting lifetime in polarization and phase switching actuators are being explored to separate surface and volume effects and those due to grain size and flaw population differences. New work has been initiated to examine Acoustic Emission as a technique, in combination with Barkhausen current pulse analysis, to separate and evaluate domain switching and microcracking in polarization switching systems.

From work on this program it has now become clear that the relaxor ferroelectrics are in fact close analogues of the magnetic spin glasses, so that the spin glass formalism can be used to explain the very wide range of dielectric, elastic and electrostrictive properties. The remaining outstanding fundamental problem is that of the detailed interrelationship between the known nano-heterogeneity in the structure and chemistry and the nanopolar regions which contribute the electrical response.

Of very high practical interest is the manner in which the relaxor can be field biased into extremely strong piezoelectric response. Work is going forward to examine this response in detail and to explore the possibility that such "super-response" can be induced by chemical (solid solution) means.

Processing studies have focused upon new lower temperature consolidations for relaxors, and upon new compositions for high temperature piezoelectric ceramics.

In parallel with the ONR Transducer Program the Laboratory has extensive DARPA sponsored research on ferroelectric thin films. Since the films structures frequently involve materials like the PZT, PMN : PT, PLT and PLZT families of compositions and do explore piezoelectric effects and applications, a small group of the most relevant papers from this program are appended to the report.

**PIEZOELECTRIC AND ELECTROSTRICTIVE MATERIALS  
FOR TRANSDUCERS APPLICATIONS**

Period February 1, 1991 to January 31, 1992

Final Report

VOLUME III

**OFFICE OF NAVAL RESEARCH**  
Contract No. N00014-89-J-1689

**APPROVED FOR PUBLIC RELEASE -- DISTRIBUTION UNLIMITED**

Reproduction in whole or in part is permitted for any purpose  
of the United States Government

L. E. Cross  
R. E. Newnham  
A. S. Bhalla  
J. P. Dougherty  
J. H. Adair  
V. K. Varadan  
V. V. Varadan



|                    |                                     |
|--------------------|-------------------------------------|
| Accession For      |                                     |
| NTIS GRA&I         | <input checked="" type="checkbox"/> |
| DTIC TAB           | <input type="checkbox"/>            |
| Unannounced        | <input type="checkbox"/>            |
| Justification      |                                     |
| By                 |                                     |
| Distribution/      |                                     |
| Availability Codes |                                     |
| Dist               | Avail and/or<br>Special             |
| A-1                |                                     |

**PENNSTATE**



**THE MATERIALS RESEARCH LABORATORY**  
UNIVERSITY PARK, PA

## TABLE OF CONTENTS

|  |    |
|--|----|
| ABSTRACT.....  | 5  |
| INTRODUCTION.....  | 7  |
| 1.0 GENERAL SUMMARY PAPERS.....  | 9  |
| 2.0 COMPOSITE MATERIALS.....   | 9  |
| 3.0 PIEZOELECTRIC CERAMICS.....  | 10 |
| 4.0 PHENOMENOLOGICAL STUDIES.....  | 11 |
| 5.0 RELAXORS AND RELATED SYSTEMS.....  | 12 |
| 6.0 PROCESSING STUDIES.....  | 13 |
| 7.0 FERROELECTRIC THIN FILMS.....  | 14 |
| 8.0 APPRENTICE PROGRAM.....  | 15 |
| 9.0 PAPERS PUBLISHED IN REFEREED JOURNALS.....                               | 17 |
| 10.0 INVITED PAPERS PRESENTED AT NATIONAL<br>AND INTERNATIONAL MEETINGS..... | 18 |
| 11.0 CONTRIBUTED PAPERS AT NATIONAL AND INTERNATIONAL MEETINGS. ....         | 19 |
| 12.0 HONORS TO MRL FACULTY AND STUDENTS.....                                 | 24 |
| 13.0 REFERENCES .....  | 24 |

## APPENDICES

### *General Summary Papers*

1. L. Eric Cross. "Ferroelectric Ceramics Tailoring Properties for Specific Applications."
2. R. E. Newnham and T. R. Shrout. "Advanced Ceramics," *Electronic Ceramics* 1, 601-620.

### *Composite Materials*

3. R. E. Newnham "Tunable Transducers: Nonlinear Phenomena in Electroceramics," National Institute of Standards and Technology Special Publication 804, Chemistry of Electronic Ceramic Materials, Proceedings of the International Conference held in Jackson, WY, August 17-22, 1990, issued January 1991.
4. R. E. Newnham. "Composite Electroceramics," *International Encyclopedia of Composites*, Vol. 6, 158-173.

TABLE OF CONTENTS  
(continued)

*Composite Materials (continued)*

5. M. Blaszkiewicz, R. E. Newnham and Q. C. Xu. "Tunable Transducers as Smart Materials," *Transducers 91*, 6th International Conference Solid State Sensors and Actuators, San Francisco, CA (June 24-28, 1991).
6. Q. C. Xu, S. Yoshikawa, J. R. Belsick and R. E. Newnham. "Piezoelectric Composites with High Sensitivity and High Capacitance for Use at High Pressure," *IEEE Transactions on Ultrasonics, Ferroelectrics, and Frequency Control* **38** (6), 634-639 (November 1991).
7. Q. C. Xu, A. Dogan, J. Tressler, S. Yoshikawa and R. E. Newnham. "Ceramic-Metal Composite Actuator."

*Piezoelectric Ceramics*

8. Q. Y. Jiang, W. Cao and L. E. Cross. "Effects of Surface Layers on the Physical Properties of Lanthanum Doped Lead Zirconate Titanate Ceramic."
9. Qiyue Jiang, Wenwu Cao and L. E. Cross. "The Influence of Surface Contamination on Electric Fatigue of Ferroelectrics."
10. L. E. Cross and Q. Jiang. "Fatigue Effects in High Strain Actuators."
11. V. Srikanth and E. C. Subbarao. "Acoustic Emission in Ferroelectric Lead Titanate Ceramics: Origin and Recombination of Microcracks," *Acta Metall. Mater.* ( received February 11, 1991)
12. M. Fukuhara, A. S. Bhalla and R. E. Newnham. "Morphotropic Phase Boundary in the  $Pb(Zr_xTi_{1-x})O_3$  System," *Phys. Stat. Sol. (a)* **122**, 677 (1990)
13. Wenwu Cao and L. E. Cross. "Theory of Tetragonal Twin Structure in Ferroelectric Perovskites with a First-Order Phase Transition," *Physical Review B* **44** (1), 5-12 (1 July 1991-I).
14. Shaoping Li, Wenwu Cao and L. E. Cross. "The Extrinsic Nature of Nonlinear Behaviour Observed in Lead Zirconate Titanate Ferroelectric Ceramic," *J. Appl. Phys.* **69** (10), 7219-7224 (15 May 1991).
15. Shaoping Li, Wenwu Cao, R. E. Newnham and L. E. Cross. "Electromechanical Nonlinearity of Ferroelectric Ceramics and Related Non-180° Domain Wall Motions."
16. Shaoping Li, Wenwu Cao and L. E. Cross. "Stress and Electric Displacement Distribution Near Griffith's type III Crack Tips in Piezoceramics," *Materials Letters* **10** (6), 219-222 (December 1990).

*Phenomenological Studies*

17. George A. Rossetti, Jr., L. E. Cross and Keiko Kushida. "Stress Induced Shift of the Curie Point in Epitaxial  $PbTiO_3$  Thin Films," *Appl. Phys. Lett.* **59** (20), 2524-2526 (11 November 1991).

TABLE OF CONTENTS  
(continued)

*Phenomenological Studies (continued)*

18. G. A. Rossetti, Jr., T. Nishimura and L. E. Cross. "X-ray and Phenomenological Study of Lanthanum-Modified Lead Zirconate-Titanates in the Vicinity of the Relaxor Phase Transition Region," *J. Appl. Phys.* **70** (3), 1630-1637 (1 August 1991).
19. Wenwu Cao and L. Eric Cross. "Distribution Functions of Coexisting Phases in a Complete Solid Solution System."

*Relaxors and Related Systems*

20. Dwight D. Viehland. "The Glassy Behaviour of Relaxor Ferroelectrics," Abstract from A Thesis in Solid State Science, The Pennsylvania State University, The Graduate School (May 1991).
21. Dwight Viehland, S. Jang, L. Eric Cross and Manfred Wuttig. "The Dielectric Relaxation of Lead Magnesium Niobate Relaxor Ferroelectrics," *Philosophical Magazine B* **64** (3), 335-344 (1991).
22. Dwight Viehland, S. J. Jang, L. Eric Cross and Manfred Wuttig. "Anelastic Relaxation and Internal Strain in Lead Magnesium Niobate Relaxors," *Philosophical Magazine A* **64** (4), 835-849 (1991).
23. Dwight Viehland, S. J. Jang, L. Eric Cross and Manfred Wuttig. "Local Polar Configurations in Lead Magnesium Niobate Relaxors," *J. Appl. Phys.* **69** (1), 414-419 (1 January 1991).
24. Dwight Viehland, J. F. Li, S. J. Jang, L. Eric Cross and Manfred Wuttig. "Dipolar-Glass Model for Lead Magnesium Niobate," *Physical Review B* **43** (10), 8316-8320 (1 April 1991).
25. Ruyan Guo. "Ferroelectric Properties of Lead Barium Niobate Compositions Near the Morphotropic Phase Boundary," Abstract from A Thesis in Solid State Science, The Pennsylvania State University, The Graduate School (December 1990).
26. R. Guo, A. S. Bhalla and L. E. Cross. "Pyroelectric Properties of Lead Barium Niobate Single Crystals," *Ferroelectrics* **118**, 77-83 (1991).
27. C. A. Randall, R. Guo, A. S. Bhalla and L. E. Cross. "Microstructure-Property Relations in Tungsten Bronze Lead Barium Niobate,  $Pb_{1-x}Ba_xNb_2O_6$ ," *J. Mater. Res.* **6** (8), 1720-1728 (August 1991).
28. Jayne R. Giniewicz. "An Investigation of the Lead Scandium Tantalate-Lead Titanate Solid Solution System," Abstract from A Thesis in Solid State Science, The Pennsylvania State University, The Graduate School (December 1991).
29. J. R. Giniewicz, A. S. Bhalla and L. E. Cross. "Pyroelectric Response and Depolarization Behaviour of  $(1-x)Pb(Sc_{1/2}Ta_{1/2})O_3$ - $(x)PbTiO_3$  Materials," *Ferroelectrics* **118**, 157-164 (1991).
30. D. J. Tyalor, D. Damjanovic and A. S. Bhalla. "Pyroelectric and Dielectric Properties of PMN-Based Ceramics Under DC Bias," *Ferroelectrics* **118**, 143-155 (1991).

TABLE OF CONTENTS  
(continued)

***Processing Studies***

31. V. Srikanth and E. C. Subbarao. "Chemical Reactions of Lead Magnesium Niobate Titanate in the Presence of a Glass," *J. Mater. Res.* **6** (6), 1-16 (June 1991).
32. Paul A. Fulrer and Robert E. Newnham. "La<sub>2</sub>Ti<sub>2</sub>O<sub>7</sub> Ceramics," *J. Am. Ceram. Soc.* **74** (11), 2876-2881 (1991).
33. G. R. Fox, J. H. Adair and R. E. Newnham. "Effects of pH and H<sub>2</sub>O<sub>2</sub> Upon Coprecipitated PbTiO<sub>3</sub> Powders," *J. Mater. Sci.* **26**, 1187-1191 (1991).
34. G. A. Rossetti, Jr., D. J. Watson, R. E. Newnham and J. H. Adair. "Kinetics of the Hydrothermal Crystallization of the Perovskite Lead Titanate," *J. Crystal Growth* **116**, 251-259 (1992).
35. A. Srivastava, A. Bhalla and L. E. Cross. "A Study of Y<sub>1</sub>Ba<sub>2</sub>Cu<sub>3</sub>O<sub>7-x</sub> Thick Films on Ferroelectric Substrates."
36. A. Srivastava, A. Bhalla and L. E. Cross. "Y<sub>1</sub>Ba<sub>2</sub>Cu<sub>3</sub>O<sub>7-x</sub> As An Electrode Materials for Ferroelectric Devices," *Ferroelectrics* **123**, 243-251 (1991).

***Ferroelectric Thin Films***

37. K. R. Udayakumar, J. Chen, P. J. Schuele, L. E. Cross, V. Kumar and S. B. Krupanidhi. "Polarization Reversal and High Dielectric Permittivity in Lead Magnesium Niobate Titanate Thin Films," *Appl. Phys. Lett.* **60** (10), 1187-1189 (9 March 1992).
38. K. R. Udayakumar, P. J. Schuele, J. Chen, K. G. Brooks and L. E. Cross. "Ferroelectric Switching in Lead Zirconate-Lead Zinc Niobate Thin Films,"
39. Keith G. Brooks, Jiayu Chen, K. R. Udayakumar and L. Eric Cross. "Lead Zirconate Titanate Stannate Thin Films for Large Strian Microactuator Applications."
40. K. R. Udayakumar, S. F. Bart, A. M. Flynn, J. Chen, L. S. Tavrow, L. E. Cross, R. A. Brooks, D. J. Ehrlich. "Ferroelectric Thin Film Ultrasonic Micromotors," *IEEE*, 109-113 (1991).
41. Anita M. Flynn, Lee S. Tavrow, Stephen F. Bart, Rodney A. Brooks, Daniel J. Ehrlich, K. R. Udayakumar and L. Eric Cross. "Piezoelectric Micromotors for Microrobots," *J. Microelectromechanical Systems* **1** (1) 47-50 (1992).



## **APPENDIX 19**

# **Distribution Functions of Coexisting Phases in a Complete Solid Solution System**

**Wenwu Cao and L. Eric Cross**

**Materials Research Laboratory**

**The Pennsylvania State University**

**University Park, PA 16802**

**Keywords:** Phase coexistence, Lead zirconate titanate, PZT, Solid solution, Solubility gap,  
Morphotropic phase boundary.

In the phase diagram of a binary system one often encounters a compositional region in which two phases coexist. A common practice is to use the *Lever Rule* to describe the distributions of the two coexisting phases. However, if the binary system is a complete solid solution system, the *Lever Rule* is in conflict with thermodynamic principles. A new type of distributions have been derived for a solid solution system without solubility gap. Applications of the theory to pure and modified lead zirconate-lead titanate (PZT) systems show excellent agreement with the experimental data. Several disputed facts about PZT are also explained satisfactorily.

## I. INTRODUCTION

A general phase diagram of a binary system A-B is given in figure 1(a). There are one liquid phase L and two solid solutions  $\alpha$  and  $\gamma$ . A and B are completely miscible in the liquid phase, but in the solid phase, there is a solubility gap in which the two solid solutions  $\alpha$  and  $\gamma$  coexist. At temperature  $T_1$ , the molar percentages,  $f_\alpha$  and  $f_\gamma$ , of the two coexisting phases are governed by the Lever Rule

$$\begin{aligned} f_\alpha : f_\gamma &= \overline{xh} : \overline{gx} , \\ f_\alpha + f_\gamma &= 1 . \end{aligned} \tag{1}$$

The two special points g and h on the isothermal tieline at  $T \approx T_1$  represent the boundaries of the solubility gap. The corresponding free energy versus composition plot is shown in figure 1(b). One can see that the two boundary compositions are located at the minima of the free energies for the  $\alpha$  and  $\gamma$  phases. For compositions falling inside this solubility gap, two phase mixtures will be formed consisting of g and h compositions, and the ratio of the two phases obeying the Lever Rule.

Figure 1(c) is another type of phase diagram for a A-B binary compound. Looking at the subsolidus region we have three solid solutions,  $\beta$ ,  $\alpha$  and  $\gamma$ . This is a complete solid solution system, viz., no miscibility gaps and no solubility gaps. However, there is a structural phase transition from  $\beta$  to either  $\alpha$  or  $\gamma$  phase depending on the composition of the solid solution. The well known lead zirconate titanate (PZT) and its derivatives are examples of this situation. From thermodynamics there should be no coexistence of the  $\alpha$  and  $\gamma$  phases, which may be understood from the free energy plot in figure 1(c) at temperature  $T = T_1$ . We can see that both free energies for the  $\alpha$  and  $\gamma$  phases are monotonic functions of composition, there is one cross over point k which is termed the morphotropic phase boundary (MPB). From energy minimization principle only one phase is stable for a given composition. However, when the transition temperature is reasonably high and the phase transition is of second order, thermal energy could induce some

amount of second phase at the transition if the two free energies are relatively parallel near the cross over point. In other words, phase coexistence can also occur for the situation shown in figure 1(c). In fact, such coexistence has been observed in the PZT system.

One must note that the phase mixing are completely different in the cases of figure 1(a) and of figure 1(c). In the former we mix two phases of different structures and of different chemical compositions but in the latter we mix two structures of the same chemical composition. Because the different chemical compositions in the former case, the conservation of matter leads to the Lever Rule. but for the case in figure 1(c), the distribution functions cannot be obtained straightforwardly and there is no reason for the two coexisting phases to obey the Lever Rule.

A new approach is proposed for the situation in figure 1(c) when the structural phase transition from  $\beta$  to  $\alpha$  or  $\gamma$  is of second order.<sup>1,2</sup> The proposed theory is applicable to the PZT system because the phase transitions for solid solutions of composition near the MPB are indeed second order.<sup>3</sup> In what follows we briefly describe the proposed model and give two example to show the good agreement between theory and experiments.

## II. THEORY

In order to visualize the concept we look at a hypothesized 2-d problem of a complete solid solution system AC-BC. The high temperature phase is a nonferroelectric square phase as shown in figure 2(a) and the two low temperature phases are rectangular and oblique ferroelectric phases as shown in figures 2(b) and 2(c) respectively. The phase diagram in the subsolidus region is given in figure 1(d). We call the starting point of the morphotropic phase boundary the eutectoid point.

Assume the phase transition at the eutectoid point is second order, strong thermal fluctuations will occur near the transition temperature  $T_c$ . Below  $T_c$  the system will be locked into one of the low temperature phases. The probabilities of going from the square to the rectangular or oblique phases are predetermined in the fluctuating state. This situation is depicted in figure 3.

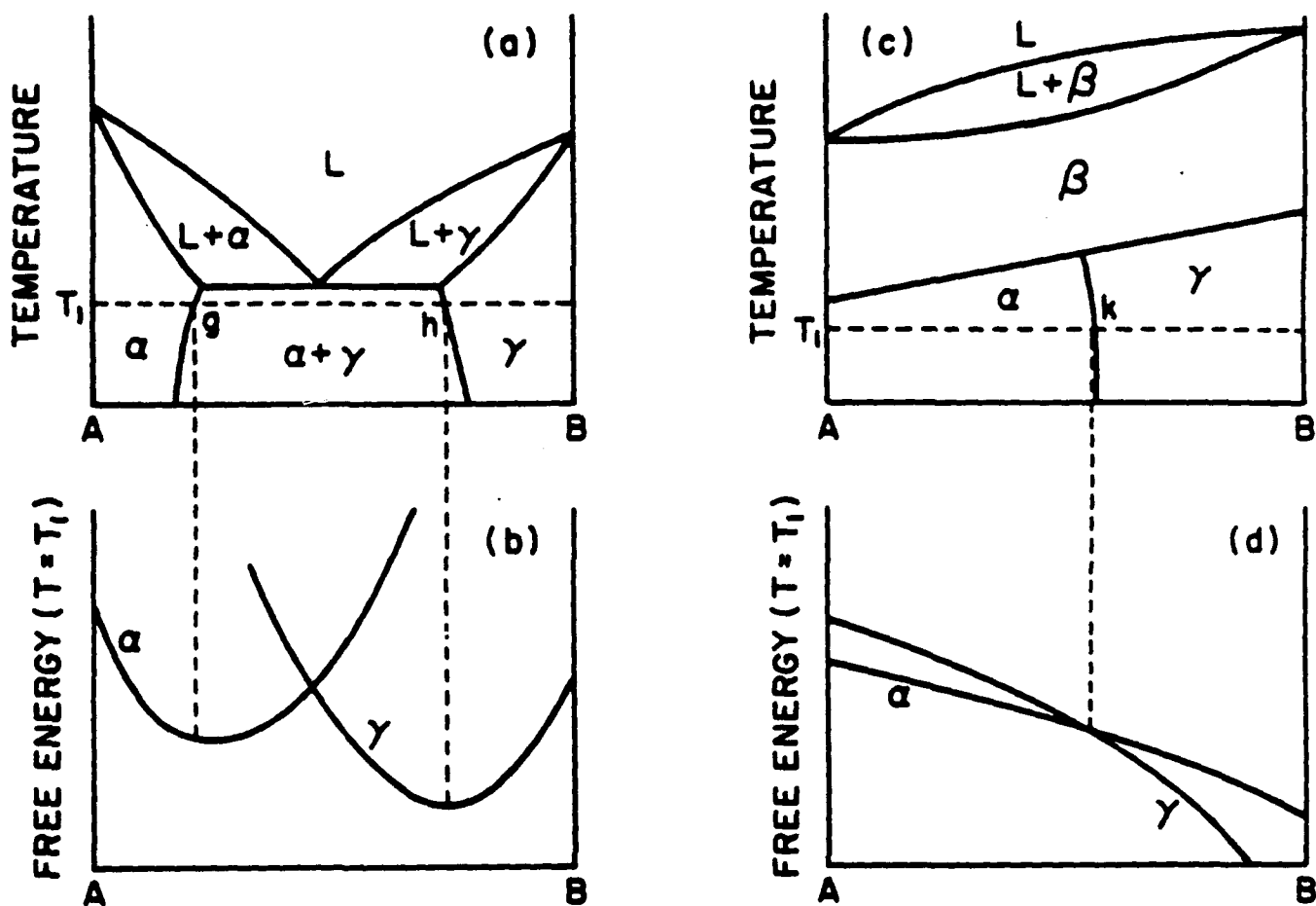
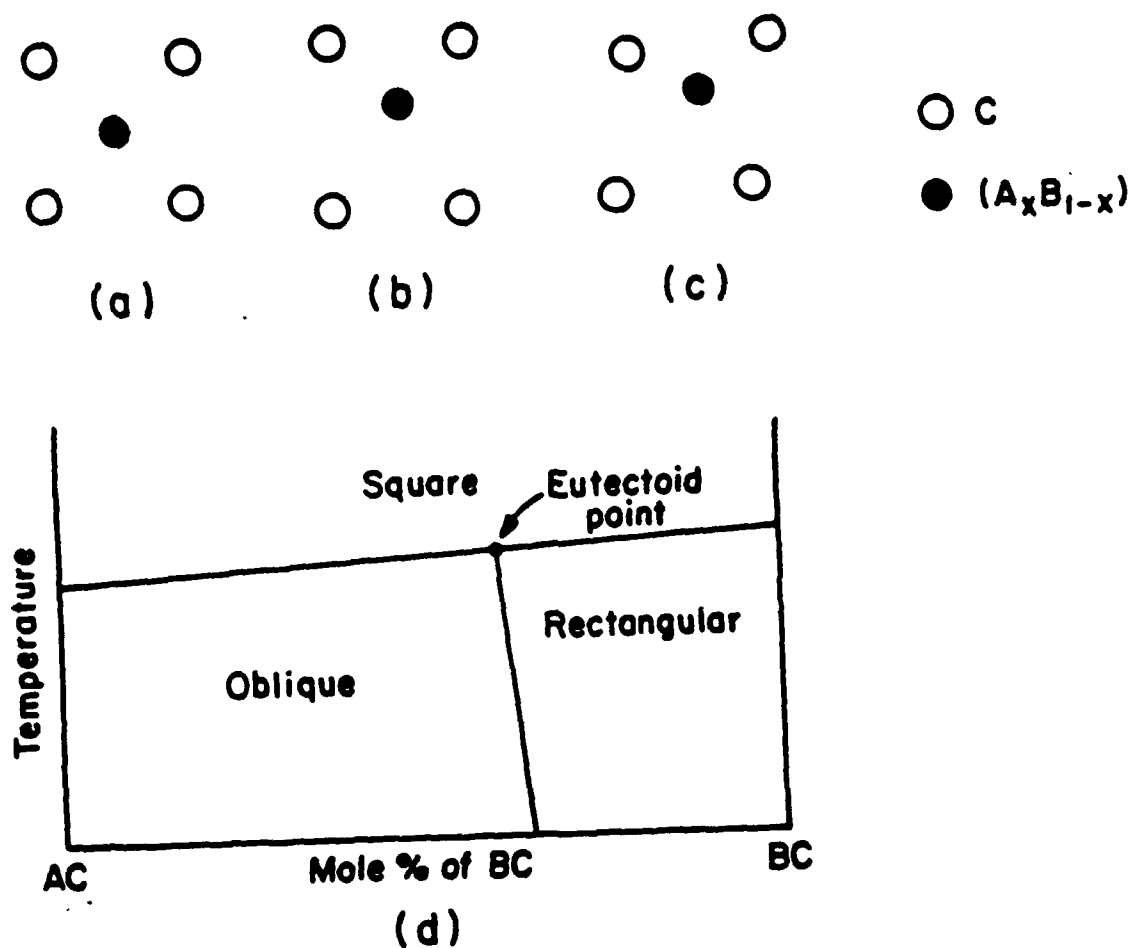


Figure 1 Phase diagram for a binary A - B system.

- (a) Solid solutions  $\alpha$  and  $\gamma$  coexist inside the solubility gap in the subsolidus region.
- (b) The free energies of  $\alpha$  and  $\gamma$  phases versus composition at temperature  $T_1$ . The two minima correspond to the edge compositions of the solubility gap.
- (c) Phase diagram for a complete solid solution system. The nearly vertical line which divides the  $\alpha$  and  $\gamma$  phase is the morphotropic phase boundary.
- (d) The free energies of  $\alpha$  and  $\gamma$  phases at temperature  $T_1$  for a complete solid solution system.



**Figure 2** Illustration of 2-dimensional square-rectangular and square-oblique structural phase transitions in a complete solid solution AC-BC. (a), (b) and (c) are the lattice structures for the paraelectric square, ferroelectric rectangular and ferroelectric oblique phases respectively, (d) is the corresponding phase diagram.

The profile of the fluctuating state near  $T_c$  and the final low temperature states are shown in figures 3(a) and 3(b), respectively in the order parameter space. The thicker line in figure 3(a) illustrates the profile for the case of square – rectangular transition [near BC region in figure 2(d)] and the thinner line is for the case of square – oblique transition [near AC region in figure 2(d)]. Near the MPB composition, the profile of the fluctuation will look like the outer rim of the pattern in figure 3(a).

There is a link between the situations described in figure 3(a) and figure 3(b), which becomes apparent if we assume that the thermal fluctuations are orientational ergodic. Thus the probability of attaining a particular low temperature state in figure 3(b) while on cooling from the fluctuating state figure 3(a) is proportional to the effective angle it occupies in the fluctuating state. A polygon may be constructed to calculate the effective angle of each low temperature state in the 2-d problem. This concept can be easily generalized to a 3-dimensional case for which the probability of attaining a low temperature state is proportional to the effective solid angle that low temperature state occupies in the fluctuating state. A polyhedron may be constructed in the order parameter space in order to calculate these effective solid angles, we name it the probability polyhedron.<sup>(1,2)</sup>

The solid angle calculations may be carried out on the surface of the polyhedron. Due to the relatively high symmetry of the problem we only need to derive a general formula for one right triangle surface as shown in figure 4, the solid angle is given by

$$\Omega_{OABC} = \iint_{\triangle ABC} \frac{a \, ds}{(\rho^2 + a^2)^{3/2}} \quad (2)$$

where  $ds$  is the area element on the surface of  $\triangle ABC$  and  $\rho$  is the distance of this area element from point A. The integration may be conventionally carried out using cylindrical coordinates

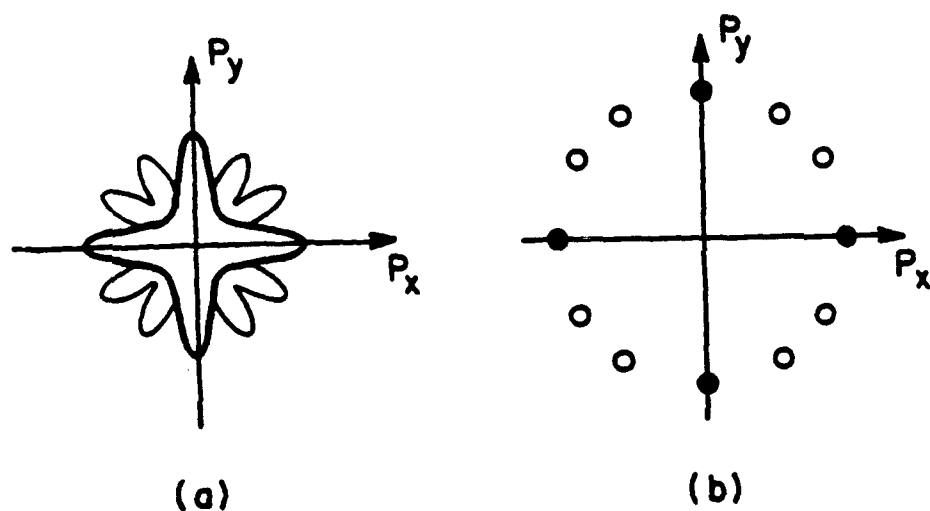


**Figure 3**

- (a) Thermal fluctuation profile at the Eutectoid point in the order parameter space for the 2-dimensional problem described in Figure 2.
- (b) Degenerate low temperature states for the morphotropic phase boundary composition. The solid circles are for the rectangular phase and the open circles are for the oblique phase respectively.



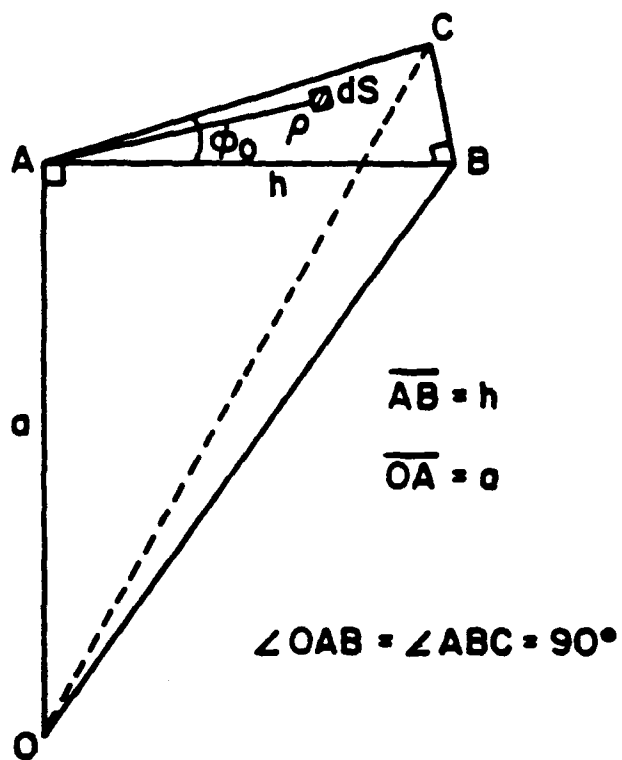


Figure 4 Solid angle subtended by a right angle  $\angle ABC$  with respect to point O.

$$\begin{aligned}
\Omega_{OABC} &= a\phi_0 \int_0^h \frac{\rho d\rho}{(\rho^2 + a^2)^{3/2}} + a \int_h^{h/\cos\phi_0} \frac{\phi_0 - \arccos(h/\rho) \rho d\rho}{(a^2 + \rho^2)^{3/2}} \\
&= \phi_0 - \frac{\pi}{4} - \frac{1}{2} \arcsin \left( \frac{1 - 2 \cos^2 \phi_0 - (h/a)^2}{1 + (h/a)^2} \right)
\end{aligned} \tag{3}$$

According to classical statistics when coexisting phases are not energetically degenerate, the probability of attaining the  $i$ th low temperature state and hence the solid angle  $\Omega_i$  in our problem is proportional to  $\exp\left(-\frac{G_i - G_h}{kT_c}\right)$ , where  $G_i$  and  $G_h$  are the free energies of the  $i$ th low temperature phase and the high temperature phase respectively. Because the solid angle subtended by a given surface area with respect to a given point in space is inversely proportional to the square of the distance between the surface and that point, we may write the distance variable  $r_i$  in the following form

$$r_i \propto \frac{1}{\sqrt{\Omega_i}} \propto \exp\left(\frac{G_i - G_h}{2kT_c}\right). \tag{4}$$

For the PZT system the probability polyhedron is given in figure 5. From eq. (4) we have  $r_T \neq r_R$  unless  $G_T = G_R$ . In order to calculate the distributions of nondegenerate states, we define a distribution anisotropy parameter  $\delta$ :

$$\delta = \frac{r_T - r_R}{r_T} = 1 - \exp\left(\frac{G_R - G_T}{2kT_c}\right). \tag{5}$$

Using the general formula eq. (3) the distribution functions  $f_T$  and  $f_R$  in terms of this single parameter  $\delta$  can be obtained for the polyhedron in figure 5:

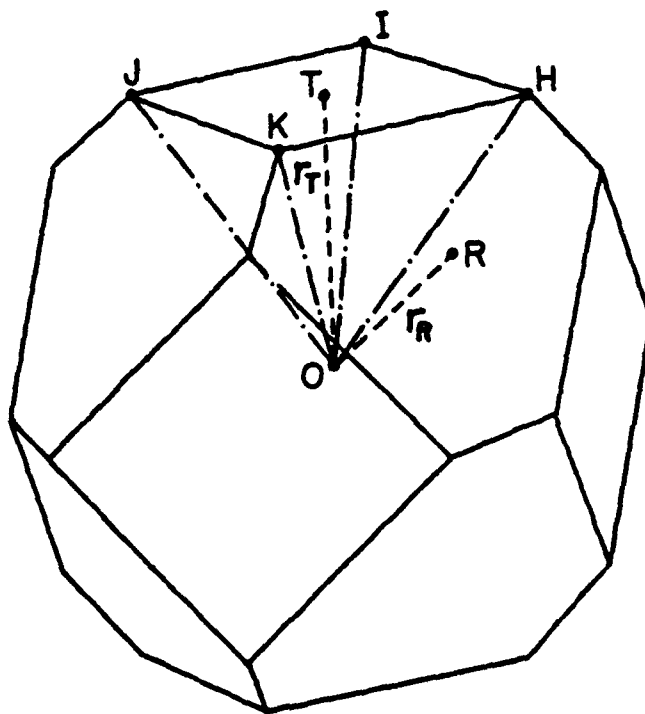


**Figure 5** Probability polyhedron for complete solid solution systems with coexisting rhombohedral and tetragonal phases, such as PZT.

$$f_T = \begin{cases} \frac{6}{\pi} \arcsin \left( \frac{\sqrt{3} [2(1-\delta) - \sqrt{3}]}{2(1-\delta)^2 + [\sqrt{3} - (1-\delta)]^2} \right), & 1 - \sqrt{3} < \delta < 1 - \frac{2}{\sqrt{3}}; \\ \frac{6}{\pi} \arcsin \left( \frac{[\sqrt{3}(1-\delta) - 1]^2}{2 + [\sqrt{3}(1-\delta) - 1]^2} \right), & 1 - \frac{2}{\sqrt{3}} < \delta < 1 - \frac{1}{\sqrt{3}}. \end{cases} \quad (6)$$

$$f_R = 1 - f_T. \quad (7)$$

At the MPB we have  $G_T = G_R$  and  $\delta = 0$ , so that the molar ratio of the rhombohedral and tetragonal phases becomes:

$$\frac{f_R}{f_T} = \frac{\pi - 6 \arcsin \left( \frac{3 - \sqrt{3}}{6} \right)}{6 \arcsin \left( \frac{3 - \sqrt{3}}{6} \right)} \approx 1.45. \quad (8)$$

The system we have discussed above refers to a single domain system. A ceramic can be treated as an ensemble of domains, therefore the probability functions  $f_R$  and  $f_T$  also represent the molar fractions of rhombohedral and tetragonal phases in a ceramic system. Thus, using eq. (8) one may determine the MPB composition from x-ray diffraction intensity measurements.

### III. COMPARISON WITH EXPERIMENTS

The difference of the two energy densities may be expanded around the MPB composition  $x_0$ :

$$g_R - g_T = \frac{1}{\nu} (G_R - G_T) = \sum_{n=1}^{\infty} \alpha_n (x - x_0)^n, \quad (10)$$

where  $v$  is the volume of an element in a statistical ensemble. Looking at figure 1(d) one finds that eq. (10) may be well represented by a linear function near  $x_0$ ,

$$g_R - g_T = \alpha_1 (x - x_0). \quad (11)$$

Now let us examine the probability polyhedron in figure 5 more carefully, when  $r_R > \sqrt{3} r_T$ , the six representative surfaces for the tetragonal phase will meet each other to form a cube, which implies that only tetragonal phase can be formed. Vice versa, where  $r_R < \frac{1}{\sqrt{3}} r_T$  the representative surfaces of the rhombohedral phase will form a closed octahedron so that only rhombohedral phase can be formed. This restricts the  $\delta$  values in the following range:

$$1 - \sqrt{3} < \delta < 1 - \frac{1}{\sqrt{3}}. \quad (12)$$

Using this relation and eqs.(5) and (11) we can drive the width of the coexistence region<sup>2</sup>,

$$\Delta x = \frac{2kT_c}{\alpha_1 v} \ln 3. \quad (13)$$

An important conclusion can be drawn from eq. (13): The width and the boundary compositions of the coexistence region are not well defined in a complete solid solution system, they depend on the volume  $v$  of the statistical elements, for instance the domain size in a ceramic system. This fact marks the physical difference between the phase coexistence inside a solubility gap and near the MPB of a complete solid solution [see figures 1(a) and 1(c)].

Substituting eq.(13) into eq.(11) we can rewrite eq. (5) to the following form

$$\delta = 1 - \exp \left[ \frac{(x - x_0) \ln 3}{\Delta x} \right]. \quad (14)$$

The parameters  $x_0$  and  $\Delta x$  may be fitted from experimental data using eqs. (14) and (6) [or (7)].

Two examples are given below to demonstrate the procedures.

It is known from experience that the coexistence region in pure PZT system is very narrow. Therefore, due to the limitations of x-ray resolution it is difficult to obtain a reliable molar ratio of the rhombohedral and tetragonal phases from x-ray measurements. However, when small amounts of dopants are added to the PZT system, the coexistence region usually becomes wider and the diffraction peaks become relatively easier to be separated from each other. The data points in figure 6 were measured by Hanh, Uchino and Nomura<sup>4</sup> on the solid solution system  $0.1 \text{ Pb}_{0.9} \text{ K}_{0.1} (\text{Zn}_{1/3} \text{ Nb}_{2/3})\text{O}_{2.95} - (0.9 - x) \text{ PbZrO}_3 - x \text{ PbTiO}_3$ . [Note the compositional variable  $x$  refers to the mole percent of  $\text{PbZrO}_3$  in reference 4 but refers to the mole percent of  $\text{PbTiO}_3$  in this paper, all data points have been converted accordingly.] The squares and circles are the molar fractions of the rhombohedral and tetragonal phases respectively. The authors of ref. 4 have fitted their experimental data to the Lever Rule, which are shown in figures 6 as the solid curves, the two edge compositions are  $x_1 = 0.45$  and  $x_2 = 0.57$ . Although it appears that the fitting is reasonably good for these limited data points, the kinks at  $x_1$  and  $x_2$  are in contradiction with the nature of a complete solid solution system. As mentioned above, the two edge compositions in the Lever Rule actually define a solubility gap. One cannot explain the physical meaning of these two edge compositions for a complete solid solution system. The dotted curves are fitted using the theory presented in this paper, the two fitted parameters are  $x_0 = 0.5027$  and  $\Delta x = 0.2066$ . We can see that the fittings are surprisingly good, all the data points are almost exactly on the curves! More importantly, the kinks have been smoothed out, which makes the current theory more consistent with the nature of complete solid solution system than the Lever Rule.

In comparison the width obtained from the current theory,  $\Delta x = 0.2066$ , is wider than that given by the Lever Rule  $x_2 - x_1 = 0.12$ . Both theories agree reasonable well if the second phase has more than 20%, but they deviate severely from each other near the edges of the coexistence

region. In practice, the long tails in our theory may be difficult to be observed because the x-Ray technique cannot detect the existence of a second phase if it is less than a few percent. The resolution would be even worse if the diffraction peaks of the two coexisting phases are closely located. For this reason we give a useful relation to estimate the width parameter  $\Delta x$ ,

$$\Delta x \approx 18.87 (x_m - x_0) , \quad (15)$$

where  $x_0$  is the MPB composition at which  $f_R:f_T \approx 60:40$ , and  $x_m$  is the equal fraction composition at which  $f_R:f_T = 50:50$ . These two compositions can be easily obtained from experiments and are indicated in figure 6.

Unlike the Lever Rule, the distribution functions eqs. (6) and (7) are asymmetric with respect to the equal fraction composition  $x_m$ , one may notice this point by looking at the dotted curves in figure 6. This asymmetric feature has been verified by experiments in other systems, for example the experimental results of Ari-Gur and Benguigui<sup>5</sup> for the PZT solid solution system (figure 7). One can clearly see this asymmetry from their data. Although it seems that some experimental errors might have occurred because the MPB composition has been shifted further to the rhombohedral side (which might be caused by the presence of impurities in their chemicals), the data can still be well fitted using eqs. (6) and (7). The two fitted parameters are  $x_0 = 0.4212$ ,  $\Delta x = 0.2554$ .

#### IV. SUMMARY AND CONCLUSIONS

The distribution functions have been derived for the coexisting phases near the morphotropic phase boundary in a complete binary solid solution system. It is shown that the phase coexistence near the MPB in a complete solid solution is different from the phase coexistence inside a solubility gap. The latter has two special compositions  $x_1$  and  $x_2$  specifying the edges of a solubility gap, and the distribution inside the gap can be described by the Lever Rule.

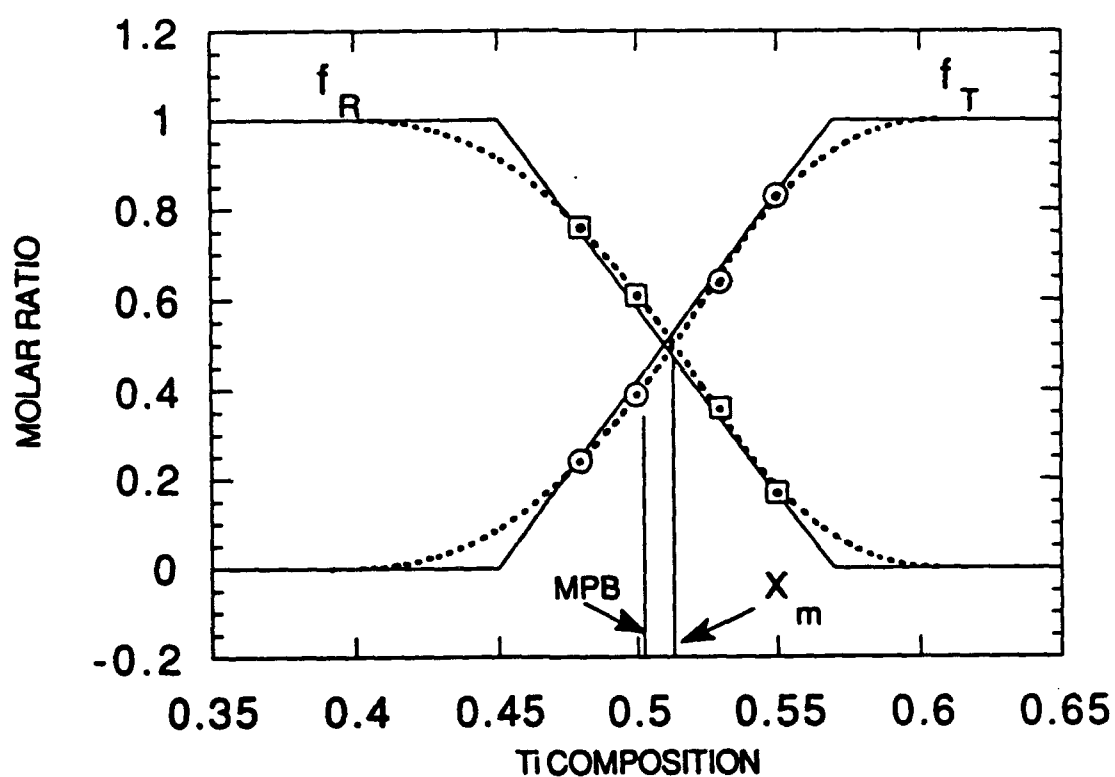
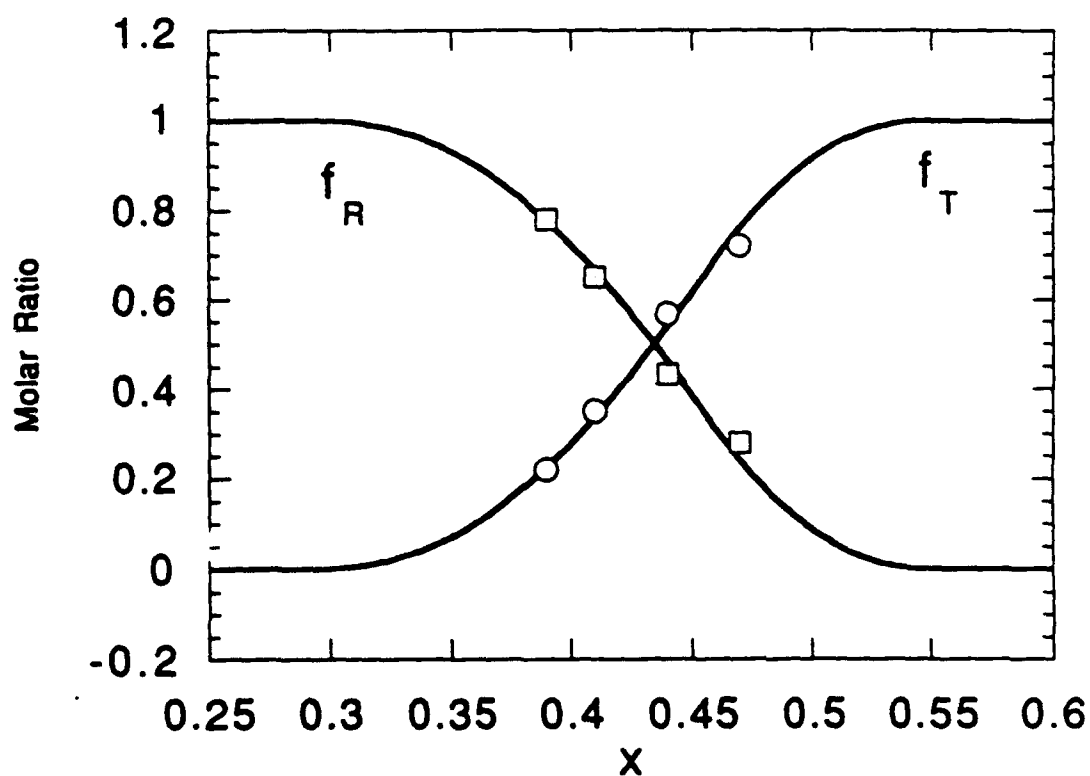


Figure 6 Molar fractions  $f_R$  and  $f_T$  of the rhombohedral and tetragonal phases inside the coexistence compositional region for  $0.1\text{Pb}_{0.9}\text{K}_{0.1}(\text{Zn}_{1/3}\text{Nb}_{2/3})\text{O}_{2.95} - (0.9 - x)\text{PbZrO}_3 - x\text{PbTiO}_3$  solid solution. The squares and circles are experimental data from ref. 4, the solid curves were fitted using the lever rule and the dotted curves were fitted using the current theory.





**Figure 7** Experimental data (the squares and circles) of Ari-Gur and Benguigui (ref. 5) on the PZT system and the fitting curves using the current theory.

While for the former, only the MPB composition  $x_0$  is well defined, the width of the coexisting region is inversely proportional to the volume of individual element in a statistical ensemble. Contrary to the customarily used criterion for the MPB, i.e.,  $f_R:f_T = 1:1$ , the ratio should be roughly given by  $f_R:f_T = 3:2$  from our theory, which agrees with the MPB determined from dielectric measurements. Superior to the Lever Rule, the current theory does not give those kinks in the distribution functions, therefore is more consistent with the nature of a complete solid solution system. The distribution functions eqs. (6) and (7) are asymmetric with respect to the middle point  $x_m$ , which is another major difference between the current theory and the Lever Rule. Experimental results show that this asymmetry indeed exist. In addition to the surprisingly good agreement between the theory and the available experimental data, the current theory also provides a reasonable explanation to the controversy regarding the width of the coexistence region in the PZT system. A well defined width can not exist in a complete solid solution system because  $\Delta x$  is inversely proportional to the domain volume, and the domain size depends very strongly on the ceramic processing procedures.

#### ACKNOWLEDGEMENTS

This research was supported in part by the Office of Naval Research.

## REFERENCES

1. Wenwu Cao and L. E. Cross, Japanese J. Appl. Phys. (in press,1992).
2. Wenwu Cao and L. E. Cross, Phys. Rev. B (submitted) (1992).
3. M. J. Haun, E. Furman, S. J. Jang and L. E. Cross, Ferroelectrics 99, 63 (1989).
4. Lu Hanh, K. Uchino and S. Nomura, Japanese J. Appl. Phys. 17, 637 (1978).
5. P. Ari-Gur and L. Benguigui, Solid State Comm. 15, 1077 (1974).

**RELAXORS AND  
RELATED SYSTEMS**

## APPENDIX 20

**The Pennsylvania State University**  
**The Graduate School**

**THE GLASSY BEHAVIOR OF  
RELAXOR FERROELECTRICS**

**A Thesis in**  
**Solid State Science**

**by**

**Dwight D. Viehland**

**Submitted in Partial Fulfillment  
of the Requirements  
for the Degree of**

**Doctor of Philosophy**

**May 1991**

## ABSTRACT

A spin-glass-like model for the relaxor ferroelectric has been developed. The glassy behavior is shown to be reflected in the dielectric, polarization, and electromechanical responses. The glassy behavior is believed to arise due to correlations, both dipolar and quadrupolar, between superparaelectric sized moments.

The complex susceptibility was measured over the frequency range of  $10^2$  to  $10^7$  Hz. The frequency dispersion of the temperature of the permittivity maximum was modelled with the Vogel-Fulcher relationship, predicting a characteristic freezing temperature which coincided with the collapse of a stable remanent polarization. The imaginary component was also found to be nearly frequency independent below this temperature, phenomenologically scaling to the Vogel-Fulcher relationship. The relaxation time distribution was then calculated by analogy to spin-glasses, and shown to extend from microscopic to macroscopic periods near freezing reflecting the onset of nonergodicity. The deviation from Curie-Weiss behavior was also investigated. At high temperatures, the dielectric stiffness was found to follow the Curie-Weiss relationship. A local (glassy) order parameter was calculated from the deviation at lower temperatures, by analogy to spin-glasses. The dependence of the complex susceptibility on an applied electric field and the degree of chemical long range ordering was then investigated using these techniques.

The remanent polarization was investigated for various electrical and thermal histories. The field-cooled and zero-field-cooled behaviors were both studied. The magnitude of both polarizations was found to be equal above a critical temperature. A macroscopic polarization developed under bias in the zero-field-cooled state, with the temperature of the maximum charging current decreasing with increasing bias.

This decrease was modelled using the deAlmedia-Thouless relationship, which predicted an average moment size freezing of approximately  $3 \times 10^{-25}$  C-cm. The time dependence of the remanent polarization was also investigated. The square-to-slim-loop hysteresis transition, measured using a standard Sawyer-Tower circuit, was phenomenologically modelled by modifying Neel's equation for the magnetization of a superparamagnet to a similar relationship for a superparaelectric. A temperature dependent internal dipole field was included to account for correlations. The slim loop polarization curves were also found to scale to  $E/(T-T_f)$ .

The electromechanical behavior was investigated using a nonlinear internal friction technique. The linear elastic response was found to stiffen at all bias levels with the maximum electroelastic coupling occurring near the Vogel-Fulcher freezing temperature. A strong frequency dependence of the kinetics of the anelastic relaxation was found at low measurement frequencies. These data are compared to recent high frequency results. The existence of an inhomogeneous internal strain was found from the line broadening of the (220) and (321) diffraction peaks. On application of an electrical field the internal strain is relieved by the development of a macrostrain which is shown to be the electrostrictive strain. Strong elastic nonlinearities, both an elastic softening and hardening under stress, have also been observed. These results are interpreted as a stress activation of the internal deformation process.



## APPENDIX 21

## The dielectric relaxation of lead magnesium niobate relaxor ferroelectrics

By DWIGHT VIEHLAND, S. JANG, L. ERIC CROSS

Materials Research Laboratory, The Pennsylvania State University,  
University Park, Pennsylvania 16802, U.S.A.

and MANFRED WUTTIG

Department of Materials and Nuclear Engineering, University of Maryland,  
College Park, Maryland 20742, U.S.A.

[Received 7 January 1991 and accepted 20 February 1991]

### ABSTRACT

The dielectric spectroscopy of lead magnesium niobate relaxor ferroelectrics has been investigated over the frequency range of  $10^2$  to  $10^7$  Hz. The imaginary component was found to become nearly frequency independent below a freezing temperature, and scaled to a phenomenological equation involving the Vogel-Fulcher relationship. The absorption and Cole-Cole plots were found to become very broad near this freezing temperature. The relaxation time distribution was subsequently calculated by analogy to spin and dipolar glasses. A strong broadening of the distribution was found in the vicinity of the freezing temperature. It is proposed that this deviation from Debye behaviour is a result of the development of correlations between polar moments leading to the onset of non-ergodicity near freezing.

### §1. INTRODUCTION

Lead magnesium niobate (PMN) is a relaxor ferroelectric. In the zero-field-cooled (ZFC) state, relaxors are characterized by a relaxational process typical of a classic dielectric relaxator, and by the lack of macroscopic polarization and anisotropy. Burns and Dacol (1983, 1986) have shown that a local polarization exists in the ZFC state to temperatures much higher than that at which a remanent polarization can be sustained. In the field-cooled (FC) state relaxation is not observed (Viehland, Jang, Wuttig, and Cross 1991), and the system is able to sustain a macroscopic polarization below a critical temperature which is significantly lower than the radio frequency permittivity maxima. Smolenski and Agranovskya (1960) originally proposed that underlying the relaxor behaviour is a chemical inhomogeneity on the B-site cation, leading to a spatially varying composition with local Curie temperatures. Randall and Bhalla (1990) and Chen, Chan, and Harmer (1989) have recently shown that in PMN there is a partitioning on the nanometer scale into chemically homogeneous clusters. It is currently believed that it is the scale of this process which underlies the relaxor behaviour. Cross has suggested that local ferroelectric phase transitions may occur inside these individual chemical regions (Cross 1987). The size of these moments is such that their orientations may be thermally agitated, analogous to superparamagnetism (Neel 1949).

Kersten, Rost, and Schmidt (1983) have shown that the dielectric relaxation is Debye-like at temperatures significantly above the temperature of the permittivity maximum ( $T_{max}$ ). Yushin, Smirnova, Dorogortsev, Smirnov and Galyamov (1987) have

recently found a broadening of the relaxation time distribution near  $T_{\max}$ , unlike a Debye process. Kirolov and Isupov (1973) have analysed the frequency dispersion of  $T_{\max}$  with the Debye relationship obtaining an activation energy and pre-exponential factor of 7 eV and  $10^{40} \text{ s}^{-1}$ , respectively. Cross *et al.* have recently analysed the frequency dispersion of  $T_{\max}$  with the Vogel-Fulcher relationship (Viehland, Jang, Wuttig and Cross 1990), analogous to spin glasses (Tholence 1979, 1980), obtaining an activation energy and pre-exponential factor of 0.04 eV and  $10^{12} \text{ s}^{-1}$ , respectively. Cross *et al.* found that the freezing temperature ( $T_f$ ) coincided with the temperature at which a stable remanent polarization can be sustained. A dipole glass model for relaxors was subsequently proposed (Viehland, Jang, Li, Wuttig, and Cross 1991), with local dipole fields between superparaelectric moments leading to the development of a frustration below the freezing temperature.

The magnetic and dielectric relaxations of spin and dipolar glasses are believed to undergo freezing, due to frustrated interactions (Edwards and Anderson 1975), (Kirkpatrick and Sherrington 1978), and random fields (Morgownik and Mydosh 1981), (Nozav, Sechovsky and Kambersky 1987). The magnetic absorption and Argrand plots are known to become broad near  $T_f$  (Huser, Wenger, vanDuyneveldt and Mydosh 1983). It is believed that on cooling through  $T_f$ , the relaxation-time distribution strongly broadens, extending from microscopic to macroscopic time periods. The broadening is believed to be due to the onset of non-ergodicity above the freezing temperature. It is the purpose of this work to investigate the dielectric dispersion of PMN around the freezing temperature, and compare the results to spin and dipolar glasses.

## §2. EXPERIMENTAL PROCEDURE

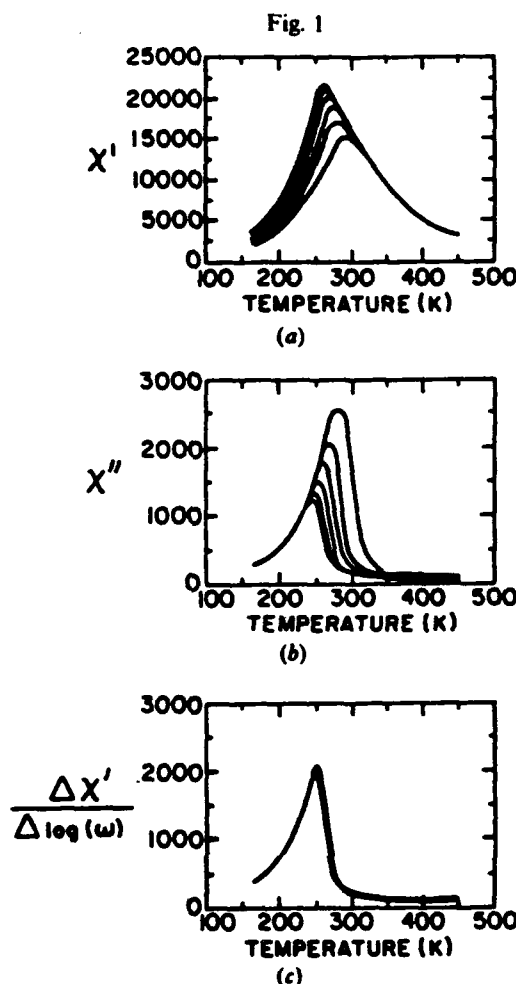
The samples used in the study were PMN single crystals. The crystals were grown by a flux method as described by Setter (1980). They were orientated along the (100) direction, were of dimensions 0.2 cm  $\times$  0.1 cm  $\times$  0.08 cm, and were electroded with gold.

The dielectric constant was measured as a function of frequency ( $\omega$ ) between 450 and 150 K at a cooling rate of  $4^\circ\text{C min}^{-1}$ . The frequencies used were  $10^2$ ,  $10^3$ ,  $10^4$ ,  $10^5$ ,  $10^6$ , and  $10^7$  Hz. The measurements were made using HP4275A and 4274A LCR meters. The dielectric curve for each frequency was smoothed and interpolated to determine the temperature of the permittivity maximum ( $T_{\max}$ ) as accurately as possible. The remanent polarization was also measured for comparison using a standard pyroelectric technique.

## §3. RESULTS AND DISCUSSION

The complex susceptibility,  $\chi = \chi' - i\chi''$ , is shown in fig. 1(a) and (b) for various measurement frequencies. The real component ( $\chi'$ ) had a maximum of approximately 22000 at 260 K for a measurement frequency of 100 Hz, and the imaginary part ( $\chi''$ ) had a maximum of approximately 1200 at 250 K. It should be noted that the inflection point of  $\chi''$  corresponds in temperature to the maximum  $\chi'$ . The quantity  $\chi''$  was essentially frequency independent below 230 K, indicative of a freezing into a glassy state. The value of  $\chi''$  seemingly extrapolated to zero near 0 K, unlike the metallic spin glasses (Mulder vanDuyneveldt 1982) whose absorption extrapolates to approximately 60% of its maximum. At lower temperatures the dispersion of  $\chi'$  was significantly less, but was observed at much lower temperatures than for  $\chi''$ .

The strong decrease in the frequency dispersion of  $\chi''$  below 230 K suggests that the data can be scaled by approximating  $\chi''(T, \omega)$  as  $h(T)R(u)$  following Courtens (1984),



(a) The dielectric permittivity ( $\chi'$ ) of PMN as a function of temperature for measurement frequencies of  $10^2$ ,  $10^3$ ,  $10^4$ ,  $10^5$ ,  $10^6$ , and  $10^7$  Hz. The top curve is the lowest frequency and the bottom the highest. (b) The imaginary part of the dielectric response ( $\chi''$ ) as a function of temperature for measurement frequencies of  $10^2$ ,  $10^3$ ,  $10^4$ ,  $10^5$ ,  $10^6$ , and  $10^7$  Hz. The bottom curve is the lowest frequency and the top the highest. (c)  $\Delta\chi'/\Delta \log(\omega)$  as a function of temperature.

where  $h(T)$  and  $R(u)$  describe the frozen and dynamic contributions respectively, and  $u(\omega, T)$  is a scaling variable. The function  $R(u)$  is given by eqn. 1

$$R(u) = \frac{1}{2}[1 + \tanh(u)], \quad (1)$$

where

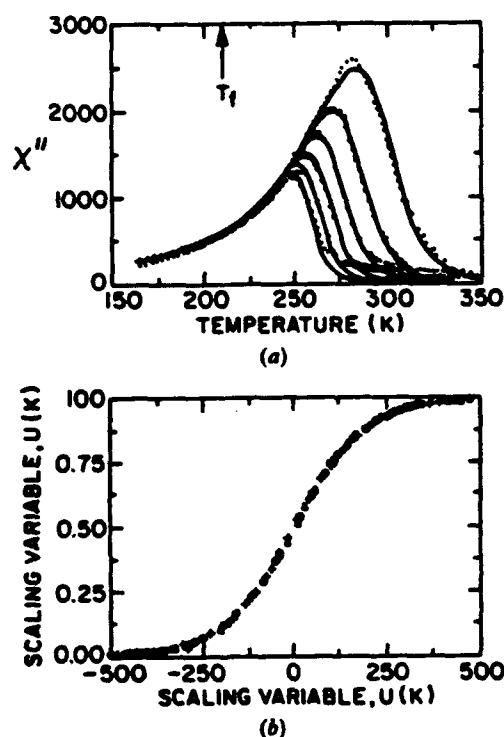
$$u = d(E_c - E),$$

and where  $d$  is a constant in units of  $\text{eV}^{-1}$ , and  $E_c$  is a cutoff energy in units of eV. The value of  $E$  can be approximated by the Vogel-Fulcher relationship  $\tau = \tau_0 \exp[E/k(T - T_f)]$  (Vogel 1921, Fulcher 1924), where  $1/\tau_0$  is the Debye frequency and  $T_f$  a freezing temperature. At lower temperatures  $R(u)$  is approximately 1, and  $\chi''$

$(T, \omega) = h(T)$ . At higher temperatures  $R(u)$  decreases approaching zero; consequently  $\chi''(T, \omega) = 0$ . At intermediate temperatures,  $R(u)$  varies as a function of frequency ( $\omega = 1/\tau$ ), as given by the Vogel-Fulcher relationship. The functional dependence of  $h(T)$  was empirically determined from low temperatures ( $T < 230$  K) by an exponential fitting,  $c_1 \exp(c_2 T)$ . The modelling was done using a Levenberg-Marquardt fitting, solving for  $d$ ,  $E_c$ , and  $T_f$ . The values of  $c_1$  and  $c_2$  were held constant during the fitting, and  $\tau_0$  was assumed to be  $1 \times 10^{-12}$  s as previously reported (Viehland *et al.* 1990). Minimum variance ( $\sim 2\%$ ) was obtained for  $d$ ,  $E_c$ , and  $T_f$  equal to  $58.89 \text{ eV}^{-1}$ ,  $0.0764 \text{ eV}$ , and  $220.33 \text{ K}$  respectively. The phenomenological model is shown alongside the experimental data in fig. 2(a). Reasonable agreement can be seen. The function  $R(u)$  is shown in fig. 2(b) for various measurement frequencies. The data scales quite readily with  $(E_c - E)$  over a wide range of frequencies.

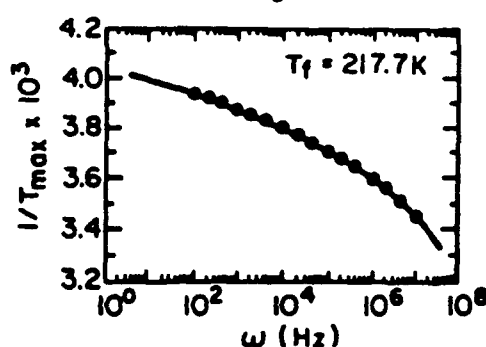
The value of  $T_f$  was also estimated by modelling the dispersion of  $T_{\max}$  with the Vogel-Fulcher relationship for comparison. Minimum variance was obtained for  $1/\tau_0$ ,  $T_f$  and  $E_c$  equal to  $10^{12} \text{ s}^{-1}$ ,  $217.7 \text{ K}$ , and  $0.0786 \text{ eV}$  respectively. The values of  $E_c$  and  $T_f$  are in close agreement with those of  $E_c$  and  $T_f$  as determined from the modelling of  $\chi''$  using eqn. 1. The fitting of the data is shown in fig. 3(a). Analysis with the Arrhenius relationship yielded an activation energy and a pre-exponential factor of  $7 \text{ eV}$  and

Fig. 2

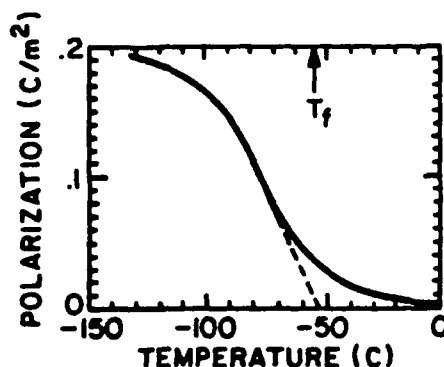


The points are the imaginary contribution of the dielectric response ( $\chi''$ ) as a function of temperature for measurement frequencies of  $10^2$ ,  $10^3$ ,  $10^4$ ,  $10^5$ ,  $10^6$ , and  $10^7$  Hz. The bottom curve is the lowest frequency and the top the highest, and where  $T_f$  is the freezing temperature. The solid line is a phenomenological fitting to eqn. 1. (b) the scaling parameter  $[R(u)]$  as a function of the scaling variable ( $u$ ) for various measurement frequencies.

Fig. 3



(a)



(b)

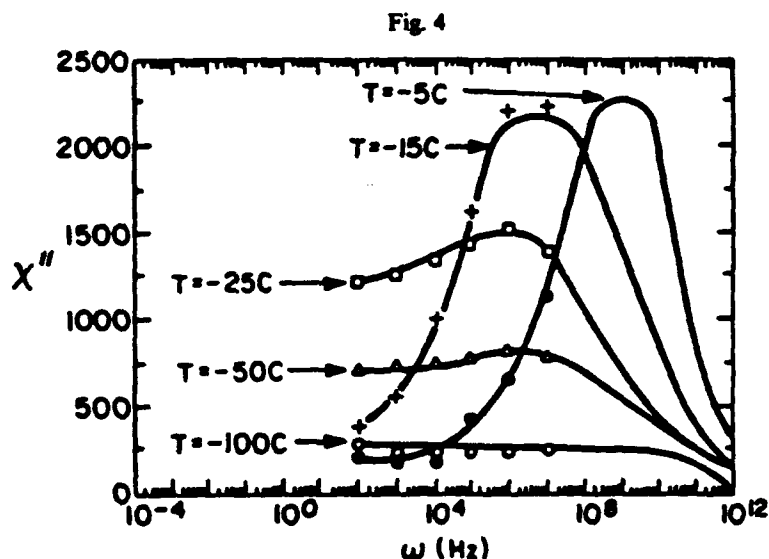
- (a) The temperature of the permittivity maximum as a function of the measurement frequency. The dots are the data and the solid line is the fitting to the Vogel-Fulcher relationship.  
 (b) The remanent polarization as a function of temperature.

$10^{40} \text{ s}^{-1}$ , respectively. Both of these values are physically unreasonable for a thermally activated process. The remanent polarization ( $P_r$ ) as a function of temperature is shown in fig. 3(b). The extrapolation of  $P_r$  to zero yielded a temperature between 215 and 220 K, which is close to  $T_f$ . This shows that on zero-field heating from the field-cooled state, the macroscopic polarization collapses near the Vogel-Fulcher freezing temperature. The implication is that the thawing temperature of the field-cooled state and freezing temperature of the zero-field-cooled state coincide, reflecting the kinetics of the polarization reversals. The static polarization of PMN-10PT has recently been determined from Sawyer-Tower measurements and shown to scale to hyperbolic functions involving a reduced temperature somewhat similar to eqn. 1 (Viehland *et al.* 1991).

The Vogel-Fulcher scaling of  $\chi''$  has been interpreted to mean that freezing does not occur by cluster growth, but rather by the freezing of local modes (Courtens 1984). The scaling in rubidium ammonium dihydrogen phosphate (RADP) is believed to be due to a competition between antiferroelectric and ferroelectric exchanges on the atomic level, Courtens (1984), Courtens, Rosenbaum, Nagler, and Horn (1984). This is further substantiated by the saturation of the correlation length at 12 Å near  $T_f$  (Courtens *et al.* 1984). The Vogel-Fulcher scaling of  $\chi''$  in PMN may have its origins in the phase

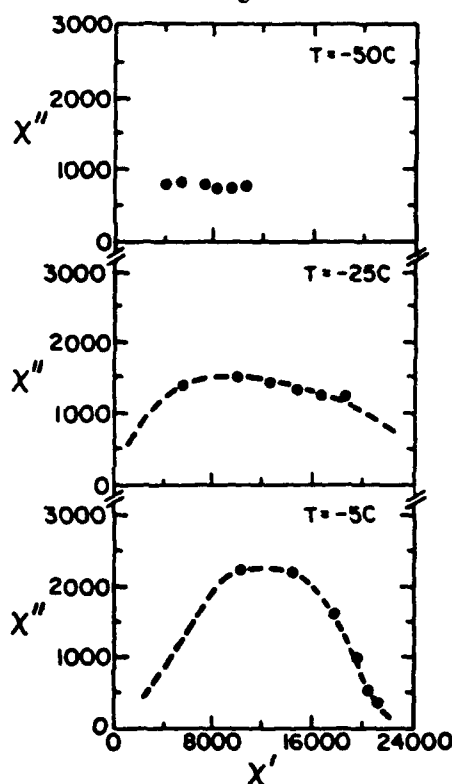
separated superparaelectric regions. Chemically homogeneous regions on the scale of approximately 50 Å have been observed by transmission electron microscopy (TEM) (Chen *et al.* 1989, Randall and Bhalla 1990). The local polarization may be homogeneous within each region and of predetermined size. Dipole fields between superparaelectric moments may subsequently lead to a freezing of the polarization fluctuations into a glassy state at lower temperatures. This is further substantiated by the saturation of the correlation length in PMN crystals at 200 Å near the Vogel-Fulcher freezing temperature (Vakhrushev, Kvyatkovsky, Naberezhov, Okuneva and Topervers 1989, Viehland, *et al.* 1991).

The absorption,  $\chi''$ , over a wide range of frequencies at various temperatures around  $T_f$  is shown in fig. 4. The width of the  $\chi''$  curves exceeds that which can be attributed to a single relaxation time, and strongly suggests a wide distribution. The absorption width increases as the temperature decreases approaching  $T_f$ , and becomes essentially flat below  $T_f$  with all curves remaining parallel. The implication is that dramatic changes occur in the relaxation time distribution on cooling through  $T_f$ . This change cannot be attributed to a normal Debye-like relaxational process, because  $\tau_{\max}$  does not shift steadily down in frequency. Kersten, Rost, and Schmidt (1983) have previously analysed the temperature dependence of  $\tau_{\max}$  with the Debye relationship, obtaining an activation energy and pre-exponential factor of approximately 0.5 eV and  $10^{-16}$  s, respectively. Their modelling was done at temperatures significantly above the permittivity maximum, where the absorption has distinct peaks as shown in fig. 4. In this temperature range the local polarization fluctuates at relatively rapid frequencies, i.e. the superparaelectric moments are nearly decoupled. The shift of  $\tau_{\max}$  can then be modelled by the Debye relationship over a limited temperature interval. But as strong correlations develop between neighbouring moments on cooling, the relaxation deviates significantly from Debye behaviour as reflected in a strong temperature dependence of the activation energy and pre-exponential factor (Kirolov and Isupov 1973). Cole-Cole plots are shown in fig. 5 around  $T_f$ . Near  $T_f$  the plot is flat; with increasing temperature curvature can be seen, and near the temperature of the radio



The dielectric absorption ( $\chi''$ ) as a function of frequency at various temperatures.

Fig. 5.



Cole-Cole plots at various temperatures around freezing.

frequency permittivity maxima semicircles are observed. The flattening of the Cole-Cole curves near the Vogel-Fulcher freezing temperature suggests as well that the relaxation time distribution is becoming very broad with the tail of the distribution extending into the macroscopic time regime.

The dielectric and magnetic responses of dipolar and spin glasses can be represented by a summation over a distribution of relaxators (Courtens 1984, Lundgren, Svedlindh and Beckman 1981), as given in eqn. 2

$$\chi''(T, \tau) = \int_{\tau_0}^{\infty} G(\tau, T) \frac{\chi'_0(T)}{1 - i\omega\tau} d \ln \tau, \quad (2)$$

where  $G(\tau, T)$  is the distribution of relaxation times,  $\chi'_0(T)$  the low-frequency limit of  $\chi'(T, \omega)$ , and  $\omega = \tau^{-1}$ . Assuming  $G(\tau, T)$  is very broad in  $\ln(\tau)$ ,  $\chi''$  can be approximated from 2 as given in eqn. 3

$$\chi''(T, \tau) \approx \chi'_0(T) G(\tau, T). \quad (3)$$

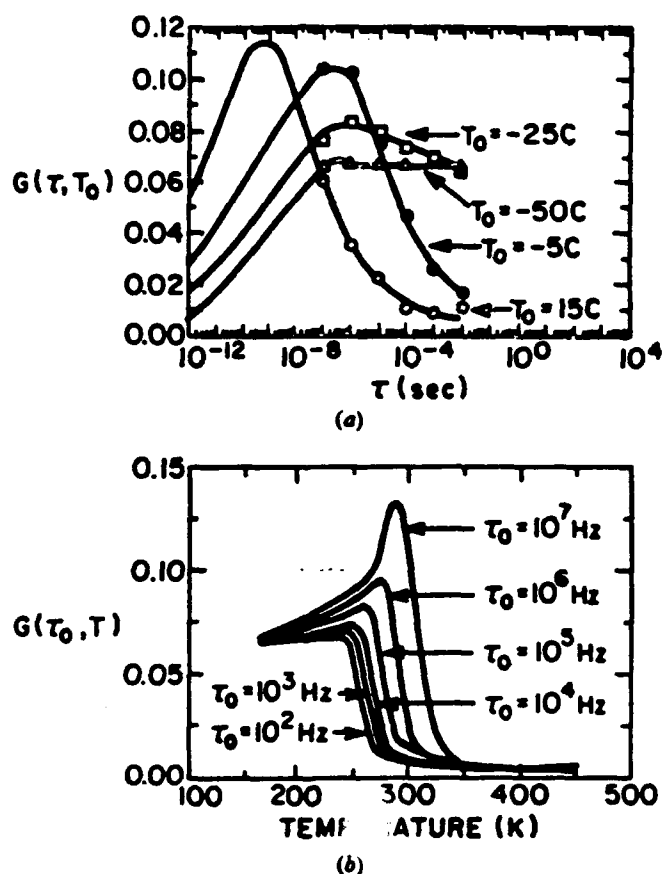
Following such a procedure causality predicts that  $\chi'' \sim \delta\chi'/\delta \ln(\omega)$  (Lundgren *et al.* 1981), which is illustrated in fig. 1(c). The agreement with the data in fig. 1(b) is quite good.

Isothermal cross sections of  $G(\tau, T_0)$  as a function of  $\tau$  for PMN are shown in fig. 6(a) at  $T = T_f$ ,  $T > T_f$ ,  $T = T_{max}$ , and  $T > T_{max}$  respectively. The value of  $\chi'_0(T)$  was assumed to



be the 100 Hz  $\chi(T)$ . Solid lines are drawn to represent what the distribution most probably looks like over the whole frequency range. The drawing of these lines was guided by the fact that  $G(\tau, T_0) = 0$  near  $\tau_{\text{Debye}}$ , and that at higher temperatures the distribution will be Gaussian. Near  $T_i$  the distribution was found to be essentially flat between  $10^{-2}$  and  $10^{-7}$  s, tailing to zero near  $10^{-12}$ . With increasing temperature the distribution sharpened, developing a distinct  $\tau_{\text{max}}$  near the temperature of the radio frequency permittivity maximum. At higher temperatures  $\tau_{\text{max}}$  was found to shift to higher frequencies, analogous to a Debye type relaxation, but the width and shape of the distribution continued to change with increasing temperature. Isotemporal cross sections,  $G(\tau_0, T)$ , are shown in fig. 6(b) at various measurement frequencies. A sharp step in  $G(\tau_0, T)$  was found near  $T_{\text{max}}$  and shifted to higher temperatures with increasing frequency. Below  $T_i$ ,  $G(\tau_0, T)$  decreased slowly with decreasing temperature. The magnitude of  $G(\tau_0, T)$  also increased with frequency, over the range investigated. The isotemporal cross sections are essentially the dielectric loss factor. A previously

Fig. 6



(a) The relaxation-time distribution  $[G(\tau, T_0)]$  as a function of  $\tau$  at various temperatures. (a)  $T = T_i$ , (b)  $T > T_i$ , (c)  $T = T_{\text{max}}$ , and (d)  $T > T_{\text{max}}$ . (b) The relaxation-time distribution  $[G(\tau_0, T)]$  as a function of temperature at various measurement frequencies. The measurement frequencies shown are  $10^2$ ,  $10^3$ ,  $10^4$ ,  $10^5$ ,  $10^6$ , and  $10^7$  Hz. The bottom curve is the lowest frequency, and the top curve the highest.

Fig. 7

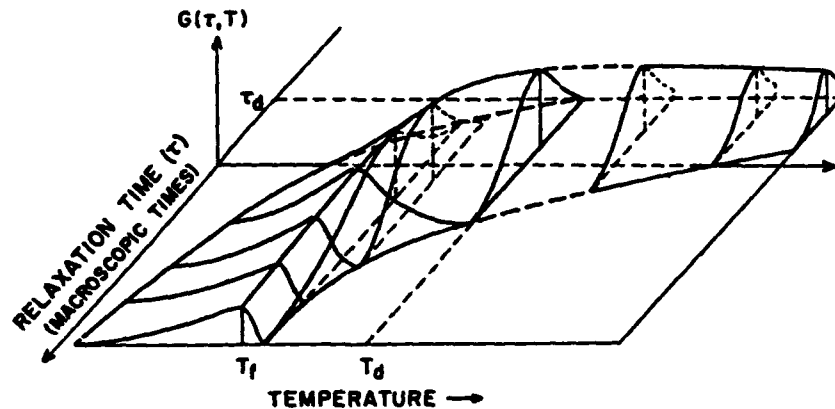


Diagram illustrating the proposed temperature-dependent relaxation-time spectrum.  $G(\tau, T)$  is the number of polar regions having a relaxation time  $\tau$ ,  $T_f$  is the freezing temperature, and  $\tau_d$  is the Debye frequency.

proposed relaxation time distribution as a function of temperature is illustrated in fig. 7 (Viehland *et al.* 1990). It can be seen that this model is supported by the experimental data. The isothermal width of the spectrum is shown to become very broad near  $T_f$ , approaching the macroscopic time regime. The shortest relaxation time ( $\tau_{\min}$ ) is shown to approach macroscopic times only at temperatures far below  $T_f$ . Above  $T_f$  the isothermal width of the relaxation time spectrum continuously sharpens as the temperature is increased with  $\tau_{\max}$  and  $\tau_{\min}$  approaching the microscopic time regime.

The dielectric spectroscopy results can be understood in terms of the interacting superparaelectric dipole glass model, discussed above. At high temperatures the moments are decoupled, exhibiting typical Debye-type behaviour, but on cooling local dipole fields couple the polarization fluctuations and  $\tau_{\max}$  varies in a nonlinear manner parameterizable by the Vogel–Fulcher relationship. It is proposed that as a consequence of increasing correlations, the relaxation-time distribution broadens and flattens out with decreasing temperature reflecting the onset of non-ergodicity. Near a critical temperature the distribution becomes extremely broad, as the polarization fluctuations undergo Vogel–Fulcher freezing into a dipole glass state. Consequently, the system can sustain a remanent polarization below this temperature. The relaxation-time distribution remains relatively wide above  $T_f$ , in effect leading to a diffuse phase transformation. The diffuse nature of the transformation is thus not a reflection of compositional heterogeneity as originally proposed by Smolenski and Agranovskaya (1960), but rather a consequence of size dispersions of polar moments and the development of correlations.

#### §4. CONCLUSIONS

The dielectric relaxation of PMN single crystals has been investigated, and shown to be similar to spin and dipole glasses. The absorption was found to be nearly frequency independent below a freezing temperature which correlated with the temperature at which a stable remanent polarization collapsed on heating from the field-cooled state. The absorption spectra and Cole–Cole plots were found to become

very broad near this freezing temperature. The relaxation-time distribution has also been calculated and shown to broaden strongly near freezing, extending from the microscopic to macroscopic time regimes.

#### ACKNOWLEDGMENTS

This work has been supported in full by contracts administered through the Office of Naval Research.

#### REFERENCES

- BURNS, G., and DACOL, F., 1982, *Solid St. Commun.*, **48**, 10, 853; 1986, *ibid.*, **58**, 9, 567.  
 CHEN, J., CHAN, H., HARMER, M., 1989, *J. Am. Ceram. Soc.*, **79**, 593.  
 COURTENS, E., 1984, *Phys. Rev. Lett.*, **52**, 69.  
 COURTENS, E., ROSENBAUM, T., NAGLER, S., and HORN, P., 1984, *Phys. Rev. B*, **29**, 1, 515.  
 CROSS, L. E., 1987, *Ferroelectrics*, **76**, 241.  
 EDWARDS, S., and ANDERSON, P. W., 1975, *J. Phys. F*, **5**, 765.  
 FULCHER, G., 1925, *J. Am. Ceram. Soc.*, **8**, 339.  
 HUSER, D., WENGER, L., VANDUYNEVELDT, A., and MYDOSH, J., 1983, *Phys. Rev. B*, **27**, 5.  
 KERSTEN, O., ROST, A., and SCHMIDT, G., 1983, *Phys. Stat. Sol. (a)*, **75**, 495.  
 KIRKPATRICK, S., and SHERRINGTON, D., 1978, *Phys. Rev. B*, **17**, 4384.  
 KIROLLOV, V., and ISUPOV, V., 1973, *Ferroelectrics*, **5**, 3.  
 LUNDGREN, L., SVEDLINDH, P., and BECKMEN, O., 1981, *J. Magn. magn. Mater.*, **25**, 33.  
 MORGOWNIK, A., MYDOSH, J., 1981, *Phys. Rev. B*, **24**, 5277.  
 MULDER, C., VANDUNEVELDT, A., 1982, *Physica B*, **113**, 123.  
 NEEL, L., 1949, *Compt. Rend. Acad. Sci.*, **228**, 664.  
 NOZAV, P., SECHOVSKY, V., and KAMBERSKY, V., 1987, *J. Magn. magn. Mater.*, **69**, 71.  
 RANDALL, C., and BHALLA, A., 1990, *J. Mater. Sci.*, **29**, 5.  
 SETTER, N., 1980, PhD Dissertation. The Pennsylvania State University.  
 SMOLENSKI, G., and AGRANOVSKAYA, A., 1960, *Soviet Phys. solid State*, **1**, 1429.  
 THOLENCE, J., 1979, *J. appl. Phys.*, **50**, 7369; 1980, *Solid St. Commun.*, **35**, 113.  
 VAKHRUSHEV, S., KVIATKOVSKY, B., HABEREZHOF, A., OKUNEVA, N., and TOPERVERS, B., 1989, *Ferroelectrics*, **90**, 173.  
 VIEHLAND, D., JANG, S., WUTTING, M., and CROSS, L., 1990, *J. appl. Phys.*, **68**, 2916; 1991, *ibid.*, **69**, 414.  
 VIEHLAND, D., JANG, S., LI, J., WUTTING, M., and CROSS, L., 1991, *Phys. Rev. B*, **43**, 8316.  
 VOGEL, H., 1921, *Phys. Z.*, **22**, 695.  
 YUSHIN, N., SMIRNOVA, E., DOROGORTSEV, S., SMIRNOV, S., and GULYAMOV, G., 1987, *Soviet Phys. solid State*, **29**, 10, 1693.

## APPENDIX 22

## Anelastic relaxation and internal strain in lead magnesium niobate relaxors

By DWIGHT VIEHLAND, S. J. JANG, ERIC CROSS†

Materials Research Laboratory, Pennsylvania State University,  
University Park, Pa. 16802, USA

and MANFRED WUTTIG

Dept. of Materials and Nuclear Engineering, University of Maryland,  
College Park, Md. 20742, USA

[Received 14 September 1990 and accepted 12 December 1990]

### ABSTRACT

Non-linear internal friction measurements have been carried out on lead magnesium niobate with 10 at.% lead titanate. The purpose of these measurements was to investigate the field dependence of the elastic and anelastic responses, and to determine how the response depends on the amplitude of an applied stress. The linear elastic response was found to stiffen at all bias levels with the maximum electroelastic coupling occurring near the Vogel-Fulcher freezing temperature. A strong frequency dependence of the kinetics of the anelastic relaxation was found at low measurement frequencies. These data are compared with recent high-frequency results. The existence of an inhomogeneous internal strain has been found from the line broadening of the (220) and (321) diffraction peaks. On application of an electrical field the internal strain is relieved by the development of a macrostrain which is shown to be the electrostrictive strain. It is proposed that the local electrostrictive strains are dynamic in nature and are at the origin of the anelastic relaxation. Strong elastic non-linearities, both an elastic softening and hardening under stress, have also been observed. These results are interpreted as a stress activation of the internal deformation process.

### §1. INTRODUCTION

Lead magnesium niobate (PMN) is a classic relaxor ferroelectric. Relaxors are ferroelectric materials which exhibit a diffuse phase transformation in which there is a strong frequency dispersion of the dielectric response at temperatures near the permittivity maximum ( $T_{\max}$ ). On heating from a poled state the remanent polarization is known to collapse at temperatures significantly below the permittivity maximum (Bokov and Myl'nikova 1960). The depolarization under an electric field is known to occur over a broader temperature interval (Xi, Zhilli and Cross 1983). An RMS polarization, as calculated from the index of refraction, is known at temperatures far above  $T_{\max}$  (Burns and Dacol 1983) which shows that a local polarization exists to much higher temperatures than that which a macroscopic polarization can be sustained. Smolenski's (Smolenski and Agranovska 1960) original model of relaxors was based on the concept of local variations of the transition temperature due to compositional heterogeneity. More recently Randall and Bhalla (1989) have observed contrast on the

---

† Also in the Engineering Department.

nanoscale in PMN using TEM which they believed to be due to short-range chemical ordering. Cross (1987) has proposed that local polar regions form where allowed by this short range chemical order, i.e. the so-called 'fossil chemistry', by a lowering of the local symmetry through ferroelectric distortions. He has further proposed that the frequency dispersion arises due to a thermal activation of the direction of spontaneous polarization, analogous to superparamagnetism. The frequency dispersion of  $T_{\max}$  has recently been found to exhibit a Vogel-Fulcher type freezing (Viehland, Jang, Wuttig and Cross 1990), and the freezing temperature was found to correlate with the collapse of the remanent polarization.

Relaxors are known to have a large electrostrictive strain (Jang 1979), and to be strong non-linear materials electrically (Shrout 1980, Glass 1969). The phenomena underlying the dielectric relaxation then might also be reflected into the elastic properties. Yushin, Smirnova, Dorogortsev, Smirnov and Galayamov (1987) have recently investigated the anelastic response of PMN in the megahertz regime. They found that the magnitude and kinetics of the relaxation were frequency independent. Elastic non-linearities have been previously known to arise from domain wall motion (Wuttig and Lin 1983) and nucleation (Anning and Wuttig 1984). In general, these elastic non-linearities are believed to be a macroscopic reflection of a strain-driven microscopic deformation process. The purpose of this work was to investigate the anelastic response in the low-frequency regime and to determine if the response is dependent on the magnitude of the applied stress, i.e. elastically non-linear.

Fig. 1

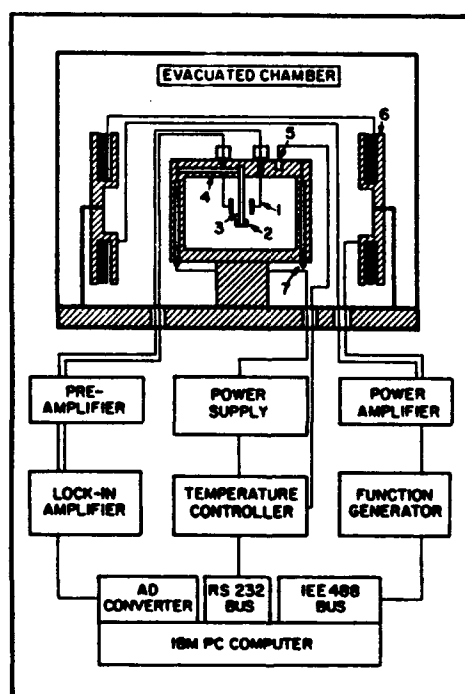


Diagram of the internal friction apparatus. 1: pick up capacitor, 2: Sm-Co magnets, 3: sample, 4: sample positioner and clamp, 5: thermocouple, 6: constant gradient Helmholtz coils, 7: resistive heating wire.

## §2. EXPERIMENTAL PROCEDURE

The elastic properties were studied using a non-linear internal friction technique developed by Wuttig and Suzuki (see Anning, Suzuki and Wuttig 1982). A diagram of the experimental apparatus is given in fig. 1. The technique uses a long thin vibrating reed which is externally driven through the natural resonance by a magnetic gradient acting on a small permanent magnet attached to the reed. The mechanical response of the reed to the driving force was measured capacitively by pick-up capacitors using a technique developed by Tomboulion (1961). The samples were driven into the non-linear regime which resulted in asymmetric resonance curves. Measurements were made using increasing and decreasing frequency sweeps to obtain the complete asymmetry of the resonance curves. The resonance curves were then analysed using a non-linear least-squares fit to an empirical response relationship developed by Nayfeh (1979) given in eqn. (1);

$$\omega = \omega_0 + \frac{3}{8} \left( \frac{\alpha a^2}{\omega_0} \right) \pm \frac{1}{2} \sqrt{\left( \frac{K}{\omega_0 a} \right)^2 - \delta^2} \quad (1)$$

where  $\omega_0$  represents the resonance frequency,  $\alpha$  the non-linear elastic constant,  $\delta$  the linear anelastic constant (damping),  $K$  the external excitation, and  $a$  the r.m.s. amplitude of vibration of the sample.

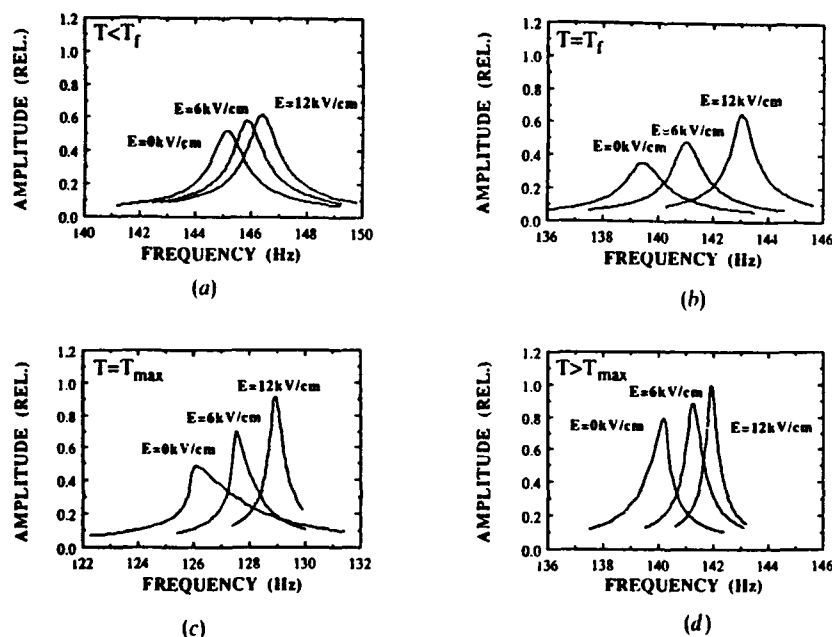
Resonance curves were measured as a function of temperature on heating between 250 and 420 K, with resonance frequencies of approximately 10, 100, and 400 Hz. Measurements were done as a function of bias, the bias levels used were 0, 1, 2, 3, 4, 5, 6, 7, 8, 10, 12, and 15 kV cm<sup>-1</sup>. X-ray line broadening measurements were also done using a position sensitive detector to supplement the data base. Measurements were made as a function of bias on the (200), (220), and (321) peaks at 25 and 0°C. The dielectric constant and polarization were also measured as a function of temperature for comparison using standard techniques.

The samples used in this study were PMN ceramics with 0 and 10 at.% PbTiO<sub>3</sub> (PMN-10PT). They were prepared as described by Pan, Jiang and Cross (1988). The samples were free of ageing as described by Pan *et al.*, were free of pyrochlore as described by Swartz and Shrout (1982), and were electroded with gold. Stoichiometric ageing-free samples were used to avoid a potential complication of the relaxation mechanism by a time-varying defect structure. Supplementary measurements were also made on La-modified lead zirconate titanate (PLZT) with Zr/Ti ratio of 65/35 and a La content of 9 at.%. The PLZT samples were donated by Honeywell Inc. of Bloomington, Minnesota.

## §3. RESULTS

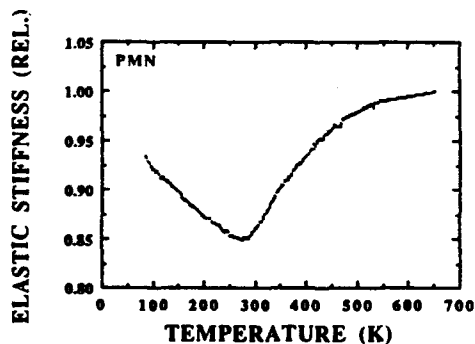
Sample resonance curves are given in figs. 2(a)-(d) for PMN-10PT at 270, 292, 310 and 340 K, respectively. Each figure contains resonance curves under bias levels of 0, and 6, and 12 kV cm<sup>-1</sup>. These curves were chosen to illustrate the field dependence of the resonance curves at various temperatures. An electrical field increased the resonance frequency, and decreased the mechanical losses. At lower temperatures the resonance curve characterized a linear oscillator. As the temperature was increased the resonance curve bent to lower frequencies with increasing displacement (elastically soft under stress), and on a further increment of the temperature the resonance curve bent to higher frequencies with increasing displacement (elastically hard under stress). The effect of a d.c. bias was to decrease the magnitude of the nonlinearity.

Fig. 2



Sample resonance curves for PMN-10PT at bias levels of 0, 6, and 12 kV cm<sup>-1</sup>. (a)  $T = -15^{\circ}\text{C}$ , (b)  $T = 15^{\circ}\text{C}$ , (c)  $T = 40^{\circ}\text{C}$ , (d)  $T = 65^{\circ}\text{C}$ .

Fig. 3



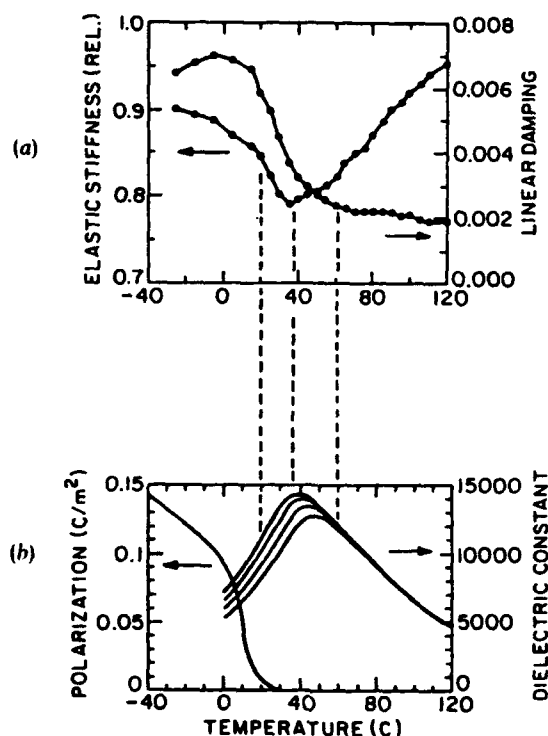
Elastic stiffness as a function of temperature for PMN.

#### § 4. DISCUSSION

The insertion of any local distortion into a crystalline lattice produces internal strains. Anelastic behaviour is a manifestation of the relaxational kinetics of this internal deformation process. In PMN the anelastic response can be anticipated to reflect the kinetics of the polarization fluctuations which can couple the applied stress to the internal strain through the electrostriction. The elastic stiffness of PMN over a wide range of temperatures is illustrated in fig. 3. The elastic stiffness started to soften



Fig. 4



(a) Elastic stiffness and linear damping as a function of temperature for PMN-10PT at a measurement frequency of 100 Hz. (b) Polarization and dielectric constant as a function of temperature for PMN-10PT. The measurement frequencies for the dielectric constant were 0.1, 1, 10, and 100 kHz.

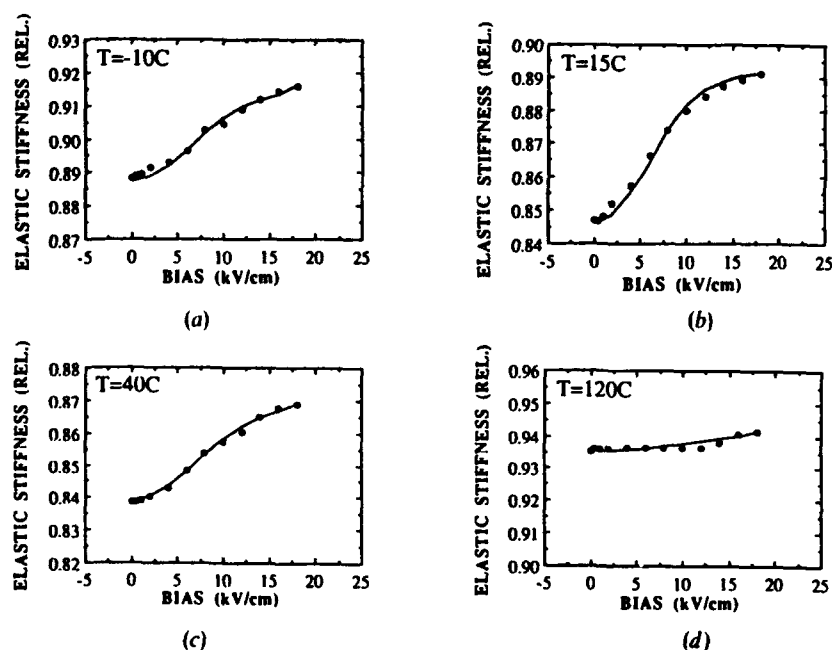
around 600 K which is close to the temperature of the onset of local polarization as originally shown by Burns and Dacol (1983). The implication is that the insertion of polarization into the prototypic phase softens the lattice, via the electrostriction. The agreement of the temperature of the maximum in the 100 Hz elastic softening with the temperature of the 100 Hz permittivity maximum, shown in fig. 4, illustrates that the relaxational processes in both responses does have a common origin. The dielectric relaxation has been shown to be glassy due to interactions between superparaelectric moments (Viehland *et al* 1990). The implication is that the anelastic relaxation may also be glassy due to local electrostrictive strain fields.

Figures 5(a)–(d) illustrate the field dependence of the stiffness at various temperatures. The points in these figures are the experimental data, and the solid line is the curve fitting to eqn. (2);

$$c(E) = c(0) + \beta E^2 + \eta E^4 \quad (2)$$

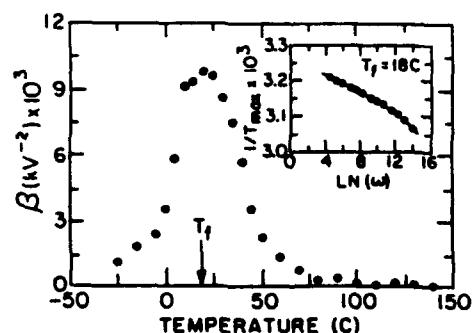
where  $c$  is the elastic stiffness, and  $\beta$  and  $\eta$  are the fourth and sixth order electroelastic couplings respectively. The experimental data was modelled using a nonlinear least-squares fitting to eqn. (2), solving for  $\beta$  and  $\eta$ .  $\beta$  as a function of temperature is shown in fig. 6. The maximum electroelastic nonlinearities occurred near 15°C. The freezing

Fig. 5



Elastic stiffness as a function of d.c. electrical bias for PMN-10PT. (a)  $T=10^\circ\text{C}$ , (b)  $T=15^\circ\text{C}$ , (c)  $T=40^\circ\text{C}$ , (d)  $T=120^\circ\text{C}$ .

Fig. 6



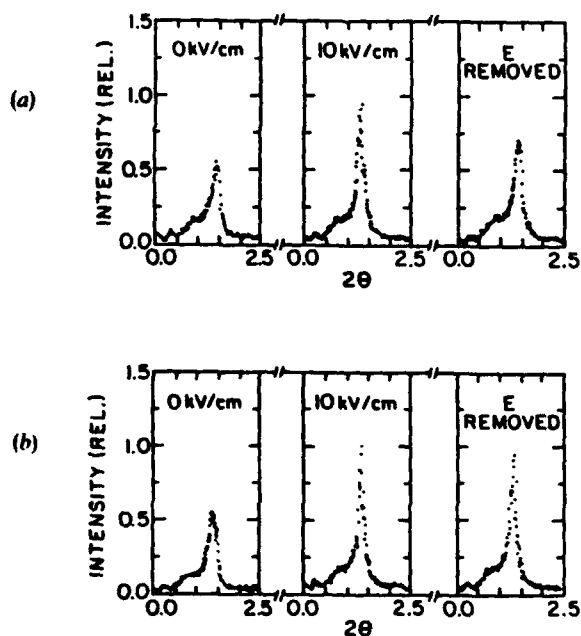
Electroelastic constant ( $\beta$ ) as a function of temperature for PMN-10PT where  $T_f$  is the freezing temperature. The inset is the fitting of the frequency dependence of the temperature of the permittivity maximum to the Vogel-Fulcher relationship.

temperature has been estimated to be  $18^\circ\text{C}$  by modelling the frequency dependence of  $T_{\text{max}}$  using the Vogel-Fulcher relationship (Viehland *et al.* 1990) which is close to the temperature of the maximum electroelastic nonlinearities. The modelling of the dielectric relaxation is shown as the inset of fig. 6. These results indicate that the local electrostrictive strains are dynamical in nature and undergo a Vogel-Fulcher type

freezing corresponding to the freezing of the polarization fluctuations. This can be interpreted to mean that the polarization fluctuations do not occur within a rigid framework, but rather inside of a soft framework which deforms in response to the polarization fluctuations. The maximum nonlinearities in the electroelastic response, then, occurs near the freezing temperature where a d.c. biasing field can most effectively repopulate the states. Yushin (1988) has reported a similar anomaly in the electroacoustic behaviour near 210 K for PMN in the zero-field-cooled state.

An electrical field stiffened the elastic response at all bias levels. If the softening of the linear elastic stiffness is solely related to the introduction of polarization into the lattice, then application of an electrical field should further soften the lattice because it would stabilize more polarized regions. A possible explanation of this discrepancy is that the inhomogeneity in the internal strain field, both in the frozen and dynamical states, enhances the deformation mechanism. Consequently on application of an electrical field the lattice stiffens as the randomness of the strain field is destroyed. The elastic behaviour of PMN may be similar to the orientational glassy state proposed for  $(\text{KBr})_{1-x}(\text{KCN})_x$  (Knorr, Volkmann and Loidl 1986, Knorr 1987) in which quadrupolar interactions between elastic dipoles leads to a freezing of the anelastic response. It is proposed here that quadrupolar interactions between polar clusters in PMN contribute to the freezing process, and that the corresponding frustration is partially orientational in nature. The main difference between the glassy response in PMN and  $(\text{KBr})_{1-x}(\text{KCN})_x$  is the scale of the inhomogeneity in the strain field. In relaxors this scale is on the order of 50–100 Å (Randall and Bhalla 1989, Chen, Chan and Harmer

Fig. 7



(220) diffraction peak for PMN-10PT under d.c. bias levels of 0, 10 and 0 kV cm<sup>-1</sup>. (a)  $T = 25^\circ\text{C}$ , (b)  $T = 0^\circ\text{C}$ .

1989), whereas in  $(\text{KBr})_{1-x}(\text{KCN})_x$  it is several unit cells. The glassy contribution to the elastic softening consequently would be expected to be much less for PMN than for  $(\text{KBr})_{1-x}(\text{KCN})_x$ , which is experimentally observed. In the tungsten bronze family of relaxors, an electrical field has been found to soften the lattice (Shrout 1980). The difference in the elastic behaviour of the PMN family of relaxors and the tungsten bronzes, can be understood by the differences in their structures. The structure of the tungsten bronzes are prototypic tetragonal with only two ferroelectric domain states. Consequently the interaction of the electrostrictive deformation with an applied stress does not reveal any internal strain. PMN is rhombohedral having non- $180^\circ$  variants which can contribute to an inhomogeneous internal strain if the cluster moments freeze in a random manner.

The (220) diffraction peak for PMN-10PT at various bias levels is shown in fig. 7 (a) and (b) at 25 and  $0^\circ\text{C}$ , respectively. The width of the peak decreased and the peak shifted to lower  $2\theta$  values with increasing bias. Upon removal of the field the width and the peak position returned to the unbiased values at  $25^\circ\text{C}$ , but remained at the biased values at  $0^\circ\text{C}$ . These results support the model of an inhomogeneity in the local strain field which has an instability to an applied bias. The inability of the inhomogeneity to recover after removal of the bias below the freezing temperature gives further evidence of the dynamical nature of the local electrostrictive strains above  $T_f$ . The shifting of the peak position shows that a macrostrain develops from the inhomogeneous internal strain on biasing. The shift in the peak position ( $\Delta 2\theta$ ) was approximately  $0.1^\circ$  between 0 and  $10\text{ kV cm}^{-1}$ . The lattice strain associated with this shift can be approximated by equating the Bragg relationships at both biases and solving for  $\Delta d/d_1$  as given in eqn. (3);

$$\varepsilon = \frac{\Delta d}{d_1} = 1 - \frac{\sin(2\theta_1)}{\sin(2\theta_1 + \Delta 2\theta)} \quad (3)$$

where  $\varepsilon$  is the lattice strain,  $d_1$  and  $d_2$  are the lattice constant under 0 and  $15\text{ kV cm}^{-1}$  respectively, and  $\Delta d$  is defined as  $d_1 - d_2$ .  $\Delta d/d_1$  can then be approximated as  $5 \times 10^{-4}$  which is comparable to the electrostrictive strain (Jang 1979). This shows that the large electrostrictive strains in these materials are not due to induced polarization, but rather to the relief of the internal strain by the development of a macrostrain. Hysteresis then occurs in the field dependence of the strain behaviour below  $T_f$ .

The 100 Hz internal friction as a function of bias at  $T_f$  is shown in fig. 8. The maximum field dependence was also found near  $T_f$ . The internal friction initially increased until  $3\text{ kV cm}^{-1}$ , then decreased upon further increment of the field. The coexistence of both dielectric and anelastic relaxation requires that the piezoelectric response ( $d_{33}$ ) must also be dispersive (Nowick and Heller 1965), which has recently been observed (Pan, Gu, Taylor and Cross 1989). The maximum response and strongest relaxation in  $d_{33}$  were also observed near this threshold bias ( $3\text{ kV cm}^{-1}$ ). This means that at the threshold bias a small applied stress can most effectively repopulate the equivalent variants; consequently the mechanical losses are maximum. The threshold bias can be interpreted to mean that in the zero-field-cooled state the orientations of the superparaelectric moments are not completely random, but rather there are local configurations of moment orientations as previously proposed from the field dependence of the dielectric response (Viehland *et al.* 1991). A small bias then acts to override these configurations, enhancing the fluctuation kinetics and the magnitude of the relaxation. It is probable that the short-range ordering in

Fig. 8

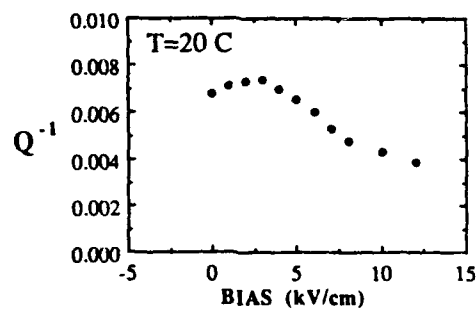
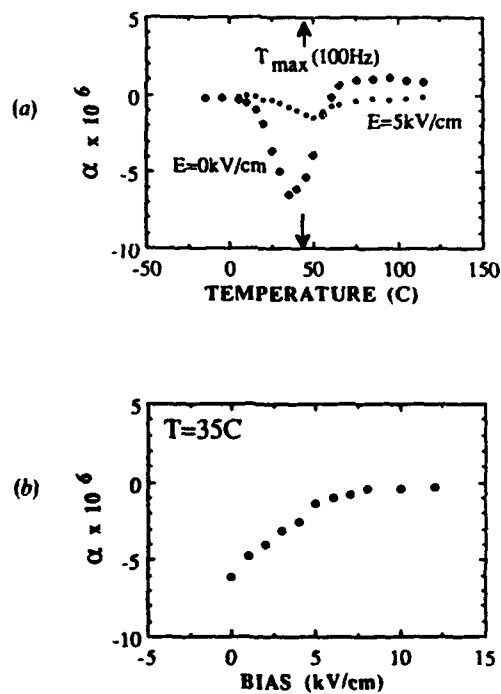
Internal friction ( $Q^{-1}$ ) as a function of d.c. electrical bias for PMN-10PT.

Fig. 9

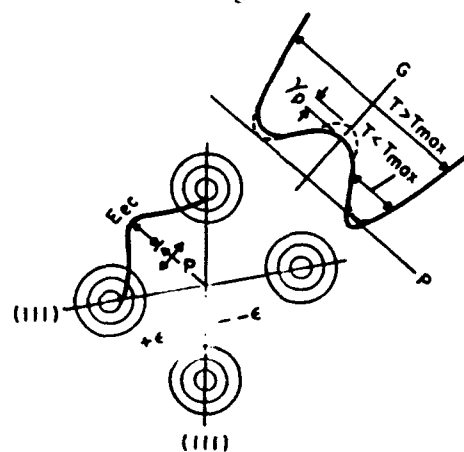


(a) Effective third-order elastic constant ( $\alpha$ ) for PMN-10PT as a function of temperature under d.c. bias levels of 0 and 5 kV cm $^{-1}$  where  $T_{\text{max}}$  is the temperature of the 100 Hz dielectric maximum. (b) Effective third-order elastic constant ( $\alpha$ ) for PMN-10PT as a function bias near the temperature of the permittivity maximum.

these configurations is determined in part by the local electrostrictive strain fields. Khachaturyan and Shatalov (1969) have previously shown that local strain fields between inclusion can lead to short-range ordering of their 'elastic dipoles'. At bias levels above threshold, the internal friction decreased probably because of the relief of the internal strain and the longer nature of the dipolar interactions.

The effective third-order elastic constant of PMN as a function of temperature under zero bias is illustrated in fig. 9 (a). The maximum softening of this constant occurred slightly below the temperature of the 100 Hz permittivity maximum. The maximum bending of the resonance curve under stress at  $T_{\max}$  in the un-electrified state can be estimated to be 1 Hz (see fig. 2(c)) which is approximately 0.1%. This translates into a 1.5% decrease in the elastic energy by the nonlinearities. This contribution is not small in consideration of the inhomogeneous nature of the applied stress. It is obvious that the elastic softening occurs when the frequency of the polarization fluctuations nearly coincides with the driving frequency of the a.c. stress field. The maximum elastic softening probably occurs when the polarization can most effectively respond to the biasing strain. Below this temperature, the fluctuations are essentially frozen with respect to the time scale of the measurement. The natural elastic hardening, consequently, is observed at higher temperatures when the kinetics of the deformation process becomes much faster than the applied a.c. stress. The softening of the elastic response shows that the kinetics of the internal deformation process can be driven by an applied a.c. stress. Higher order elastic constants usually characterize the stress dependence of the velocity of an elastic wave and/or the nonlinear interactions between 'elastic dipoles' (Wallace 1970). It is proposed that the microscopic origins of the softening arises due to interactions between cluster moments, both dipolar and quadrupolar, which in part control the kinetics of the deformation process. A potential well diagram which illustrates the effect of an applied stress along a (111) variant is shown in fig. 10. If  $T < T_{\max}$  the applied stress lowers the activation by  $\gamma_p$ ; consequently the repopulation kinetics along the axis of the stress is enhanced and the elastic

Fig. 10

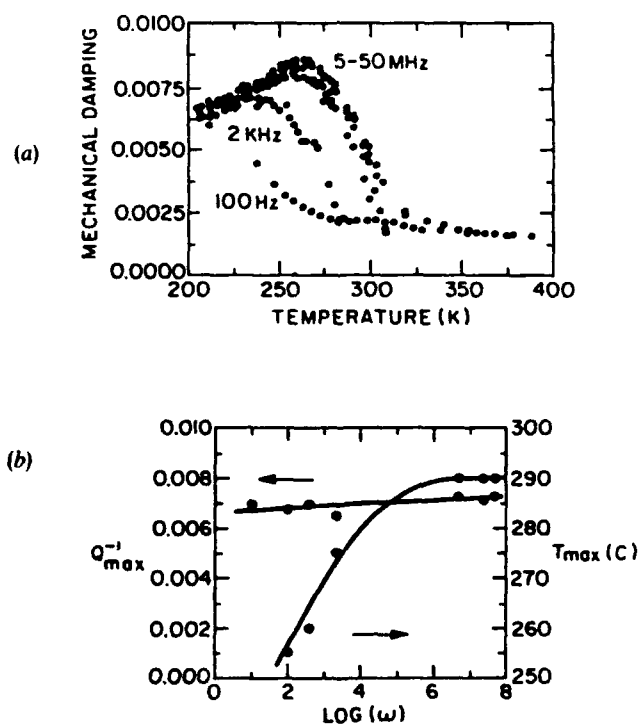


Potential-well diagram which illustrates the effect of an a.c. mechanical stress on the activation energy for a superparaelectric relaxation at various temperatures. Here  $\epsilon$  is the r.m.s. value of the stress and  $\gamma_p$  the change in the activation energy.

response is soft. If  $T > T_{\max}$  the applied stress is shown to push against the walls of the wells; consequently the elastic response is hard. The third-order elastic constant under  $5 \text{ kV cm}^{-1}$  is also illustrated in fig. 9(a). An electrical field decreased the softening and increased the temperature of its maximal response. The third-order elastic constant as a function of bias at the temperature of the permittivity maximum is shown in fig. 9(b). The elastic response is essentially linear under  $10 \text{ kV cm}^{-1}$ . The reason for the decrease in the magnitude of the elastic softening can be understood as a reflection of the decrease in the inhomogeneity of the local strain fields on biasing. Consequently the deformation process is less stress-sensitive and the magnitude of the softening of the lattice under stress decreases.

The internal friction of PMN has been reported to be frequency independent between 5 and 50 MHz (Yushin, Smirnova, Dorogortsev, Smirnov and Galayamov 1987). The internal friction of PMN at various frequencies between 100 and 50 MHz is shown in fig. 11(a). The maximum loss and temperature of its half maximum value are plotted as a function of frequency in fig. 11(b). It is obvious that the kinetics of relaxational process is temperature dependent in only the low-frequency regime,

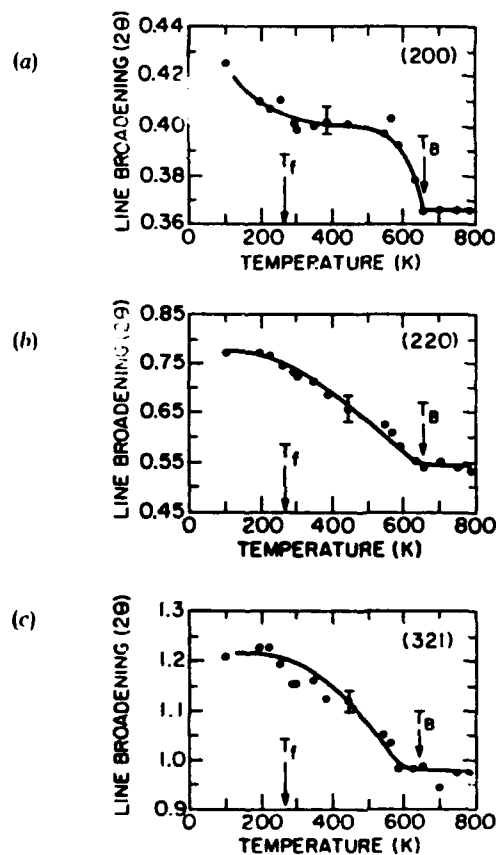
Fig. 11



(a) Mechanical damping of PMN as a function of temperature at various frequencies. The frequencies shown are 0.1 and 2.3 kHz, and 7, 10, 20 and 50 MHz. The MHz data was taken from Yushin (1988). (b) Maximum of the internal friction ( $Q_{\max}^{-1}$ ) and temperature of its half maximum value as a function of the measurement frequency for PMN-10PT.

whereas the magnitude of the relaxation is relatively frequency independent. A possible explanation for this behaviour is that the thermal fluctuations of the local electrostrictive strains cannot follow above a certain frequency. Further evidence for such a behaviour in relaxors can be found in the temperature dependence of the line broadening of the diffraction peaks in PLZT-8-7 (Darlington 1989). These results are illustrated in figs. 12(a)-(c). The broadening of the (200) peak starts near the onset of local polarization, and seems to saturate near 560 K, whereas the broadening of the (220) and (321) peaks continuously increases between approximately 500 and 250 K. This shows that the inhomogeneity in the strain field associated with the volume deformation saturates when an inhomogeneity in the shear deformation ((220) and (321) peaks) starts to develop. A possible explanation is that at high temperatures near the onset of reversible polarization, the rhombohedral strain of the individual ferroelectric distortions is largely suppressed due to their emergence in an elastically stiff matrix. The matrix is soft dielectrically (high permittivity) so the polarization can

Fig. 12



X-ray diffraction peaks as a function of temperature for PLZT-8-7 (65/35) taken from Darlington (1989) where  $T_B$  is the Burns's temperature and  $T_f$  the freezing temperature: (a) the (200) peak, (b) the (220) peak, and (c) the (321) peak.



Fig. 13

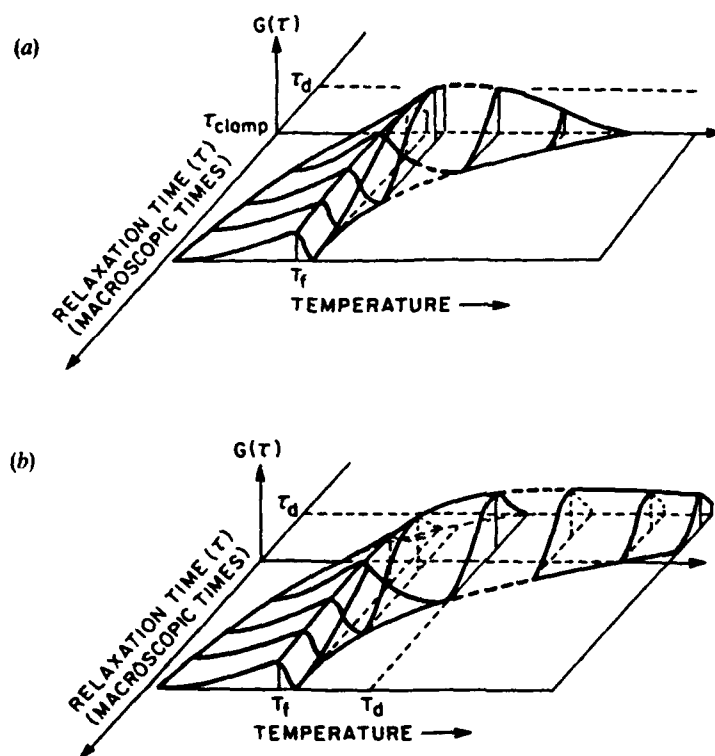


Diagram illustrating the proposed temperature-dependent relaxation time spectrum where  $G(\tau)$  is the number of micro-polar regions having a relaxation time  $\tau$ : (a) anelastic distribution, (b) dielectric distribution.

occur, but elastically the rhombohedral variants are cubically clamped. Consequently the strain fields associated with the volume deformation are inhomogeneous and static. At lower temperatures, as the kinetics of the polarization fluctuations slow down due to the build up of correlations, the polar regions may be able to lower their free energy by deforming in a correlated manner which preserves the cubic dimensions. Inversion of the polarization leaves the elastic environment unchanged, but the rotation of the polarization involves rearrangements of the local elastic minima. The free energy may then be lowered by allowing the local strain fields to become dynamic, consequently an inhomogeneity in the shear strain develops. The implication is that the anelastic and dielectric relaxation time distributions do not need to be equivalent, but rather varying differences between the two may occur as a function of temperature or frequency depending on whether the polarization is free to deform or clamped. At lower temperatures near  $T_f$  the relaxation time distributions would be very similar. For comparison the Vogel-Fulcher freezing temperature of PLZT-9 has been estimated as 265 K which is close in agreement with the temperature of the saturation in the broadening of the (220) and (321) peaks.

A model of a temperature dependent relaxation time spectrum is presented in fig. 13(a) for the anelastic response. A model previously proposed for the dielectric

response is shown in fig. 13(b) for comparison (Viehland *et al.* 1990). These models are not quantitative, but are qualitatively consistent with experimental observations. The isothermal width for both spectra is shown to become very broad near  $T_f$  with the mean value ( $\tau_{av}$ ) approaching the macroscopic time regime. Relaxation is also shown to exist to temperatures significantly below  $T_f$  as a reflection of the size dispersion of the moments. Above  $T_f$  the isothermal widths of the relaxation time spectra continuously sharpen with increasing temperature. The shortest relaxation time ( $\tau_{min}$ ) for the anelastic relaxation is shown to approach a critical frequency ( $\tau_{clamp}$ ) at which point the anelastically active orientations are becoming inaccessible to the polarization due to the stiffening of the matrix. This frequency is shown to be much lower than the Debye frequency ( $\tau_d$ ). Upon further increment of the temperature  $\tau_{av}$  and  $\tau_{max}$  are shown to approach  $\tau_{clamp}$  for the anelastic response. The maximum value of the distribution is shown to be relatively frequency independent to reflect the weak frequency dependence of the relaxation magnitude. The maximum value of the distribution for the anelastic response is shown to be smaller than that for the dielectric response to illustrate the relative magnitudes of their respective losses.

#### §4. CONCLUSIONS

Evidence for a Vogel-Fulcher type freezing of the anelastic response has been found. It has subsequently been proposed that the freezing process in relaxors is partially controlled by randomly orientated local electrostrictive strain fields. The existence of an internal strain which decreases on biasing has been confirmed by line broadening of the (220) diffraction peak. The frequency dependence of the anelastic relaxation has also been investigated. It has been found that the kinetics of the anelastic relaxation is substantially different from the dielectric relaxation at higher frequencies. A softening of the elastic response to the amplitude of the applied stress has also been found which was explained as a stress activation of the internal deformation process.

#### ACKNOWLEDGMENTS

This work has been supported in full by contracts administered through the Office of Naval Research. Recognition and appreciation must be given to Drs N. Yushin and C. Darlington for the use of their published data. Further appreciation is expressed to Drs Jacques J. Van der Klink and Gerhard Barsch for providing references and ideas.

#### REFERENCES

- ANNING, A., and WUTTIG, M. J., 1984, *Phys. Chem. Solids*, **45**, 481.
- ANNING, A., SUZUKI, T., and WUTTIG, M., 1982, *J. appl. Phys.*, **53**, 6797.
- BOKOV, V., and MYL'NIKOVA, I., 1960, *Soviet Phys. Solid St.* **3** (3).
- BURNS, G., and DACOL, F., 1983, *Solid St. Commun.*, **48**, 853.
- CHEN, J., CHAN, H., and HARMER, M., 1989, *J. Am. Ceram. Soc.*, **72**, 593.
- CROSS, L., 1987, *Ferroelectrics*, **76**, 241.
- DARLINGTON, C., 1989, *Phys. Stat. Sol.*, **a**, **113**, 63.
- GLASS, A., 1969, *J. appl. Phys.*, **40**, 4699.
- JANG, S., 1979, PhD Dissertation, The Pennsylvania State University.
- KNORR, K., VOLKMANN, U., and LOIDL, A., 1986, *Phys. Rev. Lett.*, **57**, 2544.
- KNORR, K., 1987, *Proceedings of 7th Conf. of Condensed Mat. Div. of European Phys. Soc.*, Pisa, Italy.
- KHACHATURYAN, A., and SHATALOV, G., 1969, *Soviet Phys. Solid State*, **11**, 118.
- NAYFEH, A., 1979, *Nonlinear Oscillations* (Wiley, New York), p. 166.
- NOWICK, B., and HELLER, W., 1965, *Adv. Phys.*, **14**, 101.

- PAN, W., JIANG, Q., and CROSS, L., 1988, *J. Am. Ceram. Soc.*, **71**, C-17.
- PAN, W., GU, W., TAYLOR, D., and CROSS, L., 1989, *Japan J. appl. Phys.*, **28**, 653.
- RANDALL, C., and BHALLA, A., 1990, *J. Mat. Sci.*, **29**, 5.
- SHROUT, T., 1980, Ph.D. Dissertation, The Pennsylvania State University.
- SMOLENSKI, G., and AGRANOVSKA, A., 1960, *Soviet Phys. Solid State*, **1**, 1429.
- SWARTZ, S., and SHROUT, T., 1982, *Mater. Res. Bull.*, **17**, 1245.
- TOMBOULIAN, R., 1961, IBM Research Report, RC-396.
- VIEHLAND, D., JANG, S., WUTTIG, M., and CROSS, L., 1990, *J. appl. Phys.*, **68**, 2416; 1991, *J. appl. Phys.*, **69**, 414.
- WALLACE, D., 1970, *Solid-St. Phys.*, **25**, 302.
- WUTTIG, M., and LIN, C., 1983, *Acta metall.*, 1117.
- XI, Y., ZHILLI, C., and CROSS, L., 1983, *Ferroelectrics*, **54**, 163.
- YUSHIN, N., SMIRNOVA, E., DOROGORTSEV, S., SMIRNOV, S., and GALAYAMOV, G., 1987, *Soviet Phys. Solid St.*, **29**, 1693.
- YUSHIN, N., 1988, *Proceedings of Ferroelektrizitat 1988*, (GDR: Halle), 102.

## APPENDIX 23

# Local polar configurations in lead magnesium niobate relaxors

Dwight Viehland, S. J. Jang, and L. Eric Cross<sup>a)</sup>

Materials Research Laboratory, Pennsylvania State University, University Park, Pennsylvania 16802

Manfred Wuttig

Engineering Materials Program, University of Maryland, College Park, Maryland 20742

(Received 21 June 1990; accepted for publication 21 June 1990)

The field dependence of the dielectric response has been measured for lead magnesium niobate relaxors. The frequency dispersion of the temperature of the permittivity maximum,  $T_{max}$ , was analyzed using the Vogel-Fulcher relationship. The field dependence of the permittivity at various temperatures was also modeled using a phenomenological expansion in the electric field. The activation energy and a softening of the dielectric response were found to be maximum under a small bias. The freezing temperature was found to be minimum near this same bias. These results are interpreted to mean that the moments of the polar clusters do not freeze in random orientations, but rather locally preferred configurations of moments are proposed to exist. Evidence is presented that the scale of these configurations is approximately 100 Å. At higher biases the relaxation mechanism was shut down; consequently, the nonlinear response was stiffened and  $T_{max}$  increased. The nonlinear response was also found to be maximum near the freezing temperature.

## I. INTRODUCTION

Lead magnesium niobate (PMN) was the first ferroelectric discovered which exhibited a classic dielectric relaxation<sup>1</sup> and consequently was designated a relaxor ferroelectric. Since that time, many relaxors have been identified in mixed oxide systems, primarily in the perovskite and tungsten bronze structure families. Relaxors are unable to sustain a macroscopic polarization until temperatures significantly below the dielectric maximum ( $K_{max}$ ), but a local polarization is known to exist until much higher temperatures.<sup>2</sup> These locally polarized regions are believed to have rhombohedral symmetry<sup>3</sup> and, consequently, eight equivalent variants. In consideration of these findings, Cross<sup>4</sup> suggested that the polar clusters are superparaelectric with the polarization thermally fluctuating between equivalent directions. The density of the polar clusters as observed by transmission electron microscopy<sup>5,6</sup> (TEM) is high enough that collective effects between clusters may be significant. Viehland *et al.*<sup>7</sup> have consequently suggested that the fluctuations have a freezing temperature similar to spin glasses. Similar behavior in which long-range polar order is in conflict with random freezing has been reported in  $KTa_{1-x}Nb_xO_3$ ,<sup>8,9</sup>  $K_{1-x}Li_xTaO_3$ ,<sup>10</sup> and  $K_{1-x}(NH_4)_xH_2PO_4$ .<sup>11</sup> Burns and Dacol<sup>12</sup> and Bovton *et al.*<sup>13</sup> have previously discussed the similarities of PMN relaxors to dipole and spin glasses.

Relaxors are known to be strongly nonlinear materials. The dielectric permittivity<sup>14,15</sup> and elastic constants<sup>16-18</sup> have both been reported to be altered by an electric field. It is generally believed that the nonlinearities are a reflection of the macroscopic polarization which can be sustained by an electric field to much higher temperatures. The polarization is completely reversible and collapses when the field is removed. Pan *et al.*<sup>15</sup> have investigated the field dependence of the room-temperature dielectric constant in PMN; they

found strong nonlinearities and a suppression of the frequency dispersion at higher biases. Xi, Zhilli, and Cross<sup>19</sup> proposed an electric-field-induced micro-macro domain transition in La-modified lead zirconate titanate with 8 at. % La and a Zr/Ti ratio of 65/35 near the temperature of the onset of a macroscopic polarization to account for the field dependence of the dielectric response.

Spin glasses can be viewed as interacting superparamagnetic clusters.<sup>20</sup> These materials are characterized by a freezing temperature at which the fluctuations of the magnetic moment condense and by conflicting interactions. Spin glasses are also known to be strong nonlinear materials magnetically. It is generally believed that the change in properties is a reflection of an alignment of spins and an ordering of nearest-neighbor interactions, leading to a change in the dynamics of the freezing process. The magnetic permittivity,<sup>21</sup> temperature of the permittivity maximum,<sup>22</sup> and the onset of irreversibility<sup>23</sup> have all been reported to be altered by magnetic fields. The purpose of this work was to investigate the field dependence of the freezing process and the nonlinear permittivity in PMN relaxors. The field dependence of the dielectric response has been comprehensively measured up to bias levels above saturation.

## II. EXPERIMENTAL PROCEDURE

The samples used in this study were PMN ceramics with 10 at% PT (PMN-10PT). They were prepared as described by Pan.<sup>24</sup> The 100 Hz dielectric maximum was near 40 °C. The samples were free of aging as described by Pan,<sup>24</sup> free of pyrochlore as described by Swartz and Shrout,<sup>25</sup> of dimensions 1 cm × 0.5 cm × 0.05 cm, and electroded with gold. Stoichiometric aging free samples were used to avoid a potential complication of the relaxation mechanism by a defect structure.

The dielectric response was measured as a function of frequency and temperature at bias levels of 0, 0.5, 1, 2, 3, 4, 5, 6, 7, 8, 10, 12, 14, 20, and 28 kV/cm. The frequencies used

<sup>a)</sup> Also in the Electrical Engineering Department.

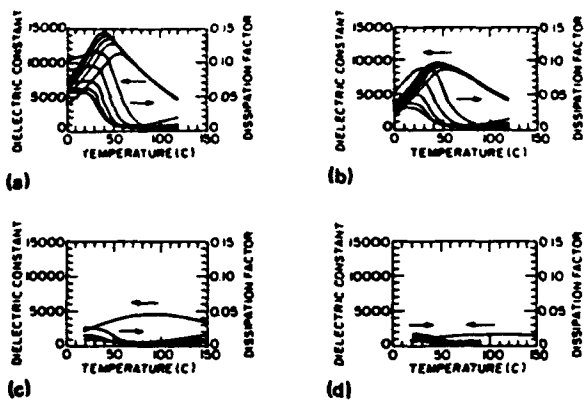


FIG. 1. Dielectric constant and dissipation factor as a function of temperature at measurement frequencies of 0.1, 1, 10, 100, and 1000 kHz. The largest dielectric constant and dissipation factor are the 0.1 kHz, the smallest are the 1000 kHz, and the other curves between are in order of increasing frequency. (a)–(d) are at bias levels of 0, 8, 20, and 28 kV/cm respectively.

were 0.1, 0.2, 0.4, 1, 2, 4, 10, 20, 40, 100, 200, 400, and 1000 kHz. Measurements were made in the temperature range of 0–150 °C by cooling at a rate of 1 °C/min. The measurements were made using an HP4275A and 4274A LCR meters. Two large blocking capacitors were used to protect the dielectric bridge from possible dielectric breakdown of the sample. A 20-M $\Omega$  resistor was put in series with the dc power supply so as not to bypass the ac current from the capacitance bridge.

### III. RESULTS

The field dependencies of the dielectric responses, both real and imaginary, are illustrated in Figs. 1(a)–1(d) for bias levels of 0, 8, 20, and 28 kV/cm, respectively. It can be seen that an electric field reduces the dielectric constant, suppresses the frequency dispersion, and increases the temperature of the dielectric maximum. Also, the dielectric loss was reduced and showed a more pronounced maximum. Under larger biases, Maxwell–Wagner losses are evident at high temperatures as shown in Figs. 1(c) and 1(d). The loss is not shown in Fig. 1(d) above 80 °C in order to make the graph distinguishable.

The field dependence of  $K_{max}$  is shown in Fig. 2(a). The 0.1-kHz  $K_{max}$  was approximately 15 000 under 0 kV/cm, decreased slowly at lower bias levels, and then decreased quadratically to approximately 1500 under 28 kV/cm. At higher frequencies,  $K_{max}$  showed less field dependence, but no dispersion of  $K_{max}$  was observed above 10 kV/cm. The field dependence of the temperature of the dielectric maximum ( $T_{max}$ ) is shown in Fig. 2(b). The 0.1-kHz  $T_{max}$  went through a minimum of approximately 38 °C under 3 kV/cm and then increased to approximately 110 °C under 28 kV/cm. Similar results were obtained for the other frequencies. At higher measurement frequencies,  $T_{max}$  was less dependent on the bias, but no dispersion was observed above 10 kV/cm in the frequency domain investigated.

### IV. DISCUSSION

The strong field dependence of the dielectric permittivity can be interpreted in terms of an alignment of the mo-

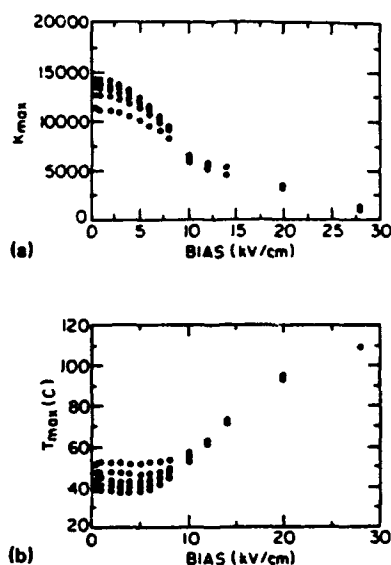


FIG. 2. (a) Permittivity maximum ( $K_{max}$ ) as a function of dc bias level. The measurement frequencies were 0.1, 1, 10, 100, and 1000 kHz. The largest  $K_{max}$ 's are the 0.1 kHz, the smallest are the 1000 kHz, and the other curves between are in order of increasing frequency. (b) Temperature of permittivity maximum ( $T_{max}$ ) as a function of bias level. The measurement frequencies were 0.1, 1, 10, 100, and 1000 kHz. The lowest temperatures are the 0.1 kHz, the highest are the 1000 kHz, and the other curves between are in order of increasing frequency.

ments of polar clusters. The permittivity decreased by approximately an order of magnitude under a bias level of 28 kV/cm relative to 0 kV/cm. At higher biases, the sample probably has reached saturation with nearly all moments aligned, and consequently the dielectric response ( $\delta P/\delta E$ ) is lower. The polarization behavior for PMN-10PT has recently been modeled by modifying Néel's equilibrium equation for superparamagnetic clusters to include an effective internal field.<sup>26</sup> A more complete understanding of the field dependence of the relaxor behavior might be obtained by a careful analysis of the kinetics of the dielectric response and its nonlinear contribution.

The frequency dependence of the temperature of the permittivity maximum can be modeled using the Vogel–Fulcher relationship<sup>7,27,28</sup> given in Eq. (1):

$$\omega = f_0 \exp\left(\frac{-E_a}{k(T_{max} - T_f)}\right) \quad (1)$$

where  $f_0$  is the Debye frequency,  $E_a$  is the activation energy,  $T_{max}$  is the temperature of the permittivity maximum, and  $T_f$  is the freezing temperature. The 13 pairs of  $(\omega, T_{max})$  for each bias level below 10 kV/cm were analyzed using a Levenberg–Marquardt nonlinear fitting to Eq. (1) solving for  $f_0$ ,  $E_a$ , and  $T_f$ . The analysis was done assuming that  $f_0$  was constant at all bias levels. A value of  $1.03 \times 10^{12} \text{ s}^{-1}$  resulted in minimum variance. The resultant values for  $E_a$  and  $T_f$  are given in Table I along with the corresponding bias level. Figures 3(a) and 3(b) show  $E_a$  and  $T_f$  as a function of bias, respectively.  $E_a$  went through a maximum near 3 kV/cm and then decreased quadratically to zero near 10 kV/cm.  $T_f$  went through a minimum near 3 kV/cm and then increased

TABLE I. Activation energy ( $E_a$ ) and freezing temperature ( $T_f$ ) tabulated along side the corresponding bias level.

| Bias (kV/cm) | $E_a$ (eV) | $T_f$ (K) |
|--------------|------------|-----------|
| 0.00         | 0.0407     | 291.50    |
| 1.00         | 0.0419     | 290.25    |
| 2.00         | 0.0426     | 289.37    |
| 3.00         | 0.0430     | 288.79    |
| 4.00         | 0.0425     | 288.85    |
| 5.00         | 0.0395     | 290.80    |
| 6.00         | 0.0363     | 293.51    |
| 7.00         | 0.0287     | 299.56    |
| 8.00         | 0.0217     | 306.20    |

dramatically above 10 kV/cm. The field dependence of the permittivity was modeled with a phenomenological expansion in the electric field as given in Eq. (2):

$$\chi(E, T) = \chi_0(T) + \chi_2(T)E^2 + \chi_4(T)E^4 + \dots, \quad (2)$$

where  $\chi(T)$  is the zero-field permittivity,  $\chi_2(T)$  is the second-order nonlinearity, and  $\chi_4(T)$  is the fourth-order nonlinearity. The fitting of the data is shown as the solid lines in Figs. 4(a)–4(d), and the experimental data as the solid circles.  $\chi_2$  and  $\chi_4$  as a function of temperature at measurement frequencies of 0.1 and 100 kHz are shown in Figs. 5(a) and 5(b), respectively. Both nonlinear components had anomalous behavior near 15 °C, which is close to  $T_f$ . The second-order nonlinearity was positive (soft) near  $T_f$ , but became negative (stiff) at higher and lower temperatures. The fourth-order nonlinearity was soft above 60 °C and became stiff at lower temperatures. Similar results were obtained at the other measurement frequencies, but are not shown in order to make the graph distinguishable. The magnitude of both nonlinear components decreased with increasing frequency.

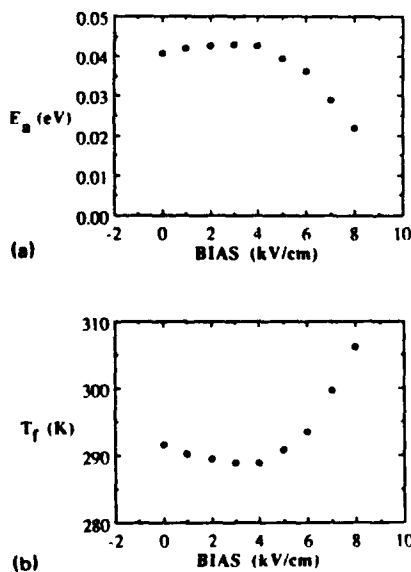


FIG. 3. (a) Activation energy ( $E_a$ ) as a function of bias level. (b) Freezing temperature ( $T_f$ ) as a function of bias level.  $E_a$  and  $T_f$  were calculated using Eq. (1).

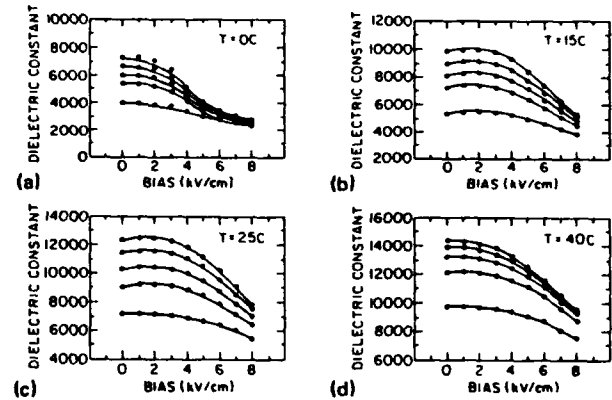


FIG. 4. Permittivity as a function of bias level at various temperatures for measurement frequencies of 0.1, 1, 10, 100, and 1000 kHz. The solid points are the experimental data, and the solid line is the curve fitting to Eq. (2). The highest dielectric response is the 0.1 kHz, the lowest is the 1000 kHz, and the other curves between are in order of increasing frequency. (a)–(d) are at measurement temperatures of 0, 15, 25, and 40 °C, respectively.

The strong decrease in  $E_a$  indicates that a large dc bias shuts down the relaxation mechanism. The electric field may split the degeneracy of the eight equivalent rhombohedral states and significantly change the depths of the potential wells. As a consequence, the polarization can no longer rotate between neighboring directions near this “pinch-off.” The degeneracy of the variants is not split in normal ferroelectrics because, before the required field level is reached, domain wall motion sets in. The field dependence of  $E_a$  for a rotation of the magnetic moment of a superparamagnetic cluster was derived by Néel.<sup>19</sup> A similar expression in terms of the electric field for a superparaelectric cluster is given in Eq. (3):

$$E_a = E_a(0) \left( 1 \pm \frac{E}{E_k} \right)^2, \quad (3)$$

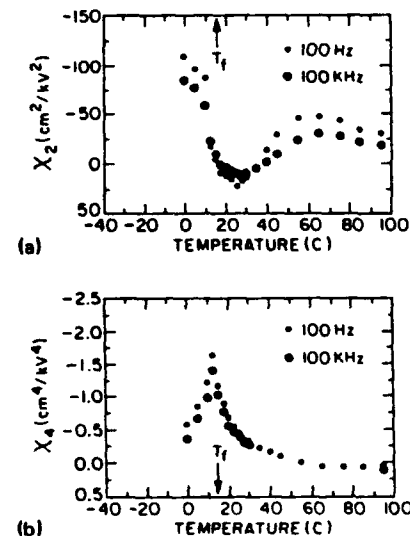


FIG. 5. (a) Second-order nonlinear dielectric response ( $\chi_2$ ) as a function of temperature where  $T_f$  is the freezing temperature. (b) Fourth-order nonlinear dielectric response ( $\chi_4$ ) as a function of temperature. Both figures show data for measurement frequencies of 0.1 and 100 kHz.

where  $E$  is the applied field, and  $E_k$  is the anisotropy field.  $E_k$  can be approximated as  $2E_a(0)/P_{\text{local}}V$ ,<sup>30</sup> where  $P_{\text{local}}$  is the local polarization, and  $V$  is the cluster volume.  $E_a(0)$  was 0.0407 eV, and the cluster diameter of PMN has been reported to be between 2 and 5 nm.<sup>5,6</sup> The mean cluster diameter can be assumed to be the average of these two values, and assuming spherical regions, the volume can be approximated as  $2.5 \times 10^{-20} \text{ cm}^3$ . The local polarization has been found to be approximately  $0.25 \text{ C/m}^2$ ,<sup>2</sup> and  $E_k$  can then be estimated as 22 kV/cm. The fluctuation frequencies at 40 °C under 10 kV/cm for the 0°, 70°, 110°, and 180° variants are then  $2 \times 10^{-8}$ , 0.5,  $2.5 \times 10^5$ , and  $1.5 \times 10^9$  Hz, respectively. Some relaxation may be detected due to rotations between the 110° and 70° variants at measurement frequencies above 100 kHz, but the population of these states is relatively small. The average relaxation time under 10 kV/cm, then, is so long compared to the half-cycle of the measurement that the system is essentially kinetically frozen. This model can qualitatively describe the shut down of the relaxation mechanism, but it predicts that  $E_a$  should increase significantly at low bias levels. The measured  $E_a$  actually increased until a threshold bias.

To more accurately describe the field dependence of  $E_a$ , the effect of cluster interactions needs to be included. Interactions have recently been accounted for by including an internal field.<sup>26</sup> The internal field was treated as a macroscopic average, but there will also be local dipole fields between cluster moments in the unelectrified state which are probably randomly orientated as evidenced by a lack of macroscopic polarization and anisotropy. One of the effects of a local field will be to change the depths of the potential wells and to make them dependent on the configurations of neighboring clusters. A possible explanation of the maximum  $E_a$  at 3 kV/cm then is that the sample becomes internally biased by finding locally preferred configurations of moments. Under a small electric field, then, a threshold is reached where on the global average the difference between the potential minima is smallest. Assuming that the local internal biases have a net direction along one of the rhombohedral orientations the 0°, 70°, 110°, and 180° variants are lowered by  $\Delta E_a$ ,  $\Delta E_a \cos 70^\circ$ ,  $\Delta E_a \cos 110^\circ$ , and  $-\Delta E_a$ , respectively. The average relaxation time ( $\tau_{\text{ave}}$ ) can be approximated by a statistical average over the entire set of relaxation times if the splitting of the degeneracy is much smaller than  $E_a$ . An approximation for  $\tau_{\text{ave}}$  is given in Eq. (4):

$$\tau_{\text{ave}} = \frac{\tau_0}{\omega} \left[ \exp\left(\frac{\bar{E}_a + \Delta E_a}{k(T_{\text{max}} - T_f)}\right) + \exp\left(\frac{\bar{E}_a - \Delta E_a}{k(T_{\text{max}} - T_f)}\right) + 3 \exp\left(\frac{\bar{E}_a + \Delta E_a \cos 70^\circ}{k(T_{\text{max}} - T_f)}\right) + 3 \exp\left(\frac{\bar{E}_a - \Delta E_a \cos 70^\circ}{k(T_{\text{max}} - T_f)}\right) \right], \quad (4)$$

where  $\bar{E}_a$  is the activation energy under 3 kV/cm, at which point  $E_a$  was maximum and presumably the energy difference between the variants smallest. Equation (4) was modeled using a nonlinear analysis program solving for  $\Delta E_a$ ,

which yielded a value of 0.005 eV. The analysis was done simultaneously for all measured frequencies under zero bias in order to obtain the best estimate.

The decrease in  $T_f$  and the softening of the dielectric response can be understood in terms of an enhanced fluctuation kinetics under small biases. The magnitude of  $\chi_2$  and  $\Delta T_f$  were small, which is undoubtedly a reflection of the small value of  $\Delta E_a$ . An approximation for an internal bias in the unelectrified state can be obtained by setting  $\Delta E_a$  equal to an electrical energy as given in Eq. (5):

$$E_{\text{int}} P_{\text{local}} V = \Delta E_a, \quad (5)$$

where  $E_{\text{int}}$  is an internal bias.  $E_{\text{int}}$  is not the mean value of the random dipole field, but rather reflects the dependence of  $E_a$  on the configurations of neighboring moments.  $V$  and  $P_{\text{local}}$  were approximated above as  $2.5 \times 10^{-20} \text{ cm}^3$  and  $0.25 \text{ C/m}^2$ , respectively.  $E_{\text{int}}$  can then be estimated as 2.5 kV/cm, which is nearly equal to the field level at which  $\chi$  was maximum and  $T_f$  minimum. This indicates that the maximum softening of the dielectric response and minimum  $T_f$  may occur at a threshold field which overrides the local configurations. The local dipole fields may tend to locally align the cluster moments consequently slowing down the fluctuations. If the number of the local configurations is small, the preferred alignment will average out on a macroscopic scale, but the effect on fluctuation kinetics will not. A small applied bias adjusts the potential wells and on a global average decreases  $\Delta E_a$ ; consequently, the fluctuation kinetics are enhanced. The maximum softening and minimum  $T_f$  then occurs when the potential variants are closest to being equivalent.

A potential well model which describes the field dependence of the equivalent variants is shown in Figs. 6(a)–6(c). Figure 6(a) represents the unbiased state and illustrates that the degeneracy of the equivalent variants is inherently split. The splitting energy is shown as  $\Delta E$ . Figure 6(b) represents the average potential well under 3 kV/cm. This figure shows that the variants are essentially all of the same depth. At this point the moment can most readily access all variants. Figure 6(c) shows the average potential well near "pinch-off" where the relaxation mechanism has essentially been shut down. This figure shows that the variant antiparallel to the field has been raised by nearly  $E_a$  and the variant parallel to the field lowered by  $E_a$ .

The glassy nature of relaxors in the unelectrified state probably arises due to the random dipole fields between cluster moments. If the dispersion in the local dipole field is of the same order as the mean local field, then the macroscopic system may try to partially order the cluster moments. If the mean local field cannot override the inhomogeneity, a global equilibrium cannot be established. Vugmeister and Glinchuk<sup>31</sup> have proposed a dipole interaction theory for strongly polarizable solids with soft phonon modes. The prediction of this theory is that if  $Nr_c^3 \gg 1$ , then the dipoles will favor a ferroelectric ordering, and if  $Nr_c^3 \ll 1$ , then the dipoles will freeze randomly, where  $N$  is the dipole density and  $r_c$  is the correlation radius.  $N$  can be approximated as  $V_p/V$ , where  $V_p$  is the volume fraction of the polar clusters.  $V_p$  is not known precisely, but will be roughly estimated here as  $\frac{1}{2}$  from



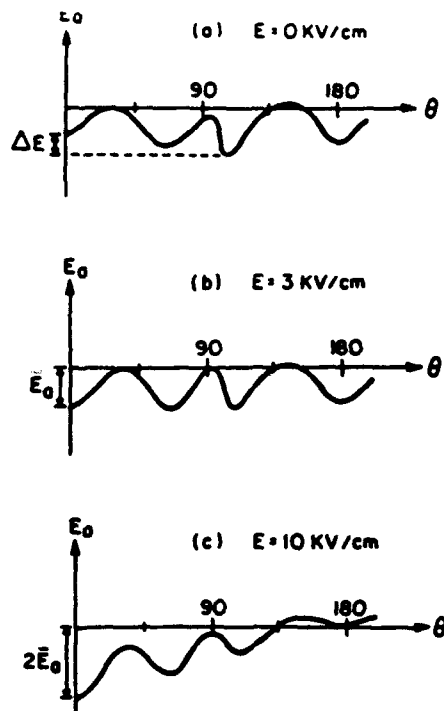


FIG. 6. Diagram illustrating the proposed potential-well model which describes the field dependence of the dielectric response.  $E_0$  is the activation energy,  $\Delta E_0$  is the inherent zero field splitting of the equivalent variants, and  $\bar{E}_0$  is the activation energy, at which point the energy difference between the variants is smallest. (a)–(c) are for dc bias levels of 0, 3, and 10 kV/cm.

TEM micrographs.<sup>3,6</sup> The correlation length has been found to saturate near freezing at 200 Å,<sup>32</sup> and the correlation radius may be approximated as 100 Å.  $Nr_c^3$  can then be estimated for PMN as 10. This indicates that relaxors are not ideal dipole glasses, but have some tendency towards ferroelectric ordering of the cluster moments. This ordering obviously does not go to completion: the macroscopic system may instead establish preferred configurations of orientations of cluster moments. Below  $T_f$  the macroscopic system is stuck in these configurations and cannot establish a normal polar state. The implication is that relaxors freeze into configurations which have a texture on the nanometer scale and that this texture is the "precursor" to long-range polar order of a macrodomain state. The scale of these configurations below  $T_f$  can be assumed to be approximately the same as the maximum correlation length. This scale is such that on a global average the preferred alignment averages out, and no macroscopic polarization or anisotropy is observed.

Locally preferred configurations could arise by the macroscopic system balancing the configurations of nearest and next-nearest cluster moments. The local effect may be that the potential minima of the variants are split by dipole-dipole interactions in such a manner that on a global average the 0° variant is lower for nearest-neighbor configurations and the 70° or 180° variant is lower for next-nearest-neighbor configurations. The macroscopic system may minimize its frustration by partially satisfying the drive for an ordering of the moments. It is generally believed that spin-glass behavior is a reflection of competing interactions which lead to freez-

ing. The implication is that the freezing in relaxors may occur when the correlation length reaches a value where polar clusters have multiple neighbors which are mutually polarizing. Other nanoscale interactions could lead to freezing in relaxors, and in fact recent results indicate that the freezing in PLZT could be due in part to strain fields.

The results suggest that there may be a hierarchy of relaxation processes associated with a complex phase space having many local energy minima associated with different configurations of moment orientations. The splitting of the degeneracy of the equivalent variants can serve as a driving force for a subsequent search for an optimum configuration suppressing the fluctuation kinetics. The cluster moments may then be able to relax below  $T_f$  when the moments of neighboring polar clusters are in certain improbable configurations. The implication is that the relaxational process is not truly stochastic in that the "random walk" has favored local minima which drives the relaxation. The measured value of  $\Delta E_0$  should be slightly different for measurements made on heating as compared to cooling, and in fact the dielectric response has been found to be different.<sup>19</sup> At the start of a cooling run, the moments may be thermally randomized, destroying the local configurations, whereas on a heating run the initial state is not disturbed. The low-field aging of the dielectric permittivity in PMN<sup>24</sup> can also be interpreted using this model. The aging occurs over long time periods near the maximum in the permittivity. The relaxation time of the aging process is much longer than that of the polarization fluctuations at this temperature, indicating that there is a hierarchy of mechanisms. Defects may be able to significantly change the optimum configuration, and consequently the permittivity decreases with time because the kinetics of the fluctuations are suppressed as more favorable configurations are found.

At biases above 3 kV/cm, the dielectric response became stiff, which indicates that the fluctuations are slowed down by large electric fields. The maximum nonlinearities occurred near  $T_f$ , which is close to the temperature where the remanent polarization collapsed.<sup>7</sup> It is perhaps logical to anticipate the nonlinear response to be optimal at this point because an electric field can most effectively repopulate the orientations of the moments in its direction. Consequently, the randomness of the dipole fields between cluster moments would be unstable to an ordering field which would effectively give a nonlinear feedback to the dielectric response. At bias levels above pinch-off,  $T_f$  and  $T_{max}$  increased rapidly, approximately 80 °C between 10 and 28 kV/cm, and seemed to be saturating at the highest bias levels. The correlation length is known to be field dependent.<sup>32</sup> As the correlation length increases, the effective cluster volume increases, and consequently the interactions between polar clusters are longer range and the kinetics of the fluctuations are slower. At bias levels above the point where the fluctuations have condensed, the electrification may override the chemical inhomogeneity which normally prevented long-range polar ordering.  $T_{max}$  then approaches the value of the homogeneous state. Near saturation, the correlation length may reach the macroscopic scale, and  $T_{max}$  saturates. The glassy character of relaxors is then destroyed by a large applied electric field

which orders the local dipole fields and establishes a global equilibrium.

## V. CONCLUSION

Evidence for local configurations of the moments of polar clusters in PMN relaxors was found. A small applied field is believed to override these configurations, enhancing the kinetics of the polarization fluctuations. Large biases are believed to order the local dipole fields between cluster moments, destroying the dipole-glass character of relaxors.

## ACKNOWLEDGMENT

This work has been supported in full by contracts administered through the Office of Naval Research.

- <sup>1</sup>G. Smolenski and A. Agranovska, *Sov. Phys. Solid State* **1**, 1429 (1960).
- <sup>2</sup>G. Burns and F. Dacol, *Solid State Commun.* **48**, 853 (1983).
- <sup>3</sup>L. Shebanov, P. Kapostius, and J. Zvirgzds, *Ferroelectrics* **56**, 1057 (1984).
- <sup>4</sup>L. Cross, *Ferroelectrics* **76**, 241 (1987).
- <sup>5</sup>C. Randall and A. Bhalla, *J. Mater. Sci.* **29**, 5 (1990).
- <sup>6</sup>J. Chen, H. Chan, and M. Harmer, *J. Am. Cer. Soc.* **72**, 593 (1989).
- <sup>7</sup>D. Viehland, S. Jang, L. Cross and M. Wuttig, *J. Appl. Phys.* **68**, 2916 (1990).
- <sup>8</sup>G. Samara, *Jpn. J. Appl. Phys.* **24**, Supl. 24-2, 80 (1985).

- <sup>9</sup>K. Lyon, P. Fleury, J. Negron, and H. Carter, *Phys. Rev. B* **36**, 2465 (1987).
- <sup>10</sup>U. Hochli, P. Kofel, and M. Maglione, *Phys. Rev. B* **32**, 4546 (1985).
- <sup>11</sup>E. Courtens, T. Rosenbaum, S. Nagler, and P. Horn, *Phys. Rev. B* **29**, 515 (1984).
- <sup>12</sup>G. Burns and F. Dacol, *Solid State Commun.* **58**, 567 (1986).
- <sup>13</sup>V. Bovtun, N. Krainik, L. Markova, Y. Poplavko, and G. Smolenski, *Sov. Phys. Solid State* **25**, 225 (1984).
- <sup>14</sup>A. Glass, *J. Appl. Phys.* **40**, 4699 (1969).
- <sup>15</sup>W. Pan, W. Gu, D. Taylor and L. Cross, *Jpn. J. Appl. Phys.* **28**, 653 (1989).
- <sup>16</sup>T. Shrout, Ph.D. dissertation, The Pennsylvania State University (1980).
- <sup>17</sup>G. Schmidt, H. Beige, G. Borchhardt, J. Cierninski, and R. Rossbach, *Ferroelectrics* **22**, 683 (1978).
- <sup>18</sup>T. Shrout, W. Schulze, and J. Biggers, *Ferroelectrics* **34**, 105 (1981).
- <sup>19</sup>Y. Xi, C. Zhilli, and L. Cross, *Ferroelectrics* **54**, 163 (1983).
- <sup>20</sup>K. Binder and A. Young, *Rev. Mod. Phys.* **58**, 4, 801.
- <sup>21</sup>S. Chikazana, Y. Yachanas, and Y. Miyalo, *J. Phys. Soc. Jpn.* **49**, 1260 (1980).
- <sup>22</sup>J. de Almedia and D. Thouless, *J. Phys. A* **11**, 983 (1978).
- <sup>23</sup>C. Paulsen, J. Nanida, S. Williamson, and H. Maletta, *J. Appl. Phys.* **55**, 1652 (1984).
- <sup>24</sup>W. Pan, Ph.D. dissertation, The Pennsylvania State University (1988).
- <sup>25</sup>S. Swartz and T. Shrout, *Mater. Res. Bull.* **17**, 1245 (1982).
- <sup>26</sup>D. Viehland, S. Jang, M. Wuttig, and L. Cross (unpublished).
- <sup>27</sup>J. Tholence, *J. Appl. Phys.* **50**, 7369 (1979).
- <sup>28</sup>S. Shtrikman and E. Wohlfarth, *Phys. Lett.* **85A**, 467 (1981).
- <sup>29</sup>L. Neel, *C. R. Acad. Sci.* **228**, 664 (1949).
- <sup>30</sup>R. Chantrel and E. Wohlfarth, *J. Magn. Magn. Mater.* **40**, 1 (1983).
- <sup>31</sup>B. Vugemeister and M. Glinchuck, *Sov. Phys. JETP* **52**, 482 (1980).
- <sup>32</sup>S. Vakhruhev, B. Kvyatkovsky, A. Naberezhnor, N. Okuneva, and B. Topervers, *Ferroelectrics* **90**, 173 (1989).

## APPENDIX 24

## Dipolar-glass model for lead magnesium niobate

Dwight Viehland, J. F. Li, S. J. Jang, and L. Eric Cross\*

*Materials Research Laboratory, Pennsylvania State University, University Park, Pennsylvania 16802*

Manfred Wuttig

*Engineering Materials Program, University of Maryland, College Park, Maryland 20742*

(Received 21 June 1990; revised manuscript received 30 October 1990)

The static polarization of lead magnesium niobate has been studied using a standard Sawyer-Tower circuit. The square-to-slim-loop hysteresis transition was phenomenologically modeled by modifying Néel's equation for the magnetization of a superparamagnet to a similar relationship for a superparaelectric. A temperature-dependent internal dipole field was included to account for cluster interactions. The slim-loop polarization curves were found to scale to  $E/(T - T_f)$ , where  $E$  is the electric field and  $T_f$  the freezing temperature. A glassy character was subsequently proposed to exist in the zero-field-cooled state with local dipole fields between superparaelectric moments controlling the kinetics of the polarization reversals and the freezing process. Recent quasielastic-neutron-scattering results have been interpreted to support this model.

## I. INTRODUCTION

Lead magnesium niobate is a dispersive ferroelectric. It is characterized by a relaxation of the dielectric permittivity, and an inability to sustain a macroscopic polarization for temperatures significantly below the permittivity maximum ( $T_{\max}$ ). Burns and Darol<sup>1,2</sup> have shown that a local polarization exists for temperatures far above  $T_{\max}$  indicating that the local symmetry is lower than the global. Randall *et al.*<sup>3</sup> and Chen, Chang, and Harmer<sup>4</sup> have shown in  $\text{Pb}(\text{Mg}_{1/3}\text{Nb}_{2/3})\text{O}_3$  that there is a partitioning on the nanometer scale into clusters which are chemically ordered and disordered. Cross<sup>5</sup> suggested that the size of these clusters is such that the polarization may be thermally reversible, analogous to superparamagnetism.<sup>6</sup> He has recently proposed that a coupling between polar clusters controls the kinetics of the polarization fluctuations and the development of frustration near the freezing temperature ( $T_f$ ), similar to spin glasses.<sup>7</sup>  $T_f$  was determined by analyzing the frequency dispersion of  $T_{\max}$  with the Vogel-Fulcher relationship and was shown to agree with the temperature at which a stable remanent polarization collapsed. Similar phenomenological modeling has been used in spin glasses.<sup>8,9</sup>

In the zero-field-cooled (ZFC) state the structure of  $\text{Pb}(\text{Mg}_{1/3}\text{Nb}_{2/3})\text{O}_3$  appears cubic indicating that the scale of the polar behavior is smaller than the coherence length of x-rays; however, in the field-cooled (FC) state the structure appears rhombohedral. Optical microscopy reveals no domain structure in the ZFC state, but normal micrometer-sized domains are observed in the FC state. Cross<sup>10</sup> has investigated the field dependence of the dielectric and elastic responses. He found the maximum nonlinearities near  $T_f$ . Bokov and Myl'nikova<sup>11</sup> and Smith<sup>12</sup> have previously investigated the static polarization. They found a large hysteresis at lower temperatures, but with increasing temperature it decreased; i.e.,

the so-called square-to-slim-loop transition.

Spin glasses are magnetic systems that cannot establish long-range magnetic ordering in the ZFC state due to some form of a chemical or structural inhomogeneity. The glassy behavior is believed to arise due to competing interactions between magnetic moments resulting in a freezing of the magnetization reversals below a characteristic temperature ( $T_f$ ). Freezing has been shown to occur due to random fields between clusters<sup>13,14</sup> and a competition between ferromagnetic and antiferromagnetic exchanges.<sup>15,16</sup> The FC state exhibits behavior resembling a normal ferromagnet below  $T_f$ , i.e., irreversibility and hysteresis.<sup>17</sup>

## II. EXPERIMENTAL PROCEDURE AND RESULTS

The samples used in this study were  $\text{Pb}(\text{Mg}_{1/3}\text{Nb}_{2/3})\text{O}_3$  ceramics with 10 at.%  $\text{PbTiO}_3$ . They were prepared as described by Pan, Jiang, and Cross.<sup>18</sup> The samples were free of aging,<sup>18</sup> were free of pyrochlore as described by Swartz and Shrout,<sup>19</sup> were of dimensions  $1 \times 0.5 \times 0.03$  cm<sup>3</sup>, and were electroded with gold. The hysteresis loops were measured as a function of temperature using a standard Sawyer and Tower circuit. Measurements were made between 150 and  $-50^\circ\text{C}$  on cooling. The samples were allowed to equilibrate for 30 minutes at each temperature. The cycling frequency was 50 Hz, and the maximum bias applied was 20 kV/cm. To decrease the low frequency impedance, a large capacitance (10  $\mu\text{F}$ ) was placed in series with the sample.

Static polarization curves are shown in Figs. 1(a)–1(d) at measurement temperatures of  $-50$ ,  $10$ ,  $50$ , and  $110^\circ\text{C}$ , respectively. The experimental data are the closed circles, and the solid line is a phenomenological model, which will be presented. The square-to-slim-loop hysteresis transition is evident in the figures. The polarization behavior became hysteretic near and below  $T_{\max}$ . The saturation polarization was approximately 20 C/m<sup>2</sup>.

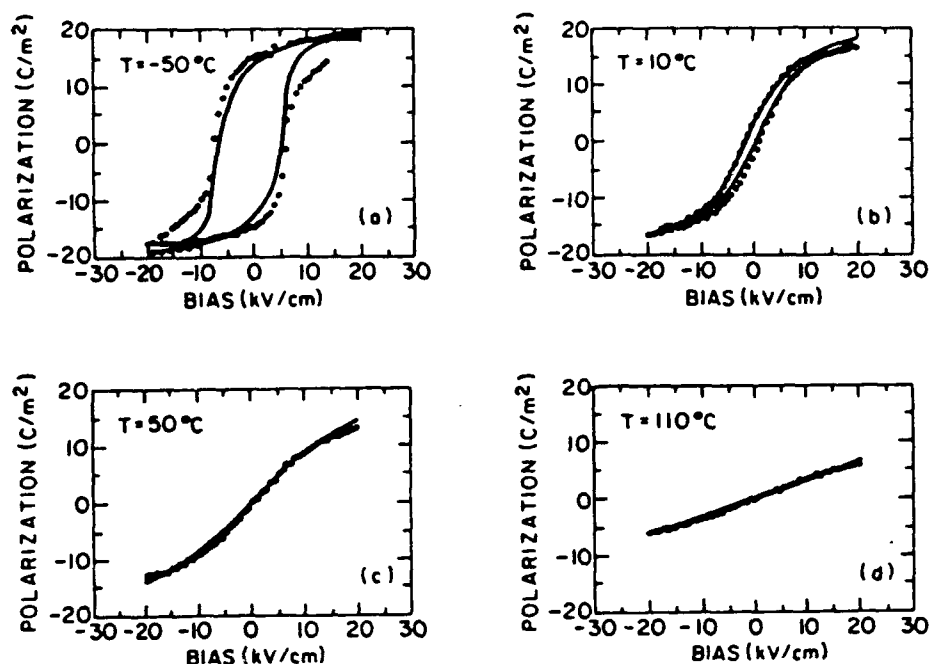


FIG. 1. Polarization curves at various temperatures. The solid points are the experimental data and the solid line is the curve fitting to Eq. (2). (a)–(d) are at measurement temperatures of  $-50$ ,  $10$ ,  $50$ , and  $110^\circ\text{C}$ , respectively.

at lower temperatures. It was not possible to drive the sample into saturation at higher temperatures because breakdown occurred. Above  $25^\circ\text{C}$  the remanence was so small that determination of the coercive field was difficult, but at lower temperatures it increased rapidly.

### III. DISCUSSION

In systems consisting of nanometer-scale ferromagnetic or ferroelectric clusters the thermal energy of the particle can strongly influence the macroscopic magnetic or polar properties. These clusters are designated as superparamagnetic or superparaelectric, respectively. The magnetic behavior with no anisotropy can be described by a Langevin function, but real systems have an anisotropy that acts as an energy barrier for reorientation as originally proposed by Neel.<sup>6</sup> The polarization behavior of an ensemble of uniform noninteracting clusters having uniaxial symmetry can be described by

$$p = \tanh \left[ \frac{EP}{kT} \right], \quad (1)$$

where  $p$  is the reduced polarization,  $E$  the electric field,  $P$  the moment of the cluster, and  $kT$  the thermal energy. A consequence of Eq. (1) is that the polarization curves at different temperatures should superimpose when plotted against  $E/T$ , the analogous behavior has been observed for numerous superparamagnets.<sup>20–22</sup> The implication of the superposition is that at higher temperatures it takes more electrical energy to align the moments against the thermal energy. The slim-loop hysteresis curves of  $\text{Pb}(\text{Mg}_{1/3}\text{Nb}_{2/3})\text{O}_3$  with 10 at. %  $\text{PbTiO}_3$  did not super-

impose when plotted against  $E/T$  as shown in Fig. 2;  $p$  is obviously more strongly temperature dependent. This may be a reflection of interactions between polar regions. Interactions might be accounted for by including a phenomenological freezing temperature.  $T_f$  has been previously estimated as  $18^\circ\text{C}$  for  $\text{Pb}(\text{Mg}_{1/3}\text{Nb}_{2/3})\text{O}_3$  with 10 at. %  $\text{PbTiO}_3$ .<sup>7</sup> The polarization curves plotted as a function of  $E/(T - T_f)$  are shown in Fig. 3. It is obvious that the polarization curves nearly superimpose.

Interactions between superparamagnetic clusters have

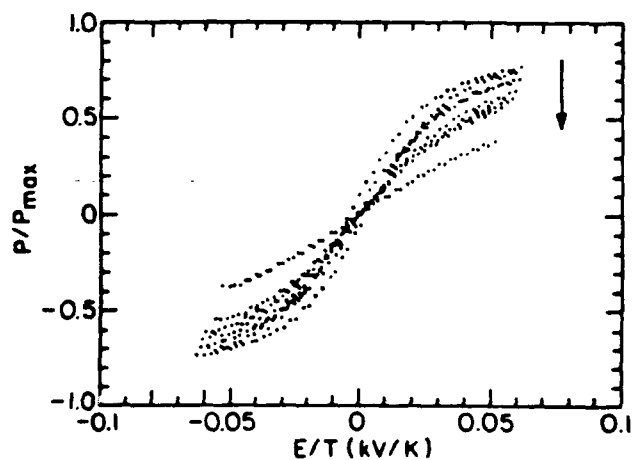


FIG. 2. Reduced polarization plotted as a function of the temperature normalized electric field at various temperatures. The arrow visually illustrates the direction of increasing temperature. The polarization curves shown are at temperatures of  $38$ ,  $48$ ,  $54$ ,  $59$ ,  $69$ ,  $86$ ,  $110^\circ\text{C}$ .

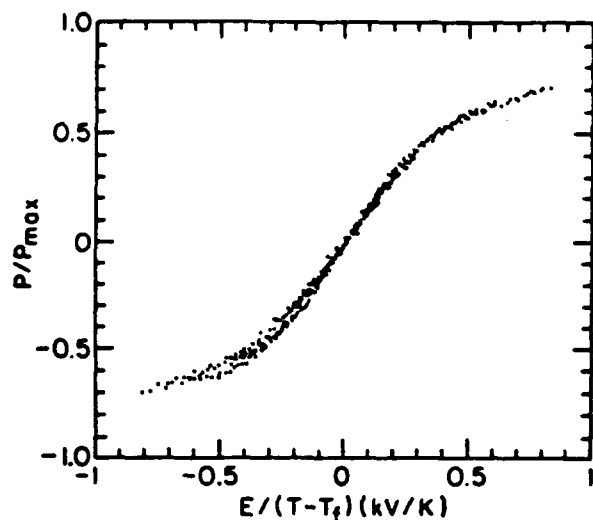


FIG. 3. Reduced polarization at various temperatures plotted as a function of  $E/(T-T_f)$  where  $T_f$  is the freezing temperature. The polarization curves shown are at temperatures of 39, 48, 54, 59, 69, 86, 110 °C.

been reported to alter magnetization curves. Local internal Lorentz fields have been used to obtain an understanding of the magnetic behavior in these systems.<sup>23,24</sup> A relationship for a superparaelectric cluster having rhombohedral symmetry including an internal dipole field follows:

$$p = \frac{\sinh \left[ \frac{P(E + \alpha p)}{kT} \right]}{\cosh \left[ \frac{P(E + \alpha p)}{kT} \right] + 3 \cosh \left[ \frac{P \cos 70^\circ (E + \alpha p)}{kT} \right]}, \quad (2)$$

where  $p$  is the reduced polarization, and  $\alpha$  the internal field. The hysteresis curves were modeled by a nonlinear least squares fitting to Eq. (2), shown as the solid lines in Figs. 1(a)–1(d). The fitting was done by allowing the temperature changes to be absorbed by  $\alpha$ .  $P$  can be approximated as  $P_S V$ , where  $P_S$  is the saturation polarization and  $V$  the cluster volume.  $P_S$  is approximately 20 C/m<sup>2</sup>, and the cluster diameter has been found to be between 20 and 50 Å.<sup>3,4</sup> Assuming an average diameter of 35 Å,  $P$  can be estimated as  $5 \times 10^{-25}$  Ccm. A normalized internal bias ( $\gamma = P\alpha/kT$ ) as a function of temperature is shown in Fig. 4. The reduced remanent polarization ( $p_r$ ) can be approximated by setting  $E = 0$  in Eq. (2). Nonzero solutions for  $p_r$  will only exist when  $\gamma > 4$ , which occurred between 10 and 20 °C.  $p_r$  as a function of temperature is shown as the inset of Fig. 4. The temperature dependence of  $p_r$  was calculated by using the experimental values for  $\gamma$ , but close to  $T_f$   $\gamma$  was determined by interpolation. These results are consistent with the experimental polarization.<sup>7,11</sup>

The magnetization and polarization of spin and dipole glasses are known to be irreversible below  $T_f$ .<sup>17,25–27</sup>

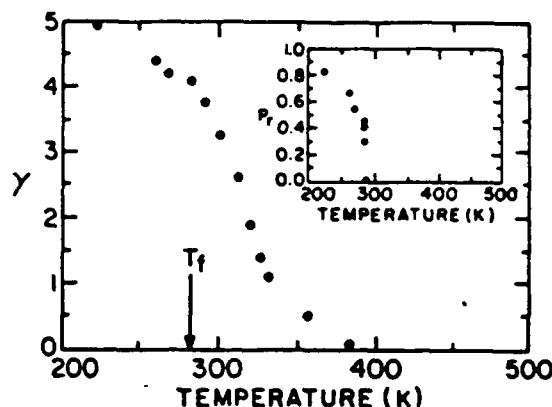


FIG. 4. Reduced internal field ( $\gamma = P\alpha/kT$ ) as a function of temperature where  $T_f$  is the freezing temperature. The inset shows the reduced remanent polarization ( $p_r$ ) as a function of temperature as calculated from Eq. (3).

The irreversibility is believed to arise due to the onset of nonergodicity. In particular if Sawyer-Tower measurements are made hysteresis is observed.<sup>17,27</sup> This hysteresis has been shown to decrease with temperature,<sup>28</sup> somewhat similar to  $\text{Pb}(\text{Mg}_{1/3}\text{Nb}_{2/3})\text{O}_3$ . The scaling of the polarization to  $E/(T-T_f)$  in  $\text{Pb}(\text{Mg}_{1/3}\text{Nb}_{2/3})\text{O}_3$  with 10 at. %  $\text{PbTiO}_3$  is strongly suggestive of a glassy mechanism, whereas the polarization equation of state was derived for a rhombohedral superparaelectric moment. Binder and Young<sup>16</sup> have suggested that interacting superparamagnetic moments should be treated as spin glasses. It is proposed that the polarization of the relaxor is glassy due to interactions between superparaelectric moments. In the ZFC state, the lack of macroscopic polarization indicates that the moments freeze into random orientations devoid of long-range order. Local dipole fields may try to polarize neighboring moments over a distance of a correlation length, as illustrated in Fig. 5. But if the dispersion in the fields is larger than the average field, long-range ordering is impossible. In the FC state the moments freeze into ordered configurations, characteristic of a normal ferroelectric. A somewhat similar superparaelectric glassy model has been proposed for  $\text{K}_{1-x}\text{Li}_x\text{TaO}_3$ , for  $x = 0.026$ .<sup>26</sup>

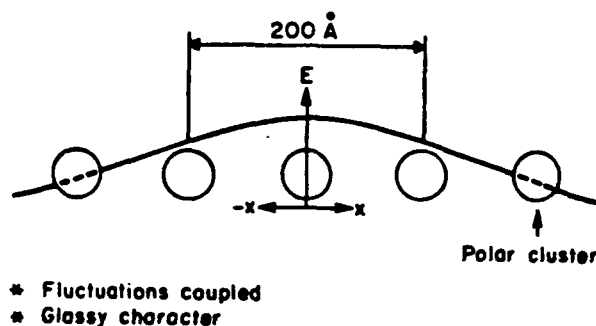


FIG. 5. Proposed model for freezing in  $\text{Pb}(\text{Mg}_{1/3}\text{Nb}_{2/3})\text{O}_3$  where  $E$  is a local internal dipole field that acts to couple the polar clusters. The open circles represent the polar clusters.

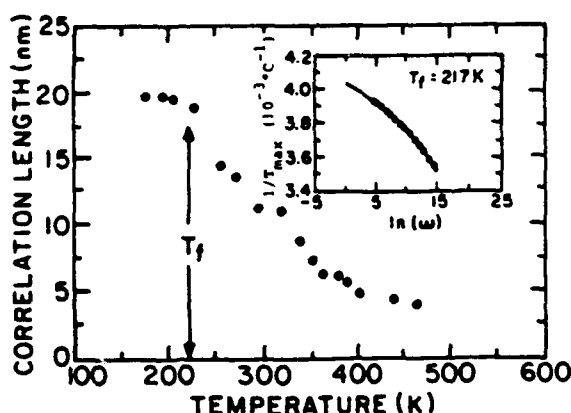


FIG. 6. The correlation length as determined by quasielastic neutron scattering as a function of temperature where  $T_f$  is the freezing temperature. This data is taken from Vakrushev.<sup>2</sup> The inset shows the modeling of the frequency dependence of the temperature of the dielectric relaxation with the Vogel-Fulcher relationship where the solid points are the experimental data and the solid line is the curve fitting.

Recent quasielastic neutron scattering (QES) results<sup>29</sup> on  $\text{Pb}(\text{Mg}_{1/3}\text{Nb}_{2/3})\text{O}_3$  revealed a temperature dependent correlation length ( $\lambda$ ) similar to spin glasses,<sup>30</sup> shown in Fig. 6. Near 400 K,  $\lambda$  was 50 Å, which is approximately equal to the cluster size observed by TEM.<sup>4,5</sup> In the temperature interval below 225 K,  $\lambda$  was nearly temperature independent with a maximum value of 200 Å. This data can be interpreted to support the hypothesis that relaxors are interacting superparaelectric moments. The scale of  $\lambda$  supports the argument that the glassy character arises due to random fields between moments on the mesoscopic level. The agreement of  $\lambda$  with the average size of the clusters at higher temperatures supports the argument that the moments are decoupled from each other behaving as ideal superparaelectrics. On cooling  $\lambda$  increased supporting the model of a temperature-dependent internal field that couples the moments more strongly. For comparison  $T_f$  has been estimated to be 217 K by analyzing the dispersion of  $T_{\text{max}}$  using the Vogel-Fulcher relationship, shown as the solid line in the inset of Fig. 6. This is close in temperature to the saturation of  $\lambda$ , a

strong broadening of the relaxation time distribution,<sup>31</sup> and the collapse of the remanent polarization. This indicates that the saturation of  $\lambda$  at 200 Å may occur by the system freezing into local configurations of moment orientations, possibly by balancing the average orientation of nearest and next-nearest neighbors effectively compensating the local polarization.

Various reasons have been proposed to explain the existence of short-range order in dipolar glasses. The glassy behavior in  $\text{K}_{1-x}\text{Li}_x\text{TaO}_3$  is believed to arise by a coupling of the Li defect structure to a soft mode lowering the local symmetry and stabilizing ferroelectric clusters.<sup>32,33</sup> In  $\text{KCl:OH}^-$ ,  $\text{OH}^-$  dipoles are believed to exist that have six orientations; local dipole fields are believed to couple the moments resulting in glassy behavior.<sup>34</sup> The low-temperature phases of  $\text{RbH}_2\text{PO}_4$  and  $(\text{NH}_4)\text{H}_2\text{PO}_4$  are ferroelectric and antiferroelectric, respectively; frustrated interactions are believed to lead to glassy behavior in their solid solution.<sup>35</sup>  $\text{Pb}(\text{Mg}_{1/3}\text{Nb}_{2/3})\text{O}_3$  is probably a normal ferroelectric that cannot establish long-range polar order due to gross inhomogeneities, i.e., the partitioning (phase separation) on the nanometer scale.<sup>5,6</sup> Local polarization may form where allowed by this "fossil chemistry" via local ferroelectric transitions; dipole fields between moments then subsequently lead to glassy behavior.

#### IV. CONCLUSION

Static polarization curves for  $\text{Pb}(\text{Mg}_{1/3}\text{Nb}_{2/3})\text{O}_3$  were parametrized using a superparaelectric model that included an internal dipole field. Local randomly orientated dipole fields between superparaelectric moments are believed to exist in the zero-field-cooled state leading to a freezing of the polarization fluctuations. A dipole glass model for relaxors was subsequently proposed.

#### ACKNOWLEDGMENTS

This work has been supported in full by contracts administered through the Office of Naval Research. Acknowledgement must also be expressed to Dr. S. Vakrushev *et al.* for the use of their published data.

\*Also in the Electrical Engineering Department.

<sup>1</sup>G. Burns and F. Dacol, *Solid State Commun.* **48**, 10 (1983); **48**, 853 (1983).

<sup>2</sup>G. Burns and F. Dacol, *Solid State Commun.* **58**, 9 (1986); **58**, 567 (1986).

<sup>3</sup>C. Randall, A. Bhalla, T. Shrout, and L. E. Cross, *J. Mat. Sci.* **29**, 5 (1990).

<sup>4</sup>J. Chen, H. Chan, and M. Harmer, *J. Am. Ceram. Soc.* **72**, 593 (1989).

<sup>5</sup>L. E. Cross, *Ferroelectrics* **76**, 241 (1987).

<sup>6</sup>L. Neel, *C. R. Acad. Sci.* **228**, 664 (1949).

<sup>7</sup>D. Viehland, S. Jang, M. Wuttig, and L. Cross, *J. Appl. Phys.* **68**, 2916 (1990).

<sup>8</sup>J. Tholence, *J. Appl. Phys.* **50**, 7369 (1979).

<sup>9</sup>J. Tholence, *Solid State Commun.* **35**, 113 (1980).

<sup>10</sup>D. Viehland, S. Jang, M. Wuttig, and L. Cross, *J. Appl. Phys.* (to be published).

<sup>11</sup>V. Bokov and I. Myl'nikova, *Fiz. Tverd. Tela (Leningrad)* **3**, 3 (1961) [*Sov. Phys. Solid State* **3**, 1 (1961)].

<sup>12</sup>James W. Smith, Ph.D. dissertation, The Pennsylvania State University, 1967.

<sup>13</sup>P. Nozav, V. Sechovsky, and V. Kambersky, *J. Magn. Magn. Mater.* **69**, 71 (1987).

<sup>14</sup>A. Morgownik and J. Mydosh, *Phys. Rev. B* **24**, 5277 (1981).

<sup>15</sup>S. Kirkpatrick and D. Sherrington, *Phys. Rev. B* **17**, 4384 (1978).

<sup>16</sup>S. Edwards and P. W. Anderson, *J. Phys. F* **5**, 765 (1975).

<sup>17</sup>K. Binder and A. Young, *Rev. Mod. Phys.* **58**, 4, 860 (1986).

<sup>18</sup>W. Pan, Q. Jiang, and L. E. Cross, *J. Am. Ceram. Soc.* **71**, C-17 (1988).

- <sup>19</sup>S. Swart and T. Shrout, *Mater. Res. Bull.* **17**, 1245 (1982).
- <sup>20</sup>W. Henkelom, J. Brodeder, and L. Van Reijen, *J. Chim. Phys.* **32**, 3 (1958).
- <sup>21</sup>M. Mayer and E. Vogt, *Z. Naturforsch.* **79**, 334 (1952).
- <sup>22</sup>C. Bean and I. Jacobs, *J. Appl. Phys.* **27**, 1448 (1950).
- <sup>23</sup>E. Vogt, W. Henning, and A. Hahn, *Berichte Arbeitsgemeinschaft Ferromagnetismus 1958* (Riederer Verlag, Stuttgart, 1959), p. 43.
- <sup>24</sup>F. Luborsky and P. Lawrence, *J. Appl. Phys.* **32**, Suppl. 231S (1961).
- <sup>25</sup>K. Lyons, P. Fleury, T. Negran, and H. Carter, *Phys. Rev. B* **36**, 2465 (1987).
- <sup>26</sup>U. Hochli, P. Kofel, and M. Maglione, *Phys. Rev. B* **32**, 4546 (1985).
- <sup>27</sup>J. Prejan, M. Joliclerc, and P. Monad, *J. Phys.* **41**, 427 (1980).
- <sup>28</sup>S. Senoussi, *J. Phys.* **45**, 315 (1984).
- <sup>29</sup>S. Vakhrushev, B. Kvyatkovsky, A. Naberezhnov, N. Okuneva, and B. Topervers, *Ferroelectrics* **90**, 173 (1989).
- <sup>30</sup>G. Aeppli, S. Shapiro, H. Maletta, R. Birgeneau, and H. Chen, *J. Appl. Phys.* **55**, 1629 (1984).
- <sup>31</sup>N. Yushin (unpublished).
- <sup>32</sup>G. Samara, *Jpn. J. Appl. Phys.* **24**, Suppl. 24-2, 80 (1985).
- <sup>33</sup>B. Vugmeister and M. Glinchuck, *Zh. Eksp. Teor. Fiz.* **79**, 8 (1980) [*Sov. Phys. JETP* **52**, 3 (1980)]; **79**, 947 (1980) [**52**, 482 (1980)].
- <sup>34</sup>M. Klein, C. Held, and E. Zuroff, *Phys. Rev. B* **13**, 8 (1976); **13**, 3576 (1976).
- <sup>35</sup>E. Courtens, T. Rosenbaum, S. Nagler, and P. Horn, *Phys. Rev. B* **29**, 515 (1984).



## APPENDIX 25

**The Pennsylvania State University**

**The Graduate School**

**Program in Solid State Science**

**FERROELECTRIC PROPERTIES OF LEAD BARIUM NIOBATE COMPOSITIONS  
NEAR THE MORPHOTROPIC PHASE BOUNDARY**

**A Thesis in**

**Solid State Science**

**by**

**Ruyan Guo**

**Submitted in Partial Fulfillment  
of the Requirements  
for the Degree of**

**Doctor of Philosophy**

**December 1990**

**© 1990 by Ruyan Guo**

## ABSTRACT

Ferroelectric properties, electrooptic properties, and the polarization mechanisms of the tungsten bronze ferroelectric lead barium niobate  $\text{Pb}_{1-x}\text{Ba}_x\text{Nb}_2\text{O}_6$  (PBN(1-x)%) solid solution system with emphasis on the morphotropic phase boundary (MPB) compositions ( $1-x \sim 0.63$ ) are the primary contents of this thesis. This study is directed toward (i) the potential applications of the PBN single crystals of the morphotropic phase boundary compositions as electrooptic devices and (ii) the improved understanding of the polarization mechanisms in lead-containing tungsten bronze ferroelectric crystals near a morphotropic phase boundary.

Ferroelectric single crystal and ceramic samples of  $\text{Pb}_{1-x}\text{Ba}_x\text{Nb}_2\text{O}_6$  ( $0.25 \leq 1-x \leq 0.84$ ) were prepared and examined during this thesis work. Single crystals were grown by the Czochralski method. It is shown that in the Ba-rich PBN (prototype point symmetry 4/mmm) the polarization vector is along the c-axis, while in the Pb-rich side of the phase diagram, the polarization vector is in the a-b plane parallel to the  $\langle 110 \rangle$  direction. However, over the range where the  $\text{PbNb}_2\text{O}_6$  content is 60 to 66 mole percent, it is evident from the X-ray studies that the two structures coexist in polycrystalline samples and appear nearly equal in ratio at 63 mole percent of  $\text{PbNb}_2\text{O}_6$ . Dielectric constant maximum and the ferroelectric-paraelectric phase transition temperature minimum are observed at the morphotropic phase boundary composition where  $1-x = 0.63$ .

Ferroelectric phase relations for the  $\text{PbNb}_2\text{O}_6$ - $\text{BaNb}_2\text{O}_6$  solid solution system are studied by measuring the dielectric and the thermal expansion properties. Ferroelectric-paraelectric phase transition in Ba-rich composition (ferroelectric 4mm  $\leftrightarrow$  paraelectric 4/mmm) is found to be diffuse near-second order type with small thermal hysteresis. However, the phase transition in Pb-rich compositions (ferroelectric m2m  $\leftrightarrow$  paraelectric 4/mmm) is predominantly diffuse first order type with large thermal hysteresis ( $\sim 30^\circ\text{C}$ ). Thermal hysteresis is more prominent in

compositions near the morphotropic phase boundary. It is found by using high temperature X-ray diffraction that in single crystal PBN61.5 two phase transitions take place. The lower temperature phase transition (at  $\sim 125^{\circ}\text{C}$ ) corresponds to the phase transition across the MPB between the orthorhombic  $m2m$  and the tetragonal  $4mm$  phases and the higher temperature phase transition (at  $\sim 290^{\circ}\text{C}$ ) is the ferroelectric-paraelectric phase transition between tetragonal  $4mm$  and  $4/mmm$  phases. Very large thermal hysteresis ( $\sim 70^{\circ}\text{C}$ ) is observed for the lower temperature phase transition. The phase diagram of PBN solid solution is updated by including our experimental data into the previously reported phase diagram (Subbarao 1959) with a curved morphotropic phase boundary into the Ba-rich side between ferroelectric  $m2m$  and ferroelectric  $4mm$ .

A qualitative thermodynamic model is suggested to account for the large thermal hysteresis observed at the phase transition across the MPB. Such a model is also useful in understanding the phase transition induced by an electric field. Very large thermal hysteresis observed for the phase transition near the morphotropic phase boundary is an indication that the two ferroelectric phases are very similar in their free energies.

Low temperature ( $10\sim 300\text{K}$ ) dielectric and pyroelectric properties of morphotropic phase boundary PBN ferroelectric single crystals have been investigated and characterized to understand the strong "Debye-like" dielectric dispersion along a nonpolar direction (perpendicular to the polarization direction) by using dielectric spectrum techniques and a direct charge measurement method, respectively. Significant dielectric relaxation phenomena have been encountered for MPB PBN single crystals in nonpolar directions at low temperatures ( $T < 210\text{K}$ ) and over a broad frequency range ( $10^2\sim 10^6\text{Hz}$ ). A small "frozen-in" polarization component has been detected in a nonpolar direction at corresponding temperatures. There is no evidence found for ferroelectric phase transitions at low temperature in the PBN system. The low temperature relaxation effects can be successfully explained by the concept of internal-reorientation type polarization perturbation and a thermally agitated local dipole fluctuation model.

Optic and electrooptic properties of PBN single crystals are studied by using various techniques. Preliminary study using ellipsometry technique on the dispersion behavior of the PBN crystals shows the crystals are transparent in the visible range without noticeable absorption bands.

By studying the conoscopic interference pattern and the transition temperature dependence on the bias electric field, it is demonstrated for the first time that an external electric field can induce ferroelectric phase switching in the morphotropic phase boundary compositions from one ferroelectric phase to the other. One of the most interesting results is that the electrically controlled optical bistable states are possible to obtain in MPB PBN single crystals.

Optic indices of refraction have been measured using the minimum deviation technique to reveal the details of a morphotropic phase transition in a single crystal. Optical birefringence as a function of temperature has been measured using different techniques, particularly the Senarmont method, and has enabled the calculation of RMS value of spontaneous polarization which is otherwise difficult to obtain for PBN single crystals of high transition temperature ( $> 270^{\circ}\text{C}$ ). The highest spontaneous polarization evaluated in this way for morphotropic phase boundary composition PBN61.5 is of the value  $47\mu\text{C}/\text{cm}^2$  at room temperature.

Transverse linear electrooptic coefficients and half-wave voltages have been measured for different PBN compositions. Morphotropic phase boundary compositions show both high  $r_c$  and  $r_{42}$  coefficients ( $r_{c2} = 311 \times 10^{-12} \text{ V/m}$ ,  $r_{42} = 862 \times 10^{-12} \text{ V/m}$  in PBN61.5), primarily because the dielectric constants perpendicular and parallel to the c-direction are both large and insensitive to temperature. In the ferroelectric tetragonal phase, the transverse electrooptic coefficient  $r_{51}$  ( $r_{51} = 1524 \times 10^{-12} \text{ V/m}$  in PBN57) is large and in the ferroelectric orthorhombic phase the  $r_c$  ( $r_{c2} = 216 \times 10^{-12} \text{ V/m}$  in PBN65) is large. Both can be attributed to the large transverse dielectric constants.

The  $g$ -coefficients were derived from the electrooptic measurements including half-wave voltage and the birefringence. Positive  $g_{33} = 0.0603 \text{ m}^4/\text{C}^2$  and negative  $g_{13} = -0.0152 \text{ m}^4/\text{C}^2$  are obtained, in agreement with theoretical predictions. Overall, the  $g$ -coefficients are smaller than Pb-free perovskites, indicating considerable electronic polarization contribution from  $\text{Pb}^{2+}$ .

Preliminary study on the electrooptic response behavior of PBN single crystals shows that PBN has fast electrooptic response of the order  $\sim 100 \text{ nsec}$  ( $\delta t_{10/90} = 50 \text{ nsec}$  has been obtained) and is therefore a potential candidate for electrooptic modulator applications.

The transmission electron microscope study reveals the manner in which the polarization manifests itself in the various ferroelectric symmetries. There exist only  $180^\circ$  ferroelectric domains in tetragonal  $4\text{mm}$ ; in orthorhombic  $m2m$ , both  $90^\circ$  twin-like domains and  $180^\circ$  domains in the  $a$ - $b$  plane are present. The domain microstructures are deduced for PBN compositions across the phase diagram. TEM study in the temperature range from  $-180^\circ\text{C}$  to  $\sim 80^\circ\text{C}$  revealed the presence of incommensurate ferroelastic domains in PBN solid solution similar to those discovered in the other tungsten bronzes BNN and SBN. The degree of incommensurability varies with temperature and compositions. These incommensurations exist at room temperature in both tetragonal and orthorhombic ferroelectric phases; however, the discommensuration density is much lower and better defined on the orthorhombic side of the phase diagram. The large thermal hysteresis at the ferroelectric-paraelectric phase transition in a Pb-rich orthorhombic composition can be understood by taking the incommensurate phase transition into consideration. The discommensuration structures, however, seem to be independent of the ferroelectric domains in the  $m2m$  phase, which indicates that the lock-in phase transition takes place at a higher temperature than the ferroelectric phase transition.

In general, the dielectric constant, pyroelectric coefficients, and linear electrooptic coefficients are found to be enhanced near the MPB compositions. The transverse linear electrooptic coefficients ( $r_{51} = 1524 \times 10^{-12} \text{ V/m}$  for PBN57) are among the highest known in oxide ferroelectric materials (e.g.,  $r_{51} = 1600 \times 10^{-12} \text{ V/m}$  in  $\text{BaTiO}_3$ ). More importantly, in the morphotropic phase

boundary compositions, the enhanced physical properties are relatively temperature insensitive at ambient temperatures (much lower than their Curie temperatures), which is of great advantage for electrooptic and photorefractive device applications.

## APPENDIX 26



## PYROELECTRIC PROPERTIES OF LEAD BARIUM NIOBATE SINGLE CRYSTALS

R. GUO, A. S. BHALLA and L. E. CROSS

*Materials Research Laboratory, The Pennsylvania State University,  
University Park, PA 16802 USA*

*(Received February 18, 1991)*

The temperature dependence of the pyroelectric coefficients of lead barium niobate  $\text{Pb}_{1-x}\text{Ba}_x\text{Nb}_2\text{O}_6$  (PBN) single crystals were investigated using the Byer-Roundy technique. Pyroelectric coefficients were found to be enhanced in single crystals of the near-morphotropic phase boundary (MPB) compositions. High pyroelectric coefficients ( $336 \mu\text{C}/\text{m}^2\text{-K}$ ,  $1-x = 0.684$ ) and switchable polarization vectors between the two perpendicular crystallographic directions ( $\{001\}$  and  $\{110\}$ ) in crystal of near-morphotropic phase boundary composition ( $1-x = 0.615$ ) were found to be of interest for pyroelectric device applications.

### INTRODUCTION

A most interesting solid solution in the family of tungsten bronze ferroelectrics is that between  $\text{PbNb}_2\text{O}_6$  and a hypothetical end member  $\text{BaNb}_2\text{O}_6$ , namely, lead barium niobate,  $\text{Pb}_{1-x}\text{Ba}_x\text{Nb}_2\text{O}_6$  (PBN[ $1-x$ ]\%).<sup>1-7</sup> Ferroelectric PBN has recently regained its intriguing importance because it is a lead-containing tungsten bronze type ferroelectric relaxor with a morphotropic phase boundary (MPB) and has potential in electrooptic applications. The morphotropic phase boundary in this solid solution system separates a tetragonal ferroelectric phase 4mm (with polarization vector along  $\langle 001 \rangle$ ) and an orthorhombic ferroelectric phase m2m (with polarization vector along  $\langle 110 \rangle$ ).<sup>5</sup> Since there is no coupling between the fourfold ( $\{001\}$ ) and the twofold ( $\{100\}$  or  $\{110\}$ ) axes in the prototype 4/mmm tetragonal symmetry, the two polarization modes adjacent to the morphotropic phase boundary are unrelated and have separate Curie-Weiss temperatures as well as distinct ferroelectric characteristics. Large dielectric,<sup>8</sup> piezoelectric,<sup>9</sup> and pyroelectric (in polycrystalline samples by Lane *et al.*)<sup>10</sup> properties of PBN compositions were reported and enhanced properties in near the MPB compositions were expected.

The earlier research (before 1980s) on PBN were based on measurements on the polycrystalline ceramic form, primarily due to the lack of single crystals. It was reported that pyroelectric coefficient  $p$  showed sharp maxima at compositions close to the morphotropic phase boundary<sup>10</sup> with  $p = 270 \mu\text{C}/\text{m}^2\text{-K}$  (measured by radiation heating method) for  $\text{Pb}_{0.6}\text{Ba}_{0.4}\text{Nb}_2\text{O}_6$  ceramic sample. Pyroelectric coefficients of PBN single crystals of several compositions were also reported<sup>9</sup>; however, the pyroelectric properties in relation to the MPB and the crystallographic phase transition have not yet been studied.

A comprehensive investigation of the phase relations and the polarization mechanisms of PBN solid solution in the near morphotropic phase boundary compositions has been carried out by this group.<sup>11</sup> It was discovered that close to the

morphotropic phase boundary in a Pb-rich composition ( $1 - x = 0.615$ ) the sample actually goes through a phase transition (at  $T \sim 125^\circ\text{C}$  via heating) from the ferroelectric orthorhombic phase to the ferroelectric tetragonal phase during which the polarization axis switches from the  $\langle 110 \rangle$  direction to the  $c$ -axis. A PBN phase diagram is shown in Figure 1 in which a curved morphotropic phase boundary into the Ba-rich side is indicated.<sup>11</sup> It was also demonstrated optically that such morphotropic phase transition can be induced electrically.<sup>12</sup> This behavior of the sample should be studied in view of its pyroelectric properties to further understandings of the polarization mechanisms and the potential applications of the PBN single crystals.

In the present paper the results of pyroelectric property study will be reported and interpreted in relation to the crystallographic structure and phase transitions of the PBN solid solution system. High remanent polarization and pyroelectric coefficients in compositions near the MPB were found to be particularly interesting for pyroelectric device applications.

#### SPECIMEN PREPARATION

Single crystal specimens used for this investigation were prepared by the Czochralski pulling technique. Starting from high purity chemicals, the charge was heated in a Pt crucible by RF induction heating to the melting temperature. Crystal was withdrawn at a rate of 1 to 2 mm/hour along with rotations of crucible (at  $\sim 5$  rpm) and the crystal boule (at  $10 \sim 15$  rpm). After the growth run was completed, the crystal was slowly cooled to room temperature in 48 hours. Transparent single crystals of the size of several millimeters of optical quality were thus obtained even though some cracking problems occurred during the slow cooling probably when the crystal passed through the paraelectric to ferroelectric phase transition. After annealing at  $550^\circ\text{C}$  for 5 hours, crystals were cleaned in acetone and then sputtered with Au electrodes on both faces for pyroelectric measurements.

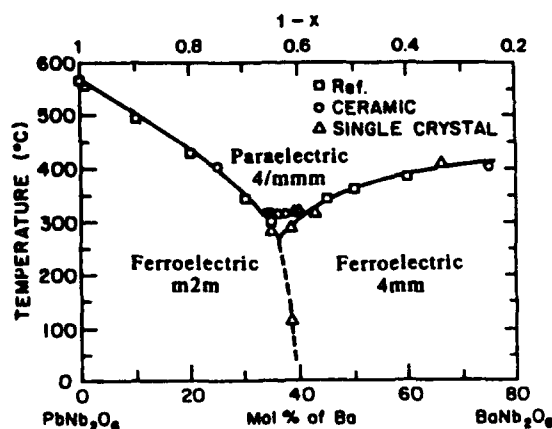


FIGURE 1 Phase diagram of  $\text{Pb}_{1-x}\text{Ba}_x\text{Nb}_2\text{O}_6$  solid solution system with the phase transition temperatures marked as they would appear during heating. The reference in the figure refers to Subbarao *et al.* (1960), Reference 7.

The composition quoted in the text, tables, and figures as PBN[(1 - x)%] where (1 - x)% is the mole percent of  $\text{PbNb}_2\text{O}_6$  in  $\text{Pb}_{1-x}\text{Ba}_x\text{Nb}_2\text{O}_6$  composition, refers to the post-growth analytical composition as determined by electron microprobe analysis. The crystal orientations used in this paper are based on the prototype tetragonal 4/mmm symmetry unless otherwise specified.

## MEASUREMENT TECHNIQUES AND PROCEDURE

A method developed by Byer and Roundy<sup>13</sup> for measuring pyroelectric coefficients was used in this work. Essentially, a prepoled or on-site poled specimen was mounted inside a specially designed sample holder in an air oven and short circuited during the measurement. The pyroelectric current  $I$  was measured using a high sensitivity ( $10^{-12}$  pA) picoammeter (model 4140B, Hewlett-Packard, Palo Alto, Ca.). The heating rate  $dT/dt$  was carefully programmed and controlled by computer interfacing to maintain constant (usually 2 to 4°C/min) while liquid nitrogen gas was used as cooling media.

The pyroelectric coefficient  $p$  was calculated from the pyroelectric current using the following equation:

$$p(T) = \frac{I}{A(dT/dt)} \text{ (C/m}^2\text{-K)}$$

where  $A$  is the electrode area and  $dT/dt$  is the rate of heating. The polarization can be calculated by integrating the pyroelectric current:

$$P \approx \int p dT = \frac{1}{A(dT/dt)} \int I dT \text{ (C/m}^2\text{)}$$

In this study, all specimens were poled inside the sample holder before measurement. The poled sample was short circuited at the starting temperature of the measurement for at least 10 minutes to eliminate surface charges. In the case of the highest temperature measured being lower than the phase transition temperature,  $\Delta P$  rather than  $P$  was obtained.

## RESULTS AND DISCUSSION

For ferroelectric tetragonal single crystal PBN34, the polar vector is parallel to the [001] direction, therefore large pyroelectric coefficient was observed in the [001]-cut crystals as shown in Figure 2. For ferroelectric orthorhombic single crystal PBN68.4, as evinced in Figure 3, the spontaneous polarization is parallel to the [110] direction therefore pyroelectric measurement on the [010] direction yielded large pyroelectric coefficient. As of the single crystal PBN61.5, it has orthorhombic symmetry at room temperature with polar vector parallel to the [110] direction and tetragonal symmetry at temperatures higher than  $\sim 125^\circ\text{C}$  with the polarization along the [001] direction, therefore measurements on two principle directions can give a general picture of the polarization sense in the material. Measured along the [010] direction, Figure 4, the spontaneous polarization first went through a

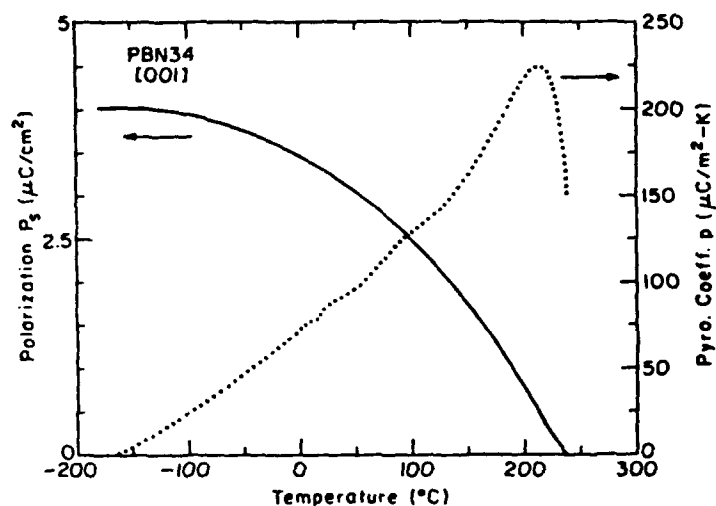


FIGURE 2 Change of the spontaneous polarization and the pyroelectric coefficient versus temperature for tetragonal PBN34.

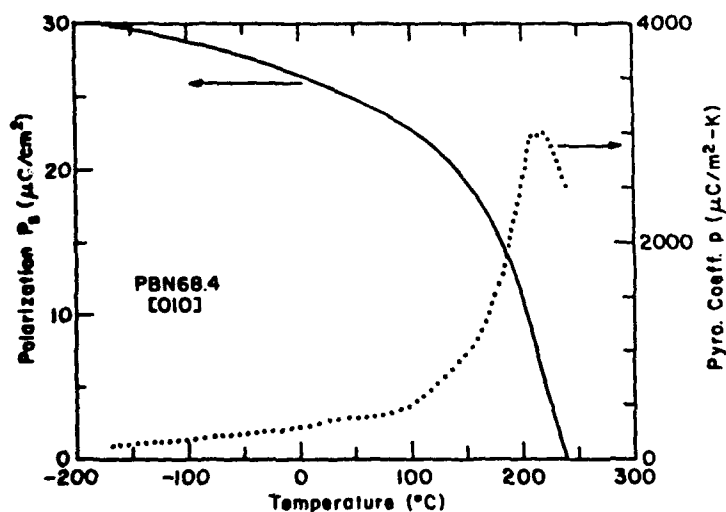


FIGURE 3 Change of the spontaneous polarization and the pyroelectric coefficient versus temperature for orthorhombic PBN68.4.

sharp depoling at the orthorhombic-tetragonal phase transition (the total amount of charge released at this phase transition corresponded to the strength of the orthorhombic polar vector and was of the magnitude of  $18 \mu\text{C}/\text{cm}^2$ ) and then became relatively constant, decreasing slowly with temperature. Measured along the  $[001]$  direction for the same crystal PBN61.5, as shown in Figure 5, polarization started to build up at the temperature above the orthorhombic-tetragonal phase transition, along with the sign change of the pyroelectric coefficient. Figures 4 and 5 demonstrated the polarization characteristics in this material at compositions close to the morphotropic phase boundary.

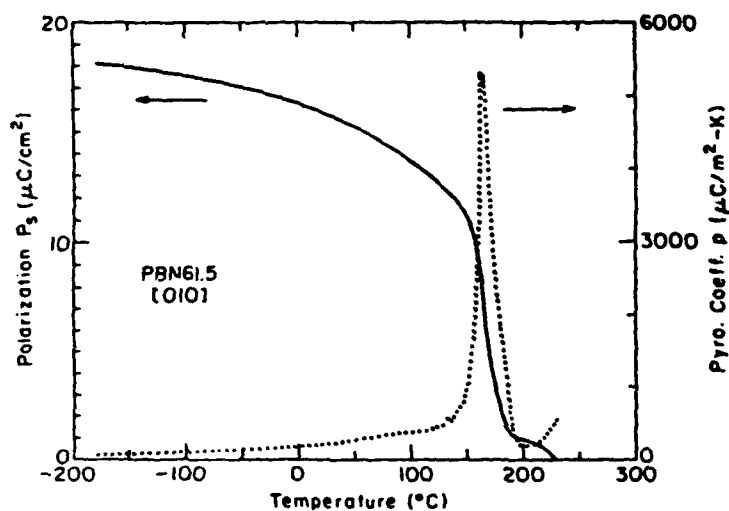


FIGURE 4 Change of the spontaneous polarization and the pyroelectric coefficient versus temperature for the MPB composition PBN61.5 measured parallel to the  $[010]$  direction.

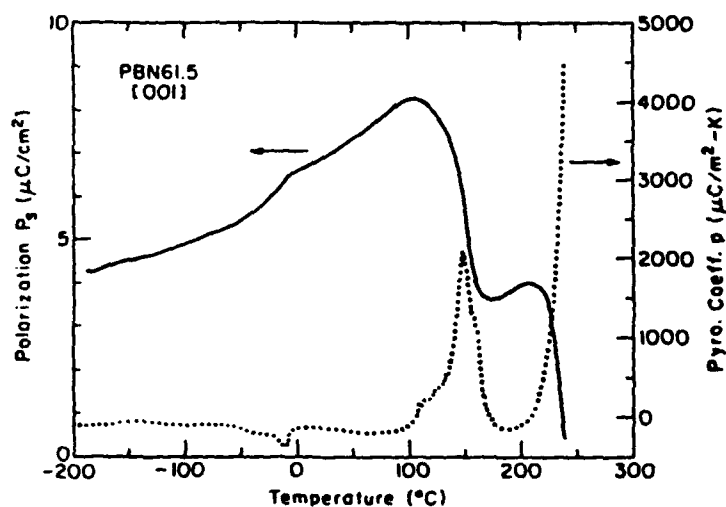


FIGURE 5 Change of the spontaneous polarization and the pyroelectric coefficient versus temperature for the MPB composition PBN61.5 measured parallel to the  $[001]$  direction.

The pyroelectric coefficients  $p$  of PBN single crystals of different compositions at room temperature ( $20^{\circ}\text{C}$ ) obtained using Byer-Roundy method are summarized in Table I (signs of the pyroelectric coefficients are omitted in the Table). The  $p$  values obtained for single crystal samples are substantially higher than those for ceramic samples from the earlier reports.<sup>10</sup>

The decrease of polarization with temperature was also calculated from the pyroelectric data. However, no absolute values of the spontaneous polarization are given because the phase transition temperatures are higher than the maximum temperature attained in the measurements.

TABLE I  
Pyroelectric coefficient of PBN compositions measured using Byer-Roundy method

| Pb <sub>1-x</sub> Ba <sub>x</sub> Nb <sub>2</sub> O <sub>6</sub><br>Composition 1-x | Symmetry                | Pyro. Coefficient (at<br>20°C) (μC/m <sup>2</sup> -K) | Pyro. Coefficient<br>Maximum Value Obtained<br>(μC/m <sup>2</sup> -K) |
|---|-------------------------|---|---|
| 0.34  | Tetragonal              | p <sub>3</sub> =82                                    | p <sub>3</sub> =221 at 213°C  |
| 0.57  | Tetragonal              | p <sub>3</sub> =134                                   | p <sub>3</sub> =1250 at 240°C   |
| 0.615   | Orthorhombic/Tetragonal | p <sub>2</sub> =196<br>p <sub>3</sub> =142            | p <sub>2</sub> =5432 at 149.8°C<br>p <sub>3</sub> =4468 at 240°C      |
| 0.684   | orthorhombic            | p <sub>2</sub> =336                                   | -30 at 21°C, 1°C  |
| *Pb <sub>0.86</sub> Ba <sub>0.14</sub> Nb <sub>1.98</sub> O <sub>6</sub>            | Orthorhombic            | 210   |   |

\* Results of Shrout et al. (1987), Reference 9.

Pyroelectric coefficients for PBN single crystals in polar directions increase as the compositions approach to the morphotropic phase boundary. However, the maximum value of pyroelectric coefficient (336 μC/m<sup>2</sup>-K) was observed in composition close to the MPB but in the orthorhombic side of the phase diagram (PBN68.4) in which the dielectric constant and the piezoelectric coefficient are not the highest<sup>9,11</sup> in the solid solution system.

In PBN61.5, polarization vector switches its direction as the crystal goes through the morphotropic phase transition. Pyroelectric coefficients in either [001] or [110] direction can be high at room temperature which is unique among ferroelectric single crystals and can be very interesting for device applications.

The reasons for the maximized pyroelectric coefficients in the near-morphotropic phase boundary compositions may be discussed as follows:

The appearance of an MPB can usually be related to the instability of one ferroelectric phase against another ferroelectric phase upon critical composition change. It is logical to expect that the two phases separated by the MPB are energetically very similar but differ slightly in composition. The mechanical restraints to preserve one phase against the other may very well be relaxed, or softened, because of the structural instability. Hence, many physical properties will be either greatly enhanced or suppressed in near the morphotropic phase boundary compositions. Remanent polarization  $P_r$ , for instance, may increase due to the increase in magnitude of dipole displacement arising from the softening of the structure or the increase in the number of possible polarization directions. Spontaneous polarization of a polar state in the tetragonal phase can have two polar directions ([001] and [00 $\bar{1}$ ]), and four directions ([110], [ $\bar{1}\bar{1}$ 0], [ $\bar{1}$ 10], and [1 $\bar{1}$ 0]) in an orthorhombic phase. In a MPB composition, spontaneous polarization hence can have total six possible polar states therefore high values of remanent polarization and pyroelectric coefficients. Unlike a ferroelectric-paraelectric phase transition, in which the phase transition is a function of temperature and the physical properties such as dielectric constants and the polarization change drastically with

temperature, morphotropic phase transition can take place at temperatures much lower than the Curie-Weiss temperature and hence moderate dielectric constants can be preserved through the phase transition over a broad temperature region. Such a feature is considered very useful particularly in pyroelectric and electrooptic device applications.

Spontaneous polarization and the pyroelectric coefficient in the temperature range 10K to 300K were also studied using direct charge measurement technique. Details on low temperature pyroelectric property studies of PBN single crystals can be found in our earlier publication.<sup>14</sup>

## SUMMARY

Physical properties of the MPB compositions have been reported in many solid solutions of perovskite structure.<sup>15</sup> The morphotropic phase boundary in PBN solid solution, separating two ferroelectric phases with mutually orthogonal polarization directions has been found so far only in tungsten bronze solid solution family. Current studies on temperature dependence of pyroelectric coefficients of PBN single crystals showed that the pyroelectric property is optimized in PBN crystals of the near-MPB compositions and large pyroelectric coefficients in either perpendicular or parallel to the c-axis can be obtained in PBN61.5 composition. The MPB PBN compositions are therefore interesting for pyroelectric device applications.

## ACKNOWLEDGEMENT

We would like to express our thanks to Dr. Z. P. Chang of the same group for his help in single crystal growth, and the Office of Naval Research and the Defence Advanced Research Project Agency for their financial support.

## REFERENCES

1. V. A. Isupov and V. I. Kosiakov, *Soviet Phys. Tech. Phys.*, **3**, 2002 (1958).
2. G. A. Smolenskii, V. A. Isupov, and A. I. Agranovskaya, *Soviet Phys. Solid State*, **1**, 400 (1959).
3. E. C. Subbarao, *J. Amer. Ceram. Soc.*, **42**, 448 (1959).
4. P. Baxter and N. J. Hellicar, *J. Amer. Ceram. Soc.*, **43**, 578 (1960).
5. M. H. Francombe, *Acta Cryst.*, **13**, 131 (1960).
6. I. G. Ismailzade, *Soviet Phys. Cryst.*, **4**, 618 (1960).
7. E. C. Subbarao, G. Shirane and F. Jona, *Acta Cryst.*, **13**, 226 (1960).
8. T. R. Shrout, L. E. Cross and D. A. Hukin, *Ferroelectric Letters*, **44**, 325 (1983).
9. T. R. Shrout, H. Chen and L. E. Cross, *Ferroelectrics*, **74**, 317 (1987).
10. R. Lane, D. L. Mack and K. R. Brown, *Trans. J. Brit. Ceramic Soc.*, **71**, 11 (1972).
11. R. Guo, A. S. Bhalla, C. A. Randall, Z. P. Chang and L. E. Cross, *J. Appl. Phys.*, **67**(3), 1453 (1990).
12. R. Guo, A. S. Bhalla and L. E. Cross, *Applied Optics*, **29**(7), 904 (1990).
13. R. L. Byer and C. B. Roundy, *Ferroelectrics*, **3**, 333 (1972).
14. R. Guo, A. S. Bhalla, C. A. Randall and L. E. Cross, *J. Appl. Phys.*, **67**(10), 6405 (1990).
15. B. Jaffe, W. R. Cook, Jr. and H. Jaffe, *Piezoelectric Ceramics* (Academic Press, London and New York, 1971).

## APPENDIX 27



# Microstructure-property relations in tungsten bronze lead barium niobate, $\text{Pb}_{1-x}\text{Ba}_x\text{Nb}_2\text{O}_6$

C. A. Randall, R. Guo, A. S. Bhalla, and L. E. Cross

The Pennsylvania State University, Materials Research Laboratory, University Park, Pennsylvania 16802

(Received 4 January 1991; accepted 10 April 1991)

Transmission electron microscopy (TEM) has been used to explore details of the structural phase transitions and corresponding microstructural features in the solid solution of  $\text{Pb}_{1-x}\text{Ba}_x\text{Nb}_2\text{O}_6$  (PBN) tungsten bronze ferroelectrics at compositions embracing the morphotropic phase boundary between orthorhombic and tetragonal ferroelectric phases. In addition to the ferroelectric domain structures that were consistent with the expected symmetries, incommensurate ferroelastic phases were observed. The "onset" and "lock-in" transition temperatures are a function of the Pb/Ba ratio, and for lead-rich compositions it appears that the incommensurate distortion may occur above the ferroelectric Curie temperature in the paraelectric phase.

## 1. INTRODUCTION

### The tungsten bronze structure and phase transitions

The tungsten bronze structure family is probably the second largest family of known oxygen octahedron based ferroelectrics.<sup>1</sup> The structure that has tetragonal symmetry in the paraelectric phase is defined by corner linked oxygen octahedra, and the section normal to the tetragonal  $c$  axis is shown in Fig. 1.<sup>2,3</sup> Chemically, it may be described by a formula of the form  $[\text{A1}(\text{A2})_2\text{C}_2][\text{B1}(\text{B2})_4]\text{O}_{15}$ , where combinations of larger monovalent ( $\text{K}^+$ ,  $\text{Na}^+$ ,  $\text{Rb}^+$ ), divalent ( $\text{Pb}^{2+}$ ,  $\text{Ba}^{2+}$ ,  $\text{Sr}^{2+}$ ,  $\text{Ca}^{2+}$ ), and trivalent ( $\text{La}^{3+}$ ,  $\text{Eu}^{3+}$ ,  $\text{Gd}^{3+}$ ) and similar ions occupy the square and pentagonal shaped tunnels, A1 and A2 sites (Fig. 1). Only very small ions such as  $\text{Li}^+$  can occupy the small triangular channels, C-sites, and small but highly charged cations such as  $\text{Nb}^{5+}$ ,  $\text{Ta}^{5+}$ ,  $\text{Ti}^{4+}$ ,  $\text{Zr}^{4+}$ , etc. occupy the octahedral B1 and B2 sites. Frequently, in consistence with charge balance, not all sites are occupied, and the very large variation in cation radii leads to many complex end member compounds and innumerable solid solutions, which satisfy the conditions to support ferroelectric phases.<sup>4,5</sup>

In spite of the immense chemical flexibility in the tungsten bronze structure systems, only two types of ferroelectric phases are known. In terms of the point symmetries the paraelectric prototype form is always in point group  $4/mmm$ . In the orthorhombic ferroelectric form the spontaneous polarization  $P_s$  is along one of the twofold axes  $(001)_P$  (of point group  $mm2$ ) or  $(110)_P$  (denoted as point group  $m2m$ ) where the suffix indicates that the orientation refers to the original prototypic axial system (see Fig. 1). In the tetragonal ferroelectric form the symmetry is  $4mm$  and two domain states have  $P_s$  oriented along  $[001]_P$  and  $[00\bar{1}]_P$ . Both orientation states are fully consistent with the group theoretical prediction

of Aizu and Shuvalov.<sup>6,7</sup> The tetragonal states exhibit only  $180^\circ$  domain walls, while in the orthorhombic ferroelectric states both  $180^\circ$  and  $90^\circ$  walls occur.

In 1981, Schneck *et al.* reported incommensurate satellite reflections in the tungsten bronzes  $\text{Ba}_2\text{NaNb}_5\text{O}_{15}$  (BNN) and  $\text{Sr}_2\text{KNb}_5\text{O}_{15}$  (SKN).<sup>8-11</sup> At present many crystals are known to have incommensurate phases. These incommensurate phases are periodic but their periodicity is not fixed by a three-dimensional lattice.

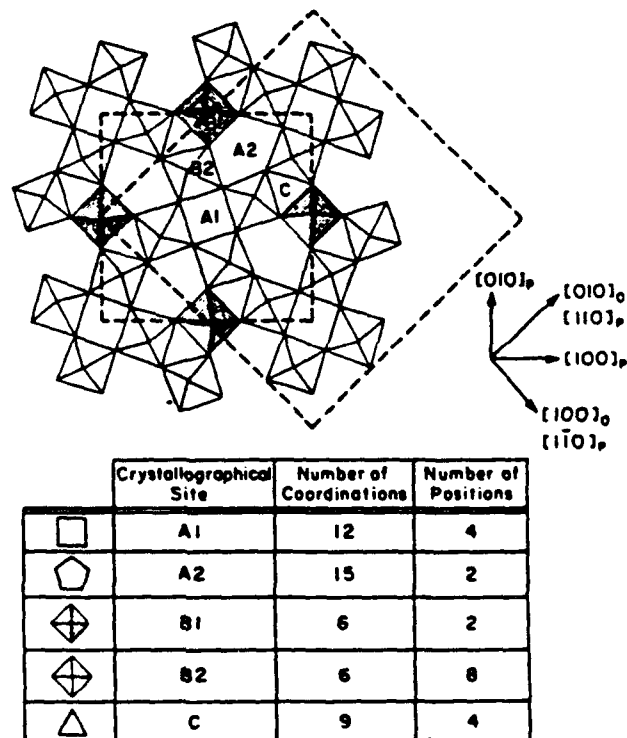


FIG. 1 The generalized crystallographic structure of tungsten bronze compositions with the indicated A, B, and C sites.

Incommensurate periodicity can be due to a number of different phenomena such as atomic displacements or occupancy of cations or anions.<sup>11</sup> The origin of incommensurability in the tungsten bronze family is presumably associated with the displacive structural change owing to ferroelastic octahedral tilting.<sup>10-18</sup>

Many of the displacive incommensurate structures 'lock-in' to low temperature commensurate superstructures.<sup>15,19</sup> The degree of incommensurability,  $\delta$ , reduces to zero at the lock-in transition temperature. The incommensurability parameter,  $\delta$ , is defined as the ratio of the difference between the distance of two adjacent superlattice reflections ( $x - y$ ) parallel to  $\langle 100 \rangle_P$  divided by the total distance between those points ( $x + y$ ).

$$\delta = \frac{x - y}{x + y} \quad (1)$$

Thus at lock-in there is an equal and rational spacing between these superlattice reflections and matrix reflections giving  $\delta = 0$ . Corresponding microstructural changes also take place in the crystals close to the lock-in transition; commensurate domains within the crystal begin to grow. These commensurate domains can be out-of-phase with each other, and at a place where two domains join, a wall known as a discommensuration may be formed. The discommensuration density,  $D$ , is inversely related to the magnitude of the incommensurability parameter,  $\delta$ ; i.e., as  $\delta \rightarrow 0$ ,  $D \rightarrow \infty$ .<sup>12</sup> However, there are some exceptions to this behavior where the incommensurability locks-in to a so-called 'quasi-commensurate' state, and the tungsten bronze family appears to be of this type. In the case of the tungsten bronzes BNN, SKN, and SBN [(Sr, Ba)Nb<sub>2</sub>O<sub>6</sub>], incommensurability reduces to about  $\delta \approx 1\%$  but does not go to zero; a quasi-commensurate structure exists along with a low density of discommensurations. Reasons for this are still not clear, but point defect pinning the motion of the discommensuration walls during growth is a popular suggestion.<sup>15</sup>

The majority of the detailed work on the incommensurate tungsten bronze phases has been on Ba<sub>2</sub>NaNb<sub>2</sub>O<sub>15</sub> (BNN).<sup>12,15,17,18</sup> The suggested sequences of phase transitions in this crystal are summarized in Table I.

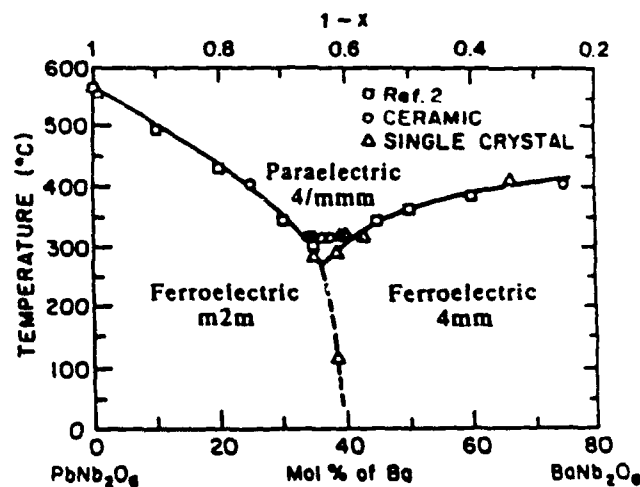
Table I shows a generalized summary of much of the work on BNN, but many uncertainties remain. There is, however, agreement that two incommensurate phases exist, namely  $1q$  and  $2q$ . The  $1q$  phase is an orthorhombic phase with a modulation existing along a single direction, whereas the  $2q$  phase corresponds to a tetragonal symmetry and there exist modulations in two perpendicular directions. These  $1q$  and  $2q$  phases are well illustrated in a study on BNN by Barre *et al.*<sup>15</sup> The  $1q$  phase is stable over  $2q$  for the lower temperatures in the incommensurate phase range. The  $2q$

TABLE I. Phase transitions in BNN.

|  |               |
|--|---------------|
| Paraelectric   |               |
| Paraelectric   | 4/ <i>mmm</i> |
| Paraelectric   |               |
| Paraelectric   | 4 <i>mm</i>   |
| Ferroelectric  |               |
| Ferroelectric + mixed incommensurate ferroelastic phases $1q$ and $2q$ |               |
| Quasi-commensurate ferroelastic Ferroelectric ( <i>mm2</i> )           |               |
| Other phases reported <sup>18</sup>                                    |               |

phase is more stable at the higher temperatures. At the lock-in temperature,  $T_L \approx 250^\circ\text{C}$ , there is a reduction of the incommensurability parameter,  $\delta$ , to develop a quasi-commensurate low temperature state. The lower temperature phases are not fully understood at this time and are still topics of debate.<sup>18</sup>

The Pb<sub>1-x</sub>Ba<sub>x</sub>Nb<sub>2</sub>O<sub>6</sub> tungsten bronze compositions studied here are of special interest owing to their potential application in a bistable optical switching device. The ferroelectric phases are tetragonal ( $4mm$ ) or orthorhombic ( $m2m$ ), depending on the composition.<sup>19,20</sup> As can be observed from the phase diagram,<sup>21</sup> Fig. 2, the Ba-rich side is tetragonal and the Pb-rich side is orthorhombic. These two phases meet at a morphotropic phase boundary close to PBN:  $1 - x = 0.63$ . This morphotropic phase boundary is curved, allowing a first order tetragonal  $\rightarrow$  orthorhombic phase transition to occur for a few restricted compositions close to this boundary. In these crystals the phase change can be

FIG. 2. Phase diagram of the tungsten bronze solid solution  $(1-x)\text{Ba}_{1-x}\text{Nb}_2\text{O}_6$  over the range  $0.2 \leq 1 - x \leq 1.0$ .<sup>20</sup>

effected either by changing temperature or by applying an appropriately oriented electric field. Hence, it is possible to electrically switch an optical indicatrix from uniaxial to biaxial symmetry.

Until recently these tetragonal and orthorhombic phases were believed to be the only ferroelectric phases existing within the tungsten bronze family; however, a study of dielectric and pyroelectric properties at low temperatures has shown additional anomalies.<sup>22,23</sup> These anomalies, as shown in Fig. 3, are very reminiscent of the relaxor anomalies found in many of the complex lead perovskites such as  $\text{Pb}(\text{Mg}_{1/3}\text{Nb}_{2/3})\text{O}_3$ .<sup>24</sup> These anomalies were found in the PBN single crystal plates of the compositions close to the morphotropic phase boundary at temperatures well below the paraelectric — ferroelectric phase transition. The dielectric constant measurements were made perpendicular to the polar axis. The present understanding of these relaxor anomalies in the PBN are small thermal agitations of the polar vector about the polar direction, but this still has to be substantiated. In addition to these transitions we also have reported the presence of incommensurate phases within the PBN.<sup>21</sup>

The aim of this paper is to study and classify the various domain microstructures existing in the PBN tungsten bronze system. The incommensurate ferroelastic phases are described and are found to vary with composition and temperature. The microstructural and crystallographic features of these ferroic phases within the PBN are related to macroscopic anomalies in dielectric and optical properties.

## II. EXPERIMENTAL PROCEDURE<sup>25</sup>

Ceramic specimens were prepared from high purity chemicals using conventional techniques of milling, pre-

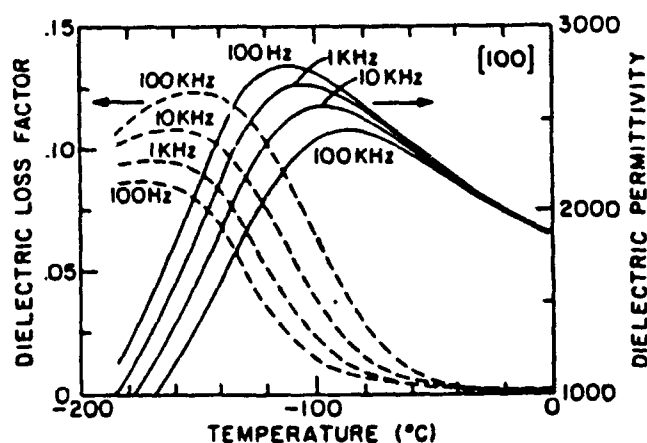


FIG. 3 Typical low temperature anomaly in the dielectric constant perpendicular to the polar direction in PBN single crystals with compositions close to the morphotropic phase boundary ( $1 - x = 0.57$ ). Note the strong frequency dependence in dielectric permittivity and loss.

firing, crushing, pressing, and firing. The specimens were prepared in the form of disks  $\sim 10$  mm in diameter and  $\sim 1.2$  mm thick. The final sintering times and temperatures, which depended on composition, were between  $1280^\circ\text{C}$  and  $1320^\circ\text{C}$  for 1 to 6 h. To compensate for  $\text{PbO}$  loss during the calcination, 3 wt. % of excess  $\text{PbO}$  was added. Well-reacted PBN ceramics with 94–99% theoretical density and 3 to  $6\text{ }\mu\text{m}$  grain size were produced. The composition chosen for TEM study was  $\text{Pb}_{1-x}\text{Ba}_x\text{Nb}_2\text{O}_6$ , where  $(1 - x) = (0.75, 0.65, 0.61, 0.60, \text{ and } 0.25)$ .

Single crystal specimens were prepared by the Czochralski growth technique. Starting from high purity chemicals, the charge was heated in a Pt crucible by RF induction up to the melting temperature. Each crystal was then withdrawn at a rate of 1 to 2 mm/h along with constant rotation of the crucible and the crystal boules. The crystal was slowly cooled to room temperature in a time period of 48 h. Single crystals several millimeters in size and of optical quality were achieved even though some cracking of the boule occurred during the cooling procedure, probably when the crystal passed through the paraelectric to ferroelectric phase transition.

TEM thin sections were prepared by grinding and polishing to  $\sim 50\text{ }\mu\text{m}$  and then ion-beam thinning of the samples after being mounted on 3 mm copper grids. Transmission electron microscopy was performed on a Philips 420 STEM, and a double-tilt liquid nitrogen cold stage made by Gatan was used for low temperature analysis,  $-168^\circ\text{C} \leq T \leq 80^\circ\text{C}$ .

## III. RESULTS

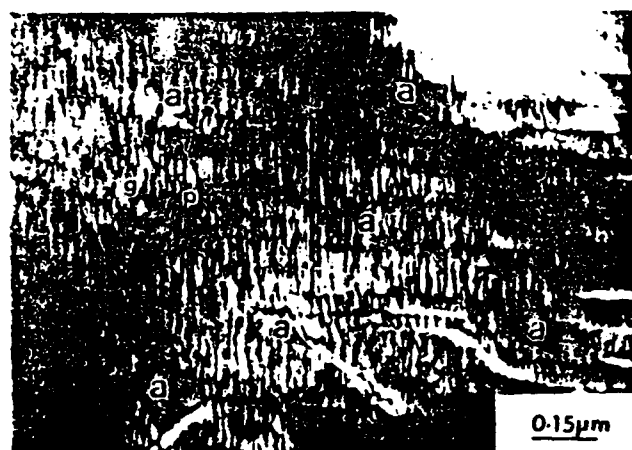
The tetragonal ferroelectric  $\text{Pb}_{0.25}\text{Ba}_{0.75}\text{Nb}_2\text{O}_6$  (PBN;  $1 - x = 0.25$ ) was studied at room temperature to liquid nitrogen temperatures. Typical  $180^\circ$  or inversion domain boundaries are observed with dark-field imaging of the diffraction vector,  $g = (001)_p$ , as seen in Figs. 4(a) and 4(b). The contrast of the  $180^\circ$  regions in neighboring domains is the result of the noncentrosymmetric nature of the crystals. The diffraction intensities of  $hkl$  and  $\bar{h}\bar{k}\bar{l}$  are not equal, and hence there is a contrast difference.<sup>26</sup>

The orthorhombic phase ( $m2m$ ) compositions  $\text{Pb}_{1-x}\text{Ba}_x\text{Nb}_2\text{O}_6$  (PBN;  $1 - x = 0.65$  and  $0.75$ ) were studied. The orthorhombic symmetry is the result of Nb–O displacements in the  $\langle 110 \rangle_p // \langle 010 \rangle_o$  directions. This gives rise to  $90^\circ$  twin ferroelectric domains on  $\{100\}_p // \{110\}_o$  habit planes and also  $180^\circ$  domains with no fixed habit plane. Selected area diffraction of the  $90^\circ$  twin domains shows electron spot splitting parallel to the diffraction vector  $g = (110)_o$ , as observed in the inset of Fig. 5(b). Also,  $\alpha$ -fringe contrast is observed in Fig. 5(b), marked “a”, and these correspond to an inclined  $180^\circ$  domain wall.<sup>25</sup>

Compositions of PBN near the morphotropic phase boundary were also chosen for study with PBN:



(a)



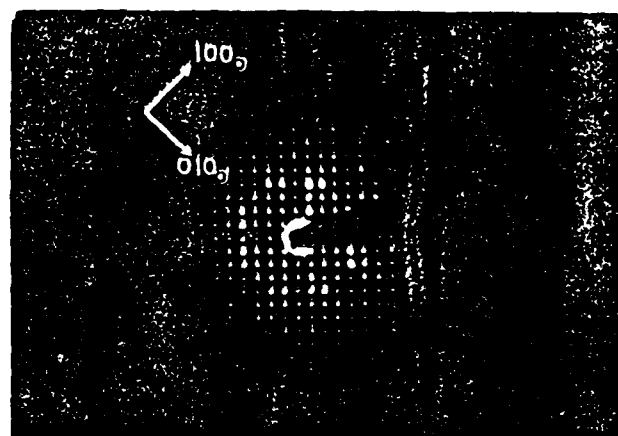
(b)

FIG. 6. (a, b) Micrographs of domain structures in PBN:  $1 - x = 0.60$  composition ceramics. Both (a) and (b) show a mixture of  $180^\circ$  ferroelectric domains and a fine textured discommensuration structure marked "a".

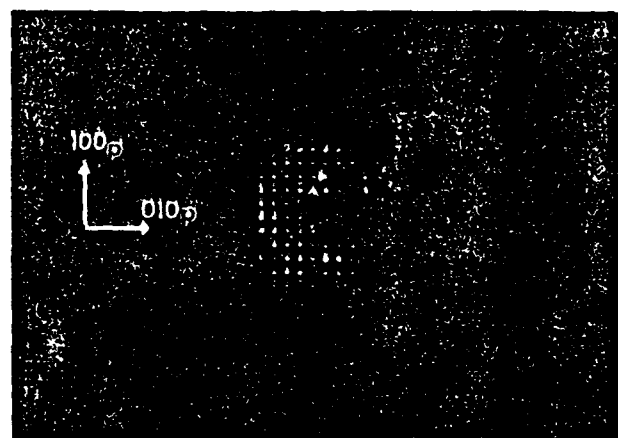
structured  $\text{Sr}_{1/2}\text{Ba}_{1/2}\text{Nb}_2\text{O}_6$ .<sup>11</sup> In their study they found additional superlattice reflections appearing at lower temperatures  $\sim -150^\circ\text{C}$ ; no such superlattice reflections were found in this study on PBN at any composition, between  $0.25 \leq (1 - x) \leq 0.75$ , and to temperatures as low as  $-170^\circ\text{C}$ .

At the outset, we stated that PBN compositions close to the morphotropic phase boundary have an additional low temperature relaxor-like anomaly in dielectric and pyroelectric studies.<sup>22,23</sup> In this TEM study no evidence of domain superlattices or satellites could be associated with this phenomenon. The reason for this is most likely that the temperature region studied by TEM was not sufficiently low to freeze in the micropolar regions.<sup>27,28</sup>

In addition to the commensurate superlattice reflections,  $\{h + 1/2, k + 1/2, 0\}_P$ , there are incommensurate superlattices also present in the PBN compositions.



(a)



(b)

FIG. 7. PBN  $\langle 001 \rangle$  electron diffraction patterns: (a) PBN: 0.75 at room temperature and (b) PBN: 0.25 at room temperature.

These incommensurate superlattices have various degrees of incommensurability, as determined by the  $\delta$ -parameter and the dark-field imaging of the discommensurate structures. Figures 8(a), 8(b), and 8(c) show three room temperatures  $[110]_P$  zone axis electron diffraction patterns, for compositions PBN:  $1 - x = 0.25, 0.60$ , and  $0.75$ , respectively). The respective room temperature incommensurability parameter is  $\delta = 17\%$ ,  $6\%$ , and  $2\%$ . Hence the orthorhombic, PBN:  $1 - x = 0.75$ , lead-rich composition is at room temperature in a quasi-commensurate state. This can also be observed from corresponding dark-field images of the incommensurate spots. The dark boundaries, marked "b," are discommensuration structures in Fig. 10(a). We will discuss this figure in more detail below.

The PBN:  $1 - x = 0.61$  single crystal is incommensurate and its  $\delta$  parameter changes from  $6\%$  at room temperature to  $4\%$  at  $-140^\circ\text{C}$ . The room temperature

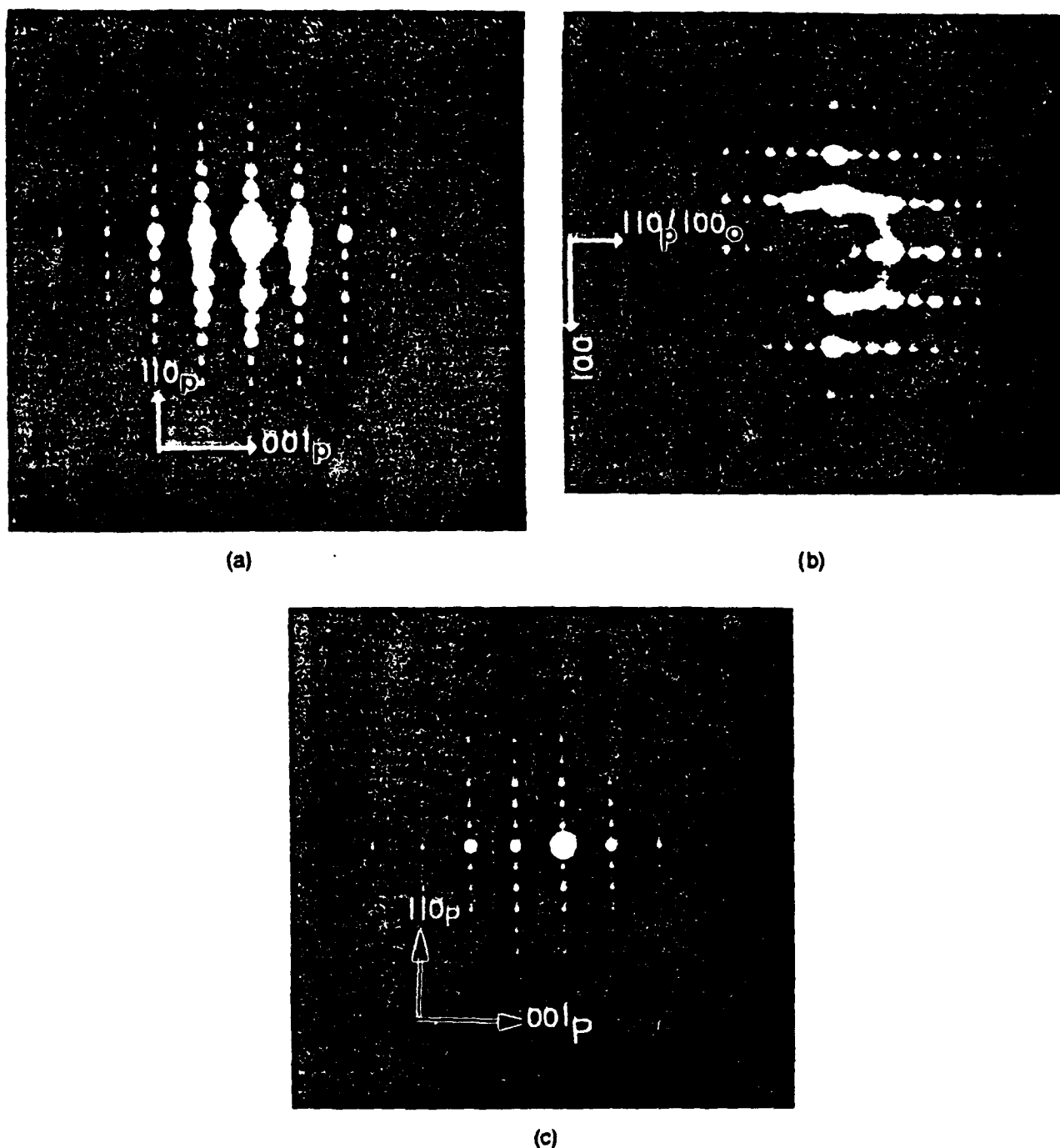
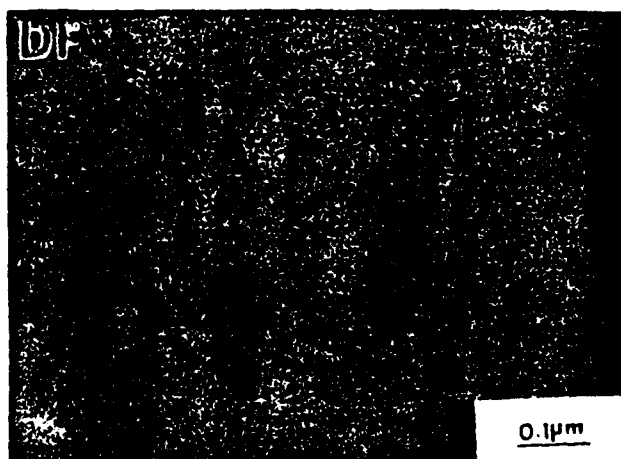


FIG. 8. Comparison of PBN (110) electron diffraction patterns at room temperature. PBN:  $1 - x =$  (a) 0.25, (b) 0.60, and (c) 0.75, respectively.

discommensurate microstructure is shown in Fig. 9(a), and is similar to discommensurate structures in the mixed  $2q$  and  $1q$  phase, as observed by Barre *et al.*, in BNN.<sup>15</sup> The discommensurate microstructures in PBN compositions change easily close to the morphotropic phase boundary. It is easy to switch to a finely textured discommensurate microstructure during the electron microscopic observations, as seen in Fig. 6(b). This

ferroelastic switching is obtained by local heating of the electron beam that gives rise to strain gradients owing to thermal expansion. These strain gradients are believed to be strong enough to switch the ferroelastic domains. Figures 6(a) and 6(b) show finely aligned discommensurate structures co-existing with  $180^\circ$  ferroelectric domains. The aligned discommensurates are parallel to the diffraction vector  $g = (110)_P$



(a)



(b)

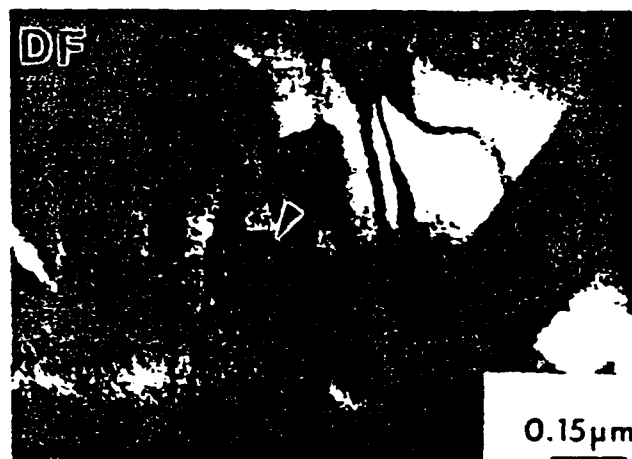
FIG. 9. (a) Room temperature discommensuration structure of single crystal PBN:  $1 - x = 0.61$ ; (b) shows the dark-field diffraction condition and also evidence of streaking of the incommensurate superlattice reflections (see inset).

or  $(100)_O$ . The diffuse streaking along  $(100)_O$  in the diffraction pattern Fig. 9(b) is thought to be related to the fine textured discommensurates, as it is perpendicular to their habit and observed only when they are present.

Returning to Fig. 10, a number of important features are to be noted. The discommensurate structures are aligned parallel to  $(010)_O$ . Also, the discommensurations are continuous across  $90^\circ$  and  $180^\circ$  domains. This implies to us that the 'lock-in' incommensurate transition was independent of the ferroelectric transition. This complex domain configuration and phase mixing can be possible only by the lock-in transition occurring in the paraelectric phase, which is not the case with other tungsten bronze phases. Also, from the discommensurate configurations a phase shift of  $\pi/2$  in the modulation can be determined by the fourfold node lines; this is similar to findings in BNN and  $2H\text{-TaSe}_2$ .<sup>14,29</sup>



(a)



(b)

FIG. 10. (a) Discommensuration and ferroelectric microstructures in PBN:  $1 - x = 0.75$ . Note that the discommensuration microstructures are independent of the ferroelectric domains; (b) shows discommensuration node structure.

#### IV. DISCUSSION

The PBN solid-solution shows a complex mixing of ferroelectric and incommensurate ferroelastic phase/domains. The incommensurate phase and ferroelectric phases are sensitive to composition. Different incommensurate parameters,  $\delta$ , are found at room temperature along with different discommensuration structures and densities.

One of the most surprising results deduced concerns the lock-in transition in the orthorhombic PBN compositions. With the discommensurate structures showing continuity through the ferroelectric  $180^\circ$  and  $90^\circ$  domain structures, one has to conclude the quasi-commensurate lock-in occurred before the paraelectric  $\rightarrow$  ferroelectric transition. This is not the case with the previously

studied SBN and BNN tungsten bronzes, which have the sequence of transitions found in Table II.

To confirm our conclusions about the departure from the previous trends of phase sequences known in tungsten bronze, we made an additional study on the temperature dependence of the birefringence in PBN single crystals.<sup>25</sup> Figure 11 shows the transmitted intensity variation as a function of temperature during a cooling run for PBN:  $1 - x = 0.65$  of orthorhombic symmetry. Besides a first-order-like phase transition (at  $\sim 213^\circ\text{C}$  during a cooling run) that corresponds to the ferroelectric orthorhombic  $m2m$  to tetragonal paraelectric  $4/mmm$  phase transition, a continuous or rather smooth but unambiguous phase transition can be detected at temperatures near  $322^\circ\text{C}$  during both cooling and heating runs. No prominent dielectric anomaly other than a small kink has been observed in this temperature region. We thus suggest that this anomaly is the incommensurate transition as inferred by the TEM domain microstructural observations. As we know that incommensurate phase transition is always a second order,<sup>30</sup> it is not surprising to us that the birefringence, being a polar second rank tensor property, is more sensitive to the onset of incommensurate modulations than other techniques such as dielectric measurements. Further results regarding the optical studies will be found in later papers.<sup>31</sup> For the Ba-rich compositions the incommensurate lock-in phase transition is below the paraelectric-ferroelectric transition and corresponds more closely to the phase sequences in BNN and SBN tungsten bronzes.

The dielectric and x-ray characterization of the PBN agrees well with the TEM observations, as reported earlier.<sup>21,23,25</sup> However, no evidence was found for domains/polar regions being associated with the low temperature relaxor-like anomalies close to the morphotropic phase boundary. The reason for this is probably that lower temperature observations would be required to eliminate electron beam heating contributions from thermal excitations, preventing a freezing-in of the domains.

## V. CONCLUSIONS

Solid solutions of tungsten bronze lead barium niobate,  $\text{Pb}_{1-x}\text{Ba}_x\text{Nb}_2\text{O}_6$ , have been studied by TEM techniques. Ferroelectric  $180^\circ$  domains have been characterized in the tetragonal part of the phase diagram.

TABLE II. Phase sequences in tungsten bronze BNN and SBN

| ( $4/mmm$ )  | ( $4mm$ )     | ( $mm2$ )     |
|--------------|---------------|---------------|
| Paraelastic  | Paraelastic   | Ferroelastic  |
| Paraelectric | Ferroelectric | Ferroelectric |

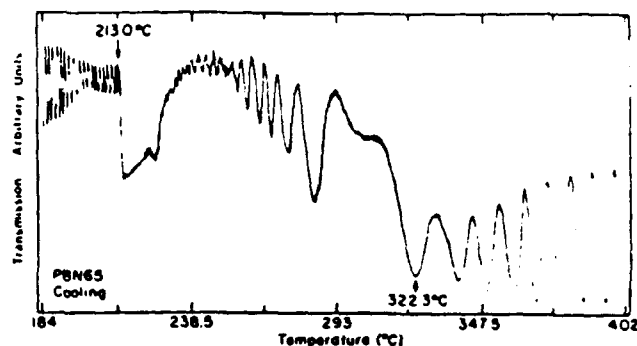


FIG. 11. Transmitted intensity recorded as a function of temperature in a cooling run for PBN:  $1 - x = 0.65$  single crystal to measure the birefringence. The light ( $\lambda = 633 \text{ nm}$ ) propagated perpendicular to both the  $[010]_P$  and the  $[001]_P$  directions.

With the orthorhombic compositions  $90^\circ$ -twin and  $180^\circ$  inversion ferroelectric domains were observed. A ferroelastic incommensurate phase is found to exist throughout the phase diagram. The degree of incommensurability varies with temperature and composition. Discommensuration structures are observed and a  $\pi/2$  phase modulation is deduced from the micrographs. From the combined TEM and birefringence study of PBN it is suggested that the quasi-commensurate 'lock-in' transition occurs within the paraelectric phase in compositions  $(1 - x) \geq 0.63$ , making the orthorhombic PBN different from previous ferroelectric incommensurate behavior in the tungsten bronze family.

## ACKNOWLEDGMENTS

We wish to acknowledge and thank the following for their support: ONR and DARPA. Also, thanks go to Dr. Steven Markgraf and Dr. Thomas Shrout for many useful discussions regarding tungsten bronzes. Thanks also to J. Baney for typing this manuscript.

## REFERENCES

1. R. Fieseler, J. Lines and A.M. Glass, *Principles and Applications of Ferroelectrics and Related Materials* (Oxford University Press, Oxford, 1977).
2. S.C. Subbarao, G. Shirane, and F. Jona, *Acta Cryst.* **13**, 226 (1960).
3. P.B. Jamieson, S.C. Abrahams, and J.L. Bernstein, *J. Chem. Phys.* **48**, 5048 (1968).
4. Landolt-Bornstein, *Ferroelectric and Antiferroelectric Substances* (Springer-Verlag, New York, 1970).
5. L. Vainshtein, M. Fridkin and V.L. Indebom, *Modern Crystallography I* (Springer-Verlag, Berlin, Heidelberg, New York, 1982).
6. K. Aizu, *Phys. Rev.* **140** (2A), A590 (1965).
7. L.A. Shuvalov, *J. Phys. Soc. Jpn.* **285**, 38 (1970).
8. J. Schneck and F. Denoyer, *Phys. Rev. B* **23**, 383 (1981).
9. J. Schneck, J.C. Toledano, R.W. Whatmore, and F.W. Ainger, *Ferroelectrics* **36**, 327 (1981).
10. C. Manolikas, *Phys. Status Solidi (a)* **68**, 653 (1981).
11. L.A. Bursill and J.L. Peng, *Philos. Mag. B* **54** (2), 157 (1986).

12. T. Janssen and A. Janner, *Adv. Phys.* **36** (5), 519 (1987).
13. C. Manolikas, J. Schneck, J. C. Toledano, J. M. Kiat, and G. Calvin, *Phys. Rev. B* **35** (16), 8884 (1987).
14. X. Q. Pan, H. S. Hu, M. H. Yao, and D. Feng, *Phys. Status Solidi (a)* **91**, 57 (1985).
15. S. Barre, H. Murka, and C. Roneau, *Phys. Rev. B* **38** (13), 9113 (1988).
16. J. L. Peng and L. A. Bursill, *Acta Cryst. B* **43**, 504 (1987).
17. M. Vermerft, G. Van Tendeloo, J. V. Landuyt, and S. Amelinckx, *Ferroelectrics* **88**, 27-36 (1988).
18. W. F. Oliver and J. F. Scott, 1st USA-USSR Meeting on Ferroelectrics, Colorado (1989).
19. M. H. Francombe, *Acta Cryst.* **13**, 131 (1960).
20. E. C. Subbarao, G. Shirane, and F. Jong, *Acta Cryst.* **13**, 226 (1960).
21. R. Guo, A. S. Bhalla, C. A. Randall, Z. P. Chang, and L. E. Cross, *J. Appl. Phys.* **67** (3), 1453 (1990).
22. L. E. Cross, *Ferroelectrics* **76**, 241 (1987).
23. R. Guo, A. S. Bhalla, C. A. Randall, and L. E. Cross, *J. Appl. Phys.* **67** (10), 6405 (1990).
24. G. A. Smolenskii, *J. Phys. Soc. Jpn.* **28** (Suppl.), 26 (1970).
25. R. Guo, Ph.D. Thesis, The Pennsylvania State University, University Park, PA (1990).
26. R. Gevers, H. Blank, and S. Amelinckx, *Phys. Status Solidi* **13**, 449 (1966).
27. C. A. Randall, D. J. Barber, and R. W. Whatmore, *J. Microsc.* **45**, 275 (1987).
28. C. A. Randall, D. J. Barber, R. W. Whatmore, and P. Groves, *Ferroelectrics* **76**, 265 (1987).
29. K. K. Fung, S. McKernan, J. W. Steeds, and J. A. Wilson, *J. Appl. Phys. C* **14**, 5417 (1981).
30. D. Weigel, *Phase Transitions* **16/17**, 341 (1989).
31. R. Guo, D. A. McHenry, A. S. Bhalla, and L. E. Cross (in preparation).



## **APPENDIX 28**

**The Pennsylvania State University**

**The Graduate School**

**AN INVESTIGATION OF THE LEAD SCANDIUM TANTALATE-  
LEAD TITANATE SOLID SOLUTION SYSTEM**

**A Thesis in  
Solid State Science**

**by**

**Jayne R. Giniewicz**

**Submitted in Partial Fulfillment  
of the Requirements  
for the Degree of**

**Doctor of Philosophy**

**December 1991**

## ABSTRACT

The unique characteristics of the solid solution  $(1-x)\text{Pb}(\text{Sc}_{1/2}\text{Ta}_{1/2})\text{O}_3$ - $(x)\text{PbTiO}_3$  make it an interesting system from both a theoretical and practical point of view. A variety of compositionally and thermally "adjustable" states of structural ordering, Curie temperatures, and material properties are accessible for these materials, making them attractive for many device applications as well as a useful model system for further exploring the fundamental nature of relaxor ferroelectrics. Selected compositions from the system have been prepared as ceramics, characterized, and subjected to various property measurements. Two structural phase boundaries have been identified between three main lower symmetry ferroelectric phase regions. Materials from each of these regions possess different states of structural ordering and exhibit distinctive ferroelectric behaviors. Structure-property relationships are highlighted for compositions representing each region and a preliminary evaluation of the material for pyroelectric device application is presented.

The  $(1-x)\text{Pb}(\text{Sc}_{1/2}\text{Ta}_{1/2})\text{O}_3$ - $(x)\text{PbTiO}_3$  ceramics were prepared by a conventional mixed-oxide method involving the use of high-purity starting compounds, a precursor-phase formulation, and controlled lead atmosphere sintering. Compositions were selected from across the entire range so as to represent all phase regions occurring in the system. Each composition was calcined at 900°C for four hours and then at 1000°C for one hour with an intermediate comminution step. Compacted specimens of all compositions were then subjected to firing at 1400°C for one hour within sealed crucibles containing  $\text{Pb}(\text{Sc}_{1/2}\text{Ta}_{1/2})\text{O}_3$  /  $\text{PbZrO}_3$  source powders. Specimens with compositions  $[x \leq 0.1]$  required a second higher temperature sintering at temperatures in the range [1500-1560°C] depending on the composition. Those specimens for which the degree of ordering could be varied by post-sintering heat-treatment were annealed in a sealed

system with a controlled lead atmosphere so as to allow negligible lead loss during the ten-hour period required to order the material.

Four distinct phase regions were identified in the system: (1) a high-temperature cubic phase, below which there exist, (2) a rhombohedral (pseudocubic) region of variable order/disorder [VOD] in the composition range  $[x=0-0.075]$ , (3) a structurally invariable rhombohedral (pseudocubic) region in the range  $[x=0.1-0.4]$ , and (4) a tetragonal region extending from  $[x=0.45]$  to  $[x=1.0]$ . Boundary regions separating the three lower symmetry phase regions were defined where the VOD phase boundary was determined to lie in the composition range  $[x=0.075-0.1]$  and the morphotropic phase boundary [MPB] between  $[x=0.4]$  and  $[x=0.45]$ . It was noted that the extent of the VOD phase region and, hence, the position of the VOD phase boundary may well depend upon the annealing conditions imposed and, therefore, the structural features reported for the system in this compositional range reflect only the nature of materials produced under the preparation conditions applied in this study.

A range of ferroelectric behaviors was observed for materials representing each of the three non-cubic phase regions, each of which was correlated with the coherence length of the ordering present as determined by means of electron and x-ray diffraction. It was thereby shown that all three of the nanostructure-property classes defined in the classification scheme of Pb-based perovskites described in Section 1.1.3 are represented in this system.

Preliminary investigation of the nanoscale ordering occurring in as-fired specimens by means of electron diffraction indicated the presence of short coherence length (20-800Å) long-range ordering up to  $[x=0.3]$  as evidenced by the presence of the "F-type" reflections associated with the ordered superstructure. The steady decrease observed in the intensity of these spots with increasing  $x$  reflects a decrease in the coherence length of the ordering. Estimation of the order domain sizes in annealed VOD

materials by means of x-ray diffraction utilizing the Scherrer expression (Equation 1.11; Section 1.3.1) yielded average order domain sizes greater than 1000Å for all of the annealed specimens.

Dielectric hysteresis was observed for all compositions [ $x=0-0.4$ ]. As-fired materials from the composition range [ $x=0-0.4$ ] were observed to display relaxor-type dielectric behavior which becomes more normal on approaching the MPB [ $x=0.4-0.45$ ] beyond which the response is essentially that of a first-order ferroelectric. Both relaxor and normal first-order type dielectric responses were found to occur for VOD compositions with the as-fired materials showing the characteristic diffuse and dispersive responses typical of a relaxor and the annealed specimens exhibiting more sharp, first-order type behaviors. The dielectric behaviors exhibited by as-fired and annealed samples under a biasing field of 5 (KV/cm) were also observed to be those typically associated with relaxor-type ferroelectrics and normal first-order ferroelectrics respectively. The general features of the temperature dependences of the remanent polarization,  $P_r$ , and the 100 KHz reduced RMS polarization,  $P_{(100K)}$ , observed for the VOD compositions highlight the nature of the polarization as it relates to the degree of positional ordering present; it becomes evident that even for the annealed samples, for which relatively high degrees of long-range ordering are achieved and near-normal first-order dielectric responses displayed, some "glassy" polarization character is retained. The depolarization curves of the remanent,  $P_r$ , and 100 KHz reduced RMS,  $P_{(100K)}$ , polarizations for compositions [ $x=0.1-0.4$ ] showed relaxor-type tendencies with a trend towards a more normal first-order type response on approaching the MPB region.

A preliminary evaluation of the pyroelectric response has been conducted in this investigation for selected  $(1-x)\text{Pb}(\text{Sc}_{1/2}\text{Ta}_{1/2})\text{O}_3-(x)\text{PbTiO}_3$  compositions in order to determine the most promising materials for thermal imaging applications and to roughly establish the optimum operating conditions for those which exhibit the highest figures of

merit (defined in Section 6.1). The relatively high dielectric constant coupled with the moderate values of the pyroelectric coefficient below  $T(\text{max})$  for all the compositions considered results in a low voltage response  $[F_V]$  making them not particularly well-suited for large area device applications. These materials do, however, show detectivities  $[F_D]$  adequate for potential use as point detectors. The VOD compositions, in particular, appear to be promising candidates for field-stabilized pyroelectric devices.

The detectivities for as-fired and annealed  $[x=0.025]$  and  $[x=0.05]$  compounds were evaluated under a DC biasing field of 5 (KV/cm). Some enhancement of  $F_D$  was observed at this field strength for the as-fired specimens which even under unbiased conditions exhibited stable responses over an extremely broad temperature range [ $T \approx 0-70^\circ\text{C}$ ; Figure 6.8]. The peak  $F_D$  of the annealed  $[x=0.025]$  material [ $F_D(\text{max}) \approx 16$  ( $10^{-5}\text{Pa}^{-1/2}$ ); Figure 6.9(a)] was observed to occur at  $\approx 20^\circ\text{C}$  and showed a much more marked enhancement under DC bias than its as-fired counterpart [ $F_D(\text{max}) \approx 2.5$  ( $10^{-5}\text{Pa}^{-1/2}$ ); Figure 6.8(a)]. The effect of the biasing field on the annealed  $[x=0.05]$  material was less dramatic with respect to the peak  $F_D$  attained [ $F_D(\text{max}) \approx 6.3$  ( $10^{-5}\text{Pa}^{-1/2}$ ); Figure 6.9(b)]; however, similar to the as-fired materials, this material exhibited an enhanced detectivity over a broad temperature range above  $T(\text{max})$ . These preliminary results, obtained under modest field conditions, have indicated that the materials from the VOD composition range are highly variable in their performance, both with respect to the maximum response achieved and the breadth of the temperature range over which a stable response is obtained.

## **APPENDIX 29**

## PYROELECTRIC RESPONSE AND DEPOLARIZATION BEHAVIOR OF (1-x)Pb(Sc<sub>1/2</sub>Ta<sub>1/2</sub>)O<sub>3</sub>-(x)PbTiO<sub>3</sub> MATERIALS

J. R. GINIEWICZ, A. S. BHALLA and L. E. CROSS

*Materials Research Laboratory, The Pennsylvania State University,  
University Park, Pennsylvania-USA*

*(Received February 18, 1991)*

The pyroelectric response of selected compositions from this solid solution system have been investigated. The nature of the temperature dependence of the pyroelectric coefficient for the compositions examined indicate the presence of a relatively broad, curved morphotropic phase boundary, [ $x = 0.3$ – $0.45$ ]. The high values of pyroelectric coefficient achievable, in particular for low  $x$  compositions [ $x = 0$ – $0.1$ ], suggest potential application of these materials as highly efficient and versatile field-stabilized devices.

### INTRODUCTION

The unique characteristics of the solid solution (1-x)Pb(Sc<sub>1/2</sub>Ta<sub>1/2</sub>)O<sub>3</sub>-(x)PbTiO<sub>3</sub> make it an interesting system from both a theoretical and practical point of view. A variety of compositionally and thermally “adjustable” states of (dis)order, Curie temperature, and dielectric and pyroelectric properties are accessible for these materials making them attractive for many device applications as well as a useful model system for further exploring the fundamental nature of relaxor ferroelectrics.<sup>1</sup> The pyroelectric properties of various compositions have been examined in this investigation in order to better define the structural phase boundaries in the system and to make a preliminary evaluation of the potential usefulness of the material in pyroelectric device applications.

### SAMPLE PREPARATION

Ceramic samples of (1-x)Pb(Sc<sub>1/2</sub>Ta<sub>1/2</sub>)O<sub>3</sub>-(x)PbTiO<sub>3</sub> [ $x$ : 0, 0.025, 0.05, 0.1, 0.3, 0.4, 0.45, 0.5] were prepared by a conventional mixed oxide technique employing the wolframite precursor method<sup>2</sup> in order to reduce the occurrence of undesirable pyrochlore phases. Starting oxides of Sc<sub>2</sub>O<sub>3</sub><sup>†</sup> and Ta<sub>2</sub>O<sub>5</sub><sup>†</sup> were batched and double calcined at 1400°C for 4 hours to form the wolframite<sup>3</sup> [ScTaO<sub>4</sub>] precursor phase. The compositions of interest were then formulated from PbO,<sup>†</sup> TiO<sub>2</sub>,<sup>†</sup> and ScTaO<sub>4</sub>, ball milled with zirconia media for ≈6 hours and subjected to double calcination in closed alumina crucibles at 900°C for 4 hours and 1000°C for 1 hour. Pellets

<sup>†</sup> PbO [Johnson Matthey-Materials Technology UK-Grade A1]; Sc<sub>2</sub>O<sub>3</sub> [Boulder Scientific Co.-99.99%]; Ta<sub>2</sub>O<sub>5</sub> [Hermann C. Starck (Berlin)-Stand. Opt. Grade]; TiO<sub>2</sub> [Aesar (Johnson Matthey Inc.)-99.999%].



[1.25 cm] in diameter were formed and sintered in sealed crucibles at 1400°C–1560°C for periods of [0.5–1.5 hours] depending on the sample composition. Source powders of  $\text{Pb}(\text{Sc}_{1/2}\text{Ta}_{1/2})\text{O}_3$  and  $\text{PbZrO}_3$  were used to maintain a suitable Pb atmosphere within the crucibles. Total weight losses after sintering were typically  $\leq 1\%$  for compositions [ $x > 0.1$ ] and somewhat higher, 2–5%, for those with [ $x \leq 0.1$ ] for which the higher sintering temperatures were required.

Samples of composition [ $0 \leq x \leq 0.1$ ] were disordered as sintered. Ordered materials in this composition range were prepared by post-sintering heat treatment.<sup>4</sup> The sample was embedded in  $\text{Pb}(\text{Sc}_{1/2}\text{Ta}_{1/2})\text{O}_3$  source powder and enclosed in a Pt envelope. The Pt-wrapped sample was then sealed in an alumina crucible with  $\text{Pb}(\text{Sc}_{1/2}\text{Ta}_{1/2})\text{O}_3$  and  $\text{PbZrO}_3$  sources and annealed at 1000°C for 10 hours. No significant weight loss was observed for any of the samples after annealing.

The degree of long-range structural ordering was determined for ordered compositions by means of x-ray diffraction using a Scintag automated x-ray diffractometer. Cu K $\alpha$  radiation was employed. The long-range order is typically evaluated for  $\text{Pb}(\text{Sc}_{1/2}\text{Ta}_{1/2})\text{O}_3$  materials in terms of the relative intensities of the superlattice/normal reflection pairs 111/200 and 311/222.<sup>5</sup>

Specimens for pyroelectric and dielectric measurement were cut as plates from the sintered disks with dielectric samples typically [0.75 cm] on edge and [0.15 cm] in thickness and pyroelectric samples [0.4 cm] on edge and [0.025–0.03 cm] in thickness. Sample surfaces were sputtered with gold and silver contact points applied.

## INSTRUMENTATION

The pyroelectric response was measured by a modified Byer-Roundy method.<sup>6</sup> The specimen was initially poled within a temperature chamber [Model 2300, Delta Design, Inc.] near the transition temperature under a poling field of [20 (KV/cm)] for 15 minutes and cooled with the field applied to  $\approx -100^\circ\text{C}$ . The poling field was then removed. A desk top computer [Model 9816, Hewlett Packard, Inc.] was used to record pyroelectric current data collected by a picoammeter [Model 4140B, Hewlett Packard, Inc.]. Pyroelectric coefficients and depolarization curves were subsequently calculated from the pyroelectric current data.

The dielectric constant and  $\tan(\delta)$  were measured as a function of temperature and frequency using an automated system consisting of an oven [Model 2300, Delta Design, Inc.], an LCR meter [Model 4274A, Hewlett Packard, Inc.], and a digital multimeter interfaced with a desk top computer [Model 9816, Hewlett Packard, Inc.]. Dielectric runs were made over a range of [ $-150$ – $+260^\circ\text{C}$ ] and at frequencies 100 Hz, 1 KHz, 10 KHz, and 100 KHz.

## RESULTS

The effect of increasing Ti-content on the pyroelectric response of the material, as manifested in the temperature dependence of the pyroelectric coefficient, is shown in Figures 1(a–c). The change in the shape of  $p(T)$  as well as the positions

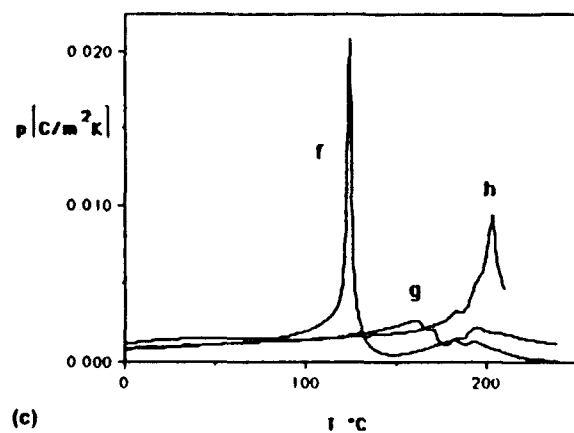
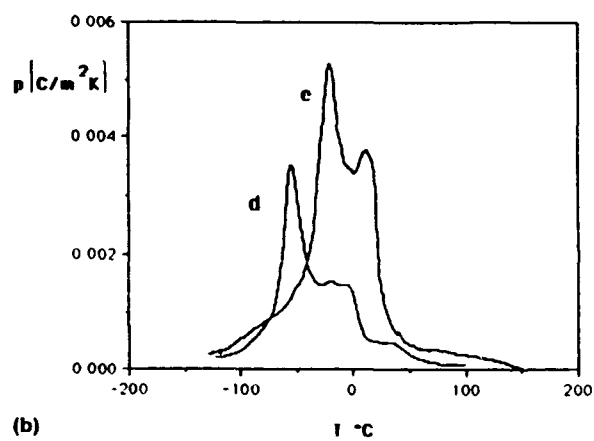
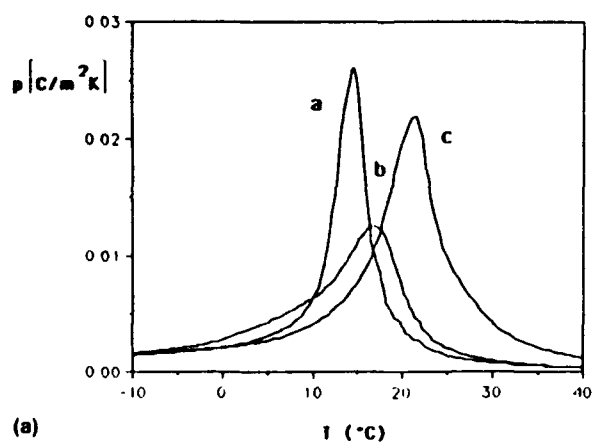


FIGURE 1(a-c) Pyroelectric coefficient as a function of temperature for compositions  $x$ : (a) 0.025 (ordered), (b) 0.05 (ordered), (c) 0.1, (d) 0.025 (disordered), (e) 0.05 (disordered), (f) 0.3, (g) 0.4, (h) 0.45.

TABLE I  
Pyroelectric and dielectric properties of  $(1-x)\text{Pb}(\text{Se}_{1/2}\text{Ta}_{1/2})\text{O}_3$ - $x\text{PbTiO}_3$  compositions.

| $x$                | $P(s)$<br>[ $-100^\circ\text{C}$ ]<br>( $\text{C}/\text{m}^2$ ) | $p(1)$<br>( $\text{C}/\text{m}^2\text{K}$ ) | $T$<br>( $^\circ\text{C}$ ) | $p(2)$<br>( $\text{C}/\text{m}^2\text{K}$ ) | $T$<br>( $^\circ\text{C}$ ) | $K(\text{max})$<br>[1 KHz] | $T$<br>( $^\circ\text{C}$ ) | $D(\text{max})$<br>[1 KHz] | $T$<br>( $^\circ\text{C}$ ) |
|--------------------|---|---|-----------------------------|---|-----------------------------|----------------------------|-----------------------------|----------------------------|-----------------------------|
| 0 <sup>†</sup>     | 0.31  | 0.023                                       | -1                          |   |                             | 18200                      | 7                           | 0.07                       | 0                           |
| 0.025              | 0.18  | 0.004                                       | -56                         | 0.002                                       | -6                          | 11300                      | 10                          | 0.08                       | -30                         |
| 0.025 <sup>†</sup> | 0.28  | 0.029                                       | 13                          |   |                             | 7400                       | 17                          | 0.05                       | 4                           |
| 0.05               | 0.34  | 0.005                                       | -23                         | 0.004                                       | 10                          | 14000                      | 29                          | 0.08                       | -8                          |
| 0.05 <sup>†</sup>  | 0.27  | 0.013                                       | 16                          |   |                             | 11300                      | 26                          | 0.07                       | 11                          |
| 0.1                | 0.39  | 0.024                                       | 20                          |   |                             | 23000                      | 38                          | 0.08                       | 24                          |
| 0.3                |   | 0.024                                       | 123                         | 0.002                                       | 185                         | 26000                      | 136                         | 0.05                       | 124                         |
| 0.4                | 0.43  | 0.003                                       | 157                         | 0.002                                       | 191                         | 28300                      | 180                         | --                         | --                          |
| 0.45               | 0.68  | 0.010                                       | 202                         |   |                             | 22000                      | 208                         | 0.06                       | 204                         |

<sup>†</sup> Partially Ordered

$T(p)$  and magnitudes of the pyroelectric coefficient peaks [Table I; Figure 3] are seen to vary significantly throughout the composition range investigated. Reasonably sharp peaks are observed for the compositions represented in Figure 1(a) [ $x = 0-0.1$ ] with a steady increase in the temperature of the pyroelectric coefficient maximum,  $T(p)$ , and an initial increase in the magnitude of  $p(T)$  [Table I] followed by a sudden decrease in the maximum and some broadening of the peak for the ordered [ $x = 0.05$ ] composition. The shape of  $p(T)$  reflects the onset of the morphotropic phase boundary [MPB] between the rhombohedral and tetragonal phases of the system at about [ $x = 0.3$ ] with the appearance of a second higher temperature peak which persists through [ $x = 0.4$ ] [Figure 1(c)]. This corresponds well with previous determinations of the general range of the MPB by means of room temperature x-ray diffraction and dielectric measurement<sup>1</sup> and further indicates a curvature to this boundary. The appearance of a second higher temperature  $p(T)$  peak for the [ $x = 0.3$ ] composition in this study and the persistence of a shoulder to that of the [ $x = 0.45$ ] composition, however, indicate a slightly broader range of compositions over which the MPB extends than was previously observed.<sup>1</sup> High temperature x-ray diffraction investigations are currently underway to better refine the breadth and curvature of the MPB region.

TABLE II  
Pyroelectric figures of merit  $(1-x)\text{Pb}(\text{Sc}_{1/2}\text{Ta}_{1/2})\text{O}_3$ - $x\text{PbTiO}_3$  compositions.

| $x$                | T<br>(°C) | $p$<br>(C/m <sup>2</sup> K) | K    | D     | F(V)<br>(m <sup>2</sup> /C) | F(D)<br>(10 <sup>-5</sup> Pa <sup>-1/2</sup> ) |
|--------------------|-----------|-----------------------------|------|-------|-----------------------------|--|
| 0 <sup>†</sup>     | -20       | 0.0022                      | 2000 | 0.055 | 0.05                        | 2.8  |
| 0.025 <sup>†</sup> | -20       | 0.0011                      | 1500 | 0.050 | 0.03                        | 1.7  |
| 0.05 <sup>†</sup>  | -20       | 0.0012                      | 1500 | 0.050 | 0.04                        | 1.9  |
| 0.1                | -20       | 0.0013                      | 2500 | 0.050 | 0.02                        | 1.6  |
| 0.3                | 25        | 0.0010                      | 1580 | 0.035 | 0.03                        | 1.7  |
| 0.4                | 25        | 0.0010                      | 1590 | 0.030 | 0.03                        | 1.9  |
| 0.45               | 25        | 0.0014                      | 2300 | 0.020 | 0.03                        | 2.8  |
| 0.5                | 25        | 0.0005                      | 1090 | 0.020 | 0.02                        | 1.4  |

<sup>†</sup> Partially Ordered

A second boundary is also evident upon examination of the changes in  $p(T)$  that occur for compositions  $[0 < x \leq 0.1]$  as shown in Figure 1(a) representing partially ordered compounds and Figure 1(b) showing the response of disordered compounds. It has been determined in another investigation<sup>4</sup> that compositions  $[0 \leq x < 0.1]$  may exhibit both compositionally and thermally variable (dis)order. In that study, this state of variable (dis)order persists in compositions up to  $[x = 0.1]$  beyond which an invariable state of structural disorder exists and develops in a manner analogous to other systems showing a transition from relaxor to normal ferroelectric behavior with compositional changes [e.g.,  $-\text{Pb}(\text{Mg}_{1/3}\text{Nb}_{2/3})\text{O}_3$ - $\text{PbTiO}_3$ ]. There are, therefore, four distinct regions [Figure 3] present in this solid solution system: (a) Region I, a region of variable order/disorder [VOID], (b) Region II, a composition range in which the material behaves as a relaxor (analogous to  $\text{Pb}(\text{Mg}_{1/3}\text{Nb}_{2/3})\text{O}_3$ ), (c) Region III, a MPB region, and (d) Region IV, in which the material exhibits normal ferroelectric behavior. The existence of a second structural boundary between variably (dis)ordered and invariably disordered states is further evidenced here where there is seen, in the ordered case [Figure 1(a)], a drop in the magnitude of the peak  $p(T)$  just before  $[x = 0.1]$  and, in the disordered case [Figure 1(b)], for compositions up to  $[x = 0.1]$  characteristic multiple peaks similar to that previously observed for disordered  $\text{Pb}(\text{Sc}_{1/2}\text{Ta}_{1/2})\text{O}_3$  single crystals.<sup>7</sup> It was suggested in that investigation that the appearance of a double peak for disordered  $\text{Pb}(\text{Sc}_{1/2}\text{Ta}_{1/2})\text{O}_3$  likely reflects the coexistence of ordered and disordered

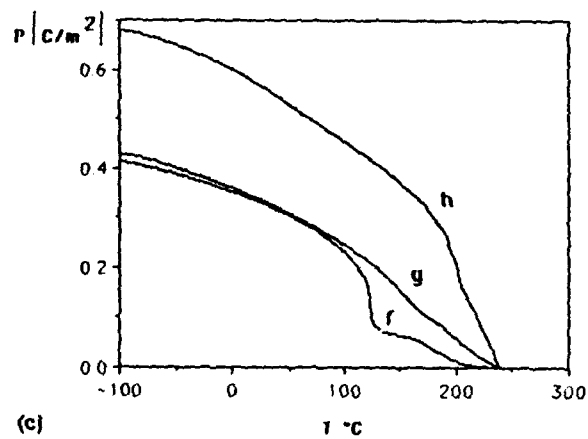
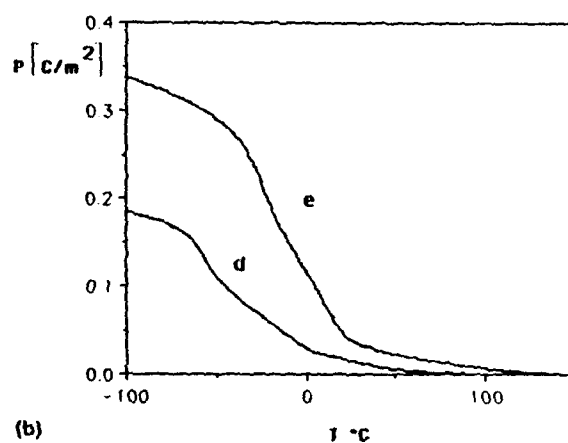
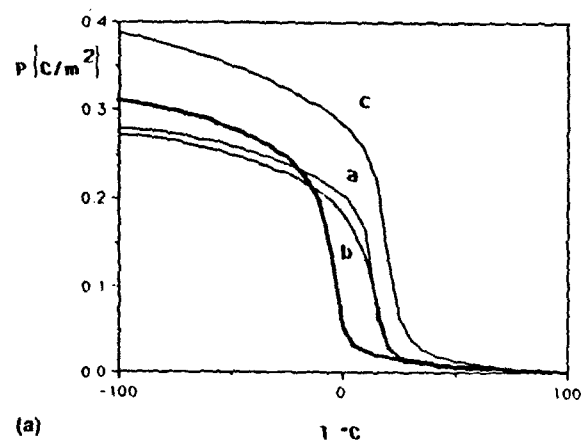


FIGURE 2(a-c) Spontaneous polarization as a function of temperature for compositions  $x$  (a) 0.025 (ordered), (b) 0.05 (ordered), (c) 0.1, (d) 0.025 (disordered), (e) 0.05 (disordered), (f) 0.3, (g) 0.4, (h) 0.45, bold curve partially ordered PST.

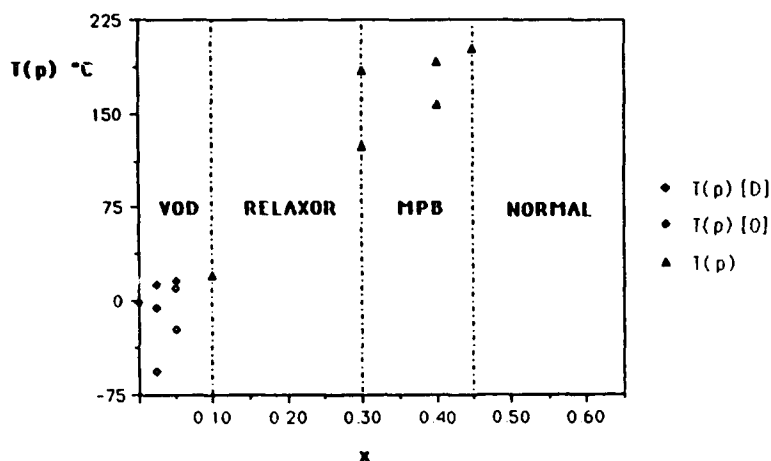


FIGURE 3 Temperature of the pyroelectric coefficient peaks,  $[T(p)]$ , for  $(1-x)\text{Pb}(\text{Sc}_{1/2}\text{Ta}_{1/2})\text{O}_3\text{-}x\text{PbTiO}_3$  compositions [ $x = 0\text{--}0.45$ ].

regions within the material. This issue and a more thorough characterization of the compositions within this VOD region are discussed elsewhere.<sup>4</sup>

The shape of the depolarization curve [Figures 2(a-c)] is observed to change markedly with compositional variations. On traversing Region I [ $0 \leq x < 0.1$ ], considering only partially ordered compositions, the depolarization curve is seen to vary gradually with a "tail" that persists well above the temperature of the dielectric maximum [Table I] in all cases. As observed previously for disordered  $\text{Pb}(\text{Sc}_{1/2}\text{Ta}_{1/2})\text{O}_3$ ,<sup>8,9</sup> the depolarization curves of the disordered compounds in this region [Figure 2(b)] are seen to decrease in a continuous, extremely gradual manner, with the high temperature polarization "tail" increased in magnitude on approaching the VOD boundary composition [ $x = 0.1$ ]. The shape of the depolarization curve becomes more continuous and extended throughout the composition range [ $x = 0.3\text{--}0.45$ ] reflecting the phase transitions occurring through the MPB with that of the [ $x = 0.45$ ] composition exhibiting a tendency to a more first-order type behavior. This corresponds well with results previously reported on the nature of the dielectric response of these materials through the MPB region.<sup>1</sup> In those studies the dielectric behavior of the [ $x = 0.45$ ] composition was observed to approach that characteristic of a normal ferroelectric but with the persistence of some of the diffuseness characteristic of a relaxor ferroelectric. Further, the temperature range required to observe the transition for this composition extended somewhat beyond the practical range of the experimental set-up thereby affecting data taken at the extreme upper limit of this range in such a way as to artificially enhance the magnitude of the  $P(r)$  values calculated from data taken at the highest temperatures. Overall, the nature of the depolarization is seen to vary with composition in a manner appropriate to the state of the material in each of the four regions defined for the system consistent with results obtained in previous investigations.<sup>1</sup>

The pyroelectric response of a material is generally rated for device application by the figures of merit  $F(V)$  [ $p/K \text{ c}'$ ] and  $F(D)$  [ $p/(K \tan \delta)^{1/2} \text{ c}'$ ] ( $\text{c}'$ : the volume

heat capacity) which reflect the voltage response and detectivity respectively.<sup>10,11</sup> A high  $F(V)$  is desirable for large area device applications while a high value of  $F(D)$  is important for point detectors. The relatively high dielectric constant coupled with moderate values of pyroelectric coefficient below  $T_c$  results in a low voltage response for all the compositions considered making them not particularly well-suited for large area device applications. These compositions do, however, show values of  $F(D)$  adequate for potential use as point detectors. The VOD compositions in particular are promising candidates for field-stabilized pyroelectric devices. The usefulness of pure  $\text{Pb}(\text{Sc}_{1/2}\text{Ta}_{1/2})\text{O}_3$  materials operated under moderate DC fields has already been established for such applications.<sup>8,9,12</sup> It has been demonstrated that variably (dis)ordered  $(1-x)\text{Pb}(\text{Sc}_{1/2}\text{Ta}_{1/2})\text{O}_3$ - $(x)\text{PbTiO}_3$  within the VOD region respond to DC bias in a manner similar to that exhibited by  $\text{Pb}(\text{Sc}_{1/2}\text{Ta}_{1/2})\text{O}_3$ .<sup>11</sup> The  $(1-x)\text{Pb}(\text{Sc}_{1/2}\text{Ta}_{1/2})\text{O}_3$ - $(x)\text{PbTiO}_3$  compositions in the VOD region are, therefore, expected to exhibit figures of merit comparable to that of the unmodified material with the added feature of being tailorable in response via both compositional variations and heat treatment.

## SUMMARY

The temperature dependence of the pyroelectric coefficient and the depolarization behavior exhibited by compositions from the solid solution system  $(1-x)\text{Pb}(\text{Sc}_{1/2}\text{Ta}_{1/2})\text{O}_3$ - $(x)\text{PbTiO}_3$  indicate the existence of two structural phase boundaries, a morphotropic phase boundary [MPB] and another between variably (dis)ordered [VOD] and invariably disordered compositions, in general agreement with dielectric and x-ray diffraction data previously reported.<sup>1</sup> The range of the MPB is observed to be rather broad [ $x = 0.3$ - $0.45$ ] and some curvature to the boundary is evident. The VOD phase region is clearly indicated by characteristic behavior within the region and an abrupt change in the nature of the pyroelectric response at the VOD phase boundary. These VOD compositions are particularly promising candidates for field-stabilized pyroelectric device applications due to their excellent pyroelectric response coupled with the versatility of design possible via simple variations in composition and annealing conditions.

## REFERENCES

1. J. R. Giniewicz, A. S. Bhalla and L. E. Cross, *Ferroelectric Lett.*, **12**, 35 (1990).
2. T. R. ShROUT and A. Halliyal, *Amer. Cer. Soc. Bull.*, **66**(4), 704 (1987).
3. JCPDS, #24-1017- $\text{ScTaO}_3$ .
4. J. R. Giniewicz, A. S. Bhalla and L. E. Cross, (to be published).
5. N. Setter, Ph.D. Thesis, The Pennsylvania State University, (1980).
6. R. L. Byer and C. B. Roundy, *Ferroelectrics*, **3**, 333 (1972).
7. C. A. Randall and A. S. Bhalla, *Ferroelectric Lett.*, **9**, 47 (1988).
8. C. Zhili, Y. Xi and L. E. Cross, *Ferroelectrics*, **49**, 213 (1983).
9. C. Zhili, Y. Xi and L. E. Cross, *Ferroelectric Lett.*, **44**, 271 (1983).
10. R. W. Whatmore, *Rep. Prog. Phys.*, **49**, 1335 (1986).
11. R. W. Whatmore, A. Patel, N. M. Shorrocks and F. W. Ainger, *Ferroelectrics*, **104**, 269 (1990).
12. N. M. Shorrocks, R. W. Whatmore and P. C. Osbond, *Ferroelectrics*, **104**, 387 (1990).
13. J. R. Giniewicz, A. S. Bhalla and L. E. Cross, (to be published).

## **APPENDIX 30**



## PYROELECTRIC AND DIELECTRIC PROPERTIES OF PMN-BASED CERAMICS UNDER DC BIAS

D. J. TAYLOR, D. DAMJANOVIC and A. S. BHALLA  
*Materials Research Laboratory, The Pennsylvania State University,  
University Park, PA 16802 USA*

(Received February 18, 1991)

The temperature dependence of the pyroelectric and dielectric response as a function of a selected DC electric bias field has been investigated for several different compositions of the PMN-based ceramic. The selected DC electric bias field which gives the maximum pyroelectric coefficient was determined by a study of the pyroelectric coefficient, measured by the Byer-Roundy method, at several poling fields. The large values of the figure of merit ( $p/(K)^{1/2}$ ) found in these PMN-based compositions, suggest this material as a promising candidate for pyroelectric point detectors since this figure of merit is comparable to the materials most widely used, TGS and LiTaO<sub>3</sub>, for point detectors.

### INTRODUCTION

Recent interest has been focused on the solid solution consisting of the relaxor ferroelectric end member PbMgNb<sub>2/3</sub>O<sub>3</sub> (PMN) and the normal ferroelectric end member PbTiO<sub>3</sub> (PT) for possible use in actuators<sup>1</sup> and transducers.<sup>2</sup> This interest has evolved because of the large dielectric and piezoelectric constants that have been reported in these materials. Throughout the entire solid solution, large dielectric values have been reported while large piezoelectric constants, have been reported not only, near the morphotropic phase boundary<sup>1</sup> (realized by Choi *et al.*, on a ceramic composition, at room temperature, to be ~0.66 PMN-0.34 PT) but also, for those compositions with less lead titanate content where with the application of an external electric bias field a very strong piezoelectric effect is induced.<sup>4,5</sup> For the compositions with less lead titanate, the application of an external DC bias field is necessary because for these compositions there is no net stable remanent polarization.

In some of our earlier publications, studies of the piezoelectric, dielectric and elastic properties of PMN-based ceramics under DC bias fields were made by laser interferometry<sup>6</sup> and a resonance method,<sup>7</sup> however, a natural question arises as to the pyroelectric properties of these ceramics as a function of DC bias. It is the intent of this paper to explore the pyroelectric properties of some of the PMN-based ceramic compositions, where with the application of an external electric field a strong piezoelectric effect is induced. This investigation includes a study of the effect of different poling voltages on each composition, the determination of the electric poling field which gives the maximum pyroelectric effect and the values of the pyroelectric and dielectric properties with this maximum electric poling field applied to the sample as a DC electric bias field. The paper then goes on to calculate the figures of merit for these compositions and based on one of these figures of merit suggests a couple of the PMN-based ceramic compositions as promising candidates for pyroelectric point detectors.<sup>8</sup>

## EXPERIMENTAL PROCEDURE

Three different compositions of the PMN-based ceramic material were chosen for a study of their pyroelectric and dielectric properties as a function of poling field. These compositions are: 0.90 PMN-0.10 PT, 0.93 PMN-0.07 PT and PMN with 1 mole % La. All of the compositions were prepared from reagent grade oxides according to the Columbite precursor method<sup>9</sup> and hot uniaxially pressed. Hot uniaxially pressing, as compared to traditional sintering methods, resulted in the formation of highly dense (>99.5% theoretical) phase pure ceramics with a uniform microstructure and it is expected that these hot pressed ceramics will give optimal pyroelectric and dielectric coefficients.

Pyroelectric measurements were made using the static method of Byer-Roundy.<sup>10</sup> In this method, a pyroelectric current is generated in the ceramic when its surrounding temperature is changed so as to vary the spontaneous polarization of the ceramic. This current is given by:

$$I = pAdT/dt \quad (1)$$

where  $p$  is the pyroelectric coefficient,  $A$  the electroded surface area of the sample, and  $dT/dt$  the rate at which the sample is heated or cooled.

In our experimental set-up the current ( $I$ ) is measured on a picoammeter (HP-4140B) and recorded on a computer (HP-9000). This computer also controls and monitors the heating and cooling rates of the liquid nitrogen fed furnace (Delta design 2300). Different DC electric bias fields were applied to the sample with a Kiethly 240A high voltage power supply. A static value of the spontaneous polarization is found by integrating  $p$  with respect to  $T$ .

The samples used in the Byer-Roundy method had areas between 0.1 cm<sup>2</sup> and 0.4 cm<sup>2</sup> and thicknesses less than 0.4 mm. Gold electrodes were sputtered on the top and bottom surfaces of the samples and a small amount of anhydrous silver paint was brushed on the center of these gold electrodes so as to ensure good electrical contacts. The samples were prepared having an area with small dimensions so that a uniform temperature could be maintained across the sample. The samples were polished with 0.3  $\mu$  Al<sub>2</sub>O<sub>3</sub> and were prepared thin so that large electric fields could be applied to the sample. For all pyroelectric measurements made, a heating and cooling rate of approximately 2°C/minute was used.

For the three different PMN-based ceramic compositions, pyroelectric coefficients at several different poling fields, including zero field, were measured with the intent of locating the maximum pyroelectric coefficient. The procedure followed for these measurements was: first to heat the sample well above its Curie range, then apply an electric field to the sample and cool the sample to a temperature well below its Curie range, next short-circuit the sample at its minimum temperature and finally measure the pyroelectric current on heating with no field applied to the sample. This procedure was followed for several electric fields, climbing in gradual increments with the electric field, until the pyroelectric coefficient saturates or the external threshold bias voltage of the picoammeter is reached.

Once the electric field which gave the maximum pyroelectric coefficient was found (or the limiting bias voltage of the picoammeter was reached) this electric field was then applied to the sample and the computer collected pyroelectric data

on both a cooling and heating run. The temperature that the cooling cycle started at was at least 25°C above the temperature at which the pyroelectric coefficient had a maximum, and the temperature that the cooling cycle finished at was at least 25°C below the temperature at which the pyroelectric coefficient had a minimum.

Dielectric measurements were made as a function of temperature on cooling and heating cycles at several frequencies for the three PMN-based ceramic compositions. These measurements were made with no field applied to the sample and at several different electric fields, including the field that gave the maximum pyroelectric coefficient, thus, allowing us to calculate the figure of merit for each composition at one electric field. The dielectric constant is determined by:

$$K = Ct/A\epsilon_0 \quad (2)$$

where  $C$  is the sample's capacitance,  $t$  its thickness,  $A$  its area, and  $\epsilon_0$  the electrical permittivity of free space ( $8.85 \times 10^{-12}$  F/m). Measurements of the capacitance were made on an LCR meter (HP4274A) and recorded on a computer (HP9816), which similar to the Byer-Roundy method for making pyroelectric measurements, controls and monitors the heating and cooling rate of the liquid nitrogen fed furnace. The DC bias voltage was applied to the samples, via the LCR meter, by a high voltage power supply (Keithly 240A) and the maximum voltage allowed is  $\pm 200$  volts. Sample preparation for the dielectric measurements is the same as that for the Byer-Roundy measurements, hence the same samples used for making Byer-Roundy pyroelectric measurements were also used for making dielectric measurements.

## RESULTS AND DISCUSSION

Presented in Figure 1 are the results of pyroelectric measurements made on 0.90 PMN-0.10 PT by the Byer-Roundy method. When no electric field is applied to the sample and the pyroelectric coefficient and spontaneous polarization are measured on heating from  $-100^\circ\text{C}$  to  $100^\circ\text{C}$ , the maximum pyroelectric coefficient is less than  $7 \times 10^{-4}$  C/m<sup>2</sup> K and the maximum spontaneous polarization is less than 0.011 C/m<sup>2</sup>. In Figure 1(a) the pyroelectric coefficient is shown as a function of temperature over the temperature range  $18^\circ\text{C}$  to  $23^\circ\text{C}$  when various electric fields were applied to the sample on cooling. These measurements which show the effect of different poling voltages on this composition were made by the following procedure: first the sample was heated to  $100^\circ\text{C}$ , then cooled to  $-100^\circ\text{C}$  with an electric field of either 1.0, 1.5, 2.0 or 2.5 kV/cm applied to the sample, next the sample was short-circuited and finally pyroelectric coefficients were measured on a heating cycle from  $-40^\circ\text{C}$  to  $120^\circ\text{C}$  at  $2^\circ\text{C}/\text{minute}$ . The pyroelectric peak for these four electric fields, over a temperature range of  $160^\circ\text{C}$  is very sharp. However, since the width of each pyroelectric peak is less than  $2^\circ\text{C}$ , we chose to plot the pyroelectric coefficient as a function of temperature over a smaller temperature range, namely  $18^\circ\text{C}$  to  $23^\circ\text{C}$ , even though the pyroelectric peak is less distinct. Also, it should be noted that the interpretation of the data was aided by extrapolating the data around the pyroelectric peak, as indicated in Figure 1(b) with a dashed line. For 0.90 PMN-0.10 PT the maximum pyroelectric coefficient ( $p \sim$

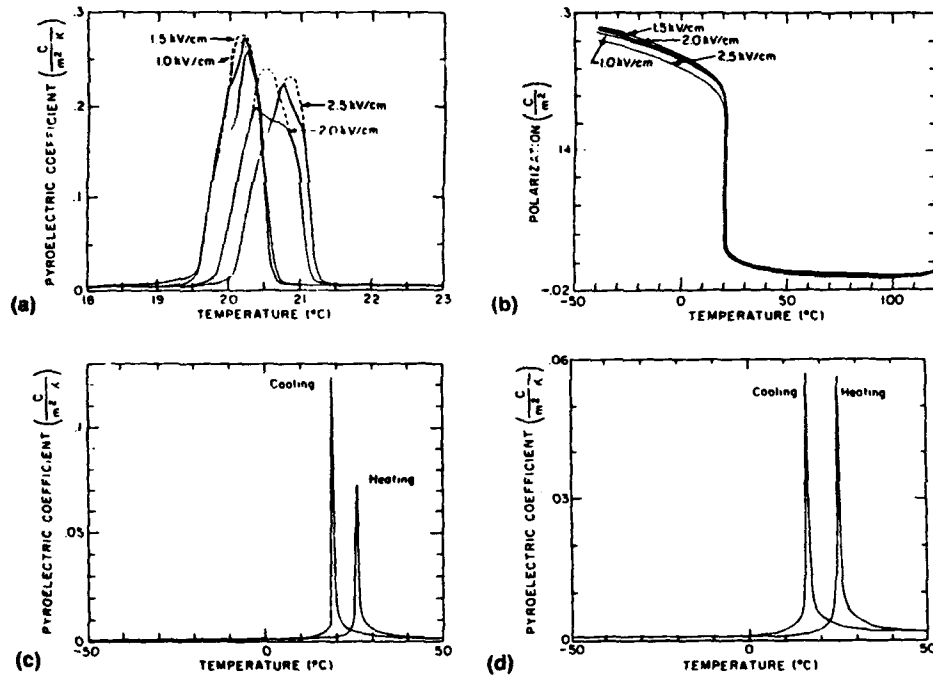


FIGURE 1 Results of measurements made on 0.90 PMN-0.10 PT. (a) The pyroelectric coefficient as a function of temperature when various DC bias fields are applied on a cooling cycle from  $100^{\circ}C$  to  $-100^{\circ}C$  and measurements are made on a heating cycle with zero field applied to the sample. (b) The spontaneous polarization as a function of temperature corresponding to the pyroelectric coefficient mentioned above. (c) Heating and cooling cycles of the pyroelectric coefficient as a function of temperature when a  $1.5 \text{ kV/cm}$  DC electric bias field is applied to the sample during measurements. (d) These measurements follow the same procedure as that discussed in Figure 1(c), however, they were made nine months later and at this time the charge build-up on the electrodes had time to dissipate.

$0.27 \text{ C/m}^2 \text{ K}$ ) is rather large and occurs when an electric field of  $1.5 \text{ kV/cm}$  is applied on cooling at a temperature near room temperature, about  $20.2^{\circ}C$  and measurements are made on heating without an electric bias field applied to the sample. Furthermore, we observe that the effect of an increase in the electric field is not only to change the value of the pyroelectric coefficient but also to slightly increase the temperature at which this maximum occurs. More specifically, for an increase in field of  $\sim 1 \text{ kV/cm}$ , the temperature corresponding to the maximum pyroelectric coefficient increases by half a degree.

Curves of the spontaneous polarization as a function of temperature corresponding to the pyroelectric measurements described for Figure 1(a) are shown in Figure 1(b) over the complete measured temperature range, that is  $-40^{\circ}C$  to  $120^{\circ}C$ . The maximum spontaneous polarization ( $\sim 0.28 \text{ C/m}^2$ ) occurs when an electric field of  $1.5 \text{ kV/cm}$  is applied to the sample on cooling and as expected the field to which this maximum polarization corresponds is the field which gives the maximum pyroelectric coefficient.

Results of the pyroelectric coefficient as a function of temperature, after applying an electric field of  $1.5 \text{ kV/cm}$  to the sample, on a heating and cooling run from  $-50^{\circ}C$  to  $+50^{\circ}C$ , are shown in Figure 1(c). For this electric field, on a cooling

run, the pyroelectric coefficient reaches a maximum of  $0.124 \text{ C/m}^2 \text{ K}$  at  $18.8^\circ\text{C}$  and on a heating run, the pyroelectric coefficient drops to  $0.072 \text{ C/m}^2 \text{ K}$  at  $25.9^\circ\text{C}$ . This change in the magnitude of the pyroelectric coefficient on cooling and heating could be explained by the build-up of charge on the electrode. In Figure 1(d) results of measurements made nine months later, just like those described for Figure 1(c), are shown. The value of the pyroelectric coefficient on a cooling and heating cycle remained the same ( $p \sim 0.06 \text{ C/m}^2 \text{ K}$ ) and the extra build-up of charge on the electrodes dissipates over time. The slight change in the values of the pyroelectric measurements made nine months later is minimal and within experimental error. The shift of the pyroelectric peak with temperature, observed in both Figure 1(c) and Figure 1(d), when cooling and heating the sample can be explained by thermal hysteresis.

Pyroelectric measurements made on 0.93 PMN-0.07 PT by the Byer-Roundy method are shown in Figure 2. When no field is applied to the sample on heating over the temperature range  $-100^\circ\text{C}$  to  $100^\circ\text{C}$ , the pyroelectric coefficients like those of 0.90 PMN-0.10 PT are insignificantly small and less than  $10^{-4} \text{ C/m}^2 \text{ K}$ . In Figure 2(a) the pyroelectric coefficient is shown as a function of temperature over the range  $-10^\circ\text{C}$  to  $0^\circ\text{C}$  for the electric fields of 2.0, 2.5, 3.0, 3.5 and  $4.0 \text{ kV/cm}$  applied to the sample. These measurements which show the effect of different poling voltages on this composition were made following the same procedure described for Figure 1(a) except that in order to find this composition's maximum pyroelectric coefficient it was necessary to apply larger electric fields to the sample. For this composition, we also note that its pyroelectric peak would likely be more distinct over a larger temperature range, however, over the small temperature range plotted,  $-10^\circ\text{C}$  to  $0^\circ\text{C}$ , the pyroelectric peak does not appear sharp, but rather smooth. Furthermore, we find: the maximum pyroelectric peak to be  $0.023 \text{ C/m}^2 \text{ K}$ , an order of magnitude less than 0.90 PMN-0.10 PT; the temperature corresponding to the maximum pyroelectric peak to be  $-5^\circ\text{C}$ , a temperature at least  $25^\circ\text{C}$  less than 0.90 PMN-0.10 PT; the width of the pyroelectric peak to be greater than  $50^\circ\text{C}$ , a width much greater than 0.90 PMN-0.10 PT and the electric field ( $3.5 \text{ kV/cm}$ ) needed to achieve this maximum pyroelectric coefficient to be larger than the electric field ( $1.5 \text{ kV/cm}$ ) needed to achieve the maximum pyroelectric coefficient in 0.90 PMN-0.10 PT. However, it should be noted that there is not a strong relationship between the increase in the electric field and the increase in the measured value of the maximum pyroelectric coefficient. Also, corresponding changes in the associated temperature are small.

For the same five different electric fields shown in Figure 2(a), the spontaneous polarization is shown in Figure 2(b). As expected, and also observed in 0.90 PMN-0.10 PT, the field which gives the maximum spontaneous polarization ( $\sim 0.27 \text{ C/m}^2$ ) corresponds to the electric field which give the maximum pyroelectric coefficient.

Shown in Figure 2(c) are the results of the pyroelectric coefficient as a function of temperature when a field of  $3.5 \text{ kV/cm}$  is applied to the sample on a cooling and heating run. The magnitude of  $p$  is essentially constant at  $\sim 0.005 \text{ C/m}^2 \text{ K}$  hence, there is no space charge build-up. Only a small amount of thermal hysteresis is observed, as can be seen by the temperature corresponding to the pyroelectric

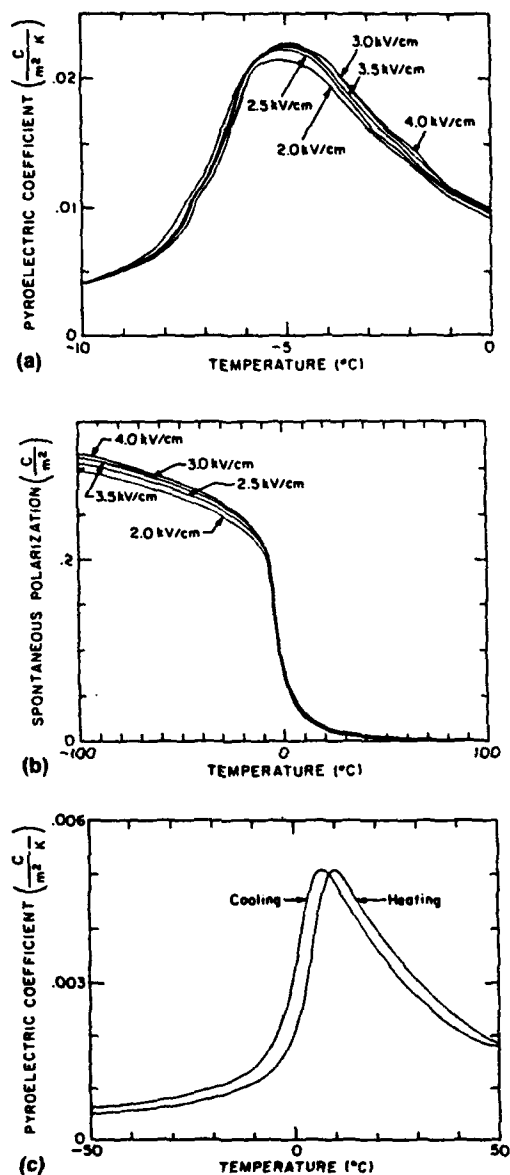


FIGURE 2 Results of measurements made on 0.93 PMN-0.07 PT. (a) The pyroelectric coefficient as a function of temperature is measured by the procedure discussed in Figure 1(a). (b) The spontaneous polarization as a function of temperature is measured by the procedure discussed in Figure 1(b). (c) Heating and cooling cycles of the pyroelectric coefficient as a function of temperature when, during measurements, a 3.5 kV/cm DC electric bias field is applied to the sample.

peaks on a heating and cooling run, this temperature increases by only about 2 $^{\circ}C$  as compared to 0.90 PMN-0.10 PT where an increase of about 10 $^{\circ}C$  is observed.

Results of the pyroelectric measurements made by the Byer-Roundy method, on PMN with 1 mole % La, are shown in Figure 3. When no field is applied to

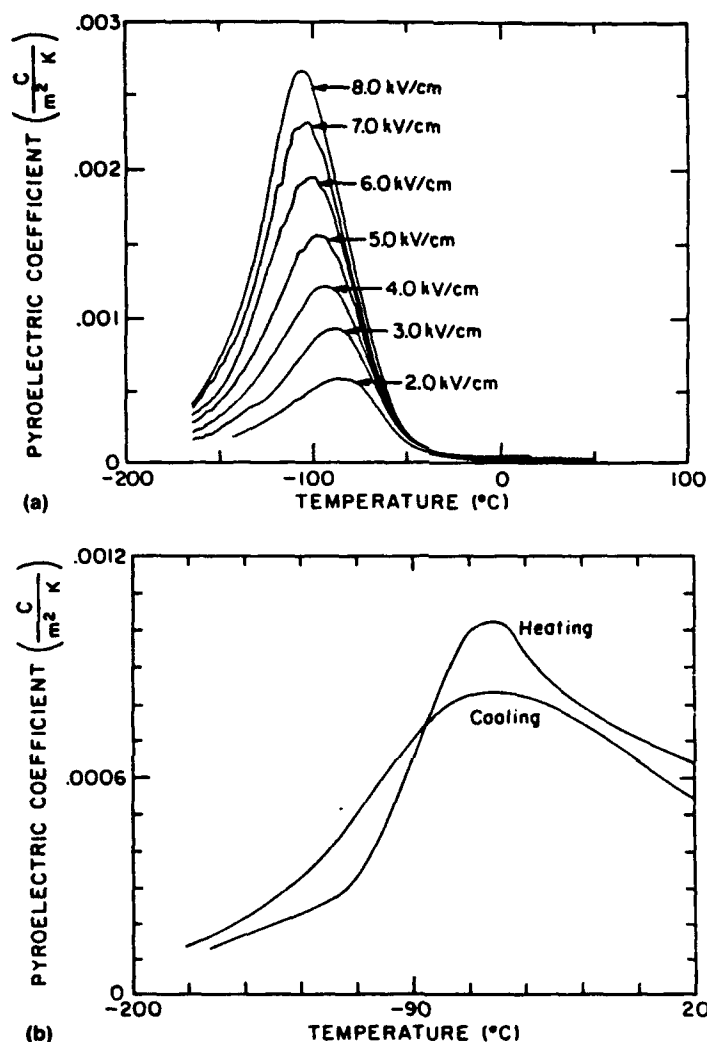


FIGURE 3 Results of measurements made on PMN with 1 mole % La. (a) The pyroelectric coefficient is measured by a procedure similar to that discussed in Figure 1(a). (b) Heating and cooling cycles of the pyroelectric coefficient as a function of temperature when, during measurements, a 8.0 kV/cm DC electric bias field is applied to the sample.

the sample on heating from  $-180^{\circ}C$  to  $100^{\circ}C$ , like the other PMN-based ceramic compositions, the pyroelectric coefficient is insignificantly small. In Figure 3(a) the pyroelectric coefficient is shown as a function of temperature over the temperature range  $-180^{\circ}C$  to  $100^{\circ}C$  for the different electric poling fields, starting at 2.0 kV/cm with successive increments of 1.0 kV/cm. Although the pyroelectric coefficient did not saturate at 8.0 kV/cm, this was the maximum electric field applied to the sample, since the external threshold voltage of the picoammeter is reached at this field. For this composition at 8.0 kV/cm the maximum pyroelectric coefficient has a value of  $0.0027 C/m^2 K$  and is two orders of magnitude less than the pyroelectric

coefficient of 0.90 PMN-0.10 PT. This value of the pyroelectric coefficient for PMN with 1% La occurs at a temperature of  $-108.4^{\circ}\text{C}$  when first, an electric field of 8.0 kV/cm is applied to the sample on cooling from  $100^{\circ}\text{C}$  to  $-180^{\circ}\text{C}$  and then, when measurements are made on heating over the same temperature range with no field applied to the sample. The pyroelectric peak for this sample is very broad, compared to 0.90 PMN-0.10 PT and 0.93 PMN-0.07 PT, and may be explained by the La in this sample's composition. Also, it is noteworthy, that an increase of the electric field applied to the sample when on a cooling run not only results in the increase of the values of the maximum pyroelectric coefficients, as it did with the other compositions discussed earlier, but also, results in the decrease in the temperature at which this maximum pyroelectric coefficient occurs. This temperature decrease did not occur with either 0.90 PMN-0.10 PT or 0.93 PMN-0.07 PT. The decrease in temperature is around  $2^{\circ}\text{C}$  to  $5^{\circ}\text{C}$  for an increase in electric field of 1.0 kV/cm and may be a result of the La in this composition causing aging.

Measurements made of the pyroelectric coefficient as a function of temperature, after applying an electric field of 8.0 kV/cm to the sample on both a cooling and heating run, in the temperature range  $-180^{\circ}\text{C}$  to  $20^{\circ}\text{C}$ , are shown in Figure 3(b). The pyroelectric peak on the cooling cycle is only slightly broader than the pyroelectric peak on heating. The value of the maximum pyroelectric coefficient on heating is only slightly greater than  $0.001\text{ C/m}^2\text{ K}$  and yet, the value of the maximum pyroelectric coefficient on cooling is only slightly greater than  $0.0008\text{ C/m}^2\text{ K}$ . The small difference in the values of  $p$  on heating and cooling could be due to the build-up of charge on the electrodes also noted for 0.90 PMN-0.10 PT and discussed in connection with Figure 1(c). For PMN with 1 mole % La some thermal hysteresis is observed since the temperature corresponding to the maximum pyroelectric coefficient on heating and cooling differs by approximately  $10^{\circ}\text{C}$ .

For the three PMN-based ceramic compositions, capacitance measurements on heating and cooling as a function of temperature at various DC electric bias fields, including zero field were made. These measurements were performed with an ac voltage of 1 volt and at several frequencies. The dielectric constant is calculated by Equation 2, at 100 Hz. It is plotted as a function of temperature, as shown in Figure 4, when the samples are cooled (at a rate of  $2^{\circ}\text{C/minute}$ ) and measurements were made on cooling with various DC electric bias fields, including zero field and the field which gives the maximum pyroelectric coefficient. For each composition, the temperature range covered for the dielectric measurements is practically the same as the temperature range covered for the pyroelectric measurements. Thus, later it will be possible to calculate the figure of merit for each composition at one electric field.

Results of measurements made on 0.90 PMN-0.10 PT at 0.5, 1.0, 1.5 and 2.0 kV/cm are shown in Figure 4(a) when the sample was cooled from  $50^{\circ}\text{C}$  to  $-50^{\circ}\text{C}$ . For an increase in the applied electric field, the Curie range increases and the dielectric constant decreases. Also for this composition, we observe that when cooling the sample for each different electric bias field, the dielectric constant drops abruptly. For an increase in the applied electric field, these drops occur at higher temperatures. Shown in Figure 4(b) are results of measurements made on 0.93 PMN-0.07 PT at 2.0, 2.5, 3.0, 3.5 and 4.0 kV/cm when the sample was cooled from  $50^{\circ}\text{C}$  to  $-50^{\circ}\text{C}$ . For an increase in the applied electric field, the Curie temperature



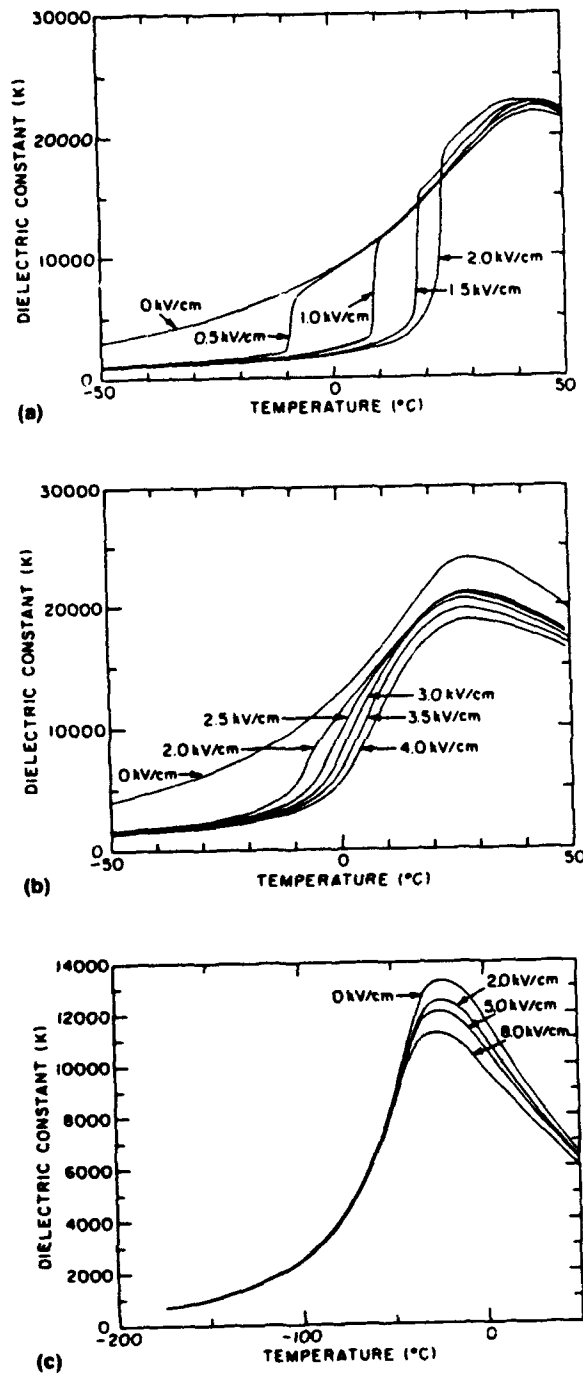


FIGURE 4 The dielectric constant as a function of temperature on a cooling cycle at 100 Hz under various DC bias fields for (a) 0.90 PMN-0.10 PT, (b) 0.93 PMN-0.07 PT and (c) PMN with 1 mole % La.

decreases, and the dielectric constant decreases. Results of measurements made on PMN with 1 mole % La at 2.0, 5.0 and 8.0 kV/cm, when the sample is cooled from 50°C to -180°C are shown in Figure 4(c). For an increase in the electric field applied to the sample, the dielectric constant decreases while the Curie range decreases slightly.

In Figure 5, dielectric and pyroelectric measurements are shown for each of the PMN-based ceramic compositions investigated on a heating and cooling cycle with an external electric bias field. The electric bias field for each composition was chosen from a study on the effect of poling for that composition. The poling field which gave the maximum pyroelectric coefficient was selected. The dielectric constant was measured at 100 Hz. Listed in Table I, for the three different compositions on heating and cooling are: the figures of merit  $p/K$ ,  $p/(K)^{1/2}$ , and  $p/(K \tan \delta)^{1/2}$ ; the value of the sample's Curie range ( $T_c$ ) and the value of  $K$  at this temperature; the temperature ( $T_m$ ) corresponding to the maximum pyroelectric coefficient and the value of this coefficient; the values of  $K$ ,  $p$  and  $\tan \delta$  at a measuring temperature ( $T_m$ ) which for both the heating and cooling cycle is at least 10°C below  $T_c$  and 5°C away from  $T_m$ , hence the composition is in a stable region of its ferroelectric phase; and, a footnote, for the sake of comparison with our PMN-based ceramics, to the values of  $p$ ,  $K$  and  $p/(K)^{1/2}$  for LiTaO<sub>3</sub> and TGS.

From Table I, we see that the figures of merit ( $p/(K)^{1/2}$ ) for 0.90 PMN-0.10 PT and 0.93 PMN-0.07 PT, found at  $T_m$  and their maximum DC electric bias field, are comparable to the figure of merits ( $p/(K)^{1/2}$ ) for LiTaO<sub>3</sub> and TGS, two of the most widely used materials for pyroelectric point detectors. However, we note that the figure of merit for 0.90 PMN-0.10 PT and 0.93 PMN-0.07 PT can be superior to that of LiTaO<sub>3</sub> and TGS if the measuring temperature ( $T_m$ ) is moved slightly. In Figure 5(a), for 0.90 PMN-0.10 PT, if  $T_m$  is ~25°C (almost at the pyroelectric peak) on a heating cycle with a 1.5 kV/cm DC bias field,  $p \sim 23,000 \mu\text{C/m}^2 \text{ K}$ ,  $K \sim 12,000$  and  $p/(K)^{1/2} \sim 210 \mu\text{C/m}^2 \text{ K}$ . Similarly in Figure 5(b), for 0.93 PMN-0.07 PT, if  $T_m \sim 10^\circ\text{C}$  (almost at the pyroelectric peak) on a heating cycle with a 3.5 kV/cm DC bias field,  $p \sim 5000 \mu\text{C/m}^2 \text{ K}$ ,  $K \sim 14,600$  and  $p/(K)^{1/2} \sim 41 \mu\text{C/m}^2 \text{ K}$ ; while for a  $T_m \sim 5^\circ\text{C}$ , there is little change in the value for  $p/(K)^{1/2}$ ,  $p \sim 4,000 \mu\text{C/m}^2 \text{ K}$ ,  $K \sim 10,000$  and  $p/(K)^{1/2} \sim 40 \mu\text{C/m}^2 \text{ K}$ .

## SUMMARY

A study of the temperature dependence of the pyroelectric coefficient at different poling fields for several of the PMN-based ceramic compositions has allowed us to determine an electric bias field which when applied to a particular composition, during heating and cooling cycles of pyroelectric measurements, will give the maximum pyroelectric coefficient. Next, a study of the temperature dependence of the dielectric constant at various fields, including the field that gave the maximum pyroelectric coefficient, was made to aid in the calculations of the figures of merit for each composition at a selected electric bias field. The figures of merit are dependent on the measuring temperature that is chosen and for the PMN-based ceramic compositions that we studied, the figures of merit also depend on the DC electric bias field applied to that composition. For 0.93 PMN-0.07 PT, at a mea-

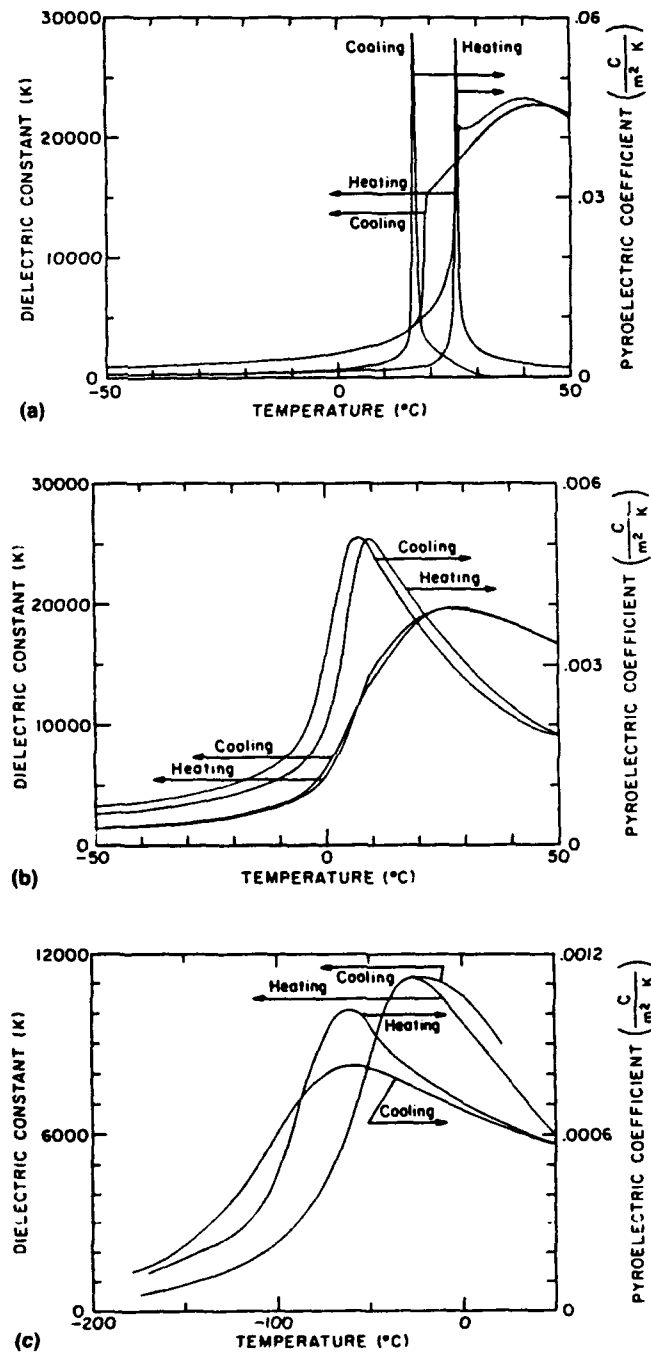


FIGURE 5 The pyroelectric and dielectric coefficients as a function of temperature, on heating and cooling cycles for (a) 0.90 PMN-0.10 PT under a 1.5 kV/cm DC electric bias field, (b) 0.93 PMN-0.07 PT under a 3.5 kV/cm DC electric bias field and (c) PMN with 1 mole % La under a 8.0 kV/cm DC electric bias field.

TABLE I  
Pyroelectric and dielectric results along with several figures of merit calculated at a maximum DC electric bias field on both a heating and cooling cycle

| Composition      | Maximum DC bias field (kV/cm) | Temp. direction (heating/cooling) | Dielectric data <sup>a</sup> |            |          |          | Pyroelectric data $\bar{a}$ |              |                               |                               | The figure of merit at $T_m$ and maximum DC bias field |                                     |  |
|------------------|-------------------------------|-----------------------------------|------------------------------|------------|----------|----------|-----------------------------|--------------|-------------------------------|-------------------------------|--|-------------------------------------|--|
|                  |                               |                                   | $T_m^b$ (°C)                 | $T_c$ (°C) | $K(T_c)$ | $K(T_m)$ | $\tan\delta(T_m)$           | $T_d^c$ (°C) | $p(T_m)$ (C/m <sup>2</sup> K) | $p(T_m)$ (C/m <sup>2</sup> K) | $p/K$ (μC/m <sup>2</sup> K)                            | $p/(K)^{1/2}$ (μC/m <sup>2</sup> K) | $p/(K \tan\delta)^{1/2}$ (μC/m <sup>2</sup> K) |
| 0.90 PMN-0.10 PT | 1.5                           | cooling                           | 10                           | 43.2       | 22733    | 3000     | 0.0169                      | 16.0         | 0.058                         | 0.0024                        | 0.800  | 43.8                                | 337.1  |
|                  | 1.5                           | heating                           | 10                           | 40.6       | 23189    | 3000     | 0.0205                      | 25.6         | 0.057                         | 0.0013                        | 0.433  | 23.7                                | 165.8  |
| 0.93 PMN-0.07 PT | 3.5                           | cooling                           | -1                           | 28.4       | 19719    | 5850     | 0.0356                      | 6.6          | 0.051                         | 0.0028                        | 0.479  | 36.6                                | 194.0  |
|                  | 3.5                           | heating                           | -1                           | 26.0       | 19673    | 5350     | 0.0294                      | 9.4          | 0.051                         | 0.0018                        | 0.336  | 24.6                                | 143.5  |
| PMN with 1% La   | 8.0                           | cooling                           | -50                          | -26.1      | 11207    | 8500     | 0.0097                      | -60.0        | 0.0008                        | 0.0008                        | 0.099  | 9.1                                 | 92.3   |
|                  | 8.0                           | heating                           | -50                          | -22.0      | 11352    | 8600     | 0.0100                      | -58.7        | 0.0010                        | 0.0010                        | 0.111  | 10.3                                | 103.0  |

<sup>a</sup> For the PMN-based ceramic material the dielectric data is measured at 100 Hz and for LiTaO<sub>3</sub> and TGS at 1 kHz.

<sup>b</sup>  $T_m$  is the temperature of measurement and for the PMN-based ceramic material  $T_m \leq T_c - 10^\circ\text{C}$ .

<sup>c</sup>  $T_d$  is the temperature which corresponds to the temperature where the pyroelectric coefficient is a maximum for the maximum DC bias field.

<sup>d</sup> Results of Putley<sup>11</sup> (1980) show LiTaO<sub>3</sub> at 25°C to have a  $K \sim 47$ ,  $p \sim 0.00023$  C/m<sup>2</sup> K and  $p/(K)^{1/2} \sim 34$  μC/m<sup>2</sup> K. These results also show TGS at 25°C to have a  $K \sim 30$ ,  $p \sim 0.00035$  C/m<sup>2</sup> K and  $p/(K)^{1/2} \sim 64$  μC/m<sup>2</sup> K.

measuring temperature of 5°C and a DC bias field of 3.5 kV/cm,  $p/(K)^{1/2} \sim 40 \mu\text{C}/\text{m}^2 \text{ K}$  and yet, for 0.90 PMN-0.10 PT, at a measuring temperature of 25°C and a DC bias field of 1.5 kV/cm,  $p/(K)^{1/2} \sim 210 \mu\text{C}/\text{m}^2 \text{ K}$ . These very large values of the figure of merit, comparable and in some cases superior to  $\text{LiTaO}_3$  ( $p/(K)^{1/2} \sim 34 \mu\text{C}/\text{m}^2 \text{ K}$ ) and TGS ( $p/(K)^{1/2} \sim 64 \mu\text{C}/\text{m}^2 \text{ K}$ ), two of the most widely used materials for pyroelectric point detectors, suggest some of these PMN-based ceramic compositions as promising candidates for pyroelectric point detectors. Chynoweth measurements, used to determine the dynamic pyroelectric response, are currently underway to see how these materials function under more practical conditions.

## REFERENCES

1. K. Uchino, *Am. Ceram. Soc. Bull.*, **65**, 647 (1986).
2. L. E. Cross in "Adaptive Structures" (edited by B. K. Wada) AD-15 (ASME, New York, 1989) p. 9.
3. S. W. Choi, T. R. Shrout, S. J. Jang and A. S. Bhalla, *Ferroelectrics*, **100**, 29 (1989).
4. Y. Tsuchiya, K. Uchino and S. Nomura, *Jap. J. Appl. Phys.*, **20**, 1841 (1981).
5. W. Y. Pan, W. Y. Gu, D. J. Taylor and L. E. Cross, *Jap. J. Appl. Phys.*, **28**, 653 (1989).
6. D. J. Taylor, D. Damjanovic, A. S. Bhalla and L. E. Cross, *J. Mater. Ltrs.*, accepted for publication (1991).
7. D. J. Taylor, D. Damjanovic, A. S. Bhalla and L. E. Cross, *Ferroelectric Ltrs.*, **11**, 1 (1990).
8. A. M. Glass, *J. Appl. Phys.*, **40**(12), 4699 (1969).
9. S. L. Swartz and T. R. Shrout, *Mater. Res. Bull.*, **17**, 1250 (1982).
10. R. L. Byer and C. B. Roundy, *Ferroelectrics*, **3**, 333 (1972).
11. E. H. Putley, *Infrared Phys.*, **20**, 149 (1980).

# **PROCESSING STUDIES**

## **APPENDIX 31**

# Chemical reactions of lead magnesium niobate titanate in the presence of a glass

V. Srikanth and E. C. Subbarao<sup>1)</sup>

Materials Research Laboratory, The Pennsylvania State University, University Park, Pennsylvania 16802

(Received 25 September 1990; accepted 7 February 1991)

A relaxor ferroelectric of composition  $0.93\text{Pb}(\text{Mg}_{1/3}\text{Nb}_{2/3})\text{O}_3-0.07\text{PbTiO}_3$  was sintered with 3 wt. % commercial sealing glass at 750 °C for 30 min to achieve  $\geq 95\%$  of theoretical density and a nearly pure perovskite phase. At higher glass additions (up to 20 wt. %), higher sintering temperatures (up to 800 °C), and longer sintering times (up to 4 h), the amount of perovskite (PMN type) decreases and that of pyrochlore ( $6\text{PbO} \cdot \text{MgO} \cdot 3\text{Nb}_2\text{O}_5$  or  $3\text{PbO} \cdot 2\text{Nb}_2\text{O}_5$ ) increases. On sintering at 800 °C for 4 h no perovskite phase is present in compositions with even 1% glass addition. The reaction of glass with the PMN phase was found to lead to the disappearance of the perovskite. Addition of 0.1 to 0.6 wt. % MgO to compositions containing 1 and 3 wt. % glass (and balance PMN-PT) results in essentially pure PMN perovskite phase on sintering at 700–800 °C for 30–240 min, confirming that the reaction of glass with PMN and depletion of MgO from PMN can be arrested. The sintered ceramics exhibit relaxor behavior and possess dielectric properties essentially commensurate with the phase composition.

## 1. INTRODUCTION

Lead magnesium niobate,  $\text{PbMg}_{1/3}\text{Nb}_{2/3}\text{O}_3$  (PMN), is a typical relaxor ferroelectric<sup>1</sup> in which the  $\text{Mg}^{2+}$  and  $\text{Nb}^{5+}$  ions are randomly distributed over the B sites of the  $\text{ABO}_3$  type perovskite lattice. The Curie temperature of PMN ( $\sim -15$  °C) can be raised to around 25 °C by forming a solid solution (0.93PMN-0.07PT) with lead titanate,  $\text{PbTiO}_3$  (PT), which is a well-known ordered ferroelectric with a Curie temperature of 490 °C involving a first order cubic to tetragonal phase transition.<sup>2</sup> The PMN-PT compositions exhibit larger electrostrictive strains and dielectric constants than other perovskites such as  $\text{BaTiO}_3$ <sup>3</sup> and lead zirconate titanate ceramics.<sup>4</sup> However, the full exploitation of these materials has been hampered due to the occurrence of a pyrochlore phase with a low dielectric constant ( $\sim 200$ ) during the synthesis of PMN and the loss of PbO at the high sintering temperatures ( $\sim 1300$  °C) required for achieving the necessary densification. The problems in the synthesis of PMN have been reviewed by Shrout and Halliyal.<sup>5</sup> The occurrence of the undesired pyrochlore phase can be minimized (or even eliminated) by a precursor route in which  $\text{MgNb}_2\text{O}_6$  of columbite structure is formed first, which then reacts with PbO to form PMN,<sup>6</sup> or by using ultrapure starting materials,<sup>7</sup> or by adding excess MgO (2–10%).<sup>8–10</sup> However, excess PbO and MgO lead to lowering and aging of dielectric properties of PMN.<sup>11,12</sup>

The high dielectric constant of PMN-type materials makes them good candidates as dielectrics for multilayer capacitors. The current multilayer capacitor manufacturing technology requires co-firing of the stack of dielectric and electrode layers at a sufficiently low temperature to permit the use of silver-rich or base metal electrodes. It is, therefore, important to lower the sintering temperature of PMN-type materials from the usual 950 °C for 4 h to 1300 °C for 0.5 h<sup>13</sup> to below 900 °C. By using fine particle material obtained by high energy milling, Papet *et al.*<sup>14</sup> have obtained  $\geq 95\%$  of theoretical density at a sintering temperature of 950–1050 °C for 2 h or by hot pressing at 825–890 °C for 2 h.

The sintering temperature of ferroelectric ceramics has been customarily reduced by liquid phase sintering.<sup>15</sup> In the case of PMN, lead germanate ( $\text{PbGe}_3\text{O}_{11}$ ),<sup>16</sup> excess PbO<sup>17–19</sup> or  $\text{LiNO}_3$ <sup>20</sup> has been used as sintering aids. Thus, Megherhi<sup>16</sup> has lowered the sintering temperature of 93PMN-7PT from 950 °C/4 h or 1050 °C/0.5 h to a range of 850° to 950 °C for 0.5 to 4 h with lead germanate (1–3 wt. %) as a sintering aid and achieved  $\geq 95\%$  of the theoretical density. With 6% excess PbO, a density of 90% of theoretical is achieved for 92.5PMN-7.5PT at 1000 °C for 6 h<sup>17</sup> and, with 1–2% excess PbO, Guha *et al.*<sup>18</sup> sintered 92PMN-8PT at 950 °C for 3 h to 97% of theoretical density. Addition of 2–4 mol %  $\text{LiNO}_3$  to 93PMN-7PT produced  $\sim 95\%$  of theoretical density of sintering at 850 °C for 30 min.<sup>20</sup>

The purpose of the present work is to lower further the sintering temperature of 93PMN-7PT ceramics to

<sup>1)</sup>Permanent address: Tata Research Development and Design Center, Pune, 411001, India.



800 °C or less by using a commercial sealing glass and to examine the development of phases and physical properties of the resulting ceramics.

## II. EXPERIMENTAL

The 93PMN-7PT power (Edo Corporation, Salt Lake City, UT) has the cubic perovskite type structure. The sintering aid was a sealing glass (Corning 7555, Corning Glass Works, Corning, NY) with the following stated characteristics: composition (wt. %) PbO (60–80), B<sub>2</sub>O<sub>3</sub> (10–30), SiO<sub>2</sub> (1–20), Al<sub>2</sub>O<sub>3</sub> (1–20), ZnO (1–20); density 5.7 g/cc; thermal expansion coefficient  $2 \times 10^{-7}/^{\circ}\text{C}$ ; softening temperature 415 °C; dielectric constant 13.7 at 25 °C and 1 kHz. Chemical analysis indicated this glass to be primarily a lead borate with small quantities of Al<sub>2</sub>O<sub>3</sub> and SiO<sub>2</sub>. Four compositions with 1, 3, 10, and 20 wt. % glass (the rest is PMN-PT) were prepared by mixing in plastic containers with zirconia media and ethyl alcohol for 24 h. The mixtures were dried at 80 °C for 24 h, mixed with 2% polyvinyl alcohol, and pressed into pellets at 105 MPa. After binder removal at 350 °C for 3 h at 550 °C for 3 h, the pellets were sintered at 700°, 750°, and 800 °C for 0.5 and 4 h. The heating rate was 5 °C/h and cooling rate 3 °C/h.

The densities were measured by the Archimedes water displacement method and grain sizes by scanning electron microscopy of fractured surfaces. The phase identification of the sintered samples was by x-ray diffraction with Cu K $\alpha$  radiation.

The dielectric constant and loss of sintered pellets with sputtered gold electrodes were measured on an automatic system consisting of a temperature control box (Model 2300, Delta Design, Inc., San Diego, CA)

and an LCR meter (Model 4274A and 4275A, Hewlett Packard, Inc., Palo Alto, CA) at a frequency of 0.1, 1, 10, and 100 kHz as the samples were cooled at the rate of 2 °C/min from 200 °C to –50 °C through the phase transition.

## III. RESULTS AND DISCUSSION

### A. Density and weight loss

The density and weight loss of all sintered samples are summarized in Table I. As expected, the density increases with sintering temperature (700° to 800 °C) in all cases, particularly between 700 °C and 750 °C [Fig. 1(a)]. Increasing the sintering time from 0.5 to 4 h at a fixed temperature had a relatively minor effect on density (Table I), suggesting that a short sintering time (0.5 h) is adequate. Of the compositions tried, those with 3 wt. % glass exhibited maximum densification (95–97% of theoretical) at 750° and 800 °C [Fig. 1(b)].

The weight loss was  $\leq 1\%$  when the glass content was  $\leq 10\%$  and sintering temperatures were 700° and 750 °C for 30 min (Table I). The same samples showed up to 1.3% weight loss at 800 °C for 30 min and up to 1.8% when the sintering time was increased to 4 h at 700° to 800 °C. The samples containing 20 wt. % glass exhibited weight losses up to 2% for sintering times of 30 min and up to 3.6% for 4 h at 700° to 800 °C. These weight loss values may be compared with 0.5 to 1.1% when 93PMN-7PT is sintered in PbO-rich atmosphere at 950° to 1250 °C for 0.5 h<sup>16</sup> and with 1 to 15.7% for compositions in the PbO–MgO–Nb<sub>2</sub>O<sub>5</sub> system at 980 °C for 4 h in oxygen, the weight loss in this case increasing with PbO content at fixed MgO content.<sup>21</sup>

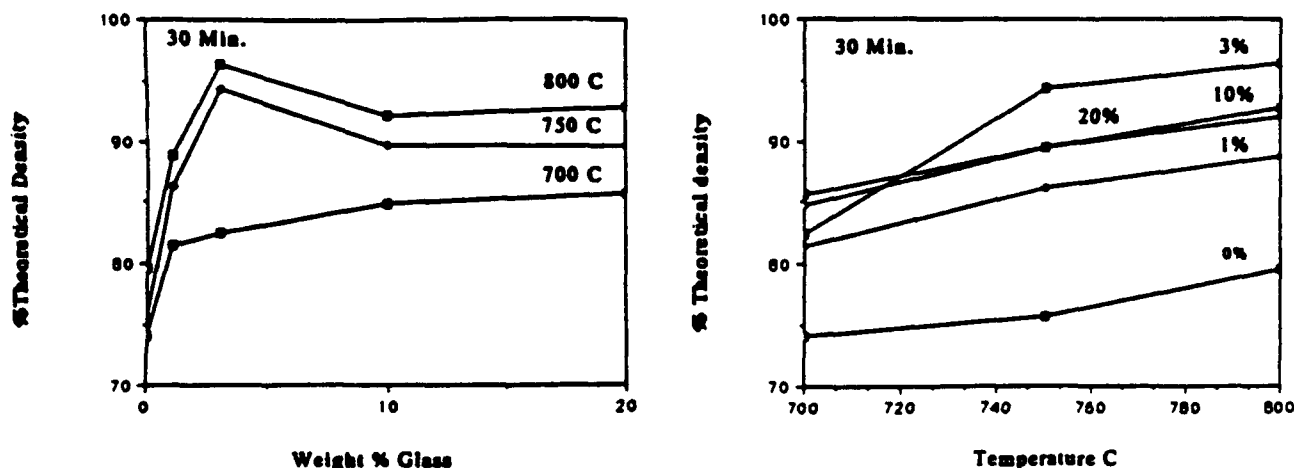


FIG. 1. Variation of density (% theoretical) with wt. % glass added (left) at 700, 750, and 800 °C for 30 min and with sintering temperature for 30 min; (right) for PMN-PT with 1, 3, 10, and 20 wt. % glass.

TABLE I. Properties of sintered 0.93PMN-0.07PT compositions.

|                             | Sintering temperature, °C |                   |                   |                   |                   |                   |
|-----------------------------|---------------------------|-------------------|-------------------|-------------------|-------------------|-------------------|
|                             | 700                       |                   | 750               |                   | 800               |                   |
|                             | 30 min                    | 240 min           | 30 min            | 240 min           | 30 min            | 240 min           |
| <b>0 wt. % glass</b>        |                           |                   |                   |                   |                   |                   |
| % theo. density             | 74.1                      | 78.2              | 76                | 81                | 80.3              | 84.6              |
| <b>1 wt. % glass</b>        |                           |                   |                   |                   |                   |                   |
| Density, g cm <sup>-3</sup> | 6.582(6.24)[6.17]         | 6.61(6.36)[6.23]  | 6.981(6.55)[6.43] | 6.996(6.63)[6.47] | 7.192(6.73)[6.54] | 7.262(6.79)[6.57] |
| % theo. density             | 81.4(78.2)[77.9]          | 81.7(79.8)[78.6]  | 86.3(82.1)[81.2]  | 86.6(83.1)[81.8]  | 88.9(84.3)[82.6]  | 89.7(85.1)[82.9]  |
| % perovskite                | 100                       | 80                | 96(100)[100]      | 100(99)[100]      | 100(100)[100]     | 0(100)[97]        |
| % wt. loss                  | 0.6                       | 0.9               | 0.6               | 0.9               | 0.7               | 1.0               |
| <b>3 wt. % glass</b>        |                           |                   |                   |                   |                   |                   |
| Density, g cm <sup>-3</sup> | 6.613(6.12)[5.97]         | 6.882(6.18)[6.03] | 7.611(6.54)[6.32] | 7.698(6.59)[6.37] | 7.823(6.79)[6.43] | 7.861(6.85)[6.47] |
| % theo. density             | 82.4(79.4)[78.6]          | 85.9(80.2)[79.4]  | 94.4(84.8)[83.2]  | 95.5(85.6)[83.9]  | 96.4(88.1)[84.6]  | 97.2(88.9)[85.1]  |
| % perovskite                | 100                       | 75                | 95(100)[100]      | 95(100)[100]      | 75(98)[100]       | 0(97)[100]        |
| % wt. loss                  | 0.8                       | 0.9               | 0.8               | 1.0               | 0.9               | 1.1               |
| <b>10 wt. % glass</b>       |                           |                   |                   |                   |                   |                   |
| Density, g cm <sup>-3</sup> | 6.614                     | 6.682             | 6.984             | 6.991             | 7.182             | 7.168             |
| % theo. density             | 84.4                      | 85.7              | 89.6              | 89.7              | 92.1              | 91.9              |
| % perovskite                | 80                        | 70                | 80                | 65                | 50                | 0                 |
| % wt. loss                  | 0.9                       | 1.1               | 1.0               | 1.7               | 1.3               | 1.8               |
| <b>20 wt. % glass</b>       |                           |                   |                   |                   |                   |                   |
| Density, g cm <sup>-3</sup> | 6.411                     | 6.481             | 6.712             | 6.819             | 6.946             | 6.912             |
| % theo. density             | 85.6                      | 86.5              | 89.6              | 92.0              | 92.7              | 92.2              |
| % perovskite                | 45                        | 35                | 50                | 60                | 40                | 0                 |
| % wt. loss                  | 1.4                       | 2.1               | 1.8               | 2.4               | 2.0               | 3.6               |

() Represents compositions in which 10% of the glass is replaced by MgO.

[] Represents compositions in which 20% of the glass is replaced by MgO.

## B. Phases

The x-ray diffraction patterns of the sintered samples showed the presence of a cubic perovskite type phase (PMN) or a pyrochlore type phase or a combination of the two. The amount (%) of the perovskite phase is estimated from the x-ray diffraction intensities of the (110) line of perovskite and that of the (222) line of pyrochlore as follows:

$$\% \text{ perovskite} = \frac{I_{(110)}}{I_{(110)} + I_{(222)}} \times 100$$

Nearly single phase perovskite (PMN) was obtained when samples with 1% glass were sintered at 700°, 750°, and 800 °C for 30 min and those with 3% glass sintered at 700° and 750 °C for 30 min (Table I). Samples with 10 and 20 wt. % glass sintered at 700°–800 °C for 30 min and those with 3% glass sintered at 800 °C for 30 min contained only 20–60% perovskite, the perovskite content generally decreasing with increase of sintering temperature for a given glass addition or with

increase in glass addition for a fixed sintering temperature (Table I). For a given glass addition and sintering temperature, the perovskite content almost always decreased when the sintering time was increased from 0.5 to 4 h (Table I). At all the sintering temperatures and times employed, the amount of the perovskite phase steadily decreased with increasing glass addition. A most remarkable feature was that the perovskite phase was absent in all samples with as little as 1% glass to as high as 20% glass when they were sintered at 800 °C for 4 h. This is clear from the x-ray patterns of a sample with 1% glass addition sintered at 800 °C for 30 min (only PMN phase is present) and for 4 h (PMN is absent) as well as one with 3% glass addition under the same sintering conditions, where the perovskite phase predominates for 0.5 h sintering and is absent for 4 h sintering (Fig. 2). Loss of PbO is known to decrease the perovskite content during the preparation of PMN. Provision of PbO atmosphere<sup>6</sup> or addition of extra PbO during milling<sup>14,15</sup> maximizes the perovskite content. When PbO-rich glass

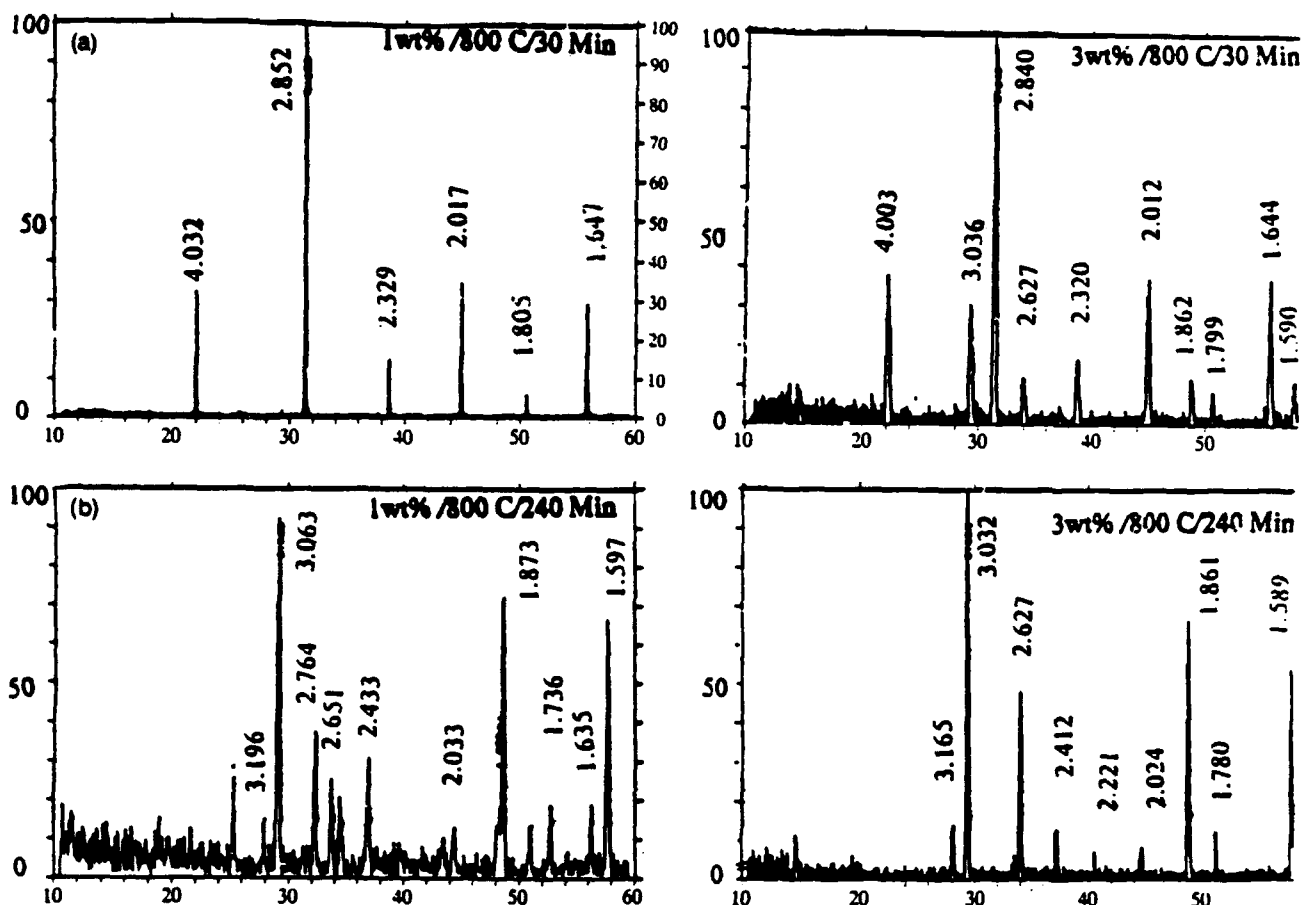
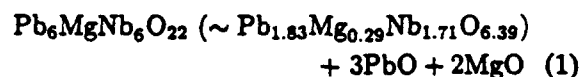


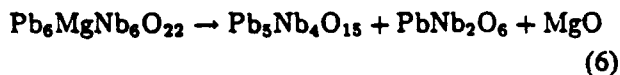
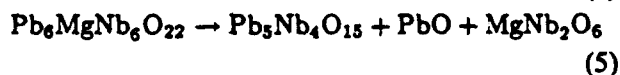
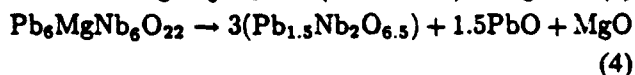
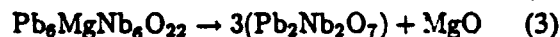
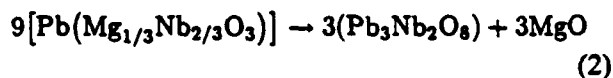
FIG. 2. X-ray diffraction patterns of PMN-PT with (a) 1 wt % glass and (b) 3 wt % glass, sintered at 800 °C. Note the predominance of the perovskite phase for a sintering time of 30 min (top) and the absence of perovskite phase for a sintering time of 4 h (bottom) for both compositions.

is used in the present work, the perovskite phase appears to be destabilized at very low (1%) glass additions and at relatively low temperatures (800 °C). This may be due to the gradual depletion of MgO from the PMN by some constituent such as B<sub>2</sub>O<sub>3</sub>, SiO<sub>2</sub>, or Al<sub>2</sub>O<sub>3</sub> in the sealing glass employed. It is known that when PMN becomes deficient in MgO, a cubic pyrochlore phase of approximate composition Pb<sub>1.83</sub>Mg<sub>0.29</sub>Nb<sub>1.71</sub>O<sub>6.39</sub> or Pb<sub>6</sub>MgNb<sub>6</sub>O<sub>22</sub> arises.<sup>22</sup> When MgO is completely depleted, one or more lead niobate phases may appear. Chen and Harmer<sup>23</sup> have shown that the increase of Nb<sub>2</sub>O<sub>5</sub> at the expense of MgO in the PbO–MgO–Nb<sub>2</sub>O<sub>5</sub> compositions increases the pyrochlore content steadily until the perovskite phase totally disappears. On the other hand, the addition of 2–10% excess MgO to PMN-based ceramics minimizes and even eliminates the formation of the pyrochlore phase.<sup>8–10</sup>

The possible reactions in the PbO–MgO–Nb<sub>2</sub>O<sub>5</sub> system in the vicinity of the PMN phase may be depicted as follows:



or



These reactions involve PMN (cubic perovskite with  $a = 0.4049$  nm), Pb<sub>1.83</sub>Mg<sub>0.29</sub>Nb<sub>1.71</sub>O<sub>6.39</sub> or Pb<sub>6</sub>MgNb<sub>6</sub>O<sub>22</sub> (cubic pyrochlore with  $a \approx 1.060$  nm),<sup>22</sup> and five lead niobate phases in order of increasing PbO content: PbO·Nb<sub>2</sub>O<sub>5</sub> (tetragonal and rhombohedral); 3PbO·2Nb<sub>2</sub>O<sub>5</sub> (or Pb<sub>3</sub>Nb<sub>4</sub>O<sub>13</sub> or Pb<sub>1.5</sub>Nb<sub>2</sub>O<sub>6.5</sub>), which

TABLE II. Phases in sintered samples.

| Sintering<br>Temp. (°C)        | 1% glass   |                                | 3% glass  |   | 10% glass                      |   | 20% glass                      |                                       |
|--------------------------------|--|--------------------------------|---|---|--------------------------------|---|--------------------------------|---------------------------------------|
|                                | Major  | Minor                          | Major   | Minor                                     | Major                          | Minor   | Major                          | Minor                                 |
| <u>Sintering time: 30 min</u>  |  |                                |   |   |                                |   |                                |                                       |
| 700                            | PMN  |                                | PMN   |   | PMN                            | P <sub>6</sub> MN <sub>3</sub>                                      | P <sub>3</sub> N <sub>2</sub>  | PMN<br>P <sub>6</sub> MN <sub>3</sub> |
| 750                            | PMN<br>(PMN)<br>[PMN]                            | Py (tr)                        | PMN<br>(PMN)<br>[PMN]   | Py (tr)                                   | PMN                            | P <sub>3</sub> N <sub>2</sub>                                       | P <sub>6</sub> MN <sub>3</sub> | PMN<br>P <sub>3</sub> N <sub>2</sub>  |
| 800                            | PMN<br>(PMN)<br>[PMN]                            | Py(tr)                         | PMN<br>(PMN)<br>[PMN]   | P <sub>3</sub> N <sub>2</sub><br>(Py(tr)) | PMN                            | P <sub>3</sub> N <sub>2</sub><br>P <sub>6</sub> MN <sub>3</sub>     | P <sub>6</sub> MN <sub>3</sub> | PMN                                   |
| <u>Sintering time: 240 min</u> |  |                                |   |   |                                |   |                                |                                       |
| 700                            | PMN  | P <sub>6</sub> MN <sub>3</sub> | PMN   | P <sub>6</sub> MN <sub>3</sub>            | PMN                            | P <sub>6</sub> MN <sub>3</sub><br>P <sub>3</sub> N <sub>2</sub> (?) | P <sub>3</sub> N <sub>2</sub>  | PMN<br>P <sub>6</sub> MN <sub>3</sub> |
| 750                            | PMN<br>(PMN)<br>[PMN]                            | Py(tr)                         | PMN<br>(PMN)<br>[PMN] <sup>a</sup>                            | P <sub>6</sub> MN <sub>3</sub>            | PMN                            | P <sub>6</sub> MN <sub>3</sub><br>P <sub>3</sub> N <sub>2</sub> (?) | PMN                            | P <sub>6</sub> MN <sub>3</sub>        |
| 800                            | P <sub>6</sub> MN <sub>3</sub><br>(PMN)<br>[PMN] | Unknown<br>[Py(tr)]            | P <sub>6</sub> MN <sub>3</sub><br>(PMN)<br>[PMN] <sup>a</sup> | Unknown<br>(Py(tr))                       | P <sub>6</sub> MN <sub>3</sub> |   | P <sub>6</sub> MN <sub>3</sub> |                                       |

P = PbO; M = MgO; N = Nb<sub>2</sub>O<sub>5</sub>; Py = pyrochlore.

() Refers to compositions with 10% of the glass replaced by MgO.

[] Refers to compositions with 20% of the glass replaced by MgO.

<sup>a</sup> Represents splitting of the perovskite lines.

is a cubic oxygen-deficient pyrochlore with  $a = 1.056$  nm;  $2\text{PbO} \cdot \text{Nb}_2\text{O}_5$  (or  $\text{Pb}_2\text{Nb}_2\text{O}_7$ ), which is a distorted pyrochlore of monoclinic symmetry with  $a = 1.3021$ ,  $b = 0.7483$ ,  $c = 3.4634$  nm, and  $\beta = 125.3^\circ$ ;  $5\text{PbO} \cdot 2\text{Nb}_2\text{O}_5$  or  $\text{Pb}_5\text{Nb}_4\text{O}_{15}$ , which is monoclinic with  $a = 1.22948$ ,  $b = 0.7419$ ,  $c = 3.3614$  nm, and  $\beta = 108^\circ 66'$ ;  $3\text{PbO} \cdot \text{Nb}_2\text{O}_5$  or  $\text{Pb}_3\text{Nb}_2\text{O}_8$ , which is a distorted pyrochlore of tetragonal symmetry with  $a = 0.7536$  and  $c = 1.0829$  nm. It may be noted that four of these lead niobates ( $\text{PbO}:\text{Nb}_2\text{O}_5 = 3:2$ ,  $2:1$ ,  $5:2$ , and  $3:1$ ) are cubic or distorted pyrochlores with increasing PbO content. Thus, any one or more of these lead niobates may be formed, depending upon the availability of PbO and the kinetics of formation.

In the present work, PMN was found to be the predominant ( $\geq 50\%$ ) phase when the glass addition was  $\leq 10$  wt. % and sintering temperatures were  $700^\circ\text{--}800^\circ\text{C}$  for 30 min, while the pyrochlore phase dominates with a glass addition of 20 wt. % under the same sintering conditions. When the sintering time is increased to 4 h, PMN is the major phase for glass additions of  $\leq 10$  wt. % and sintering temperatures of 700 and  $750^\circ\text{C}$  with pyrochlore phases dominating for glass

additions of  $\leq 10$  wt. % at  $800^\circ\text{C}$  and for glass additions of 20 wt. % at  $700^\circ\text{--}800^\circ\text{C}$  (Table II). The effect of sintering temperature ( $700^\circ$ ,  $750^\circ$ , and  $800^\circ\text{C}$ ) and sintering time (30 and 240 min) on the gradual disappearance of the perovskite phase in the sample with 3 wt. % glass addition is shown in Fig. 3. The presence of the pyrochlore phase as the predominant phase with some diffraction lines unaccounted for in all samples sintered at  $800^\circ\text{C}$  for 4 h is shown in Figs. 4, 2(b), and 2(d). It is noteworthy that PbO, MgO, and  $\text{MgNb}_2\text{O}_6$  are not detected in any of the samples. Wang and Schulze<sup>10</sup> have detected MgO inside grains and in the intergranular regions in SEM backscattered images of PMN-5% MgO samples. No clear evidence for the noncubic pyrochlore lead niobate phases is available in the x-ray patterns.

It may be recalled that the weight loss in most cases was  $\leq 1\%$  and only in an extreme case it was 3.6%. Therefore, the reaction products must be as per Eqs. (1)–(6). If some compounds are not found, then the corresponding reaction products must be below the limit of detection by x-ray diffraction ( $\sim 2\%$ ) if they are crystalline or, alternately, must be present in an amorphous state. Thus, on sintering PMN-PT with  $\leq 10$  wt. %

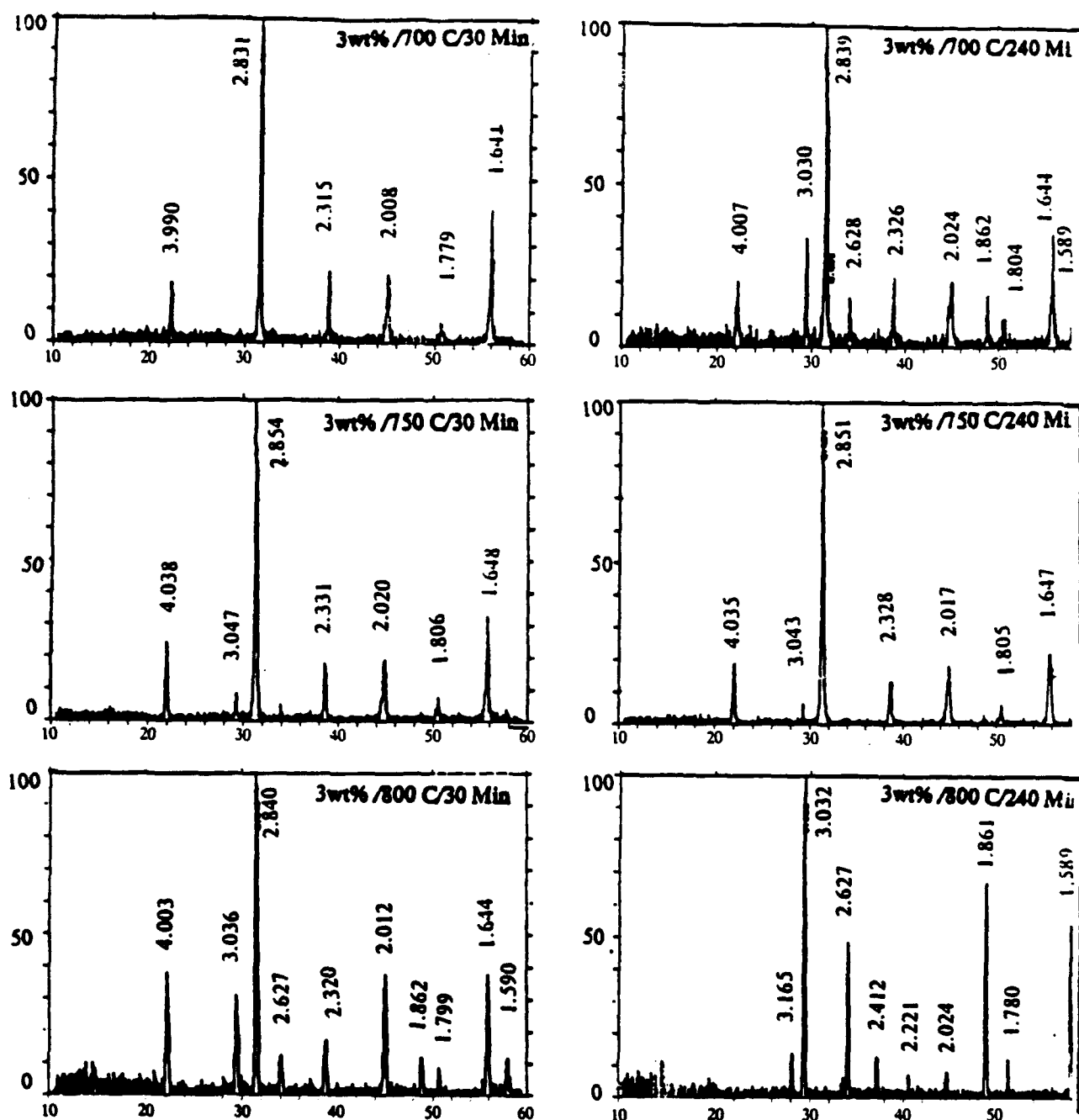


FIG. 3. X-ray diffraction patterns of PMN-PT with 3 wt.% glass sintered at 700, 750, and 800 °C for 30 min and 4 h, as marked. Note the gradual disappearance of the perovskite phase with increasing sintering temperature and sintering time.

glass addition at 700° and 750 °C for 30 min, reaction (1) with  $P_6MN_3$  as the predominant phase occurs. Under other conditions employed in the present study, reaction (4) also takes place with  $P_3N_2$  as the major phase. No clear x-ray evidence could be found for reactions (2), (3), (5), and (6), involving  $3PbO \cdot Nb_2O_5$ ,  $5PbO \cdot 2Nb_2O_5$ ,  $2PbO \cdot Nb_2O_5$ ,  $PbO \cdot Nb_2O_5$ , and  $MgNb_2O_6$  as reaction products. The other reaction products of Eqs. (1)

and (4), namely  $PbO$  and  $MgO$ , also could not be detected in the x-ray patterns. It is assumed that these oxides combine with the constituents of sealing glass ( $PbO$ ,  $SiO_2$ ,  $B_2O_3$ ,  $Al_2O_3$ ) to form a glassy phase.

The present study which involves reaction of preformed PMN-PT with a  $PbO$ -rich glass cannot be directly compared with the earlier studies of reaction sequence in the synthesis of PMN from the constituent

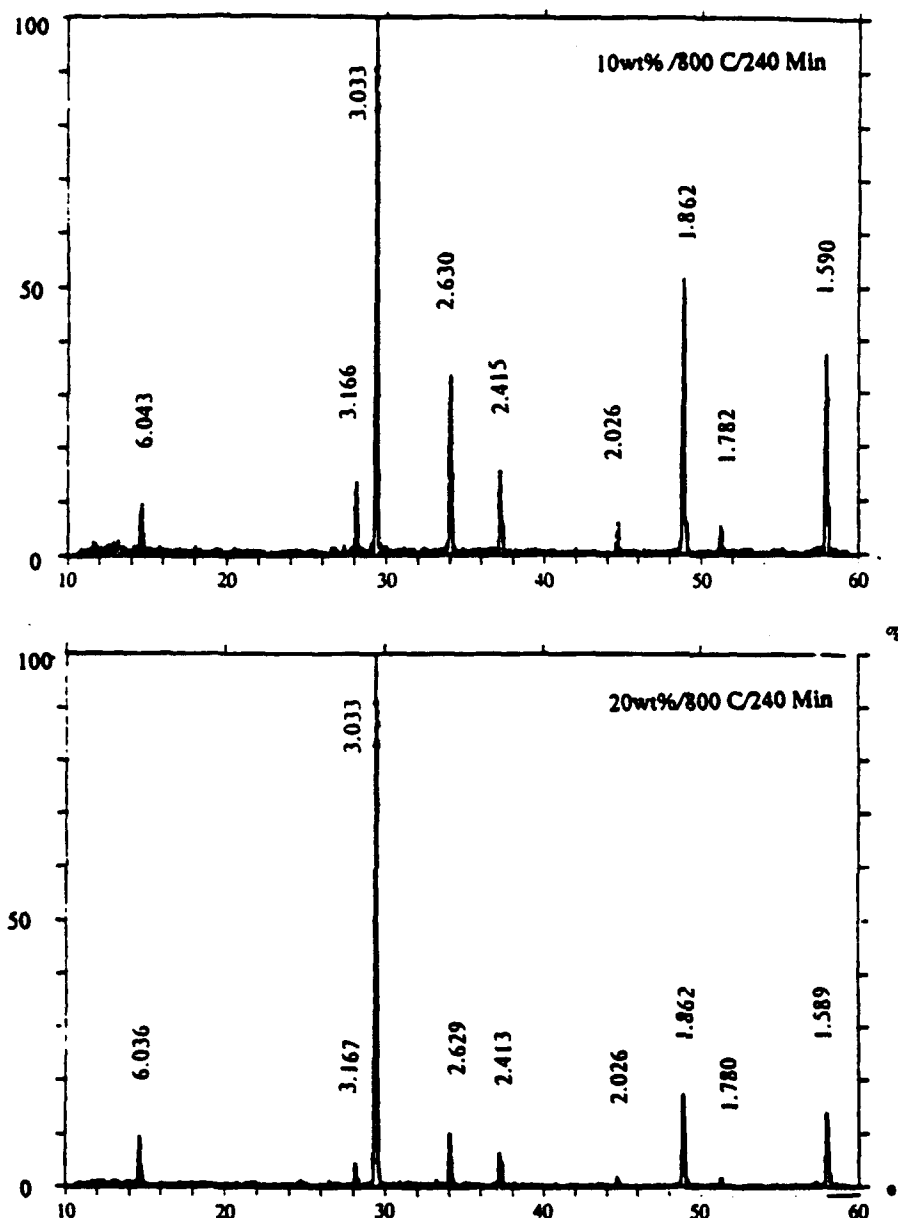


FIG. 4. X-ray diffraction patterns of PMN-PT with 10 (top) and 20 wt. % glass (bottom) sintered at 800 °C for 4 h. Note the predominance of the pyrochlore phase.

oxides ( $\text{PbO}$ ,  $\text{MgO}$ , and  $\text{Nb}_2\text{O}_5$ ).<sup>5,25</sup> The question that can, however, be asked is: When 1 to 6 wt. % excess  $\text{PbO}$  is found to be beneficial in obtaining nearly pure PMN phase (with near absence of the pyrochlore phase), why is the result different in the present case when 1–20 wt. %  $\text{PbO}$ -rich glass is added? The relatively poor stability of lead-based perovskites such as PMN and the greater stability of the lead-based compounds with defect pyrochlore structure has been discussed by Shrout and Halliyal.<sup>5</sup> The greater affinity between  $\text{PbO}$  and  $\text{Nb}_2\text{O}_5$  than between  $\text{PbO}$  and  $\text{MgO}$  leads to easy decomposition of perovskite PMN into cubic pyrochlore  $\text{P}_6\text{MN}_3$  or

$\text{P}_3\text{N}_2$ , particularly in the presence of some species which can dissolve or react with  $\text{MgO}$  easily, such as some of the constituents in the sealing glass. This undesirable development of the pyrochlore phase can be avoided by using minimal (1–3%) glass addition and sintering at 750 °C to achieve  $\geq 95\%$  of theoretical density and nearly pure PMN phase. This may be compared with a sintering temperature of 900 °C for 6 h when 4–6 wt. %  $\text{PbO}$  is used as a sintering aid for PMN to achieve the same end product<sup>26</sup> and the sintering of PMN-7.5PT with 6 wt. % excess  $\text{PbO}$  at 1000 °C to obtain 90% of theoretical density.<sup>17</sup>

TABLE III. Selected diffraction lines in sintered sample.

| Wt. %<br>glass | 700 °C           |                  | 750 °C           |                  | 800 °C                     |               | Diffraction line                             |
|----------------|------------------|------------------|------------------|------------------|----------------------------|---------------|--|
|                | 30 min           | 240 min          | 30 min           | 240 min          | 30 min                     | 240 min       |  |
| 0              | 0.2852           |                  |                  |                  |                            |               | Perovskite (110), nm                         |
| 1              | 0.2847           | 0.2851<br>0.3046 | 0.2843<br>0.3041 | 0.2871<br>...    | 0.2852<br>0.3046           | ...<br>0.3062 | Perovskite (110), nm<br>Pyrochlore (222), nm |
| 3              | 0.2831           | 0.2839<br>0.3030 | 0.2854<br>0.3047 | 0.2851<br>0.3043 | 0.2840<br>0.3036           | ...<br>0.3032 | Perovskite (110), nm<br>Pyrochlore (222), nm |
| 10             | 0.2862<br>0.3056 | 0.2850<br>0.3040 | 0.2852<br>0.3043 | 0.2854<br>0.3046 | 0.2834<br>0.3027<br>0.3044 | ...<br>0.3033 | Perovskite (110), nm<br>Pyrochlore (222), nm |
| 20             | 0.2842<br>0.3032 | 0.2848<br>0.3033 | 0.2833<br>0.3023 | 0.2867<br>0.3063 | 0.2835<br>0.3027           | ...<br>0.3033 | Perovskite (110), nm<br>Pyrochlore (222), nm |

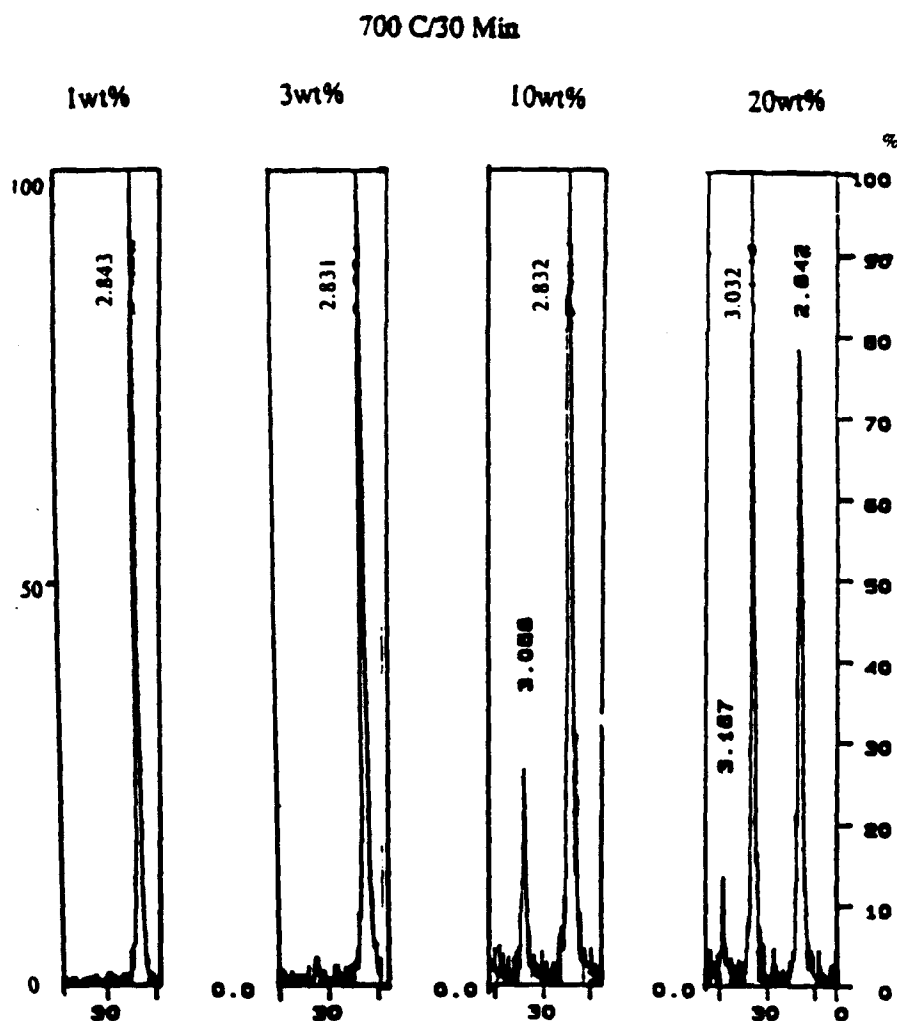


FIG. 5. Portion of the x-ray diffraction patterns of PMN-PT with (a) 1, (b) 3, (c) 10, and (d) 20 wt. % glass, at 700 °C for 30 min. Note the shift of the (110) line of perovskite at ~0.28 nm and the (222) line of pyrochlore at ~0.31 nm, with composition.

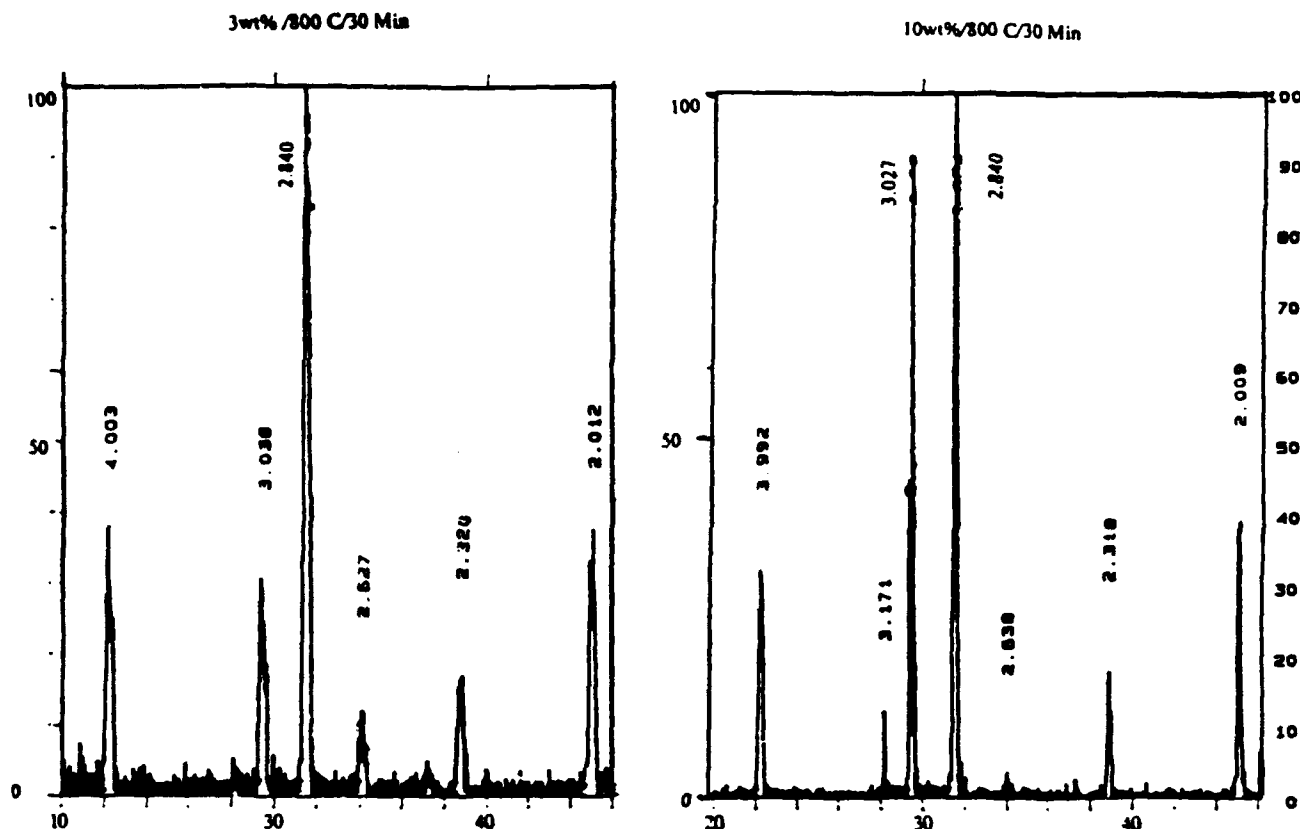


FIG. 6. The splitting of x-ray diffraction lines is illustrated by PMN-PT with 3 wt. % and 10 wt. % glass, sintered at 800 °C for 30 min.

The (110) peak of the perovskite (PMN) phase occurs at  $0.2847 \pm 0.0004$  ( $a = 0.4026$ ) nm for most of the sintered samples, though values as low as 0.2834 ( $a = 0.4007$ ) nm and as high as 0.2871 ( $a = 0.4060$ ) nm have also been observed (Table III) in some cases. These variations may indicate that the composition of PMN may accommodate some range of Mg/Nb ratio as well as excess PbO.<sup>11</sup> The most common pyrochlore phase encountered in this work is  $P_6\text{MN}_3$  ( $P = \text{PbO}$ ,  $M = \text{MgO}$ ,  $N = \text{Nb}_2\text{O}_5$ ), which is cubic with  $a = 1.060$  nm, followed by  $P_3\text{N}_2$  which is also cubic with a slightly smaller cell edge ( $a = 1.056$  nm). It is therefore difficult to distinguish between these two cubic pyrochlores, though the intensities of some of the diffraction lines differ significantly. The lattice parameter and relative intensities were the basis for the phases indicated in Table II. Guha and Anderson<sup>24</sup> have reported solid solution between the two cubic pyrochlores ( $P_6\text{MN}_3$  and  $P_3\text{N}_2$ ). The x-ray patterns of samples with 1 to 20 wt. % glass addition sintered at 700 °C for 30 min, shown in Fig. 5, clearly demonstrate the shift of the perovskite and pyrochlore lines with the amount of glass added (see Table II also). The splitting of the lines corresponding to the perovskite and the pyrochlore phases in samples with 3 and 10 wt. % glass addition sintered at 800 °C

for 30 min is illustrated in Fig. 6.

Another important observation during the present work concerns the anomalous variations in the x-ray diffraction intensities of the perovskite (110) and pyrochlore (222) lines as well as the sum of the intensity of these two lines as a function of the amount of glass addition, sintering temperature, and time (Fig. 7). The data for 30 min and 240 min are plotted separately. There is a steep decrease in the  $I_{\text{perov}}$  as the glass content is increased from 1 to 3 wt. % at 700°, 750°, and 800 °C for 30 min. This is not accompanied by a corresponding increase in  $I_{\text{pyro}}$  or  $I_{\text{total}}$ . This may mean the perovskite PMN significantly reacts with the sealing glass without forming any new crystalline phase. There is only a small gradual decrease in  $I_{\text{perov}}$  and a corresponding increase in  $I_{\text{pyro}}$  as the glass content is increased from 3 to 20 wt. % at 700° and 750 °C for 30 min. This leaves  $I_{\text{total}}$  nearly unaffected in these cases. However, at 800 °C for 30 min, there is an increase in  $I_{\text{perov}}$  between 3 and 10 wt. % glass and a decrease between 10 and 20 wt. % glass. Under the same conditions,  $I_{\text{pyro}}$  increases steeply between 3 and 10 wt. % glass and less steeply between 10 and 20 wt. % glass. As a consequence, there is a steep increase, followed by a slight decrease, in  $I_{\text{total}}$  as the glass content in-

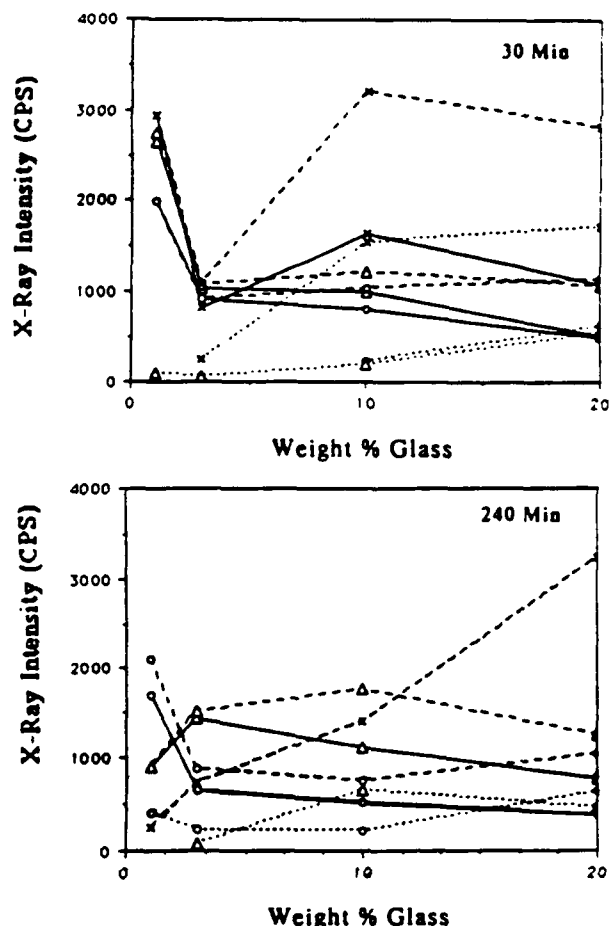


creased from 3 to 10 and 10 to 20 wt. %, respectively. Thus, at 700° and 750 °C, part of the PMN is transformed into a pyrochlore phase. At 800 °C, some of the amorphous phase which had already been formed by reaction of PMN with the sealing glass crystallizes as a pyrochlore phase. The behavior of  $I_{\text{perov}}$  on sintering for 240 min is generally similar to that for 30 min, except that  $I_{\text{perov}} = 0$  for all compositions sintered at 800 °C for 240 min and  $I_{\text{pyro}}$  increases steeply with increasing glass addition, under these conditions. Further, for a given glass addition sintered at 700° to 750 °C, there is a general decrease in  $I_{\text{perov}}$ , while  $I_{\text{pyro}}$  remains unchanged or increases somewhat as the sintering time is increased from 30 to 240 min. At the same time, for all glass additions sintered at 800 °C,  $I_{\text{perov}}$  drops to zero and  $I_{\text{pyro}}$  increases steeply as the sintering time is increased from 30 to 240 min. This clearly indicates that the pyrochlore phase crystallizes from the amorphous mass at 800 °C and the amount of crystallized pyrochlore increases with time, as expected.

### C. Testing of the hypothesis

The above results clearly indicate that the sealing glass employed here reacts with PMN-PT at as low a concentration of glass as 1% and as mild sintering conditions as 700 °C/4 h or 750 °C/30 min (Table I) to give rise to the undesirable pyrochlore phase. This is attributed to the depletion of MgO from PMN and possible enriching the glass in MgO. In order to test the above hypothesis, a set of samples were prepared using the same PMN-PT and sealing glass as before, except that 10 and 20 wt. % of the glass is replaced by MgO. The original compositions with 1 and 3 wt. % glass and the corresponding modified compositions are given in Table IV. Thus, 0.1 to 0.6 wt. % excess MgO was added to the overall batch composition before calcination and processed in the same manner as the original samples, including sintering at 700, 750, and 800 °C for 30 and 240 min.

The results of these experiments are also included in Tables I and II. The sintered densities decreased with increasing MgO addition under the same sintering conditions. The trend of densification with % glass and sintering conditions is the same with and without MgO addition. The most significant result is the near absence (0–3%) of the pyrochlore phase when 0.1 to 0.6 wt. % MgO was added to the batch compositions. This is brought out clearly in Fig. 8, illustrating the x-ray diffraction patterns of four compositions sintered at 800 °C for 4 h, which may be compared with the x-ray patterns [Figs. 2(b) and 2(d)] of the same compositions without the MgO addition sintered under the same conditions. This conclusively establishes that the provision



|       | Pyrochlore (222) | Perovskite (110) | Total   |
|-------|------------------|------------------|---------|
| 700 C | .....○.....      | ——○——            | ---○--- |
| 750 C | .....△.....      | ——△——            | ---△--- |
| 800 C | .....×.....      | ——×——            | ---×--- |

FIG. 7. X-ray diffraction intensities of (110) line of perovskite, (220) line of pyrochlore, and the sum of these two as a function of glass addition at different sintering temperatures (700, 750, and 800 °C) for sintering times of 30 min (top) and 4 h (bottom).

of an alternate source of MgO prevents the depletion of MgO from PMN by reaction with glass and thereby retains the perovskite form of PMN intact. It is also remarkable how little (0.1%) MgO addition is necessary to maintain the perovskite PMN phase.

Two further observations may be made regarding the x-ray diffraction data: one concerns the large increase in  $I_{110}$  of perovskite when MgO is added (Fig. 9), suggesting that the reaction between PMN-PT and glass (and consequent decomposition of PMN) is drastically decreased by the addition of MgO into the batch composition. The second observation concerns the splitting of the perovskite diffraction lines when 0.6 wt. % MgO

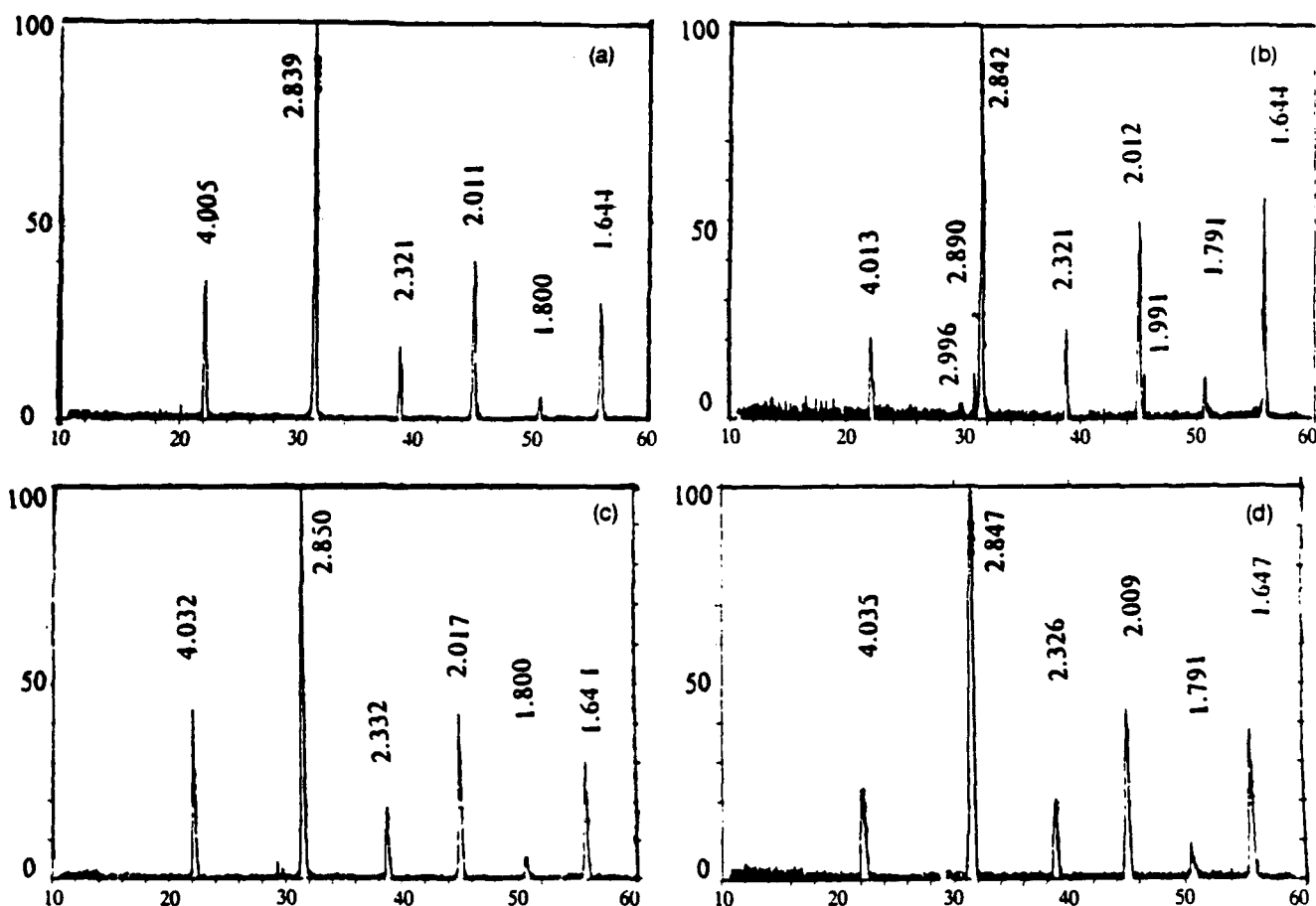


FIG. 8. X-ray diffraction patterns of compositions sintered at 800 °C for 4 h. (a) 99PMN-PT, 0.9 glass, 0.1MgO; (b) 99PMN-PT, 0.8 glass, 0.2MgO; (c) 97PMN-PT, 2.7 glass, 0.3MgO; and (d) 97PMN-PT, 2.4 glass, 0.6MgO. Note the near absence of pyrochlore phase. Compare with Figs. 2(b) and 2(d).

TABLE IV. Original and modified compositions (wt. %).

|        | Original | Modified |     |
|--------|----------|----------|-----|
|        |          | (1)      | (2) |
| PMN-PT | 99       | 99       | 99  |
| Glass  | 1        | 0.9      | 0.8 |
| MgO    |          | 0.1      | 0.2 |
| PMN-PT | 97       | 97       | 97  |
| Glass  | 3        | 2.7      | 2.4 |
| MgO    |          | 0.3      | 0.6 |

In (1) and (2), 10 and 20% of glass is replaced by MgO, respectively.

is added to the batch (Fig. 10). The intensity of the split lines (e.g., 110) is nearly half of that when no splitting takes place, suggesting the possible coexistence of two perovskite PMN phases with slightly different lattice parameters (and compositions). No MgO could be detected in the x-ray patterns.

#### D. Microstructure

The scanning micrographs of PMN-PT samples sintered at 750 °C for 30 min with 1, 3, 10, and 20 wt. % glass addition are shown in Fig. 11. The samples with 1 and 3 wt. % glass show a more or less uniform microstructure with an average grain size of about 3  $\mu\text{m}$ , while the samples with 10 and 20 wt. % glass show a bimodal distribution of grain sizes with the larger size (about 5  $\mu\text{m}$ ) being 2–3 times the smaller grains. The effect of sintering temperature (700° and 800 °C) and time (30 and 240 min) on the microstructure of a sample with 3 wt. % glass addition, illustrated in Fig. 12, indicates that the grains become more rounded as the sintering temperature is increased from 700° to 800 °C for 30 min or when sintering time is increased from 30 to 240 min at 700 °C and more particularly at 800 °C. In fact, the original crystallite shapes seen in the sample sintered at 700 °C for 30 min are nearly obliterated in the sample sintered at 800 °C for 240 min. Raising the sintering temperature from 700° to 800 °C is more effective than

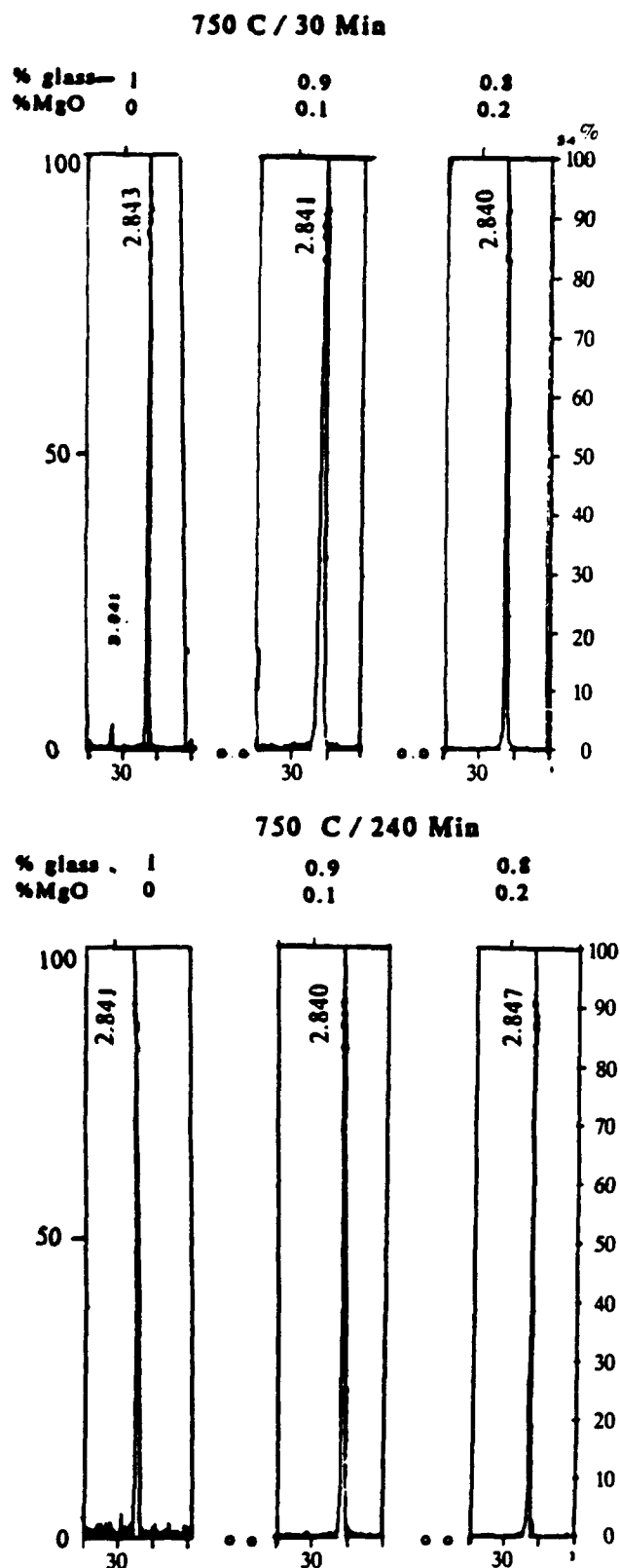


FIG. 9. X-ray diffraction intensity of (110) of perovskite PMN-PT for compositions sintered at 750 °C for 30 and 240 min as a function of MgO addition (0, 10, and 20% of glass).

increasing the sintering time at 700 °C from 30 min to 240 min in rounding the grain shapes. An enlarged view of the sample with 20 wt. % glass addition, sintered at 750 °C for 30 min [shown in Fig. 11(d)], displays grains with octahedral morphology (Fig. 13), which were identified by Chen and Harmer<sup>23</sup> as pyrochlore. The presence of an amorphous or glassy phase facilitates the development of the octahedral morphology.

#### E. Dielectric properties

All the samples, irrespective of the perovskite content, show relaxor type dielectric behavior, as shown in Fig. 14 for samples with 3 (sintered at 700 °C for 30 min) and 20 (sintered at 750 °C for 30 min) wt. % glass. The peak dielectric constant increases with glass additions up to 3 wt. % and decreases at higher glass contents. This is clearly related to the amount of the perovskite phase present, since both the pyrochlore and the amorphous phases have low dielectric constants. Since many samples in the present study were diphasic, no detailed study of dielectric properties was undertaken.

#### IV. CONCLUSIONS

(1) The relaxor ferroelectric composition 0.93PMN-0.07PT can be sintered to  $\geq 95\%$  of theoretical density and with nearly pure perovskite phase at 750°–800 °C for 30 min by adding 3 wt. % of commercial sealing glass.

(2) The amount of the perovskite phase decreases and that of the pyrochlore phase increases with increasing glass content (up to 20 wt. %), sintering temperature (up to 800 °C), and time (up to 4 h). The perovskite phase is absent in all samples sintered at 800 °C for 4 h, even with the addition of 1 wt. % glass.

(3) The important role that depletion of MgO from PMN plays in destabilization of PMN is clear. The presence of a second phase (crystalline or glassy) which can accommodate MgO contributes to the instability of PMN.

(4) The addition of 0.1 to 0.6 wt. % MgO to the batch compositions originally containing 1 and 3 wt. % glass results in a pure perovskite phase, when the samples are sintered at 700–800 °C for 30 to 240 min.

(5) The grain size remains nearly constant at 3  $\mu\text{m}$  in the range of glass addition and sintering conditions employed. The microstructure reveals rounding of the grains due to reactions between the crystalline and glassy phases. The distinct octahedral morphology of the pyrochlore particles crystallizing from the liquid phase is noted.

(6) Relaxor behavior is exhibited by all the samples. The dielectric constant is dictated primarily by the amount of the perovskite phase.

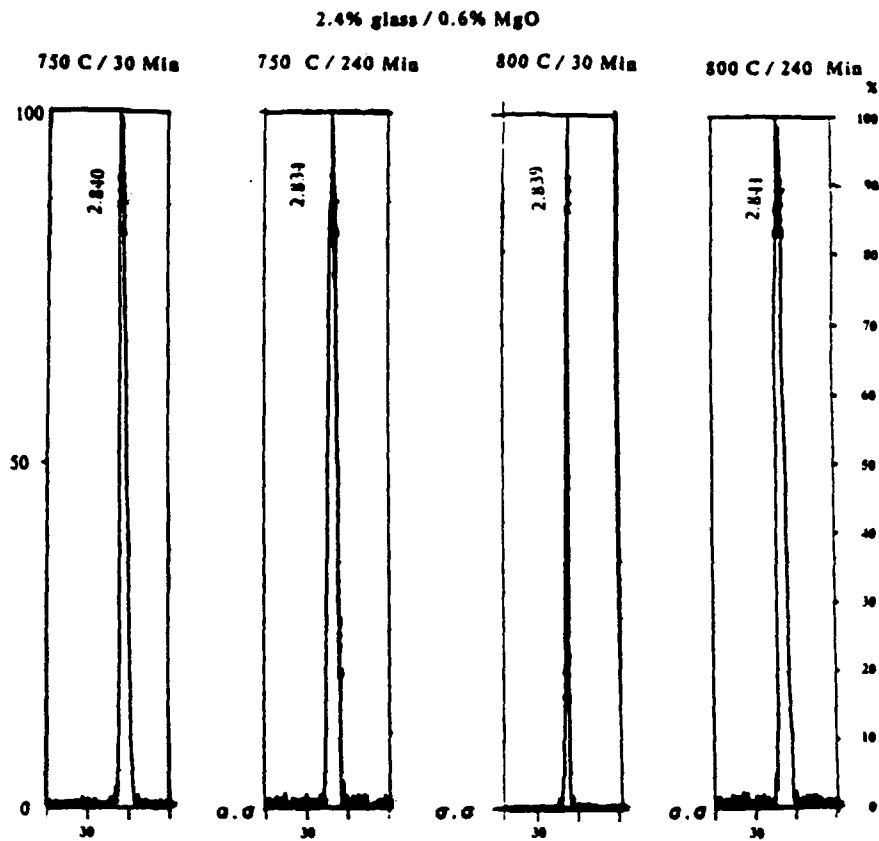
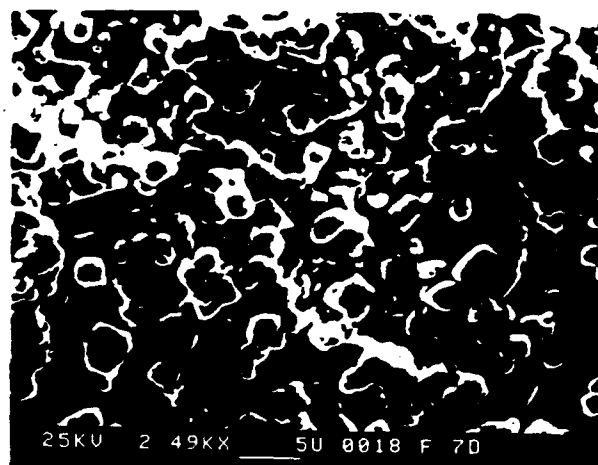
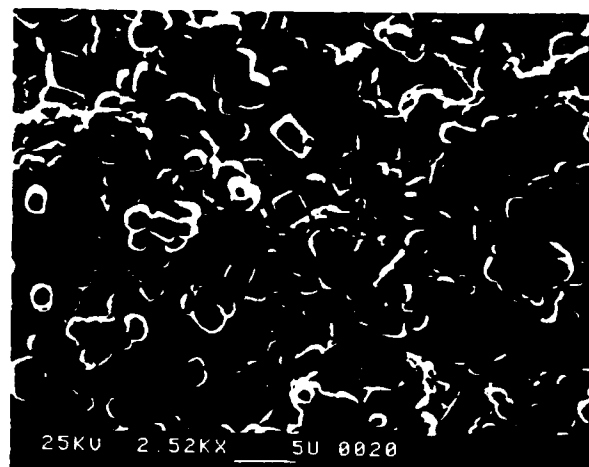


FIG. 10. Note the splitting of the (110) diffraction line of perovskite PMN-PT compositions with 0.6 wt. % MgO, sintered at 750 and 800 °C.

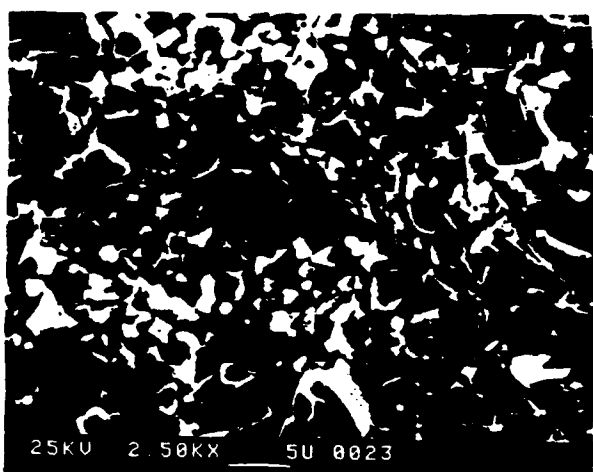
750 °C / 30 min



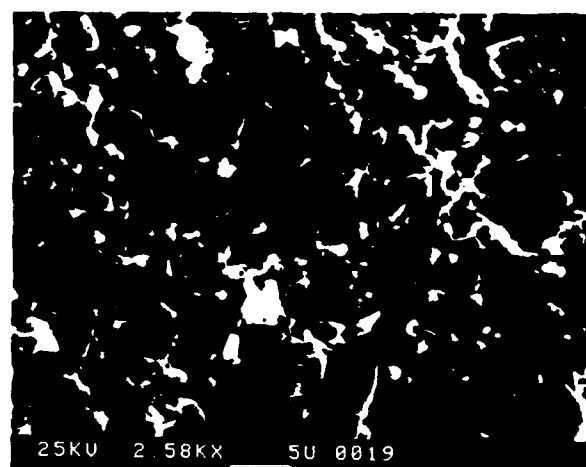
(a)



(b)



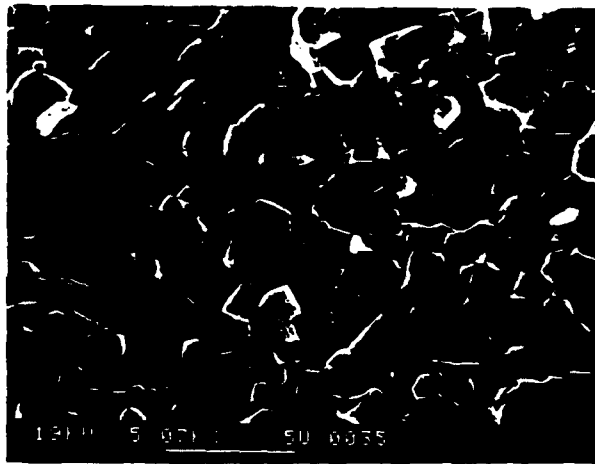
(c)



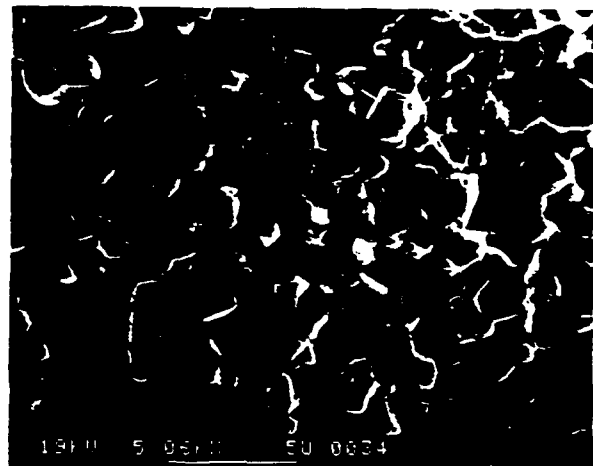
(d)

FIG. 11. Scanning electron micrographs of PMN-PT with (a) 1, (b) 3, (c) 10, and (d) 20 wt. % glass, sintered at 750 °C for 30 min.

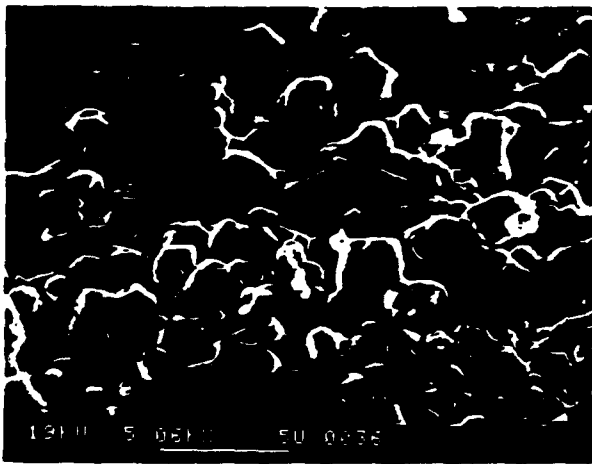
3 wt % glass



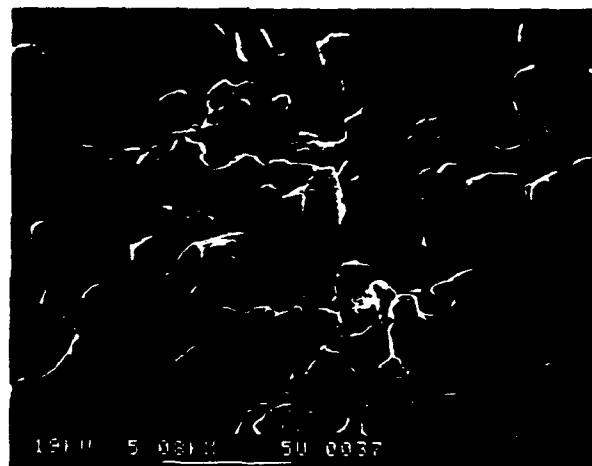
700 C / 30 min



700 C / 4 hr

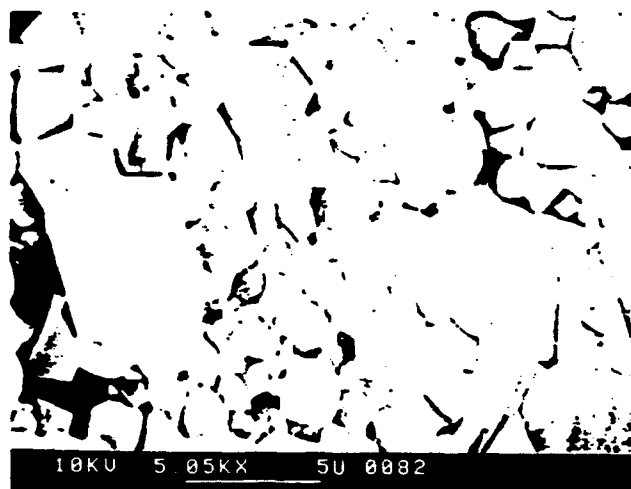


800 C / 30 min



800 C / 4 hr

FIG. 2. Microstructure of PMN-PT with 3 wt. % glass, sintered at 700 and 800 °C for 30 min and 4 h.



20 wt % glass, 750 C / 30 min

FIG. 13. Microstructure of PMN-PT with 20 wt.% glass, sintered at 750 °C for 30 min. Same as in Fig. 11(d), but at a larger magnification.

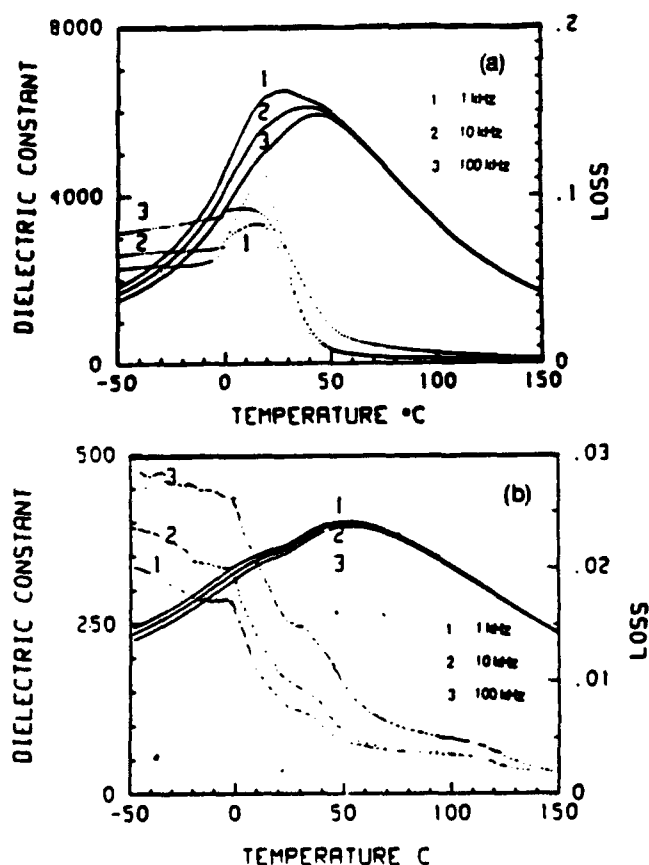


FIG. 14. Dielectric constant and  $\tan \delta$  of PMN-PT with (a) 3 wt.% glass sintered at 700 °C for 30 min and (b) 20 wt.% glass sintered at 750 °C for 30 min, as a function of temperature at 1, 10, and 100 kHz.

## ACKNOWLEDGMENTS

The authors are grateful to C.A. Randall, T.R. Shrout, J.P. Dougherty, M.H. Megherhi, and L.E. Cross for critical comments and to ONR and DARPA for financial support.

## REFERENCES

1. G.A. Smolenskii, *J. Phys. Soc. Jpn. Suppl.* **28**, 26 (1970).
2. F. Jona and G. Shirane, *Ferroelectric Crystals* (McMillan, New York, 1962).
3. L.E. Cross, S.J. Jang, and R.E. Newnham, *Ferroelectrics* **23**, 187 (1980).
4. S. Nomura and K. Uchino, *Ferroelectrics* **41**, 117 (1982).
5. T.R. Shrout and A. Halliyal, *Am. Ceram. Soc. Bull.* **66**, 704 (1987).
6. S.L. Swartz and T.R. Shrout, *Mater. Res. Bull.* **XVII**, 1245 (1982).
7. J. Chen, A. Gorton, H.M. Chen, and M. Harmer, *J. Am. Ceram. Soc.* **69**, C303 (1986).
8. S.L. Swartz, T.R. Shrout, W.A. Schulze, and L.E. Cross, *J. Am. Ceram. Soc.* **67**, 311 (1984).
9. E. Goo, T. Yamamoto, and K. Okazaki, *J. Am. Ceram. Soc.* **69**, C188 (1986).
10. H.C. Wang and W.A. Schulze, *J. Am. Ceram. Soc.* **73**, 825 (1990).
11. A.D. Hilton, C.A. Randall, D.J. Barber, and T.R. Shrout (to be published).
12. T.R. Shrout, W. Huebner, C.A. Randall, and A.D. Hilton, *Ferroelectrics* **93**, 361 (1989).
13. T.R. Shrout, U. Kumar, M. Megherhi, N. Yang, and S.J. Jang, *Ferroelectrics* **76**, 479 (1987).
14. P. Papet, J.P. Dougherty, and T.R. Shrout (to be published).
15. K. Ramesh Choudhary and E.C. Subbarao, *Ferroelectrics* **37**, 689 (1981).
16. M.H. Megherhi, M.S. Thesis, The Pennsylvania State University (1988).
17. M. Lejeune and J.P. Boilet, *Mater. Res. Bull.* **XX**, 493 (1985).
18. J.P. Guha, D.J. Hong, and H.U. Anderson, *J. Am. Ceram. Soc.* **71**, C152 (1988).
19. D.H. Kang and K.H. Yoon, *Ferroelectrics* **87**, 255 (1988).
20. M.H. Megherhi, J.P. Dougherty, G.O. Dayton, and R.E. Newnham (to be published).
21. M.F. Yan, H.C. Ling, and W.W. Rhodes, *J. Mater. Res.* **4**, 930 (1989).
22. T.R. Shrout and S.L. Swartz, *Mater. Res. Bull.* **XVIII**, 663 (1983).
23. J. Chen and M.P. Harmer, *J. Am. Ceram. Soc.* **73**, 68 (1990).
24. J.P. Guha and H.U. Anderson, in *Powder Ceramic Science*, edited by G. Messing, E.R. Fuller, Jr., and H. Housner, **1**, 1123 (1988).
25. M. Lejeune and J.P. Boilet, *Ceram. Int.* **8**, 99 (1982).
26. M. Lejeune and J.P. Boilet, *Am. Ceram. Soc. Bull.* **64**, 679 (1985).

## **APPENDIX 32**



La<sub>2</sub>Ti<sub>2</sub>O<sub>7</sub> Ceramics

Paul A. Fuierer\* and Robert E. Newnham\*

Materials Research Laboratory, The Pennsylvania State University, University Park, Pennsylvania 16802

La<sub>2</sub>Ti<sub>2</sub>O<sub>7</sub> powders were prepared using three different techniques. Single-phase material was obtained at 1150°C by calcination of mixed oxides, at 1000°C by molten salt synthesis, and at 850°C by evaporative decomposition of solutions. Particle sizes and morphologies of the powders differed substantially, as did the sintered microstructures and dielectric properties. Very dense (99%), translucent, grain-oriented lanthanum titanate was fabricated by hot-forging at 1300°C under a 200-kg load. Anisotropy was demonstrated by X-ray diffraction, scanning electron microscopy, thermal expansion, and dielectric measurements. [Key words: lanthanum, titanates, ferroelectrics, microstructure, orientation.]

## I. Introduction

LANTHANUM TITANATE (La<sub>2</sub>Ti<sub>2</sub>O<sub>7</sub>) is a member of the family of ferroelectrics with a perovskite-like layer structure (PLS) sometimes referred to as the strontium pyroniobate family. Single crystals of lanthanum titanate were found to exhibit strong piezoelectric and electrooptic effects,<sup>1</sup> and to be ferroelectric with an extremely high Curie temperature ( $T_c = 1500^\circ\text{C}$ ).<sup>2</sup> The room-temperature structure of La<sub>2</sub>Ti<sub>2</sub>O<sub>7</sub> has been reported to have two modifications, one with symmetry  $P2_1$ <sup>3,4</sup> and one with symmetry  $Pbn2_1$ .<sup>5</sup> At approximately 780°C the structure transforms into orthorhombic space group  $Cmc2_1$ , and at 1500°C it transforms into the paraelectric phase with symmetry  $Cmcm$ .<sup>6</sup> The various polymorphs of all A<sub>2</sub>B<sub>2</sub>O<sub>7</sub> PLS compounds originate from this high-temperature prototype structure. It is characterized by corner-shared BO<sub>6</sub> octahedra and 12-coordinated A cations within the perovskite-like slabs, which are linked by A cations at their boundaries. The anisotropy of the structure is expected to lead to anisotropy in dielectric and electrical properties.

Because of its extremely high Curie temperature, La<sub>2</sub>Ti<sub>2</sub>O<sub>7</sub> is a promising candidate for high-temperature piezoelectric and electrooptic devices. Lanthanum titanate ceramics are also under consideration as a low temperature coefficient of capacitance (TCC) material and as a microwave frequency dielectric.<sup>7</sup>

To date, La<sub>2</sub>Ti<sub>2</sub>O<sub>7</sub> ceramics have been fabricated only by conventional solid-state reaction of the oxides.<sup>8-10</sup> Coprecipitation has been used to prepare powders,<sup>10,11</sup> but sintering, microstructural, and property measurements have not been carried out. We have prepared La<sub>2</sub>Ti<sub>2</sub>O<sub>7</sub> powder using three different processes: (1) conventional calcining and milling of mixed oxides (MO), (2) evaporative decomposition of solutions (EDS), and (3) molten salt synthesis (MSS).

In the EDS process, a solution containing the proper ratio of metal atoms is atomized into a hot reaction furnace. The product collected at the output is usually a chemically homogeneous, highly reactive oxide powder of uniform particle

size and shape. Many different oxides have been prepared using EDS or one of the related techniques described in a review article by Sproson and Messing.<sup>12</sup>

The MSS process uses a molten salt solvent to act as the medium of reaction between the constituent oxides.<sup>13</sup> The desired compound will form if it is thermodynamically more stable than the starting oxides, that is, if its solubility in the molten salt is less than that of the reactants. Compared with solid-state reaction, a relatively high mobility of reacting species in the molten salt can lead to complete reaction at lower temperatures and shorter times.

Hot-forging is a means of achieving textured metals or ceramics. Applying a uniaxial load to a compact at high temperatures without constricting the lateral "flow" can lead to densification with grain growth and orientation in the direction perpendicular to the forging axis. Takenaka and Sakata used this technique to make oriented Bi<sub>2</sub>Ti<sub>2</sub>O<sub>7</sub> and other bismuth layer structure ferroelectrics, and demonstrated the anisotropy in electrical and piezoelectric properties.<sup>14</sup>

The present investigation compares the morphology, sintering behavior, and sintered microstructures of the three different La<sub>2</sub>Ti<sub>2</sub>O<sub>7</sub> powders and relates them to the observed dielectric properties. Further comparison is made with the anisotropy in hot-forged La<sub>2</sub>Ti<sub>2</sub>O<sub>7</sub> ceramics.

## II. Experimental Procedure

## (A) Powder Synthesis

(A) *Mixed Oxide:* Reagent-grade (99.9% purity) La<sub>2</sub>O<sub>3</sub> and TiO<sub>2</sub> in 1:2 mole ratio were mixed for 4 h in alcohol using zirconia media. The slurry was dried and then calcined at 1150°C for 3 h and remilled for 4 h. Loss on ignition of the raw materials prior to weighing was required because of the hygroscopic behavior of La<sub>2</sub>O<sub>3</sub>.

(B) *Evaporative Decomposition of Solutions:* Starting materials were reagent-grade TiCl<sub>4</sub> and La<sub>2</sub>O<sub>3</sub>. An aqueous solution was prepared by mixing stoichiometric amounts of a lanthanum nitrate solution, titanium tetrachloride solution, and distilled water. The concentration was 0.05 mol of La<sub>2</sub>Ti<sub>2</sub>O<sub>7</sub> per liter. The solution was fed into an ultrasonic atomizer creating a fine mist which was carried through the fused silica reaction tube of the vertical furnace. A description of the EDS system can be found in a previous publication.<sup>15</sup> The hot zone of the furnace was fixed at 960°C. Samples of the as-sprayed powder were then heat-treated at temperatures from 500 to 900°C.

(C) *Molten Salt Synthesis:* Reagent-grade La<sub>2</sub>O<sub>3</sub> and TiO<sub>2</sub> were mixed in a 1:2 ratio in deionized water and zirconia media. A salt of composition 50 mol% NaCl/50 mol% KCl was then added, in most cases constituting 50 wt% of the total reaction mixture. The mixing was continued for 1 h, and the slurry was then dried at 150°C. The dried mass was then lightly ground with mortar and pestle and dry blended into a granular powder. This powder was placed in a closed alumina crucible and reacted at temperatures ranging from 800 to 1500°C. The cooled fused mass was washed using distilled water and centrifuge. Washing was repeated until the specific conductance of the decanted liquid fell below 3  $\mu\text{S}$ , measured using a conductance meter. (The conductance of deionized water was 1.5  $\mu\text{S}$ .)

D. Clarke—contributing editor

Manuscript No. 196825. Received March 25, 1991; approved July 9, 1991.  
Supported by the Eastman Kodak Co. through a fellowship grant.  
\*Member, American Ceramic Society.

## (2) Ceramic Fabrication

(A) *Conventional:* Ceramic samples were prepared from each of the three  $\text{La}_2\text{Ti}_2\text{O}_7$  powders by addition of 2 wt% binder, pressing 12.5-mm-diameter pellets at 1.38 MPa, and sintering on zirconia setters for 5 h at various temperatures.

(B) *Hot-Forged (HF):* Pellets (12.5 mm) from the calcined and milled mixed oxide powder were presintered to roughly 60% of theoretical density. A uniaxial load of 200 kg was applied to the pellet for 3 h at 1300°C in a hot-pressing apparatus.

## (3) Characterization

X-ray diffraction (XRD) was used for phase identification of the various powders. The  $\text{La}_2\text{Ti}_2\text{O}_7$  patterns were indexed to  $Pbn2_1$  symmetry and used for lattice parameter calculation using a least-squares procedure. A scanning electron microscope (SEM) was used for microstructural characterization of both powders and sintered bodies. Sintered cross sections were prepared for the SEM by polishing down to 1- $\mu\text{m}$ -diamond finish, followed by a thermal etch at 1450°C/30 min. Particle sizes were estimated from several micrographs taken at random. Densification was determined by the average geometric densities as a function of sintering temperature. A dilatometer was used to measure the thermal expansion of bar-shaped samples over the temperature range 25° to 1000°C. Dielectric testing was carried out on 12-mm-diameter disk samples ground and polished to  $\sim 0.5$ -mm thickness and electroded with a layer of sputtered platinum followed by fired-on platinum paste. A Q-meter was used for measurement of  $Q$  ( $\tan \delta^{-1}$ ) and capacitance at high frequency. An LCR bridge and oven interfaced with a computer were used to determine the temperature coefficient of capacitance.

## III. Results and Discussion

### (1) Phase Development and Microstructure

Calcination at 1150°C for 3 h was found to be necessary to obtain single-phase  $\text{La}_2\text{Ti}_2\text{O}_7$  via the conventional MO technique. By using the EDS and MSS processes, we were able to achieve phase pure material at 850° and 1000°C, respectively. Although the EDS furnace was set at its maximum temperature of 960°C, the particle dwell time ( $\sim 0.5$  s) was not long enough to yield a highly crystalline oxide. Figure 1 illustrates the development of the  $\text{La}_2\text{Ti}_2\text{O}_7$  X-ray pattern from the as-

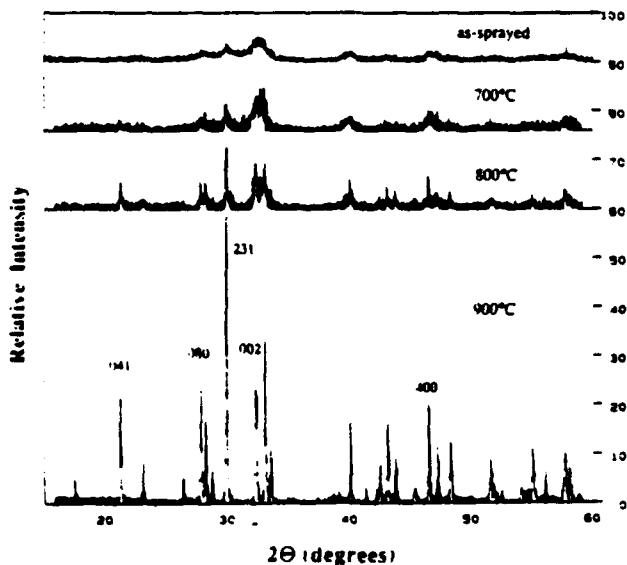


Fig. 1. X-ray diffraction powder patterns of lanthanum titanate prepared by the evaporative decomposition of solutions, as-sprayed and heat-treated for 3 h at various temperatures.

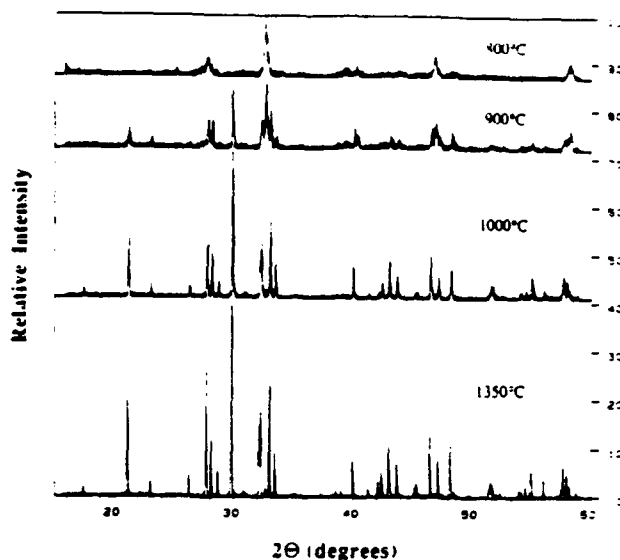


Fig. 2. X-ray diffraction patterns of lanthanum titanate powders prepared by molten salt solvent synthesis at various reaction temperatures.

sprayed powder upon heat treatment. Figure 2 shows the patterns from MSS powders reacted at different temperatures. At 800°C, the product was a poorly crystallized cation-deficient perovskite  $\text{La}_{2-x}\text{Ti}_2\text{O}_{7-x}$ . Abe and Uchino<sup>10</sup> reported the synthesis of this compound at 1350°C in a controlled  $\text{CO}_2$ - $\text{H}_2$  atmosphere. At 900°C the product was a mixture of  $\text{La}_2\text{Ti}_2\text{O}_7$  and  $\text{La}_2\text{Ti}_3\text{O}_{10}$ , and at 1000°C single-phase  $\text{La}_2\text{Ti}_2\text{O}_7$  was obtained. Table I gives the calculated lattice parameters along with the single-crystal values from the literature.

The particle morphologies of the three types of  $\text{La}_2\text{Ti}_2\text{O}_7$  powders were very different and are shown in Fig. 3. The calcined and milled MO powder consisted of hard aggregates of submicrometer, almost equiaxed particles. The as-sprayed EDS material was made up of 5- to 25- $\mu\text{m}$  diameter, free-flowing, smooth, spherical particles. After heating to 900°C, the primary crystallites (0.1 to 0.5  $\mu\text{m}$ ) making up the spherical aggregates were apparent (Fig. 3(d)). The MSS powders contained free or lightly agglomerated platelets, the size of which depended on the reaction temperature. Table II summarizes the characteristics of the lanthanum titanate resulting from various MSS reaction conditions. Generally, the higher the temperature, the larger the particle size. Platelets with the largest aspect ratio (longest/smallest dimension) were obtained at 1350°C. Note that when a large amount of salt solvent was available (90 wt%), a bimodal distribution of particle sizes resulted.

Because of the very different nature of the powders, different sintering behavior was expected. Figure 4 is a plot of theoretical density as a function of sintering temperature. The microstructures of the highest-density samples are shown in Figure 5. Maximum densities were achieved at 1500°C for MO and MSS  $\text{La}_2\text{Ti}_2\text{O}_7$ , and at 1450°C for the EDS powder. The EDS compact sintered at a lower temperature because of the intimate mixing of La and Ti atoms inherent in solution

Table I.  $\text{La}_2\text{Ti}_2\text{O}_7$  Lattice Parameters ( $Pbn2_1$  symmetry)

|                         | $a$<br>(Å) | $b$<br>(Å) | $c$<br>(Å) | Cell volume<br>(Å <sup>3</sup> ) |
|-------------------------|------------|------------|------------|----------------------------------|
| Single crystal (Ref. 5) | 7.810      | 25.745     | 5.547      | 1115                             |
| MO                      | 7.803      | 25.687     | 5.542      | 1111                             |
| EDS (heated 900°C)      | 7.811      | 25.687     | 5.542      | 1112                             |
| MSS 1000                | 7.806      | 25.698     | 5.544      | 1112                             |
| MSS 1100                | 7.811      | 25.725     | 5.546      | 1114                             |

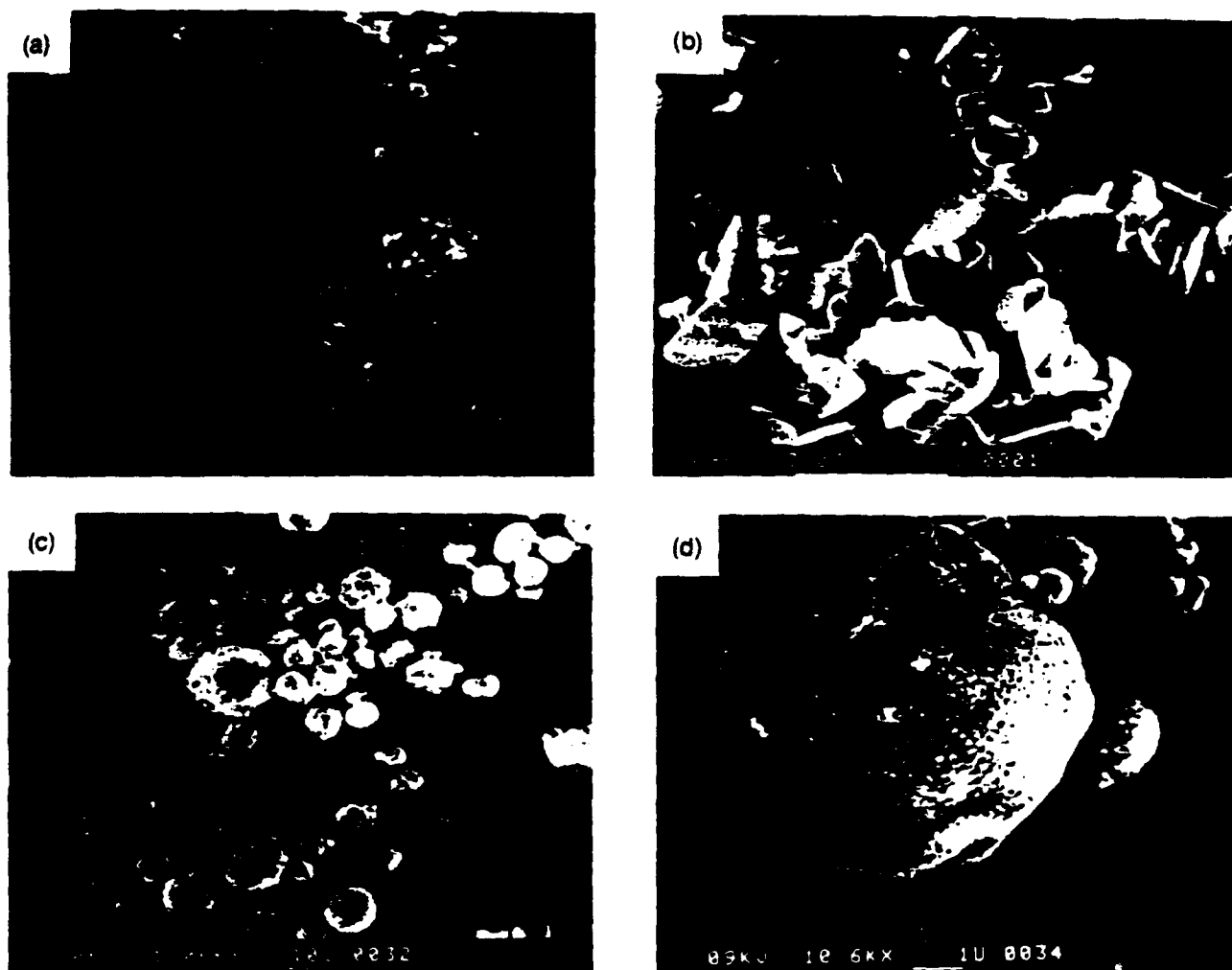


Fig. 3. Scanning electron micrographs of  $\text{La}_2\text{Ti}_2\text{O}_7$  powder prepared by (a) calcined and milled mixed oxides, (b) molten salt synthesis at  $1350^\circ\text{C}$ , (c) EDS (as-sprayed), and (d) EDS (heated at  $900^\circ\text{C}$ ).

precursor processes. However, the hollow spherical aggregates left pores behind, and a maximum density of only 92% was realized. Regions of large and regions of small grains in the microstructure suggest the occurrence of exaggerated grain growth.

MO lanthanum titanate reached 97.5% (theoretical density =  $5.782 \text{ g/cm}^3$ ). Randomly oriented, irregularly shaped grains had a wide size distribution from 5 to  $100 \mu\text{m}$ . The densification of MSS1100 closely followed that of the MO compact because of a similar starting particle size; however, the final grain shape was more platelike and the size distribution much narrower. Randomly oriented, highly anisometric

particles usually lead to inefficient packing and low sintered density, as demonstrated in sample MSS1350. The micrograph shows, though, that some alignment of the plates perpendicular to the pressing direction took place. This was confirmed by XRD of the surface. The degree of orientation is explained below.

Hot-forging yielded a 99% dense, highly translucent ceramic with the very high degree of preferred orientation shown in Fig. 6. The XRD pattern from the surface perpendicular to the forging direction (Fig. 7) shows the increased intensities of the  $0k0$  reflections of the  $\text{Phn}2$  modification. This means the thin dimension of the platelets corresponds to

Table II. Results for Molten Salt Synthesized Powders

| Reaction temp time<br>( $^\circ\text{C}$ h) | Salt solvent (wt%) |      | Phases present* | Avg particle size<br>( $\mu\text{m}$ ) | Aspect ratio | Comments                                |
|---|--------------------|------|-----------------|--|--------------|---|
|   | Starting           | Loss |                 |  |              |   |
| 800/3                                       | 50                 | 8.3  | LT              |  |              |   |
| 900/3                                       | 50                 | 9.9  | LT and LT       |  |              |   |
| 1000/3                                      | 50                 | 14.5 | LT              | <1                                     | 3:1          | Agglomerates of small platelets         |
| 1100/1                                      | 50                 | 14.8 | LT              | 1.0                                    | 5:1          | Agglomerates of small platelets         |
| 1200/24                                     | 50                 | 43.5 | LT              | 1.4                                    | 5:1          | Agglomerates of small platelets         |
| 1300/1                                      | 50                 | 20.2 | LT              | 1.6                                    | 5:1          | Agglomerates of small platelets         |
| 1350/5                                      | 50                 | 48.0 | LT              | 4.5                                    | 12:1         | Well-defined platelets                  |
| 1400/5                                      | 50                 | 100  | LT              | 4.0                                    | 11:1         | Well-defined platelets                  |
| 1465/5                                      | 50                 | 100  | LT              | 5.0                                    | 3:1          | Not well-defined, plates fused together |
| 1350/5                                      | 90                 | 55.0 | LT              | 5.0                                    | 10:1         | Bimodal distribution                    |
|   |                    |      |                 | 150                                    | Large        |   |

\*LT =  $\text{La}_2\text{Ti}_2\text{O}_7$ ; LT =  $\text{La}_2\text{Ti}_2\text{O}_7$

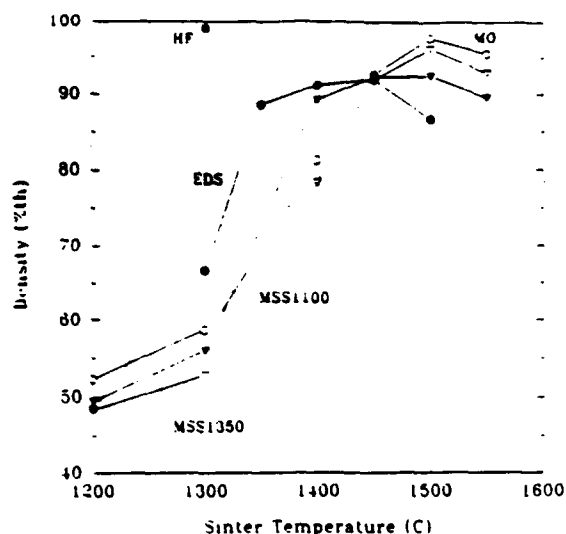


Fig. 4. Percent of theoretical density vs sintering temperature for conventionally sintered  $\text{La}_2\text{Ti}_2\text{O}_7$  powder produced by mixed oxides, evaporative decomposition of solutions, and molten salt synthesis; and the hot-forged compact.

the large  $b$ -axis (perpendicular to the perovskite slabs in the structure), consistent with the general finding that the habit of the crystal corresponds to the reciprocal lattice of the structure. The degree of orientation can be quantified by calculation of the Lotgering orientation factor,  $f$ , from XRD

peak intensities:

$$f = (p - p_0)/(1 - p_0) \quad (1)$$

where

$$p = \sum_{hkl} I_{hkl} / \sum_{hkl} I_{hkl} \quad (2)$$

over a certain range of  $2\theta$  values.<sup>14</sup>  $p_0 = p$  for an unoriented sample. Thus  $f$  increases from 0.0 for a randomly oriented sample to 1.0 for perfect alignment. For the hot-forged  $\text{La}_2\text{Ti}_2\text{O}_7$ ,  $f = 0.79$ , while for the MSS1350 sintered sample  $f = 0.25$ .

## (2) Dielectric Measurements

Table III lists the dielectric data measured at 100 kHz for the various types of lanthanum titanate ceramics. Figure 5 shows the frequency dependence of the dielectric quality factor,  $Q$ . The dielectric permittivities,  $\epsilon$ , remained constant up to 50 MHz, within the error of measurement. MO lanthanum titanate ceramics had higher permittivity (48.8) than the previously reported value of 44 (Ref. 7). The  $Q$  remained high (8000) up to 2 MHz, but then dropped off rapidly to 250 at 50 MHz. The EDS sample had high dielectric loss with even greater frequency dependence, possibly caused by voids, poor densification, and the presence of a reduced state of titanium,  $\text{Ti}^{3+}$ . The EDS ceramics were yellower when compared to the off-white color of the other  $\text{La}_2\text{Ti}_2\text{O}_7$  samples. The mixed valence state  $\text{Ti}^{3+}$ - $\text{Ti}^{4+}$  could lead to an electron-hopping mechanism of conduction and higher losses. The reason for the possible mixed valency is not clear.

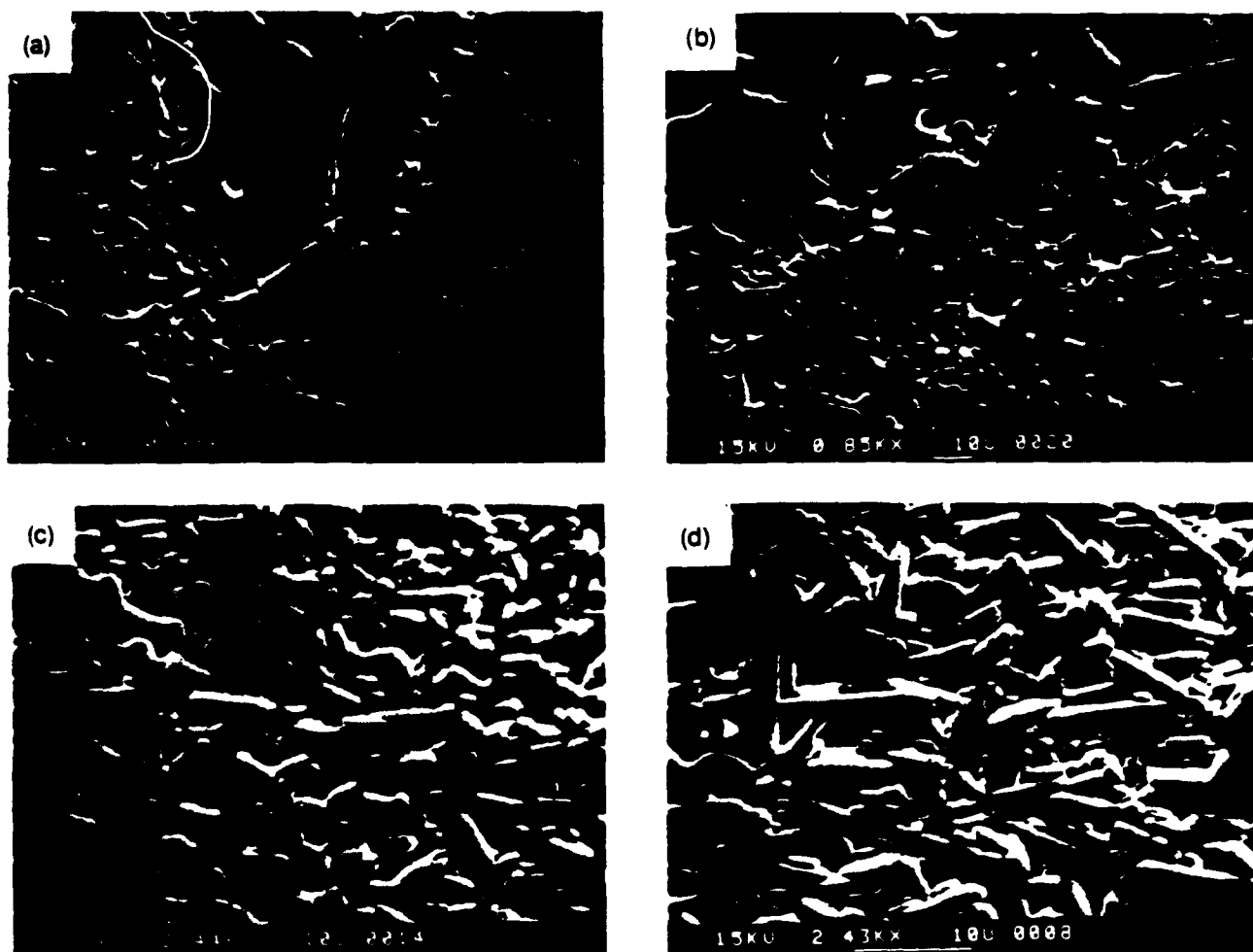


Fig. 5. Scanning electron micrographs of sintered  $\text{La}_2\text{Ti}_2\text{O}_7$  ceramics: (a) MO, (b) EDS, (c) MSS at 1100°C, and (d) MSS at 1350°C.



Fig. 6. The cross section of  $\text{La}_{0.7}\text{Ti}_{0.3}\text{O}_3$  hot-forged at  $1300^\circ\text{C}/200\text{ kg}/3\text{ h}$ . The forging axis was in the vertical direction with respect to the micrograph.

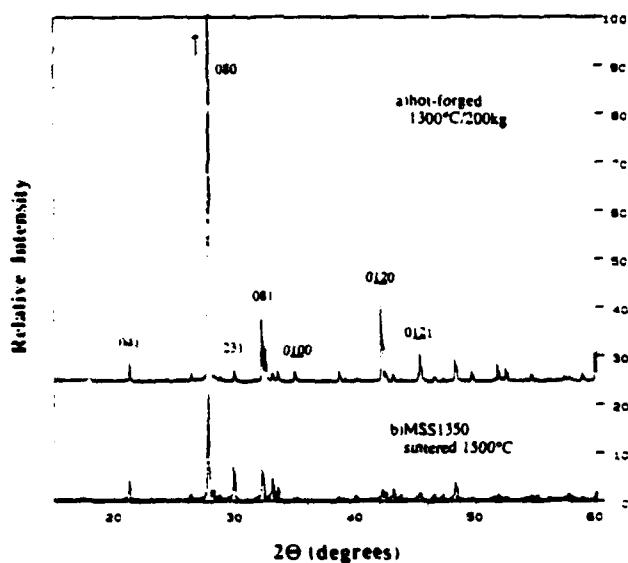


Fig. 7. X-ray diffraction pattern from the polished surface of  $\text{La}_{0.7}\text{Ti}_{0.3}\text{O}_3$  ceramic: (a) hot-forged and (b) MSS1350 sintered at  $1500^\circ\text{C}$ .

MSS1100, with small and uniform grain size and dense microstructure, had a high  $Q$  over the frequency range of the meter. The rather low dielectric constant of MSS1350 is a consequence of a low sintered density (92.4%) and some degree of grain alignment.

The anisotropy in dielectric constant is clear from measurements of the hot-forged sample. With the electric field,  $E$ , applied parallel to the forging axis (FA),  $\epsilon = 42.5$ , in good agreement with the single-crystal value  $\epsilon_a = 42$ . With  $E$  applied perpendicular to FA, and thus along the plane defined

by the crystallographic axes  $a$  and  $c$ ,  $\epsilon_c = 54.1$ . The corresponding single-crystal values are  $\epsilon_a = 52$  and  $\epsilon_c = 62$ , ( $c$  is the polar direction.) The  $Q$  of the very dense hot-forged samples exhibited the least frequency dependence, especially with  $E$  applied perpendicular to FA.

Table III also lists important temperature dependence parameters. A low temperature coefficient of capacitance (TCC) is necessary for stable capacitors. The capacitances at 100 kHz varied approximately linearly over the temperature range  $0^\circ$  to  $230^\circ\text{C}$ . The TCC of MO  $\text{La}_{0.7}\text{Ti}_{0.3}\text{O}_3$  was  $41\text{ ppm}/^\circ\text{C}$ . This is in good agreement with  $30\text{ ppm}/^\circ\text{C}$  at 1 MHz from  $-40^\circ$  to  $260^\circ\text{C}$ , reported by Marzullo and Bunting. The TCC of hot-forged  $\text{La}_{0.7}\text{Ti}_{0.3}\text{O}_3$  was found to be very direction dependent:  $-188\text{ ppm}/^\circ\text{C}$  parallel to FA, and  $-14\text{ ppm}/^\circ\text{C}$  perpendicular to FA. MSS1350, with a more random arrangement of similar size platelets, had a TCC between these two values.

Thermal expansion was nearly constant from  $25^\circ$  to  $1000^\circ\text{C}$ . For dense, randomly oriented  $\text{La}_{0.7}\text{Ti}_{0.3}\text{O}_3$ , TCE =  $11.3\text{ ppm}/^\circ\text{C}$ . The TCE was lower parallel to the  $b$ -axis ( $9.8\text{ ppm}/^\circ\text{C}$ ) than perpendicular to  $b$  ( $13.7\text{ ppm}/^\circ\text{C}$ ).

A low temperature coefficient of resonant frequency is desirable for microwave dielectric resonators ( $\text{TC}_f < 3\text{ ppm}/^\circ\text{C}$ ).<sup>10</sup>  $\text{TC}_f$  is calculated from TCC and TCE:

$$\text{TC}_f = -\frac{1}{2}(\text{TCC} + \text{TCE}) \quad (3)$$

This value is effectively zero for the hot-forged sample with  $E$  and  $\Delta f$  perpendicular to the FA.

#### IV. Conclusions

For the first time,  $\text{La}_{0.7}\text{Ti}_{0.3}\text{O}_3$  ceramics have been prepared by evaporative decomposition of solutions, molten salt synthesis, and hot-forging. The powder morphologies, ceramic microstructures, and dielectric properties were compared to conventional ceramics sintered from calcined and milled oxides. Single-phase  $\text{La}_{0.7}\text{Ti}_{0.3}\text{O}_3$  powders were synthesized by heat treatment of EDS powders at  $850^\circ\text{C}$ , and by reaction of oxides in a molten salt at  $1000^\circ\text{C}$ . EDS powders were spherical agglomerates of submicrometer crystallites and were very reactive, but resulted in a sintered ceramic with poor microstructure, significant porosity, and high dielectric loss. The MSS process yielded well-defined platelets. The size of these platelets could easily be controlled by selection of the reaction temperature and time. A high-density, uniform microstructure, low-loss ceramic was made with MSS powders reacted at  $1100^\circ\text{C}$ . Tape casting of these MSS powders could be used for grain orientation.

High-density lanthanum titanate ceramic with high degree of preferred orientation was fabricated using a hot-forging method. The samples showed anisotropy in dielectric constant, TCC, and thermal expansion, and an improved frequency dependence of  $Q$  over conventionally prepared ceramic. Since  $\text{Nd}_{0.7}\text{Ti}_{0.3}\text{O}_3$  and  $\text{La}_{0.7}\text{Ti}_{0.3}\text{O}_3$  are used as major components in high- $K$  microwave dielectric formulations,<sup>11</sup> this information concerning the anisotropy in properties could be used to further improve the loss and temperature dependence characteristics of ceramic dielectric resonators. We are presently carrying out a study of hot-forged  $\text{La}_{0.7}\text{Ti}_{0.3}\text{O}_3$ .

Table III. 100-kHz Dielectric Data and Thermal Dependence for  $\text{La}_{0.7}\text{Ti}_{0.3}\text{O}_3$  Ceramics

|                                | $\epsilon_{\text{RT}}$<br>( $\pm 2\%$ ) | $Q_{\text{RT}}$<br>( $\times 10^3$ ) | TCC( $0-230^\circ\text{C}$ )<br>(ppm/ $^\circ\text{C}$ ) | TCE( $25-1000^\circ\text{C}$ )<br>(ppm/ $^\circ\text{C}$ ) | $\text{TC}_f$<br>(ppm/ $^\circ\text{C}$ ) |
|--------------------------------|---|--------------------------------------|--|--|---|
| MO                             | 48.8                                    | 5300                                 | 41   | 11.3   | -26                                       |
| EDS                            | 45.9                                    | 900                                  | 147  | 9.9  | -78                                       |
| MSS1100                        | 46.5                                    | 4750                                 | 58   | 11.3   | -34                                       |
| MSS1350                        | 44.0                                    | 3500                                 | 77   | 10.9   | -44                                       |
| HF ( $E \parallel \text{FA}$ ) | 42.5                                    | 2950                                 | 188  | 9.8*   | -99                                       |
| HF ( $E \perp \text{FA}$ )     | 54.1                                    | 2600                                 | -14  | 13.7*  | 0   |

\*  $E \parallel \text{FA}$ ,  $\Delta f \perp \text{FA}$ .

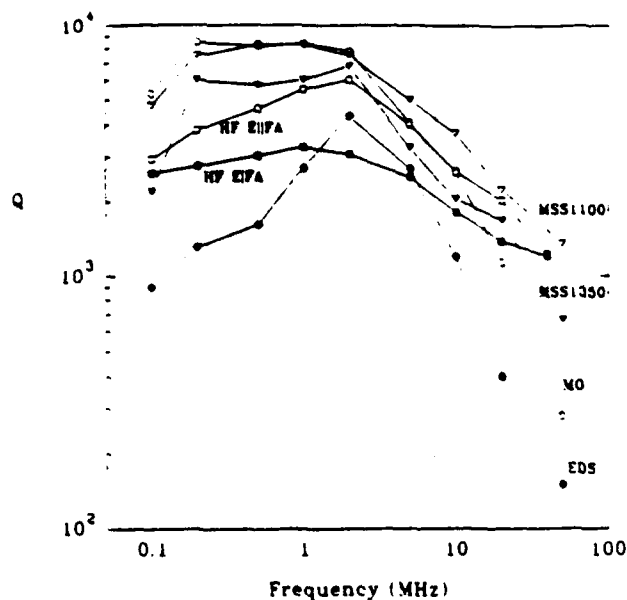


Fig. 8. Dielectric quality factor,  $Q$ , as a function of frequency for different  $\text{La}_2\text{Ti}_2\text{O}_7$  ceramics.

and other compounds in the PLS family for use in high-temperature piezoelectric and electrooptic devices.

## References

- M. Kimura, S. Nanamatsu, K. Doi, S. Matsushita, and M. Takahashi, "Electrooptic and Piezoelectric properties of  $\text{La}_2\text{Ti}_2\text{O}_7$  Single Crystal," *Jpn J Appl Phys.*, **11**, 404 (1972).
- S. Nanamatsu, M. Kimura, K. Doi, S. Matsushita, and N. Yamada, "A New Ferroelectric  $\text{La}_2\text{Ti}_2\text{O}_7$ ," *Ferroelectrics*, **8**, 511-13 (1974).
- M. Gasperin, "Dititanate de Lanthane," *Acta Crystallogr.* **B31**, 2129-30 (1975).
- L. Balachandran and N. G. Eror, "X-ray Diffraction and Vibrational Spectroscopy Study of the Structure of  $\text{La}_2\text{Ti}_2\text{O}_7$ ," *J. Mater. Res.*, **4**, 12-15 (1989).
- K. Scheunemann and H. K. Müller-Buschbaum, "Zur Kristallstruktur von  $\text{La}_2\text{Ti}_2\text{O}_7$ ," *J. Inorg. Nucl. Chem.*, **37**, 1878-81 (1975).
- N. Ishizawa, F. Marumo, S. Iwai, M. Kimura, and T. Kawamura, "Compounds with Perovskite-Type Slabs. V. A High-Temperature Modification of  $\text{La}_2\text{Ti}_2\text{O}_7$ ," *Acta Crystallogr.* **B38**, 368-72 (1982).
- S. Marzullo and E. N. Bunting, "Dielectric Properties of Titanate or Titanate Containing Varying Proportions of Rare-Earth Oxides," *J. Am. Ceram. Soc.*, **41**, 40-41 (1958).
- H. Ouchi and S. Kawashima, "Dielectric Ceramics for Microwave Application," *Jpn J Appl Phys. Suppl.*, **24** (24-2) 60-64 (1985).
- J. B. MacChesney and H. A. Sauer, "The System  $\text{La}_2\text{O}_3\text{-TiO}_2$  Phase Equilibria and Electrical Properties," *J. Am. Ceram. Soc.*, **45**, 416-22 (1962).
- A. M. Sych, Y. A. Titov, and S. A. Nedilko, "Synthesis and Investigation of Compounds with a Layer Perovskite-like Structure," *Russ J. Inorg. Chem. (Engl. Transl.)*, **25**, 1139-42 (1980).
- J. Takanashi and T. Ohtsuka, "Vibrational Spectroscopic Study of Structural Evolution in the Coprecipitated Precursors to  $\text{La}_2\text{Sn}_2\text{O}_7$  and  $\text{La}_2\text{Ti}_2\text{O}_7$ ," *J. Am. Ceram. Soc.*, **72**, 426-31 (1989).
- D. W. Soroson and G. L. Messing, "Ceramic Powder Synthesis by Thermal Reaction of Atomized Solutions," pp. 99-108 in *Advances in Ceramics*, Vol. 21, *Ceramic Powder Science*, Edited by G. L. Messing, K. S. Mazumdar, J. W. McCauley, and R. A. Haber, American Ceramic Society, Westerville, OH, 1987.
- R. H. Arendt, J. H. Rosolowski, and J. W. Szymaszek, "Lead Zirconate Titanate Ceramics from Molten Salt Solvent Synthesized Powders," *Mater. Res. Bull.*, **14**, 703-709 (1979).
- T. Takenaka and K. Sakata, "Grain Orientation and Electrical Properties of Hot-Forged  $\text{Bi}_2\text{Ti}_2\text{O}_7$  Ceramics," *Jpn J Appl Phys.*, **19**, 31-34 (1980).
- T. Takenaka and K. Sakata, "Grain Orientation Effects on Electrical Properties of Bismuth Layer-Structured Ferroelectric  $\text{Pb}(\text{Bi}_{1-x}\text{Ti}_x)_2\text{O}_7$  Solid Solution," *J. Appl. Phys.*, **55**, 1092-99 (1984).
- P. A. Fuierer, T. T. Srinivasan, and R. E. Newnham, "Synthesis of Y-Ba-Cu-O Powders via Evaporative Decomposition of Solutions," pp. 156-61 in *Ceramic Superconductors II*, Edited by M. F. Yan, American Ceramic Society, Westerville, OH, 1988.
- M. Abe and K. Ichino, "X-Ray Study of the Deficient Perovskite  $\text{La}_2\text{Ti}_2\text{O}_7$ ," *J. Mater. Res. Bull.*, **9**, 147-56 (1974).
- F. K. Lotgering, "Topotactical Reactions with Ferrimagnetic Oxides Having Hexagonal Crystal Structures—I," *J. Inorg. Nucl. Chem.*, **9**, 113-23 (1959).
- K. Wakino, K. Minari, and H. Tamura, "Microwave Characteristics of  $\text{Zr-Sn-TiO}_2$  and  $\text{BaO-PhO-Nd}_2\text{O}_3\text{-TiO}_2$  Dielectric Resonators," *J. Am. Ceram. Soc.*, **67**, 278-81 (1984).
- K. Kageyama and T. Mitsuhiro, "Dielectric Characteristics of  $\text{PbO-BaO-La}_2\text{O}_3\text{-TiO}_2$  at Microwave Frequencies," *Jpn J Appl Phys.*, **24** (Supplement 24-2), 1045-47 (1985).

## **APPENDIX 33**

# Effects of pH and $\text{H}_2\text{O}_2$ upon coprecipitated $\text{PbTiO}_3$ powders

## Part II *Properties of calcined powders*

G. R. FOX, J. H. ADAIR, R. E. NEWNHAM

*Materials Research Laboratory, The Pennsylvania State University, University Park, Pennsylvania 16802, USA*

$\text{PbTiO}_3$  was prepared by coprecipitation and calcination from mixed solutions of  $\text{TiCl}_4$  and  $\text{Pb}(\text{NO}_3)_2$ . The effect of pH in the precipitation solution on the properties of calcined powders was studied by calcining coprecipitated precursor powders prepared at pH values between 8.00 and 10.50. The effects of  $\text{H}_2\text{O}_2$  were studied by preparing  $\text{PbTiO}_3$  powders from mixed solutions containing  $\text{H}_2\text{O}_2$ : $\text{PbTiO}_3$  ratios between 0:1 and 6:1. Synthesis of phase pure  $\text{PbTiO}_3$  by coprecipitation and calcination is highly dependent upon the complex ionic equilibria dictated by the pH. The pH used for precipitation determines the types of crystalline phases formed from coprecipitated precursor powders. The rate at which amorphous precipitates transform to crystalline  $\text{PbTiO}_3$  during calcination is also affected by both the pH and  $\text{H}_2\text{O}_2$  additions. High purity (greater than 98%)  $\text{PbTiO}_3$  with a rapid amorphous-to-crystalline transformation rate was obtained for  $\text{H}_2\text{O}_2$ : $\text{PbTiO}_3 = 1.1:1$ , and pH = 9.65 to 9.75.

### 1. Introduction

The formation of crystalline  $\text{PbTiO}_3$  from coprecipitated precursor powders followed by calcination is dependent upon the species contained in the precursor. In part I of this study [1] the properties of the precipitated precursor powders prepared from  $\text{Pb}(\text{NO}_3)_2$  and  $\text{TiCl}_4$  solutions were presented. This paper presents the powder properties after calcination of the coprecipitated powders prepared in part I and discusses how the properties of the precursor powders are related to the properties of the calcined powders. Since pH, speciation, and concentration of species influence the properties of precursor powders, the effects of these variables upon the calcined materials will be discussed.

### 2. Procedure for $\text{PbTiO}_3$ preparation and powder characterization

Two sets of coprecipitated powders were prepared from stock solutions of  $\text{Pb}(\text{NO}_3)_2$  and  $\text{TiCl}_4$  as described in the first part of this study [1]. The first set of powders was prepared with an  $\text{H}_2\text{O}_2$ : $\text{PbTiO}_3$  ratio of 1.1:1 but the five powders were prepared over different pH ranges of 8.00 to 8.20, 8.50 to 8.65, 8.90 to 9.15, 9.65 to 9.75, and 10.15 to 10.30. The second set of precipitated powders was prepared at a constant pH of 9.90 to 10.05 with the five powders in the set composed of  $\text{H}_2\text{O}_2$ : $\text{PbTiO}_3$  ratios of 0:1, 0.5:1, 1.1:1, 2:1, and 6:1. 3 g samples of each resulting powder

were fired in covered alumina crucibles at 600 °C with a 5 h hold time. The samples were heated and cooled at 5 °C min<sup>-1</sup>.

All calcined powders were analysed by X-ray diffraction\* using  $\text{CuK}\alpha$  radiation at a scan rate of 1° 2 $\theta$  min<sup>-1</sup>. Integrated peak intensities were obtained at a scan rate of 0.1° 2 $\theta$  min<sup>-1</sup> with a coprecipitated  $\text{PbTiO}_3$  powder (pH = 9.90 to 10.05,  $\text{H}_2\text{O}_2$ : $\text{PbTiO}_3 = 1.1:1$ , calcined at 800 °C for 262 h) used as an external, fully crystallized standard. All samples were prepared as back loaded packed powder specimens. The specific surface areas of the calcined powders were obtained by a nitrogen adsorption technique.†

### 3. Results and discussion

#### 3.1. Effects of pH on properties of calcined precipitates

Table I lists the crystalline phases within each of the calcined powders as determined by X-ray diffraction. X-ray diffraction patterns of the first set of powders prepared at constant  $\text{H}_2\text{O}_2$ : $\text{PbTiO}_3$  ratio 1.1:1 and various pH conditions exhibit formation of  $\text{PbTiO}_3$ , but a low intensity unidentified peak is observed at  $d = 0.294$  nm (see Fig. 1). The intensity of the unidentified peak increases with decreasing pH values below 9.00. The pH value at which the intensity of the extraneous peak begins to increase corresponds to the

\* Scintag Pad V diffractometer, Santa Clara, California, USA.

† Quantachrome monosorb, model MS-12, Syosset, New York, USA.



TABLE I Phases formed under various pH and H<sub>2</sub>O<sub>2</sub> concentrations

| pH          | H <sub>2</sub> O <sub>2</sub> :PbTiO <sub>3</sub> | Phases                              |
|-------------|---|-------------------------------------|
| 8.00-8.20   | 1.1:1   | PbTiO <sub>3</sub> + unknown (4%)   |
| 8.50-8.65   | 1.1:1   | PbTiO <sub>3</sub> + unknown (3%)   |
| 8.90-9.15   | 1.1:1   | PbTiO <sub>3</sub> + unknown (< 2%) |
| 9.65-9.75   | 1.1:1   | PbTiO <sub>3</sub> + unknown (< 2%) |
| 9.90-10.05  | 1.1:1   | PbTiO <sub>3</sub> + unknown (< 2%) |
| 10.15-10.30 | 1.1:1   | PbTiO <sub>3</sub> + unknown (< 2%) |
| 9.90-10.05  | 0:1   | PbTiO <sub>3</sub> + unknown (< 2%) |
| 9.90-10.05  | 0.5:1   | PbTiO <sub>3</sub> + unknown (< 2%) |
| 9.90-10.05  | 2:1   | PbTiO <sub>3</sub> + unknown (< 2%) |
| 9.90-10.05  | 6:1   | PbTiO <sub>3</sub> + unknown (< 2%) |

pH for the solubility minimum and speciation change for the lead system.

Since the intensity of the unidentified diffraction peak does not increase at pH values above 9.00, it is likely that the formation of the second phase, causing the appearance of the diffraction peak, is not controlled merely by solubility of the lead. Also, if solubility did control the formation of the unidentified phase, aqueous lead or titanium species should have been observed in the filtrate of the precipitates. It was stated in part I that less than  $1 \times 10^{-5} \text{ mol}^{-1}$  of lead and titanium species were observed in the filtrate solutions [1]. Change in the speciation of the lead from  $\text{HPbO}_2^-$  and other complex lead hydroxo ions to  $\text{Pb}^{2+}$  below pH = 9.34 correlates with the appearance of the second phase. A study surveying a wider pH range than the present study is required to determine conclusively whether solubility of the lead species, change in the

lead speciation, or a combination of these phenomena is responsible for the appearance of the second phase.

The specific surface area is plotted against pH for the calcined powders in Fig. 2. There is negligible change in the specific surface area with increasing pH, indicating that the calcined powders consist of particles of the same size, assuming similar morphologies for all particles. The ultimate particle size of the calcined powders is apparently independent of the specific surface area and particle size of the as-precipitated powders shown in part I, Fig. 5 [1].

Fig. 3 shows the concentration of crystalline PbTiO<sub>3</sub> as a function of pH for the calcined powders. Only the calcined powder prepared at pH = 9.65 to 9.75 exhibits 100% crystalline PbTiO<sub>3</sub>. The precise maximum in the curve may occur anywhere between pH = 9.2 to 9.7. Again, the solubility minimum for the lead species corresponds with this finding. The fact that Fig. 3 exhibits an inverse relation to the solubility against pH curve for the lead system strongly suggests that the formation of crystalline PbTiO<sub>3</sub> is controlled by the solubility of the lead species.

The effect of pH upon the quantities of crystalline PbTiO<sub>3</sub> within the calcined powders cannot entirely be attributed to changes in rates of transformation from the amorphous to the crystalline state. As noted in Table I and Fig. 1 a small quantity of second phase was observed in the X-ray diffraction patterns. The increased quantity of unidentified second phase with pH values below 9.00 will correspondingly decrease the fraction of PbTiO<sub>3</sub> present in the powder specimens. If it is assumed that all the calcined powders consist of crystalline PbTiO<sub>3</sub> and the unidentified

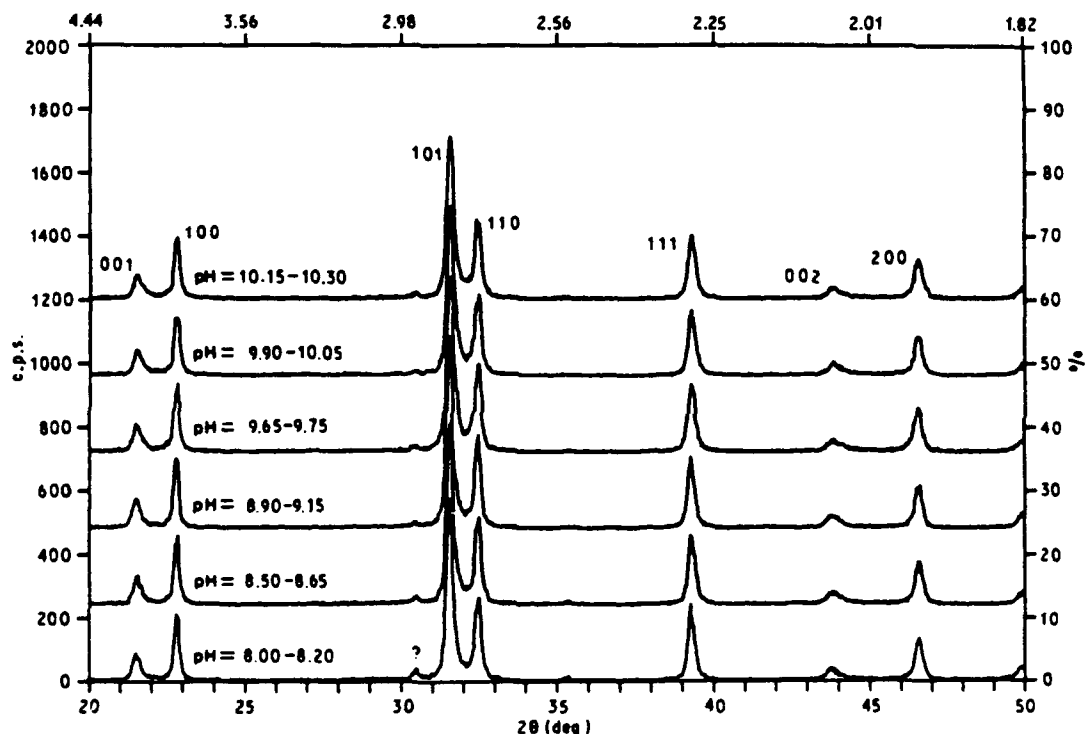


Figure 1 X-ray diffraction patterns of calcined powders (600 °C for 5 h) precipitated at various pH conditions. PbTiO<sub>3</sub> is the primary phase but an unidentified peak is found at  $d = 0.294 \text{ nm}$  marked by (?).

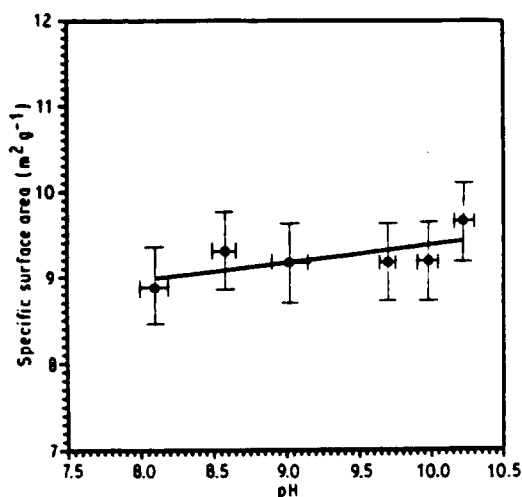


Figure 2 Effects of precipitation pH upon the specific surface area of calcined powders (600 °C for 5 h).

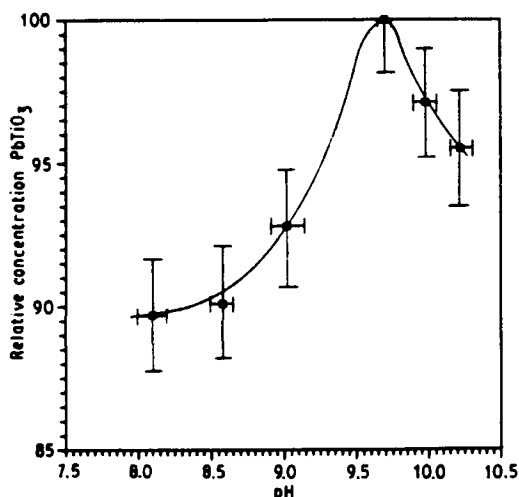


Figure 3 Effects of precipitation pH upon the concentration of crystalline PbTiO₃ in the calcined powders (600 °C for 5 h).

second phase, then formation of the second phase would appear to be controlled by the solubility of the lead species. As stated previously, however, a study covering a wider pH range is needed to determine whether the formation of the unidentified phase is controlled by lead solubility, changes in speciation of the lead, or a combination of these phenomena. Both the transformation rate of the amorphous powder and the formation of the second phase are likely to contribute to the pH dependency of the quantity of crystalline PbTiO₃ observed in calcined powders.

### 3.2. Effects of H₂O₂ upon properties of calcined precipitates

All X-ray diffraction patterns of the calcined powders from set two, with increasing H₂O₂:PbTiO₃ ratios, exhibited primarily PbTiO₃ peaks with less than 2% by weight unidentified second phase. This finding indicates that H₂O₂ additions do not affect the

crystalline phases present in the calcined powders. Although the type of crystalline phases formed from the precipitates is not influenced by the H₂O₂ additions, the widths and intensities of the diffraction peaks change with increasing H₂O₂ concentration (see Fig. 4).

The change in specific surface area of the calcined powder as a function of H₂O₂ concentration during precipitation is shown in Fig. 5. There is a minimum in the specific surface area at an H₂O₂:PbTiO₃ ratio 1.1:1. The as-precipitated powders described in the first part of the study [1] exhibited a maximum in the specific surface area at H₂O₂:PbTiO₃ = 1.1:1. The powders with the highest specific surface areas before calcination have the lowest specific surface areas after calcination. Therefore, the powder prepared with H₂O₂:PbTiO₃ = 1.1:1 exhibits the highest growth rate during calcination which is consistent with the large surface area of the precipitate prior to calcination.

In Fig. 6, the X-ray diffraction integrated 111 peak intensities were used to determine the concentration of crystalline PbTiO₃ relative to an external PbTiO₃ standard. The concentration of PbTiO₃ displays a maximum as a function of increasing H₂O₂ concentration. The results indicate that the powder prepared with H₂O₂:PbTiO₃ = 1.1:1 contains the highest concentration of crystalline PbTiO₃ and therefore transforms from the amorphous to the crystalline state at the fastest rate. Comparison of the data in Figs 5 and 6 supports the contention that the precipitate prepared with H₂O₂:PbTiO₃ = 1.1:1 has the highest nucleation and growth rate during transformation from the amorphous to the crystalline state.

The reason why H₂O₂ affects the nucleation and growth rate of crystalline PbTiO₃ during transformation from the amorphous precipitates may be due to several factors. First, since the free energy for the transformation to the crystalline state is partly dependent upon the reduction of surface area [2, 3], the amorphous powders exhibiting the highest specific surface area will have the largest driving force for transformation. Therefore, the effect of H₂O₂ upon the nucleation and growth rates may only be an artifact due to the influence of H₂O₂ on the specific surface area of the precipitated powders. Evidence for this is given by the correlation between the maximum in the specific surface area plotted against H₂O₂:PbTiO₃ for the as-precipitated powders (see Part I, Fig. 3) [1], and the maximum for concentration of PbTiO₃ against H₂O₂:PbTiO₃ (Fig. 6). This correlation in maxima suggests that the powder prepared at H₂O₂:PbTiO₃ = 1.1:1 exhibits the highest amorphous to crystalline transformation rate because it exhibits the highest specific surface area, and therefore, the highest surface free energy change upon transformation and growth.

Another reason why H₂O₂ influences the nucleation and growth rates of the crystalline PbTiO₃ may be due to the effect that H₂O₂ has on the anionic species present in the precipitates. As found in Part [1], carbonates are formed when no H₂O₂ is added to the system, and changes in structural water content may occur at high H₂O₂ concentrations. Therefore,

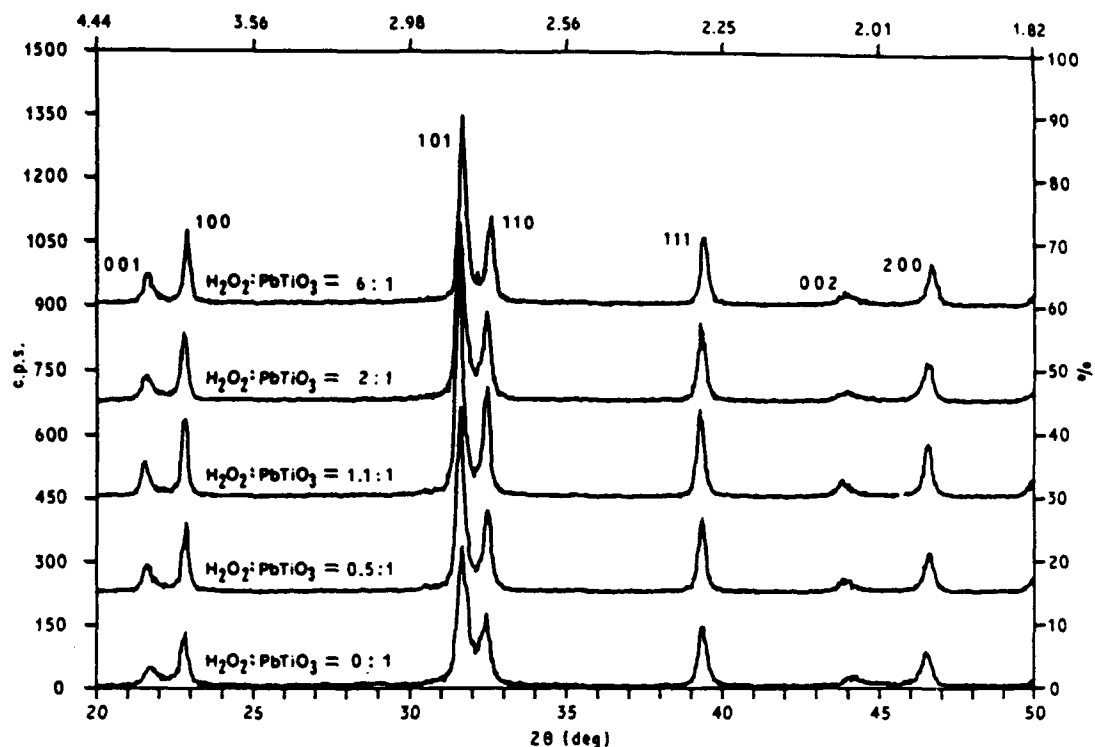


Figure 4 X-ray diffraction patterns for calcined precipitates (600 °C for 5 h) prepared with increasing  $\text{H}_2\text{O}_2$  concentration. Pure  $\text{PbTiO}_3$  is observed for each of the powders.

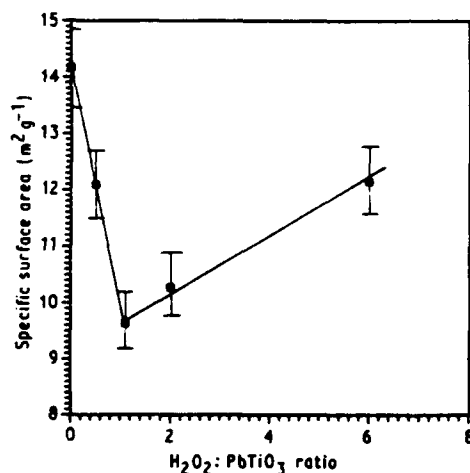


Figure 5 Specific surface area of calcined precipitates (600 °C for 5 h) with increasing  $\text{H}_2\text{O}_2$  concentration.

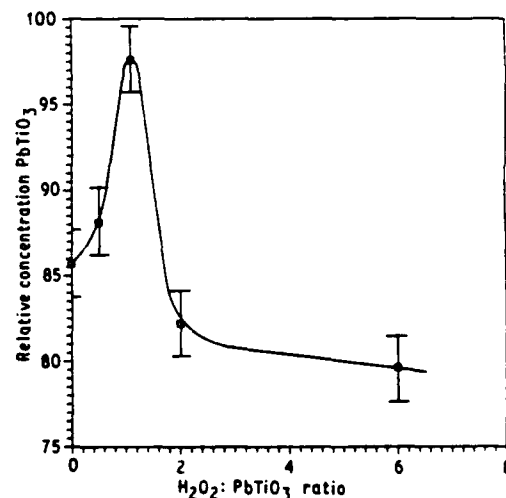


Figure 6 Effects of  $\text{H}_2\text{O}_2$  concentration upon concentration of crystalline  $\text{PbTiO}_3$  in calcined precipitates (600 °C for 5 h).

the pronounced effect that  $\text{H}_2\text{O}_2$  has upon the transformation of the amorphous precipitates to crystalline  $\text{PbTiO}_3$  is most likely due to a combination of the effects that  $\text{H}_2\text{O}_2$  has on both the specific surface area of the precipitates and the anionic species contained in the precipitates.

#### 4. Conclusions

Formation of crystalline  $\text{PbTiO}_3$  in powders prepared by the coprecipitation–calcination process is found to be highly dependent upon the solubility and speci-

ation of lead and titanium and their chemical derivatives. Both solubility and speciation are dependent upon concentration and pH, and therefore, both concentration and pH will affect the phases formed during the precipitation–calcination process. The final crystalline phases are not affected by  $\text{H}_2\text{O}_2$  additions. Pure  $\text{PbTiO}_3$  is not obtainable at pH below 9.00 because of the appearance of a persistent second phase. Above pH 9.00 greater than 98% by weight pure  $\text{PbTiO}_3$  is formed but the rate at which the amorphous precipitates transform to crystalline  $\text{PbTiO}_3$  exhibits a maximum as a function of both pH

and  $\text{H}_2\text{O}_2$  concentration. The maximum transformation rate from amorphous precipitates to greater than 98% pure crystalline  $\text{PbTiO}_3$  is with  $\text{H}_2\text{O}_2:\text{PbTiO}_3 = 1.1:1$  and  $\text{pH} = 9.65$  to  $9.75$ .

#### Acknowledgements

The authors would like to thank Anne Casciani for the specific surface area measurements.

#### References

1. G. R. FOX, J. H. ADAIR and R. E. NEWNHAM, *J. Mater. Sci.* **25** (1990) 3634-40.
2. V. K. LA MER, *Ind. Eng. Chem.*, **44** (1952) 1270.
3. R. SMOLUCHOWSKI, *ibid.* **44** (1952) 1321.

*Received 24 January  
and accepted 24 August 1989*

## **APPENDIX 34**

## Kinetics of the hydrothermal crystallization of the perovskite lead titanate

G.A. Rossetti, Jr., D.J. Watson<sup>1</sup>, R.E. Newnham and J.H. Adair<sup>2</sup>

*Materials Research Laboratory, The Pennsylvania State University, University Park, Pennsylvania 16802, USA*

Received 21 March 1991; manuscript received in final form 16 October 1991

The hydrothermal crystallization kinetics for the perovskite  $\text{PbTiO}_3$  have been investigated under autogenous conditions at temperatures in the range of 225–250°C and feedstock concentrations of 0.1–1.0 M. At these temperatures, crystalline perovskite particles were obtained in approximately 4–7 h. Transmission electron microscopy (TEM) of the product oxides showed nanometer sized crystallites with an elongated morphology. The crystallization kinetics were monitored using X-ray powder diffraction on samples extracted from the reaction mixture at various times. The crystallization rate data were analyzed according to a generalized solid-state kinetic treatment which, along with microstructural evidence, suggest that the  $\text{PbTiO}_3$  formation reaction proceeds via a dissolution–recrystallization mechanism. It is proposed that the precursor amorphous hydrous oxides of lead and titanium dissolve and recrystallize to form the perovskite phase. The relative rates of dissolution and recrystallization were found to be strongly temperature dependent within the range examined. At all temperatures, the recrystallization kinetics appeared to obey a zero-order rate law. An apparent activation energy of 7.2 kcal/mol was estimated for the hydrothermal  $\text{PbTiO}_3$  formation reaction.

### 1. Introduction

Hydrothermal particle synthesis involves the treatment of aqueous solutions or suspensions of precursor particles at elevated temperatures and pressures. The reactions occurring in hydrothermally treated solutions of inorganic compounds can produce fine, high purity, and homogeneous particles of single and multicomponent metal oxides under the appropriate conditions [1–8]. Furthermore, particle sizes from nanometer to centimeter ranges can be synthesized depending on the configuration of the hydrothermal equipment. However, the reaction sequences in hydrothermal systems are complex, and at the present time there is scant information regarding the reaction kinetics and underlying mechanisms [9]. Hydrothermal reactions are analogous to solid-state

reactions, but with correspondingly enhanced diffusion rates [9]. The reaction mechanisms and sequences that can lead to crystalline particle formation therefore include dissolution or transformation of any solid precursor phase(s), diffusion in solution, adsorption at the solid–liquid interface, surface diffusion, incorporation of solute material into the lattice, and crystal growth steps [8–12]. Unfortunately, the relatively high temperatures and pressures for hydrothermal syntheses (e.g., 100–500°C and 0.1–14 MPa, respectively) prohibit in most cases the use of in-situ systems to monitor the course of the reactions leading to product particle formation. Consequently, meaningful data relating to particle formation can at present often be obtained only by studying the solid-state nature of the reaction.

In the present work, we have evaluated the hydrothermal formation of the binary lead titanium oxide,  $\text{PbTiO}_3$ . The solution speciation and phase equilibria for this relatively complex, but technologically important, system have not been studied. However, there have been several studies

<sup>1</sup> Currently with IBM Fishkill, Hopewell Junction, New York 12533, USA.

<sup>2</sup> Currently with Material Science and Engineering, University of Florida, Gainesville, Florida 32611, USA.

verifying that lead titanate is the stable compound under a wide range of hydrothermal reaction temperatures and pressures [2–8]. Furthermore, studies that preceded the work currently being reported have demonstrated that a range from pH 9 to pH 10 is suitable to produce stoichiometric  $\text{PbTiO}_3$  with the perovskite crystal structure [6]. The objective of this study was to obtain kinetic data on this system to better understand the particle formation mechanisms for the complex binary oxides and, in particular, the perovskite family of materials.

## 2. Materials and methods

The hydrothermal synthesis of particulate lead titanate employed a solution crystallization process carried out at relatively modest temperatures and pressures (225–250°C and 1.38–5.17 MPa, respectively) [6]. The preparation of the feedstock materials was conducted according to the flowchart shown in fig. 1. Experiments were performed in a 1 liter 316 stainless steel autoclave equipped with a magnetically driven stirring unit (Model 4521, Parr Instruments Co., Moline, IL).

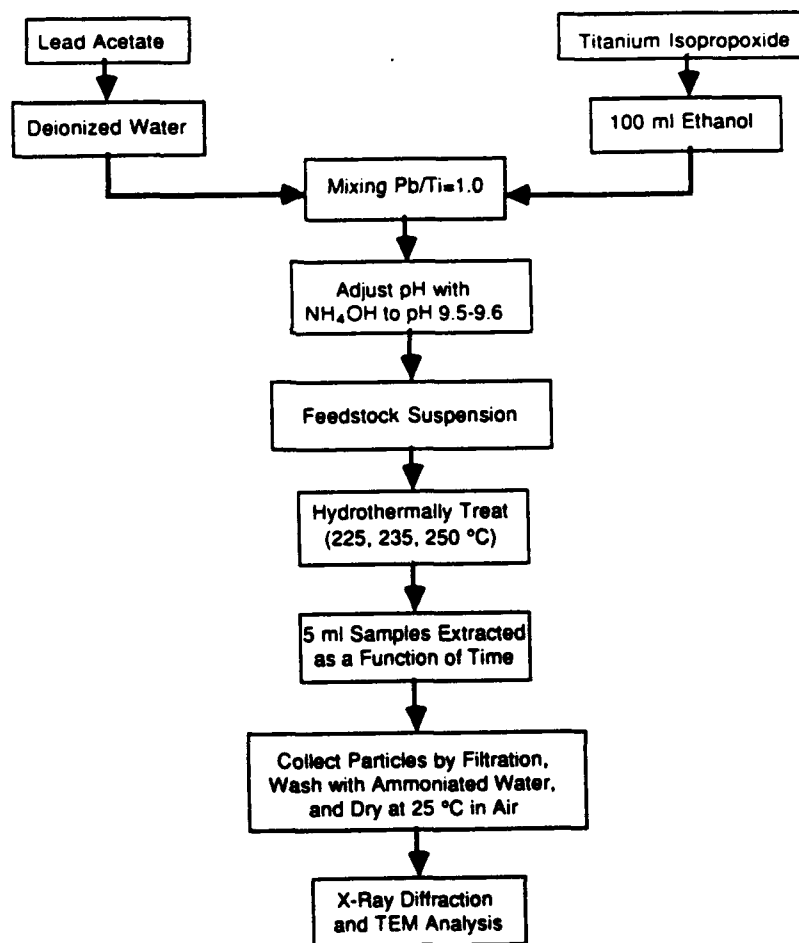


Fig. 1. Flow chart for the hydrothermal synthesis of  $\text{PbTiO}_3$  designed to collect crystallization data as a function of time.

Samples of 5 ml size were extracted under isothermal conditions at various times during the crystallization process. The extraction of these relatively small samples was accompanied by minimal reactor pressure losses ( $\sim 0.014$ – $0.034$  MPa). The solid portion was immediately separated from the extracted suspensions by filtration and/or centrifugation depending on particle size. The solids were then washed with deionized water whose pH had been previously adjusted to pH 9.5 with ammonium hydroxide, filtered again, and air dried at room temperature. It was observed in preliminary studies that washing the powders with a solution near the pH for the minimum solubility of lead oxide and lead titanate was necessary to limit incongruent dissolution of the lead from the hydrothermally treated powders. X-ray powder diffraction patterns for the extracted samples were obtained using an automated diffractometer employing  $\text{Cu K}\alpha$  radiation. The degree of crystallinity of the solids was assessed by integrated intensity analysis of the (101) reflection [13]. Bright field transmission electron micrographs (TEM) were obtained on selected samples and used to estimate the mean particle size. The surface areas of the powders were determined by an automated nitrogen adsorption technique (Monosorb, Quantachrome Corp., Syosset, NY).

### 3. Results and discussion

#### 3.1. Materials characterization

Typical X-ray powder diffraction patterns for the  $\text{PbTiO}_3$  crystallization sequence as a function of hydrothermal reaction time are shown in fig. 2 for samples from a 0.33 molar feedstock solution at  $225^\circ\text{C}$ . As shown in the figure, the starting feedstocks were amorphous and became increasingly crystalline with time. Under these conditions, no change in crystallinity was detected by X-ray diffraction after hydrothermal treatment for  $\sim 7$  h. TEM micrographs corresponding to these samples are shown in fig. 3. The amorphous feedstock particles were 20 nm in diameter, equiaxed, and could be clearly distinguished from the product  $\text{PbTiO}_3$  particles, which crystallized

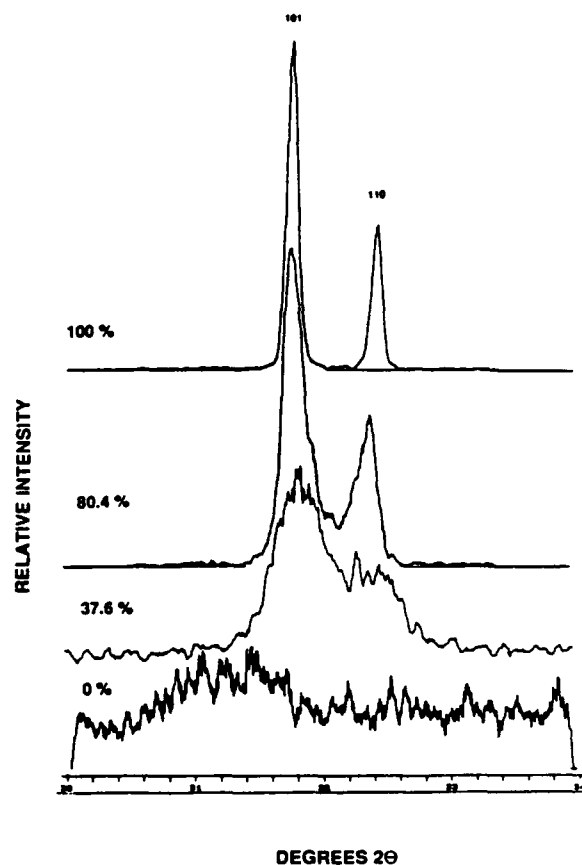


Fig. 2. Examples of X-ray diffraction patterns showing the typical change in crystallinity as a function of reaction time for hydrothermally treated  $\text{PbTiO}_3$ . Data are for 0.33M feedstock hydrothermally treated at  $225^\circ\text{C}$  for 0 time (0% crystallinity), and 37.6%, 80.4%, and 100% crystallinity.

with a relatively uniform, acicular morphology. The influence of feedstock concentration on particle size and surface area for the  $\text{PbTiO}_3$  crystallized at  $225^\circ\text{C}$  is shown in table 1. Particle size increases with feedstock concentration as judged by direct observation from the TEM micrographs and specific surface area measurements.

#### 3.2. Crystallization kinetics

The kinetics of  $\text{PbTiO}_3$  crystallization from a 0.33 molar feedstock suspension are shown at three temperatures in fig. 4. Qualitatively, the crystallization process may be divided into three



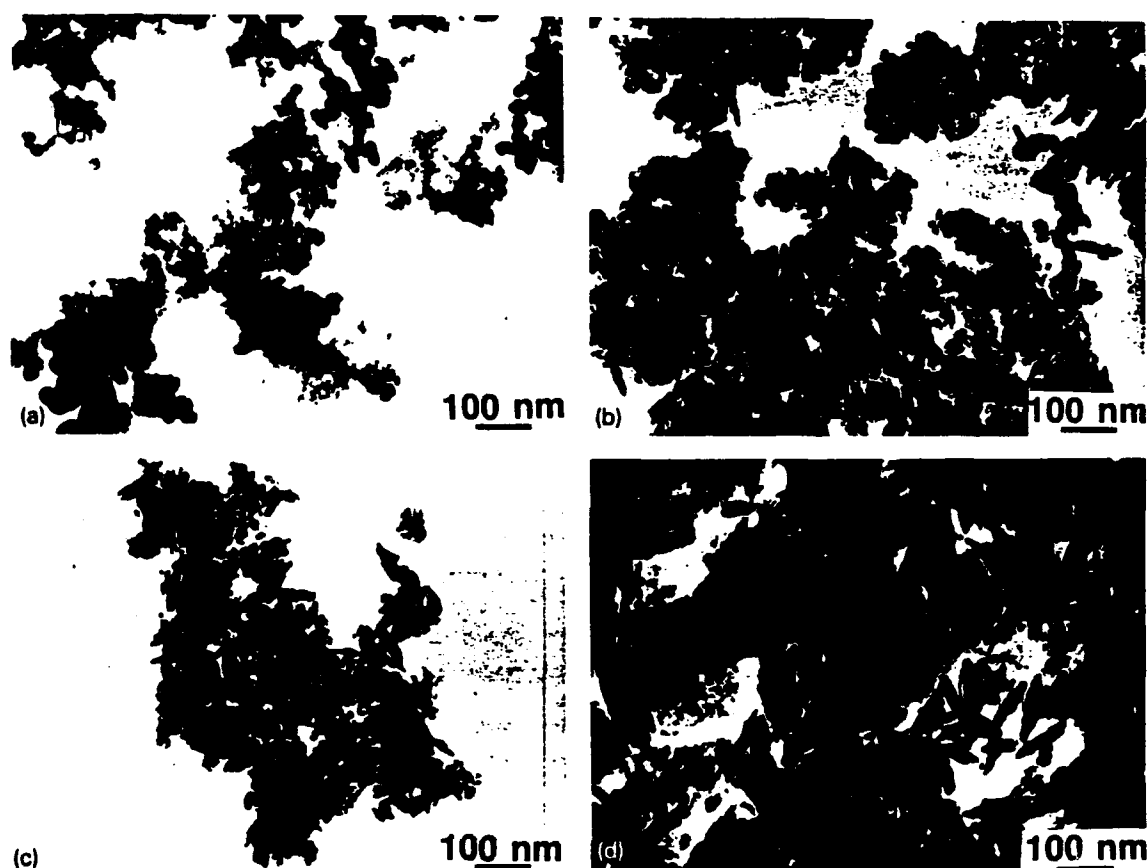


Fig. 3. Examples of transmission electron micrographs of some typical particle samples extracted from a 0.33M feedstock at 225°C as a function of reaction time: (a) 0%, (b) 37.6%, (c) 80.4%, and (d) 100% crystallinity.

distinct kinetic regimes. At relatively short reaction times there is a temperature-dependent induction time with no measurable crystallization taking place, followed by an initial period of rapid crystallization at intermediate times, and,

last, a second period of crystallization at a lower rate than during the intermediate regime. The transition between the two periods of crystalliza-

Table 1

Crystallite sizes and specific surface areas for the  $\text{PbTiO}_3$  particles hydrothermally synthesized at 225°C to 100% crystallinity as a function of feedstock concentration

| Feedstock concentration (mol/l) | Crystallite size <sup>a</sup> (length/diameter) (nm) | Specific surface area ( $\text{m}^2/\text{g}$ ) |
|---------------------------------|--|---|
| 1.00                            | 750/220  | 7.8   |
| 0.50                            | 560/160  | 13  |
| 0.33                            | 280/90   | 22  |
| 0.10                            | 70/20  | 33  |

<sup>a</sup> Estimated from TEM photomicrographs.

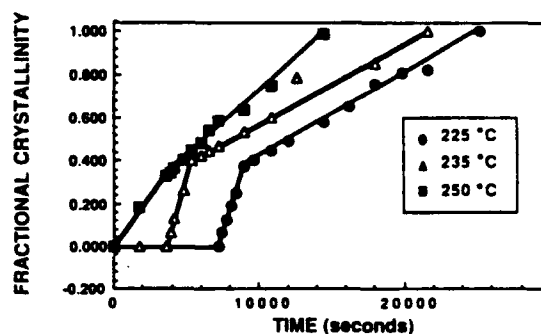


Fig. 4. Fractional  $\text{PbTiO}_3$  crystallinity as a function of time for 0.33M feedstocks hydrothermally treated at 225, 235, and 250°C.

tion occurred at approximately 30–40% crystallinity for all temperatures.

In order to gain further insight into the factors controlling the hydrothermal formation of crystalline  $\text{PbTiO}_3$ , the rate data in fig. 4 were analyzed according to the generalized solid-state kinetic treatment of Hancock and Sharp [14]. This method was originally applied to isothermal solid-state transformations such as the dehydroxylation of brucite [14] and has also been successfully applied to more complex heterogeneous reaction sequences in both oxide [15] and non-oxide [16] systems. Care must be exercised, however, to ensure that a literal interpretation is not assigned to the rate constants or rate laws determined in this way from the simple regression analyses. Even when precise statistical data sets are available, best-fit rate constants obtained from regression analyses can be substantially in error [17]. Despite these reservations, careful application of simple kinetic treatments is often helpful in developing a qualitative understanding of the dominant processes in complex solid-state reaction systems, particularly when corroborated by microstructural evidence and other data.

Recognizing these limitations, and considering only the solid-state nature of the transformation, a kinetic analysis was applied based on the Johnson-Mehl-Avrami equation [18,19]:

$$f = 1 - \exp(-rt^m), \quad (1)$$

or, in linear form,

$$-\ln \ln(1 - f) = \ln(r) + m \ln(t), \quad (2)$$

where  $f$  is the fraction crystallized isothermally at time  $t$ ,  $r$  is a constant that partially depends on nucleation frequency and rate of grain growth, and  $m$  is a constant that varies with the system geometry. Hancock and Sharp have shown that for reactions obeying a single theoretical rate expression, plots of  $-\ln \ln(1 - f)$  against  $\ln(t)$  over  $f = 0.15$ – $0.50$  yield approximately straight lines with slopes  $m$  having a value falling within a range characteristic of three distinct reaction mechanisms. When  $m = 0.54$ – $0.62$ , a diffusion controlled mechanism is indicated, while a zero-order, first-order, or phase boundary controlled mechanism is indicated for  $m = 1.0$ – $1.24$ . A mechanism involving nucleation and growth control is indicated when  $m = 2.0$ – $3.0$ . Values of  $m$  lying outside the specified ranges have no obvious mechanistic interpretation, but can sometimes be indicative of competing processes [14]. The various standard solid-state reaction rate equations and associated values of  $m$  are summarized in table 2. It is not possible to distinguish the most appropriate rate law within a given group solely on the basis of the value of  $m$ . Instead, the individual rate laws must be tested and compared over the complete conversion range [20].

In fig. 5, plots of  $-\ln \ln(1 - f)$  against  $\ln(t)$  over  $f = 0.15$ – $0.50$  for the data in fig. 4 are presented. For  $\text{PbTiO}_3$  crystallization at 225 and 235°C, it is shown in figs. 5a and 5b that the kinetics are described by a two-stage rate law. In each case, the kinetics of the first stage are characterized by a large  $m$  exponent ( $m > 5$ ) followed by a sharp transition at  $f = 0.3$ – $0.4$  to a second

Table 2  
Solid-state reaction rate equations (from ref. [14])

| Function | Implied mechanism     | Equation                        | $m$  |
|----------|-----------------------|---------------------------------|------|
| $D_1(f)$ | Diffusion controlled  | $f^2 = kt$                      | 0.62 |
| $D_2(f)$ | Diffusion controlled  | $(1 - f) \ln(1 - f) + f = kt$   | 0.57 |
| $D_3(f)$ | Diffusion controlled  | $[1 - (1 - f)^{1/3}]^2 = kt$    | 0.54 |
| $D_4(f)$ | Diffusion controlled  | $1 - 2f/3 - (1 - f)^{2/3} = kt$ | 0.57 |
| $F_1(f)$ | First order           | $-\ln(1 - f) = kt$              | 1.00 |
| $R_2(f)$ | Phase boundary        | $1 - (1 - f)^{1/2} = kt$        | 1.11 |
| $R_1(f)$ | Phase boundary        | $1 - (1 - f)^{1/3} = kt$        | 1.07 |
| $Z_1(f)$ | Zero order            | $f = kt$                        | 1.24 |
| $A_2(f)$ | Nucleation and growth | $[-\ln(1 - f)]^{1/2} = kt$      | 2.00 |
| $A_1(f)$ | Nucleation and growth | $[-\ln(1 - f)]^{1/3} = kt$      | 3.00 |

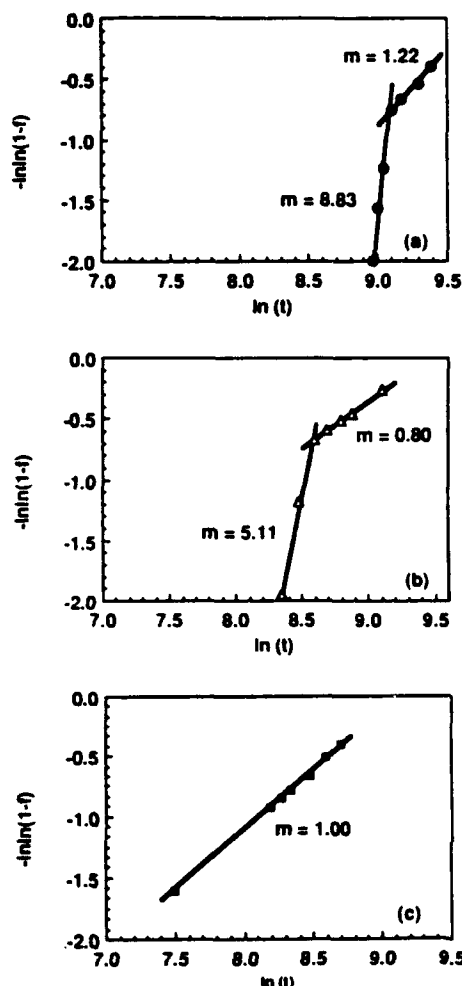


Fig. 5. Plots based on the Johnson-Mehl-Avrami analyses of the kinetic data from fig. 4.

stage characterized by an  $m$  value close to unity. The  $m$  exponent for the first stage decreases rapidly with increasing temperature, so that for crystallization at  $250^\circ\text{C}$ , the first stage is not obvious and the kinetics may apparently be described in terms of a single rate law, as shown in fig. 5c.

In figs. 5a and 5b, the  $m$  exponent of the first stage ( $m = 8.83$  and  $5.11$ , respectively) reflects the initial period of rapid crystallization in the early portions of the corresponding curves of fig. 4. Comparison of these  $m$  exponents with the theoretical values presented in table 2 shows that the kinetics of the initial stage of crystallization

cannot be simply described by any of the ten standard solid-state reaction rate equations.

On the other hand, the  $m$  exponent of the second-stage crystallization in figs. 5a and 5b, along with the single  $m$  value of fig. 5c ( $m = 1.22$ ,  $0.80$ , and  $1.00$ , respectively), suggest a reaction mechanism best described in terms of zero-order, first-order, or phase boundary controlled rate expressions. Consequently, the rate expressions for zero-order, first-order and phase boundary controlled mechanisms were tested over the second-stage crystallization ranges indicated by the  $m$  values of fig. 5. The first-order and phase boundary controlled rate equations gave poor fits of the raw kinetic data when continued to complete crystallization ( $f = 1.0$ ). In accordance with a zero-order rate law, however, fig. 4 shows that the second-stage ( $f > 0.3-0.4$ ) plots of  $f$  against  $t$  for  $\text{PbTiO}_3$  crystallization at  $225$  and  $235^\circ\text{C}$  are in fact linear. Fig. 4 indicates that the  $\text{PbTiO}_3$  crystallization kinetics at  $250^\circ\text{C}$  are also linear for  $f > 0.3-0.4$ . Over the specified crystallization ranges, therefore, the zero-order rate expression is most appropriate to describe the apparent crystallization kinetics. In fig. 4, the slight nonlinearity in the crystallization kinetics at  $250^\circ\text{C}$  for  $f < 0.3-0.4$  is contrary to the expectation from fig. 5c that only a single rate expression should be obeyed. However, it is likely that the crystallization kinetics at  $250^\circ\text{C}$  also conform to a two-stage rate law, but that first-stage crystallization was not detected due to the rapid initial rates at the higher temperature.

An Arrhenius plot for the hydrothermal  $\text{PbTiO}_3$  formation reaction is given in fig. 6. Using a method similar to that of Culfaz and Sand [21], the values plotted along the ordinate in fig. 6 represent the instantaneous rate determined at 50% crystallinity. This method was chosen because it makes no assumption regarding the underlying reaction mechanisms and associated rate laws. Even in the crystallization regime where the reaction is apparently isokinetic (i.e.,  $f > 0.4$ ), the rate data were used in preference to rate constants in constructing the plot because the error in the zero-order fits, as well as the extent to which the initial rapid crystallization at various temperatures affects the subsequent

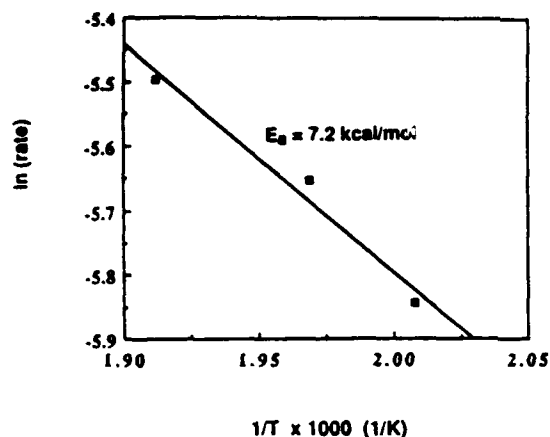


Fig. 6. Arrhenius plot for the hydrothermally crystallized  $\text{PbTiO}_3$ . The apparent activation energy for hydrothermal crystallization of  $\text{PbTiO}_3$  from the plot is 7.2 kcal/mol.

zero-order rate, is uncertain. The apparent activation energy obtained in this way is 7.2 kcal/mol.

### 3.3. Mechanistic interpretation

The microstructural and kinetic data presented above provide some insight into the mechanism of the hydrothermal formation of crystalline  $\text{PbTiO}_3$ . Based on the microstructural data of fig. 3, a mechanism involving a liquid assisted solid-state transformation [22–24] is deemed unlikely. The crystalline material in the micrographs of Fig. 3 does not appear to have grown out of the amorphous precursor. Furthermore, at no stage in the crystallization is there any evidence of partially or poorly crystalline material, as would be expected during the progress of a solid-state transformation. Similarly, the morphologies of the particles in the micrographs of fig. 3 would not be expected for a material precipitated via a classical nucleation and growth mechanism [11,12]. The particles are seen to be nearly the same size with similar acicular morphologies. A larger size distribution is expected if particles are precipitated from a heterogeneous, locally supersaturated solution [11]. In contrast, a narrow size distribution is more typical of particles precipitated from homogeneous solution [25–28]. Moreover, the particle size and surface area data of table I show that the average particle size decreases with decreas-

ing feedstock concentration. Such a result is not supported by a classical nucleation and growth model, which would predict higher supersaturation conditions and smaller particles at higher feedstock concentrations [11].

Alternatively, the generation of reacting species by the process generally known as precipitation from homogeneous solution (PFHS) [26–28] is often observed in systems where temperature is used to thermally decompose precursor reactants [24–27]. It is generally acknowledged that a major limitation in the PFHS reaction scheme is that relatively low concentrations of precursor species must be used to avoid continuous nucleation throughout the particle formation process. In the current work, the microstructural data strongly support the contention that PFHS is taking place in the  $\text{Pb-Ti-H}_2\text{O}$  system under hydrothermal conditions. However, in this system, a sparingly soluble precursor hydrous oxide was used to generate the reacting species. Under these conditions, a high yield of product powder is potentially attainable using relatively concentrated precursor suspensions. Furthermore, the high concentration of feedstock is not expected to compromise the generation of nuclei as it does in classical PFHS because the reservoir of nutrient stored in the solid precursor does not influence solution factors such as supersaturation and ionic strength.

Consequently, with reference to the schematic solubility curves shown in fig. 7, it is proposed that as the hydrothermal temperature is increased, the dissolution of the precursor hydrous oxides dictates the supersaturation ( $S_{12}$ ) at which  $\text{PbTiO}_3$  crystallizes. Assuming normal solubility behavior, this is consistent with the temperature-dependent induction time observed in the kinetic data of fig. 4. When the hydrothermal temperature is increased to the range where the solubility of the precursor hydrous oxide ( $S_p$ ) is greater than that of the anhydrous oxide ( $S_{pm}$ ), crystallization of the latter will take place with the nutrient precursor material acting as a reservoir for the precipitating species. If the particle growth is not topotactic with the precursor particles, then nucleation of the  $\text{PbTiO}_3$  is required. It is believed that this corresponds to the rapid, first-

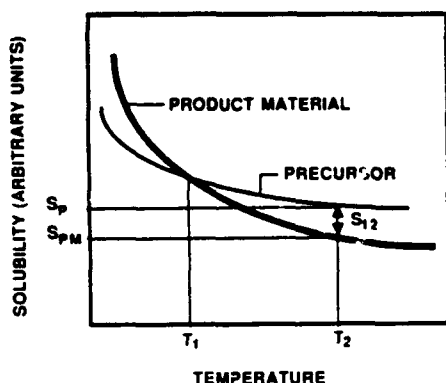


Fig. 7. Reaction scheme proposed for the hydrothermal crystallization of  $\text{PbTiO}_3$ . It is proposed that the difference in solubility of the precursor hydrous oxide and the product material,  $\text{PbTiO}_3$ , at the hydrothermal reaction temperature provides the driving force or supersaturation,  $S_{12}$ , necessary to nucleate and grow  $\text{PbTiO}_3$  particles via precipitation from homogeneous solution.

stage crystallization. As might be expected for a such a complex dissolution-recrystallization process, the  $m$  exponents for this stage of crystallization (fig. 5) did not correspond to any of the theoretical values for the standard solid-state reaction rate equations (table 2).

Once sufficient nuclei are formed, as dictated by the relative supersaturation at a particular temperature, growth will commence. It is believed that this corresponds to the sharp transition to a second-stage crystallization at  $f \approx 0.3$ – $0.4$  as observed in fig. 5. With the dissolution of a precursor solid providing the nutrient for the ultimate crystalline phase, uniformly shaped, nearly monosized particles are produced, provided that the dissolution or decomposition of the precursor material is the rate-limiting step. The zero-order kinetic dependence of the second-stage crystallization is consistent with this requirement. Zero-order kinetics imply that the reaction rate is independent of the concentration of the reactants, and are observed in systems where the rate is controlled by a large excess of one reactant, or is dictated by an external variable, such as the intensity of light in a photocatalyzed reaction [29]. In the mechanism proposed, crystallization can continue only so long as there is sufficient nutrient to maintain supersaturation.

When the nutrient is depleted to the point where this is no longer possible, the crystallization might be expected to end abruptly, with little premonitory diminution of the crystallization rate as 100% crystallinity is approached.

#### 4. Summary

Crystalline, nanometer sized  $\text{PbTiO}_3$  particles were synthesized under autogenous hydrothermal conditions at temperatures in the range of 225–250°C and feedstock concentrations of 0.1–1.0 molar. Under these conditions, the product particles crystallized with a relatively uniform acicular morphology. In contrast to expectations based on classical nucleation and growth models, the particle size was found to increase at higher feedstock concentrations. A simple solid-state analysis of the crystallization rate data showed that the kinetics could be characterized by three regimes corresponding to a temperature-dependent induction period, an initial period of rapid crystallization, and a second period of crystallization obeying a zero-order rate law. To account for these observations, a particle formation mechanism was proposed wherein an anhydrous oxide leading to the perovskite phase is precipitated from a homogeneous solution, the supersaturation condition of which is dictated by the solubility of a sparingly soluble amorphous hydrous oxide precursor. It is suggested that this reaction scheme may be useful in preparing uniform, monosized particles of complex oxides from high concentrations of nutrient and at high yields.

#### Acknowledgment

The authors would like to thank Dr. C.A. Randall of the Materials Research Laboratory for performing the transmission electron microscopy.

#### References

- [1] E.P. Stambaugh and R.A. Foos, US Patent #3,090,770, 1963.

- [2] T.R.N. Kutty and R. Balachandran, *Mater. Res. Bull.* 19 (1984) 1479.
- [3] M. Suzuki, S. Uedaira, H. Masuya and H. Tamura, in: *Ceramic Transactions, Ceramic Powder Science II* (Am. Ceram. Soc., 1987) p. 163.
- [4] K. Takai, S. Shoji, H. Naito and A. Sawaoka, in: *Proc. 1st Intern. Symp. on Hydrothermal Reactions*, Ed. S. Somiya (Gakujutsu Bunken Fukyo-kai, c/o Tokyo Inst. Technol., 1982) p. 877.
- [5] S. Kaneko and F. Imoto, *Bull. Chem. Soc. Japan* 51 (1978) 1739.
- [6] D.J. Watson, C.A. Randall, R.E. Newnham and J.H. Adair, in: *Ceramic Transactions, Ceramic Powder Science II* (Am. Ceram. Soc., 1987) p. 154.
- [7] I. Abe, M. Aoki, H. Rikimaru, T. Ito, K. Hidaka and K. Segawa, US Patent #4,643,984, 1987.
- [8] N.A. Ovramenko, L.I. Shvets, F.D. Ovcharenko and B.Yu. Kornilovich, *Inorgan. Mater.* 15 (1979) 1560.
- [9] V.A. Kuznetsov, *Kristallografiya* 9 (1963) 123.
- [10] A. Norlund Christensen, *Acta Chem. Scand.* 24 (1970) 2447.
- [11] A.E. Nielsen, *Kinetics of Precipitation* (Pergamon, Oxford, 1969).
- [12] A.G. Walton, *The Formation and Properties of Precipitates* (Krieger, 1979).
- [13] G.R. Fox, E. Breval and R.E. Newnham, *J. Mater. Sci.* 26 (1991) 2566.
- [14] J.D. Hancock and J.H. Sharp, *J. Am. Ceram. Soc.* 55 (1972) 74.
- [15] R.A. Gardner, *J. Solid State Chem.* 9 (1974) 336.
- [16] G.A. Rossetti, Jr. and R.P. Denkwicz, Jr., *J. Mater. Sci.* 24 (1989) 3081.
- [17] A.H. Weiss, *Catal. Rev.* 5 (1971) 283.
- [18] M.J. Avrami, *J. Chem. Phys.* 7 (1939) 1103; 8 (1946) 212.
- [19] B.V. Erofe'ev, *Compt. Rend. Acad. Sci. URSS* 52 (1946) 511.
- [20] J.H. Sharp, G.W. Brindley and B.N.N. Achar, *J. Am. Ceram. Soc.* 49 (1966) 379.
- [21] A. Culfaz and L.B. Sand, *Advan. Chem. Ser.* 121 (1987) 41.
- [22] W.J. Dawson, *Am. Ceram. Soc. Bull.* 67 (1988) 1673.
- [23] J.H. Adair, R.P. Denkwicz, F.J. Arriagada and K. Osseo-Asare, in: *Ceramic Trans., Ceramic Powder Science, Vol. I* (Am. Ceram. Soc., Westerville, OH, 1988) p. 135.
- [24] E. Tani, M. Yoshimura and S. Somiya, *J. Am. Ceram. Soc.* 66 (1983) 11.
- [25] L. Gordan, M.L. Salutsky and H.H. Willard, *Precipitation from Homogeneous Solution* (Wiley, New York, 1959).
- [26] H.H. Willard and N.K. Tang, *J. Am. Chem. Soc.* 59 (1937) 1190.
- [27] J.T.G. Overbeek, *Advan. Colloid Interface Sci.* 15 (1982) 251.
- [28] V.K. LaMer and R.H. Dinegar, *J. Am. Chem. Soc.* 72 (1950) 4847.
- [29] O. Levenspiel, *Chemical Reaction Engineering* (Wiley, New York, 1972) pp. 51-53.